

# Triggered Lightning Risk Assessment for Reusable Launch Vehicles at Four Regional Spaceports

April 30, 2010

Richard L. Walterscheid<sup>1</sup>, Lynette J. Gelinis<sup>1</sup>, Glenn W. Law<sup>2</sup>, Grace S. Peng<sup>3</sup>,  
Robert W. Seibold<sup>2</sup>, Frederick S. Simmons<sup>4</sup>, Paul F. Zittel<sup>5</sup>

John C. Willett  
Consultant, Garrett Park, Maryland

E. Philip Krider  
Institute of Atmospheric Physics  
University of Arizona, Tucson, Arizona

<sup>1</sup>Space Sciences Department, Physical Sciences Laboratories;

<sup>2</sup>Civil and Commercial Launch Systems, Space Launch Projects;

<sup>3</sup>Computer Systems Research Department, Computer Science and Technology Subdivision;

<sup>4</sup>Sensor Systems Subdivision, Electronics and Sensors Division;

<sup>5</sup>Remote Sensing Department, Physical Sciences Laboratories

Prepared for:

Volpe National Transportation Systems Center  
U.S. Department of Transportation  
Cambridge, Massachusetts

Contract No. DTRT57-05-D-30103  
Task 13A

Authorized by: Space Launch Operations

Public release is authorized.

<b>REPORT DOCUMENTATION PAGE</b>			<i>Form Approved</i> <i>OMB No. 0704-0188</i>		
<p>The public reporting burden for this collection of information is estimated to average 1 hour per response, including the time for reviewing instructions, searching existing data sources, gathering and maintaining the data needed, and completing and reviewing the collection of information. Send comments regarding this burden estimate or any other aspect of this collection of information, including suggestions for reducing the burden, to the Department of Defense. Executive Services and Communications Directorate (0704-0188). Respondents should be aware that notwithstanding any other provision of law, no person shall be subject to any penalty for failing to comply with a collection of information if it does not display a currently valid OMP control number.</p> <p><b>PLEASE DO NOT RETURN YOUR FORM TO THE ABOVE ORGANIZATION.</b></p>					
<b>1. REPORT DATE (DD-MM-YYYY)</b> 30-04-2010		<b>2. REPORT TYPE</b> Contractor Final Report		<b>3. DATES COVERED (FROM - TO)</b> August 08, 2007 – April 30, 2010	
<b>4. TITLE AND SUBTITLE</b>  Triggered Lightning Risk Assessment for Reusable Launch Vehicles at Four Regional Spaceports			<b>5A. CONTRACT NUMBER</b> DTRT57-05-D-30103		
			<b>5B. GRANT NUMBER</b>		
			<b>5C. PROGRAM ELEMENT NUMBER</b>		
<b>6. AUTHOR(S)</b>  Richard L. Walterscheid*, John C. Willett (Consultant), E. Philip Krider (University of Arizona), Lynette J. Gelinias*, Glenn W. Law*, Grace S. Peng*, Robert W. Seibold*, Frederick S. Simmons*, Paul F. Zittel*			<b>5D. PROJECT NUMBER</b> FA2R DL411		
			<b>5E. TASK NUMBER</b> Task Order #13A		
			<b>5F. WORK UNIT NUMBER</b> FA2R DL411		
<b>7. PERFORMING ORGANIZATION NAME(S) AND ADDRESS(ES)</b> U.S. Department of Transportation Research and Innovative Technology Administration Volpe National Transportation Systems Center Safety Information Systems Division Cambridge, MA 02142-1093			<b>8. PERFORMING ORGANIZATION REPORT NUMBER</b> DOT-VNTSC-FAA-10-01		
<b>9. SPONSORING/MONITORING AGENCY NAME(S) AND ADDRESS(ES)</b> U.S. Department of Transportation, Federal Aviation Administration Office of the Assoc. Administrator for Commercial Space Transportation Washington, DC 20591			<b>10. SPONSOR/MONITOR'S ACRONYM(S)</b> FAA AST-300		
			<b>11. SPONSOR/MONITOR'S REPORT NUMBER(S)</b>		
<b>12. DISTRIBUTION/AVAILABILITY STATEMENT</b> Public Release is Authorized.					
<b>13. SUPPLEMENTARY NOTES</b> *The Aerospace Corporation, El Segundo, CA 90245-4691, under contract to the Volpe National Transportation Systems Center—Contract No. DTRT57-05-D-30103, Task 13A. Aerospace Corporation Report No. ATR-2009(5387)-1					
<b>14. ABSTRACT</b> The Aerospace Corporation was tasked by the Volpe National Transportation Systems Center to provide technical support to the Federal Aviation Administration, Office of Commercial Space Transportation, in assessing the risks involved with triggered lightning during suborbital launches and reentries of reusable launch vehicles (RLVs) from four regional spaceports, viz., Spaceport America in New Mexico, the Oklahoma Spaceport, the Mojave Air and Space Port in California, and the West Texas Spaceport. Risk of triggered lightning was studied for four conceptual RLVs originating and/or landing at these spaceports. Five areas were addressed: (1) observed frequencies of natural cloud-to-ground lightning at four spaceports, including data from two existing lightning-mapper arrays, plus estimates of violation frequencies of the other existing lightning flight commit criteria (LFCC), (2) literature summary and new approximate analysis of the effective conducting length of the vehicle plumes, (3) review of the current LFCC to determine if the criteria are relevant to each suborbital RLV concept, including an evaluation of local geographical effects pertaining to each spaceport to determine whether additional LFCC are necessary to conduct safe launch operations there, (4) evaluation of risk based on airborne electric field measurements and cloud, temperature and lightning data, and (5) evaluation of an aircraft icing index as an indicator of high electric fields in clouds at sites that are not instrumented with weather radars and temperature sounders.					
<b>15. SUBJECT TERMS</b> Commercial Space Transportation, Reusable Launch Vehicle, RLV, Suborbital Launch Vehicle, Triggered Lightning, Spaceport, Spaceport America, Oklahoma Spaceport, Mojave Air and Space Port, West Texas Spaceport, Licensing, Regulation, Lightning Launch Commit Criteria					
<b>16. SECURITY CLASSIFICATION OF:</b>			<b>17. LIMITATION OF ABSTRACT</b> UU	<b>18. NUMBER OF PAGES</b> 202	<b>19A. NAME OF RESPONSIBLE PERSON</b> Ruth A. Hunter
<b>A. REPORT</b> U	<b>B. ABSTRACT</b> U	<b>C. THIS PAGE</b> U			

# Triggered Lightning Risk Assessment for Reusable Launch Vehicles at Four Regional Spaceports

April 30, 2010

Richard L. Walterscheid<sup>1</sup>, Lynette J. Gelinis<sup>1</sup>, Glenn W. Law<sup>2</sup>, Grace S. Peng<sup>3</sup>,  
Robert W. Seibold<sup>2</sup>, Frederick S. Simmons<sup>4</sup>, Paul F. Zittel<sup>5</sup>

John C. Willett  
Consultant, Garrett Park, Maryland

E. Philip Krider  
Institute of Atmospheric Physics  
University of Arizona, Tucson, Arizona

<sup>1</sup>Space Sciences Department, Physical Sciences Laboratories;

<sup>2</sup>Civil and Commercial Launch Systems, Space Launch Projects;

<sup>3</sup>Computer Systems Research Department, Computer Science and Technology Subdivision;

<sup>4</sup>Sensor Systems Subdivision, Electronics and Sensors Division;

<sup>5</sup>Remote Sensing Department, Physical Sciences Laboratories

Prepared for:

Volpe National Transportation Systems Center  
U.S. Department of Transportation  
Cambridge, Massachusetts

Contract No. DTRT57-05-D-30103  
Task 13A

Authorized by: Space Launch Operations

# Triggered Lightning Risk Assessment for Reusable Launch Vehicles at Four Regional Spaceports

April 30, 2010

Richard L. Walterscheid<sup>1</sup>, Lynette J. Gelinis<sup>1</sup>, Glenn W. Law<sup>2</sup>, Grace S. Peng<sup>3</sup>,  
Robert W. Seibold<sup>2</sup>, Frederick S. Simmons<sup>4</sup>, Paul F. Zittel<sup>5</sup>

John C. Willett  
Consultant, Garrett Park, Maryland

E. Philip Krider  
Institute of Atmospheric Physics  
University of Arizona, Tucson, Arizona

<sup>1</sup>Space Sciences Department, Physical Sciences Laboratories;

<sup>2</sup>Civil and Commercial Launch Systems, Space Launch Projects;

<sup>3</sup>Computer Systems Research Department, Computer Science and Technology Subdivision;

<sup>4</sup>Sensor Systems Subdivision, Electronics and Sensors Division;

<sup>5</sup>Remote Sensing Department, Physical Sciences Laboratories

Prepared for:

Volpe National Transportation Systems Center  
U.S. Department of Transportation  
Cambridge, Massachusetts

Contract No. DTRT57-05-D-30103  
Task 13A

Authorized by: Space Launch Operations

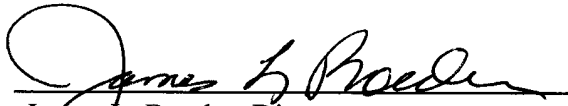
Public release is authorized.



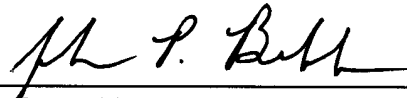


# Triggered Lightning Risk Assessment for Reusable Launch Vehicles at Four Regional Spaceports

Approved by:



James L. Roeder, Director  
Space Sciences Department  
Physical Sciences Laboratories



John P. Brekke, Systems Director  
Civil/Commercial Launch Systems  
Launch Systems Division

## Abstract

The Aerospace Corporation was tasked by the Volpe National Transportation Systems Center to provide technical support to the Federal Aviation Administration, Office of Commercial Space Transportation, in assessing the risks involved with triggered lightning during suborbital launches and reentries of reusable launch vehicles (RLVs) from Spaceport America in New Mexico, the Oklahoma Spaceport, the Mojave Air and Space Port in California, and the West Texas Spaceport. The Aerospace Corporation is pleased to submit this final report, in accordance with the requirements delineated in section F, Deliveries or Performance, of Volpe Center Contract No. DTRT57-05-D-30103, Task 13A.

Risk of triggered lightning was studied for four conceptual RLVs originating and/or landing at these spaceports. Five areas were addressed:

1. Observed frequencies of natural cloud-to-ground lightning at four spaceports, including data from two existing lightning-mapper arrays, plus estimates of violation frequencies of the other existing lightning flight commit criteria (LFCC)
2. Literature summary and new approximate analysis of the effective conducting length of the vehicle plumes
3. Review of the current LFCC to determine if the criteria are relevant to each suborbital RLV concept, including an evaluation of local geographical effects pertaining to each spaceport to determine whether additional LFCC are necessary to conduct safe launch operations there
4. Evaluation of risk based on airborne electric field measurements and cloud, temperature, and lightning data
5. Evaluation of an aircraft icing index as an indicator of high electric fields in clouds at sites that are not instrumented with weather radars and temperature sounders

## Acknowledgments

Gratitude is extended to Ms. Karen Shelton-Mur at the Office of the Associate Administrator for Commercial Space Transportation, Federal Aviation Administration, for valuable guidance on FAA/AST weather-related regulatory and licensing needs. The authors also wish to thank Ms. Ruth A. Hunter, who served as the Contracting Officer's Technical Representative (COTR) at the Volpe National Transportation Systems Center and provided valuable insight into government needs and regulations.

The authors thank Prof. William Rison of the New Mexico Institute of Mining and Technology (NMIMT) for providing the lightning mapper array (LMA) data and for answering numerous questions about data processing and archiving. Terry Huck of the White Sands Missile Range (WSMR) is also thanked for permission to use its data in the present analysis, as is Prof. Donald R. MacGorman of the University of Oklahoma. Dr. Ronald J. Thomas of New Mexico Tech was very helpful to the essential efforts of Michael T. Redding of The Aerospace Corporation, who modified the UNIX version of the Extensible Markup Language for Analysis (XMLA) software to run under Windows. Martin J. Murphy of Vaisala, Inc. suggested an invaluable and efficient and detection-efficiency-independent way to compute lightning statistics from LMA data. Many others participated in helpful discussions along the way.

The authors would also like to thank Drs. Frank McDonough, Brooke E. Lewis, Cory A. Wolff, and Marcia K. Politovich, all of the National Center for Atmospheric Research (NCAR) Research Applications Laboratory for providing the Current Icing Potential (CIP) data and for several helpful discussions, and Dr. Kenneth L. Cummins at Vaisala, Inc., for providing maps of cloud-to-ground lightning.

Dr. Douglas M. Mach at the National Aeronautics and Space Administration (NASA) Marshall Space Flight Center provided recalibration and re-analysis of the airborne electric data originally obtained during the airborne field mill (ABFM)-I experiments at and near the NASA Kennedy Space Center during 1991 and 1992. These results made it possible to estimate of risk of triggered lightning from satellite cloud data and ground-based data on natural lightning.

## Executive Summary

The Aerospace Corporation was tasked by the Volpe National Transportation Systems Center to provide technical support to the Federal Aviation Administration, Office of Commercial Space Transportation (FAA/AST), in assessing the risks involved with triggered lightning during suborbital launches and reentries of reusable launch vehicles (RLVs) from Spaceport America in New Mexico, the Oklahoma Spaceport, the Mojave Air and Space Port in California, and the West Texas Spaceport. The Aerospace Corporation is pleased to submit this final report, in accordance with the tasking.

### 1. Introduction

The purpose of this study was to determine the risk of triggered lightning during suborbital launches of four different RLV concept vehicles originating and/or concluding at the above spaceports. Three areas were addressed:

1. Observed frequencies of cloud-to-ground CG lightning at the spaceports, including estimates of violation frequencies of the existing LFCC
2. Estimates of the ambient fields required for triggering by each of the concept vehicles, including consideration of potential methods for estimating the probability of encountering these field magnitudes from the measured radar returns of thunderstorm anvil clouds
3. Review of the current LFCC

This report covers:

- A survey of the threat (probability) of natural and triggered lightning due to convective and layered clouds, both seasonally and diurnally, at each spaceport.
- A risk level of triggered lightning calculated for each RLV concept vehicle by analyzing the vehicle design (i.e., shape, materials), propellants, and type of operations (i.e., launch altitude, launch platform) at each of the launch sites.
- Review of the current lightning flight commit criteria (LFCC) to determine if the criteria are relevant to each suborbital RLV concept.
- Evaluation of local geographical effects pertaining to each spaceport and a determination of additional LFCC (if any) necessary to conduct safe launch operations for a given RLV design.
- Pros and cons of current electric field measurement techniques and a discussion of new techniques (if any) for direct measurement of the electric field inside the clouds.

In an earlier study [Krider, E. P., J. C. Willett, G. S. Peng, F. S. Simmons, G. W. Law, and R. W. Seibold, *Triggered Lightning Risk Assessment for Reusable Launch Vehicles at the Southwest Regional and Oklahoma Spaceports*, Aerospace Report No. ATR-2006(5195)-130, January 2006, Volpe National Transportation Systems Center U.S. Department of Transportation Contract No. DTRS57-99-D-00062.], the climatology of lightning was examined at Spaceport America (SA) in New Mexico and the Oklahoma Spaceport (OS). The present study extends the climatology to include the Mojave Air and Space Port (MJSP) and the West Texas Launch Site (WTLS) to determine if the

criteria are relevant to each suborbital RLV concept, including an evaluation of local geographical effects to determine whether additional LFCC are necessary to conduct safe launch operations there.

## 2. Spaceports

For this analysis, four spaceports were evaluated: Spaceport (SA) America in New Mexico, the Oklahoma Spaceport (OS), the Mojave Air and Space Port (MJSP) in California, and the West Texas Launch Site (WTLS).

**Spaceport America:** The State of New Mexico is developing Spaceport America near Upham, New Mexico, approximately 45 miles north of Las Cruces and 30 miles east of Truth or Consequences. This location is along the western boundary of the White Sands Missile Range, and will encompass a 27-square-mile site consisting of open, generally level, range land with an average elevation of 4,700 ft. The plans for the spaceport facility call for a launch complex, a landing strip and aviation complex, a payload assembly complex, a support facilities complex, and a system development complex.

**Oklahoma Spaceport:** The Oklahoma Spaceport is located at Burns Flat, Oklahoma, approximately 100 miles west of Oklahoma City. The Oklahoma Spaceport encompasses approximately 3,000 acres and has two runways, at 13,500 ft and 5,200 ft in length. The Spaceport has an operational control tower and an instrument landing system (ILS) capability that can support a full range of aircraft operations.

**Mojave Air and Space Port:** The Mojave Air and Space Port is located in Kern County on the east side of the unincorporated town of Mojave, California. It encompasses approximately 3,000 acres and has three runways of 9,502 ft, 7,050 ft, and 3,943 ft in length.

**West Texas Spaceport:** The West Texas Launch Site (WTLS) is located in Culbertson County, Texas, approximately 25 miles north of Van Horn, Texas. The site encompasses a 75-square-mile site with an average elevation of 3,700 ft. The launch site lies within a larger, privately owned property known as the Corn Ranch.

## 3. Suborbital Vehicles

### 3.1 Vehicle Concepts

In order to determine the electric fields that could trigger lightning to suborbital vehicles, the specific vehicle and trajectory characteristics must be known. As this information is difficult to obtain or may be unavailable from the various suborbital vehicle companies, four representative suborbital vehicle configurations were developed that closely resembled currently proposed suborbital vehicle concepts. The four representative vehicles are:

1. Horizontal takeoff and landing vehicle with jet engines and rocket engines. This vehicle takes off using jet engines and proceeds to an airborne launch point, where it then climbs to apogee using rocket power and glides to a landing on a runway.
2. Ferried and horizontal landing vehicle with rocket engines. The vehicle is carried aloft by a carrier aircraft to the drop point, where it is released and climbs to apogee using rocket power, and glides to a landing on a runway.

3. Horizontal takeoff and landing vehicle with rocket engines. This vehicle takes off using rocket engines, climbs to apogee using rocket power, and glides to a landing on a runway.
4. Vertical takeoff and landing vehicle with rocket engines. This vehicle takes off vertically using rocket engines, coasts to apogee, and lands by rocket-powered descent.

### **3.2 Vehicle Hardening**

None of the concept vehicles are hardened against lightning strikes. An examination of lightning vulnerability based on aircraft experience was performed. Lightning effects may be characterized as direct or indirect, depending on whether the damage is to the structure (destructive) or to the functionality of the systems (e.g., electronics). To harden a vehicle the following measures should be taken and tested.

#### **3.2.1 Direct Effects**

External surfaces and associated hardware (air data probes, antennas, radomes, navigation lights, etc.) and fuel systems should be designed to withstand lightning currents.

#### **3.2.2 Indirect Effects**

The topology of aircraft wiring should be designed such that induced transients or (or “pick-up”) are minimized. To suppress transients, transient surge suppressors should be applied at key points in avionics systems.

### **4. Triggering Related to Electrical Conduction in Plume Exhausts**

The threshold electric environment for triggering depends upon ambient electric fields and the conductive length of the vehicle and the conducting part of the plume. One can use simplified analysis to estimate the relevant conductivity levels for determining plume electrical length. A sophisticated plume model and three simplified models were applied:

1. A time-scale argument that assumes the plume will effectively add to the conducting length to the extent that it can exclude the ambient field on a time scale shorter than the transit time of plume material from the nozzles to a point down the plume
2. A model that allows one to explore the interaction between spatially varying conductivity and charge convection
3. A model of the time to achieve charge neutrality that takes into account the plumes electrical resistance and capacitance per unit length

Calculations suggest that the conductivities of concern will be only a few orders of magnitude above ambient and suggest that the electrical effective length of the plume is much longer than 30 meters. This means that the triggering conditions estimated in Krider, Willet, et al. [2006] might be a significant underestimate.

### **5. Relevancy of Existing LFCC to Proposed RLV Concepts**

The FAA natural and triggered lightning flight commit criteria (LFCC) are not based on a direct measurement of the electric field along the flight path, which, however, is the only way the risk of lightning can be assessed with any certainty, based on knowledge of the triggering potential for a

given vehicle. Rather the risk must be inferred from meteorological conditions combined perhaps with measurements of surface electric fields. The large uncertainties in these inferences lead to a high degree of conservatism of the risk.

## 6. Lightning Climatology

### 6.1 Analysis of NLDN Data

In the earlier study [Krider et al., 2006] the climatology of lightning was examined at Spaceport America in New Mexico and the Oklahoma Spaceport. This study is extended to include the Mojave Air and Space Port and the West Texas Launch Site. The lightning data was from a nearly 15-year lightning climatology study [Schaub, 1996a] of all cloud-to-ground lightning strikes detected by the National Lightning Detection Network (NLDN) within a 100 km radius from the respective sites.

The climatology of naturally occurring cloud-to-ground lightning for the sites added since the Krider et al. [2006] study (the Mojave and West Texas sites) was examined for seasonal variability (Table 1). This indicates that the West Texas site is far more lightning prone than MJSP. The most lightning-prone site over all four spaceports is Spaceport America, and the West Texas site is comparable to this site. The climatology of naturally occurring cloud-to-ground lightning for the Mojave and West Texas sites was also examined for diurnal variability. These results agree with the general tendency for all four test sites to show minimal activity in the morning hours and maximum activity in the afternoon or evening hours.

Table 1. Approximate Number of Days with Indicated Chance of Lightning Within 100 km on That Day of Year (DOY)

Site	Approx. DOY Range > 20%	Approx. Date Range >20%	Approx. DOY Range > 40%	Approx Date Range >40%
MJSP	No significant activity	No significant activity	No significant activity	No significant activity
WTLS	150-260	Late May/ Early Jun to Mid-Sep	No significant activity	No significant activity

### 6.2 Natural-Lightning Statistics from Analysis of Lightning Mapper Array (LMA) Data

Two data sets are available with which to estimate natural-lightning statistics at locations of interest. The National Lightning Detection Network (NLDN) locates the ground strike points of most cloud-to-ground (CG) discharges within the continental United States. The NLDN does not report intracloud (IC) discharges. A small but growing number of lightning mapping arrays (LMAs) have been installed at locations of interest around the country. The LMA system is a very-high-frequency (VHF) time-of-arrival (TOA) system that gives three-dimensional maps of both CG and IC in proximity to its array. LMA networks have been operating more or less continuously out of the University of Oklahoma at Norman since 2004, covering the Oklahoma Spaceport, and out of the U.S. Army's White Sands Missile Range (WSMR) since 2005, covering the New Mexico Spaceport (SA). LMA data has not been established within range of MJSP and WTLS.

Lightning events occurring within approximately 40 km of SA and OS were counted in 1-hour intervals. Approximately three-year datasets were obtained for SA from the White Sands Missile



Range and for OS from the University of Oklahoma. After correcting for biases due to differing operating hours, the overall probability of an hour with lightning is found to be almost 7 percent at SA, compared to 4 to 5 percent at OS. The peak probabilities are much higher: 55 percent in New Mexico at 2300 Universal Time (UT) in July and 21 percent in Oklahoma at midnight UT in August. The seasonal variations are similar at both the New Mexico and Oklahoma locations, with a broad peak in the period from June to August.

## **7. Quantitative Risk Assessment**

This section summarizes the risk assessment for the four concept RLVs at the four spaceports. The frequencies of violations of cloud, lightning, and temperature-based lightning commit criteria (LCC) have been estimated. To make the connection between the LFCC-violation frequencies and the triggering conditions, one needs the probability of occurrence of the relevant electric-field magnitudes in clouds that violate the various LFCC. Data provided by Marshall Space Flight Center (MSFC) from the Airborne Field Mill I (ABFM I) campaign have been analyzed in combination with an analysis of LFCC violations obtained from the database of clouds, lightning, and temperatures for the various sites. The relevant MSFC data is probabilities of electric fields for various LFCC violations.

The rule violation probabilities averaged over months representative of the seasons (January, April, July, and October) and over all hours for the entire data set are shown in Figure 1.

## **8. Alternative Method for Estimating the Frequency of Electrified Clouds**

The meteorological conditions that produce high electric fields in clouds are similar to the conditions that pose an in-flight icing hazard on aircraft, for example, supercooled water drops and ice particles [Bernstein et al., 1997; 2007, and the references therein]. The current icing potential (CIP) index that has been developed for the FAA by the University Corporation for Atmospheric Research (UCAR) combines data from a number of sources (radars, aircraft, satellites, radiosondes, etc.) and applies the relevant physics. Figure 2 shows that the CIP index is indeed highly correlated with clouds that produce natural cloud-to-ground lightning flashes. Correlated with other data, the CIP index might be particularly useful at launch sites that are not well-supported by weather radars, ground-based electric field mills, lightning mapping arrays, and other related sensors.

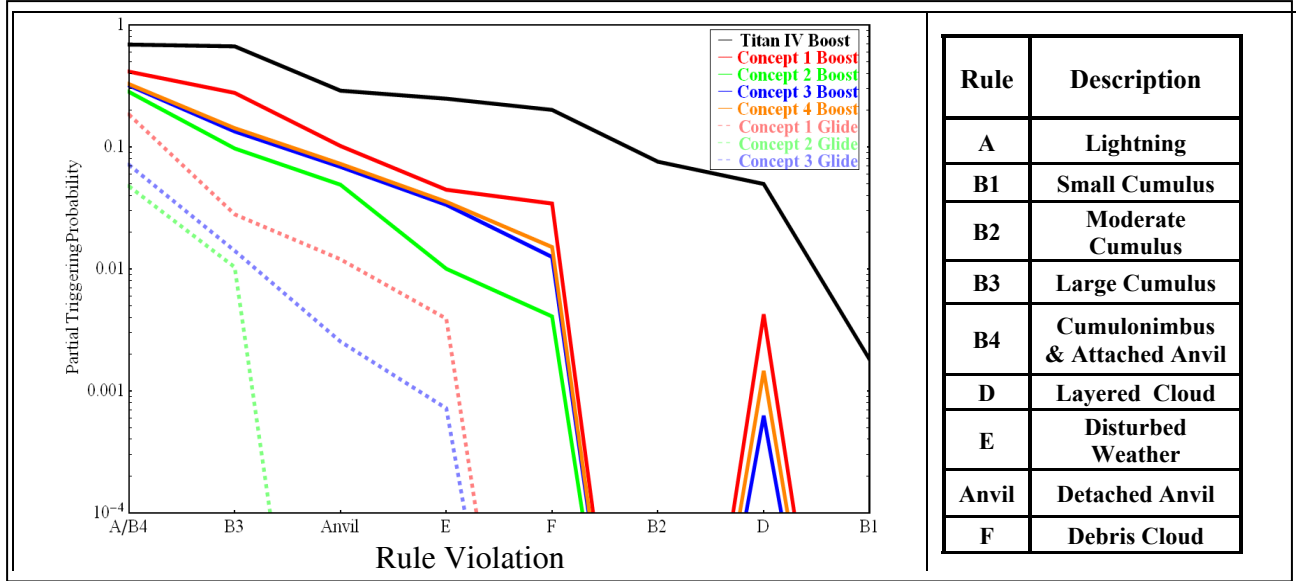


Figure 1. The frequency of rule violations determined from cloud, temperature, lightning, and electric field data. The electric field data is from the Airborne Field Mill I (ABFM I) campaign. The rules are those that were contemporaneous with the campaign. Note the absence of violations for small and moderate cumulus clouds. The vertical axis is logarithmic.

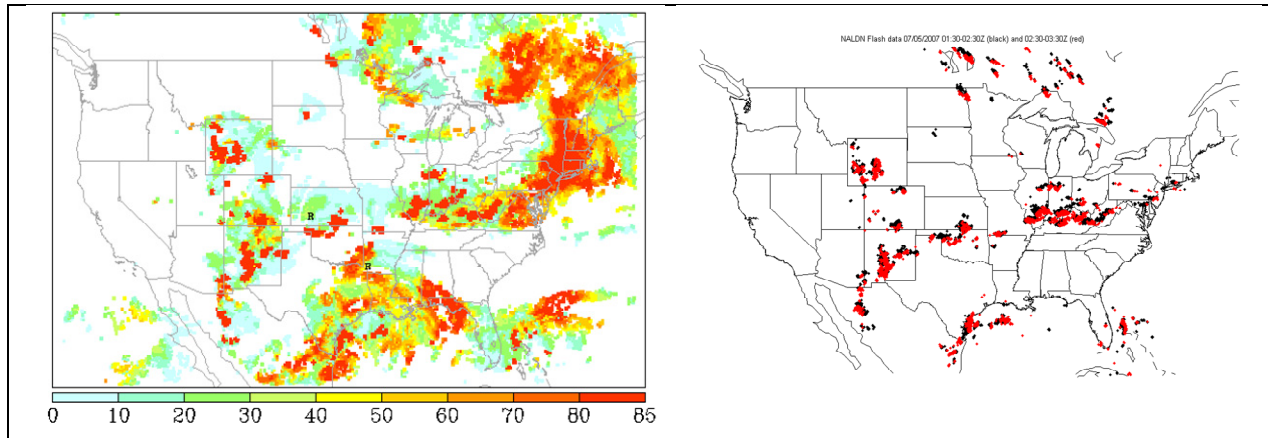


Figure 2. Icing pilot report indicators (left) panel versus National Lightning Detector Network (NLDN) lightning flash reports for two different time periods on the same day (right) (With permission)

## 9. Recommendations

Because of the risk based on the analysis of fields associated with the lightning rules for small and moderate cumulus clouds, we recommend that these rules be relaxed subject to a rigorous statistical analysis suited to infrequently occurring events (e.g., extreme value analysis). Also, because these rules refer to clouds that can undergo rapid development, the rules should be relaxed only when

collateral data (e.g., CIP indices) indicate little potential for growth. Our recommendations are the following:

- Examine the correlation between the CIP index and high electric fields in clouds not producing lightning  
To demonstrate the utility of the CIP index for triggered lightning, the CIP should be correlated with electric fields measured over nonlightning-producing clouds, such as in NASA-MSFC airborne campaigns. Changes to the CIP index should be examined to improve lightning discrimination.
- Improved plume characterization  
To improve plume characterization, field tests and advanced simulations should be performed. Model simulations using new state-of-the-art models with hydrodynamics and improved chemical schemes should be performed. To characterize plume conductivity and validate plume models, experiments with static tests of small rocket motors should be performed. Static tests can be performed in collaboration with amateur rocket groups (i.e., Reaction Research Society) to help keep the cost of experiments to reasonable levels.
- Improved LFCC for RLVs
  - Rule relaxation for small cumulus  
To confirm indications that rules may be relaxed for small and moderate cumulus clouds, a suitable statistical analysis (such as extreme value analysis) should be performed.
  - Use of CIP index  
Along with a study of the CIP index utility for triggered lightning, an investigation of CIP use in the LFCC should be performed. This index could serve to simplify the rules for locations where meteorological data is limited.
  - Use of LMA data  
The LMA is more capable than the NLDN system because it detects in-cloud lightning. The siting of an LMA near the West Texas site should be considered.

# Contents

Abstract .....	iii
Acknowledgments .....	iv
Executive Summary .....	v
1. Introduction .....	1
1.1 Historical Lightning Strike Incidents .....	1
1.1.1 Apollo 12 Incident .....	1
1.1.2 Atlas-Centaur 67 Incident .....	1
1.2 The Problems .....	2
1.2.1 Lightning Hazards to Aircraft .....	2
1.2.2 Triggered Lightning .....	2
1.2.3 Triggering Models .....	3
1.3 Possible Solutions .....	4
1.3.1 Vehicle Hardening .....	4
1.3.2 Lightning Avoidance .....	4
2. The Current Study .....	7
2.1 Four Representative Suborbital Vehicle Concepts .....	7
2.1.1 Horizontal Takeoff with Jet and Rocket Engines Representative Vehicle .....	8
2.1.2 Air Launch Representative Vehicle .....	8
2.1.3 Horizontal Takeoff with Rocket Engines Representative Vehicle .....	8
2.1.4 Vertical Takeoff and Landing Representative Vehicle .....	8
2.2 Spaceports .....	12
2.2.1 Spaceport America .....	12
2.2.2 Oklahoma Spaceport .....	13
2.2.3 Mojave Air and Space Port .....	14
2.2.4 West Texas Spaceport .....	14
2.3 Hazards Associated with Natural and Triggered Lightning on Safety-Critical Systems and Recommended Mitigation Methods .....	16
2.3.1 Lightning Effects .....	16
2.3.2 Vehicle Hardening .....	17
2.4 Instrumentation Survey .....	17
2.4.1 National Lightning Detection Network .....	17
2.4.2 Lightning Mapper Arrays (LMAs) .....	18
2.4.3 NEXRAD .....	18
2.5 Alternative for Estimating the Frequency of Electrified Clouds That Do Not Produce Lightning .....	19
2.6 Estimate Quantitative Triggering Conditions .....	24
2.6.1 Threshold Electric Field Environment for Triggering Lightning .....	24
2.6.2 Models of Positive-Leader Viability .....	24
2.6.3 Altitude (Density) Dependence of Triggering .....	24
2.6.4 Velocity Dependence of Triggering .....	25
2.6.5 Modeling of Electrical Conduction in Plume Exhausts .....	25
2.6.6 Triggering Conditions .....	38

2.7	Lightning Climatology.....	39
2.7.1	Likelihood of Lightning-free Days.....	44
2.7.2	Temperatures within Clouds.....	44
2.7.3	Natural-Lightning Statistics from Analysis of LMA Data .....	46
2.7.4	Summary of Lightning and Cloud Climatology .....	64
2.8	Quantitative Risk Assessment .....	64
2.8.1	Estimated Probability of LFCC Violations.....	64
2.8.2	Estimated Triggering Conditions.....	66
2.8.3	Estimated Probability of Triggered Lightning.....	66
2.9	Relevancy of Existing LFCC to Proposed RLV Concepts.....	75
2.9.1	Cloud Electrification .....	75
2.9.2	FAA Lightning Flight Commit Criteria (LFCC).....	75
2.9.3	Risk Assessment Based on ABFM I Data .....	76
3.	Recommended Lightning Flight Rules .....	79
4.	Recommendations for the Future.....	81
4.1	Statistical Analysis of Existing Data to Better Determine LLCC and LFCC Applicability to RLVs.....	81
4.2	Current Icing Potential (CIP).....	81
4.3	Instrumentation .....	81
4.4	Quantification of Electric-field Triggering Conditions and Effects of Vehicle Plumes.....	81
4.5	Numerical Calculation of the Critical Conductivity Magnitude in Exhaust Plumes .....	82
4.5.1	Construct a Model of Plume-Conductivity Distributions Valid Near this Critical Magnitude.....	82
4.5.2	Validate These Critical-Conductivity Models Experimentally .....	82
4.5.3	Conduct Experiments to Validate Existing Modeling of the Altitude Dependence .....	82
4.6	ABFM System to Provide Measurements of Electric Field Aloft in Support of RLV Operations.....	82
5.	Acronyms and Abbreviations .....	83
6.	References .....	87
Appendix A.	Lightning Mapper Array Event Validation .....	101
Appendix B.	Reanalysis of the Airborne Field Mill Campaign-I Dataset.....	129
Appendix C.	Proposed Natural and Triggered Lightning Flight Commit Criteria with Radar-Based Changes.....	155
Appendix D.	Criteria for Converting Cloud and Lightning Data to Lightning Launch Constraint Rule Violations.....	165
Appendix E.	Table of U.S. NEXRAD Locations .....	169
Appendix F.	The Variation of Lightning Occurrence Versus the Current Icing Potential Index..	173
Appendix G.	The Monthly and Seasonal Variation of Rule Violations .....	177

## Tables

Table 1.	Approximate Number of Days with Indicated Chance of Lightning Within 100 km on That Day of Year (DOY) .....	viii
Table 2-1.	Representative Vehicle Design Information .....	11
Table 2-2.	Indirect Effects of 214 Lightning Strikes to Commercial Aircraft (Based on Fisher et al., 1999) .....	16
Table 2-3.	The Variation of Lightning Occurrence in CIP Bins for Four Months over All Four Spaceports (MJSP, OS, SA, and WTLS).....	23
Table 2-4.	Seven Related Tables of Numerical Results Extracted from Solutions of Eq. (2-20) for Various Parameter Combinations (see text).....	35
Table 2-5.	Estimated Triggering Fields.....	38
Table 2-6.	Site Coordinates and Cloud-to-Ground Lightning Occurrence within 100 km .....	39
Table 2-7.	Approximate Number of Days with Greater Than Indicated Chance of Lightning within 100 km .....	44
Table 2-8.	Times of Minimum and Maximum Probability of Naturally Occurring Lightning in July within 100 km .....	44
Table 2-9.	Spaceport Coordinates for Purpose of Centering 80x80 km Squares .....	49
Table 2-10.	Effect of Bias Correction on the Annual-Average Rates .....	57
Table 2-11.	Average Occurrence Frequency of Rule Violations by NASA/MSFC Priority Category over All Hours, Months (Jan, April, Jul, Oct) and Years .....	65
Table 2-12.	Effective Relative Air Densities Assigned to the Various Rule Violations.....	68
Table 2-13.	Partial Triggering Probabilities for Each Combination of Vehicle Concept and Rule Violation. (Values Scaled According to Effective Relative Air Densities in Table 2-11).....	69
Table 2-14.	Overall Triggering Probabilities (Annual Average) by Vehicle and Spaceport .....	71
Table 2-15.	Maximum Hourly Triggering Probability for Concept 1 Boost at the Various Spaceports, Ranked in Descending Order, and the Month and UT Hour in which that Maximum Occurs. (The Overall Values from Table 2-13 are also shown for Comparison).....	72

## Figures

Figure 2-1.	Horizontal takeoff with jet and rocket engines representative vehicle. ....	9
Figure 2-2.	Air launch representative vehicle.....	9
Figure 2-3.	Horizontal takeoff with rocket engines representative vehicle.....	10
Figure 2-4.	Vertical takeoff and landing representative vehicle.....	10
Figure 2-5.	Location of Spaceport America. ....	12
Figure 2-6.	Location of Oklahoma Spaceport. ....	13
Figure 2-7.	Location of Mojave Air and Space Port. ....	14
Figure 2-8.	Location of West Texas Launch Site. ....	15
Figure 2-9.	Coverage of NLDN sensors over the continental United States [Cummins and Murphy, 2009]. The network consists of 113 lightning sensors [Grogan, 2004]. ....	18
Figure 2-10.	Location and coverage of NEXRAD (WSR-88D) radars for the continental U.S.....	19

Figure 2-11.	The Current Icing Product (CIP) at 2 UT on 5 July 2007 (upper panel) and CG lightning flashes (lower panel) detected by the National Lightning Detection Network (NLDN) during 1-hour intervals centered on the time of the CIP map (with permission). This data corresponds to the LMA data shown in Figure A-7 pertaining to SA. ....	21
Figure 2-12.	The Current Icing Product (CIP) at 2 UT on 2 April 2006 (upper panel) and CG lightning flashes (lower panel) detected by the National Lightning Detection Network (NLDN) during 1-hour intervals following the time of the CIP map. (With permission) This data corresponds to the LMA data shown in Figure A-1 pertaining to OS. ....	22
Figure 2-13.	Plot of time of flight (Integral of $1/v$ —the black diamonds) and electrical relaxation time ( $\tau$ —the red triangles) in an exhaust parcel vs. downstream distance, based on results from the model discussed in section 2.6.5.2 at a rocket altitude of 9.4 km and an alkali-metal concentration of 5 ppm. ....	29
Figure 2-14.	Nondimensional numerical results for $W = 2270$ and $\Lambda = 1/100,000$ . Solutions of Eq. (2-20) for $E'(z')$ [red curve], $\tau'(z')$ [green curve], and the limiting form of the solution for $\lambda(z) \rightarrow \lambda_\infty$ [cyan curve] are shown as functions of the dimensionless downstream position, $z'$ . ....	34
Figure 2-15.	Average annual area-density of cloud-to-ground lightning flashes based on NLDN data for the years 1997 to 2007. Units are flashes per square kilometer per year. Stars indicate spaceport locations [With permission from Vaisala]. ....	40
Figure 2-16.	The number of hours of lightning versus month and day-of-month for CCAFS. The values plotted are the percentage of hours with lightning over the 15-year length of the data set. The white areas on the right indicate where data does not exist because the length of the month in question is less than 31 days. ....	41
Figure 2-17.	Same as Figure 2-15 except for SA. ....	41
Figure 2-18.	Same as Figure 2-15 except for OS. ....	42
Figure 2-19.	Same as Figure 2-15 except for MJSP. ....	42
Figure 2-20.	Same as Figure 2-15 except for WTLS. ....	43
Figure 2-21.	Cloud top heights for selected cloud types are shown in black (+). Isotherm heights for 5, -5, -10, and -20°C are shown in red, green, aqua, and blue, respectively, MJSP. Data is for July 2004. The symbol “cb” in the title of the bottom panel refers to cumulonimbus. ....	45
Figure 2-22.	Cloud top heights for selected cloud types are shown in black (+). Isotherm heights for 5, -5, -10, and -20°C are shown in red, green, aqua, and blue, respectively, for WTLS. Data is for July 2004. The symbol “cb” in the title of the bottom panel refers to cumulonimbus. ....	46
Figure 2-23.	XLMA display of a large MCC passing over Norman, OK, showing all source points (reduced chi-squared $\leq 1.0$ ) within range of the Oklahoma LMA during the hour after 0300 UT on April 2, 2006 (20060402). The upper two strips are time series of source altitude. (The distinction between them will become evident in subsequent figures.) The lower left panel is a plan view, in this case showing all detected lightning. To its right is a latitude-altitude projection ( <i>both</i> scales in km in this case) and above it is a longitude-altitude projection ( <i>both</i> scales in km in this case). (In these projections latitude and longitude refer to distances in the N-S and E-W directions, respectively. These distances may be demarcated either in degrees of latitude/longitude or in km. Which convention is used will be obvious.) An altitude histogram is also included (vertical scale always in km), showing the total number of sources plotted. Each	

	source point is color-coded according to time within the hour in each panel. For unknown reasons this particular hour of data has two-minute gaps every ten minutes.48	
Figure 2-24.	“Rainbow plot,” as described in the text, of the operating hours of the New Mexico LMA over the years 2005 through 2007.....	53
Figure 2-25.	Similar to Figure 2-24, but for the Oklahoma LMA over the years 2004 through 2006. ....	53
Figure 2-26.	“Rainbow plot” of the “lightning-event” rate at the SA over the years 2005 through 2007. ....	55
Figure 2-27.	Similar to Figure 2-26, but for the Oklahoma LMA over the years 2004 through 2006. ....	55
Figure 2-28.	“Rainbow plot” of the “hours-with-lightning” rate at SA over the years 2005 through 2007. Compare to Figure 2-26.....	56
Figure 2-29.	Similar to Figure 2-28, but for the Oklahoma LMA over the years 2004 through 2006. Compare to Figure 2-27. ....	56
Figure 2-30.	Bias-corrected (see text) diurnal variation of the “lightning-event” rate at SA. ....	58
Figure 2-31.	Octobers-only diurnal variation of the “lightning-event” rate at SA. Compare to Figure 2-30.....	58
Figure 2-32.	Seasonal variation of the “lightning-event” rate at SA. ....	59
Figure 2-33.	Bias-corrected diurnal variation of the “hours-with-lightning” rate at SA. Compare to Figure 2-30.....	59
Figure 2-34.	Seasonal variation of the “hours-with-lightning” rate at SA. Compare to Figure 2-32.....	60
Figure 2-35.	Similar to Figure 2-32, but for the Oklahoma Spaceport.....	61
Figure 2-36.	Similar to Figure 2-31, but for March and the Oklahoma Spaceport. Compare to Figure 2-37.....	62
Figure 2-37.	Similar to Figure 2-32, but for the Oklahoma Spaceport.....	62
Figure 2-38.	Similar to Figure 2-30, but for the Oklahoma Spaceport. Compare to Figure 2-35. ...	63
Figure 2-39.	Similar to Figure 2-34, but for the Oklahoma Spaceport. Compare to Figure 2-37. ...	63
Figure 2-40.	Overall triggering probabilities (annual average) by vehicle and spaceport.....	71
Figure 2-41.	(a) Hourly triggering probability of Concept 1 boost for all hours and seasons at the Eastern Range (EST is UT - 5 hr.); (b) Similar to (a) at the New Mexico Spaceport (MST is UT - 7 hr); (c) Similar to (a) at the West Texas Spaceport (MST is UT - 7 hr); (d) Similar to (a) at the Oklahoma Spaceport (CST is UT - 6 hr); (e) Similar to (a) at the Mojave Spaceport (PST is UT - 8 hr); (f) Similar to (a) at the Western Range (PST is UT - 8 hr). ....	73
Figure 2-42.	Average diurnal variation of triggering probability for all vehicles at SA. ....	74
Figure 2-43.	Average seasonal variation of triggering probability for all vehicles at SA. ....	74
Figure 2-44.	Partial triggering probabilities for the various vehicles, plotted against the various possible LCC violations on a semilogarithmic scale. Where the broken lines disappear off the bottom of the graph, these probabilities are too small to distinguish from zero. ....	77



# 1. Introduction

The purpose of this study was to determine the risk of triggered lightning during suborbital launches of four different RLV concept vehicles originating and/or concluding at four spaceports. Three areas were addressed:

1. Observed frequencies of cloud-to-ground lightning at the spaceports, including estimates of violation frequencies of the existing LFCC,
2. Estimates of the ambient fields required for triggering by each of the concept vehicles, including consideration of potential methods for estimating the probability of encountering these field magnitudes from the measured radar returns of thunderstorm anvil clouds, and
3. Review of the current LFCC.

## 1.1 Historical Lightning Strike Incidents

Lightning strikes to flying vehicles are often unexpected, because they can occur inside or near clouds that are not producing lightning. There is no known remote-sensing technique that is capable of reliably detecting the high electric fields that create lightning hazards unless the clouds are producing lightning. This means that it is very important to avoid flying through or near any clouds that are producing natural discharges.

The Apollo 12 and Atlas-Centaur 67 are the only two U.S. space vehicles that have been struck by lightning, and in each case, one or more discharges were initiated when the launch vehicle and its exhaust plume flew into clouds that contained a high electrostatic field. These incidents provided the motivation for the Air Force (AF) Lightning Launch Commit Criteria (LLCC) and the Federal Aviation Administration's Lightning Flight Commit Criteria (LFCC), respectively.

### 1.1.1 Apollo 12 Incident

Apollo 12 was launched on November 14, 1969, into a weak cold front that was passing over the Kennedy Space Center, Florida. Major electrical disturbances, subsequently attributed to vehicle-triggered lightning, were observed at 36.5 and 52.0 seconds into the mission. Nine nonessential sensors with solid-state circuits were permanently damaged. Temporary upsets included loss of communication, flashing and sounding of various warning lights and alarms, disconnection of three fuel cells from the power bus, loss of attitude reference by the inertial platform in the spacecraft guidance system, and disturbances to the timing system, clocks, and other instruments. Fortunately, the mission was able to reach Earth orbit under control of the launch vehicle. No other lightning was reported in the area 6 hours prior to or after the launch.

### 1.1.2 Atlas-Centaur 67 Incident

The Atlas-Centaur 67 rocket, carrying a Fleet Satellite Communications satellite payload, was launched on March 26, 1987, from Cape Canaveral, Florida, under weather conditions that were similar to those at the time of the Apollo 12 launch. Forty-nine seconds after lift-off, when the vehicle's altitude was about 3,636 m, a lightning flash was photographed striking the ground near the launch complex. This discharge caused a memory upset in the vehicle guidance system, which in turn caused the vehicle to begin an unplanned yaw rotation. The stresses associated with this motion caused the vehicle to begin breaking apart. About 70 seconds after liftoff, the range safety officer ordered the vehicle destroyed. After the incident, examination of ground-based electric field records showed that a small cloud discharge probably occurred in the vicinity of the launch pad about 2 minutes before launch. There were no nearby ground strikes reported other than the one that struck the vehicle during ascent, and approximately 40 percent of the telemetry outputs showed anomalous

electrical behavior at the time of this event. Substantial portions of the payload fairing were subsequently recovered from the Atlantic Ocean, and these pieces showed physical evidence of having been struck by lightning.

## 1.2 The Problems

Three problem areas are addressed below:

1. Lightning hazards to aircraft
2. Triggered lightning
3. Triggering models

### 1.2.1 Lightning Hazards to Aircraft

Brief introductions to the characteristics of natural and artificially initiated (or “triggered”) lightning discharges can be found in Uman and Krider (1989), Rakov and Uman (2003, Chapter 10), and Uman and Rakov (2003). These authors summarize data that shows at least 80–90 percent of all lightning strikes to aircraft and spacecraft are “triggered,” in the sense that they are initiated locally by the penetration of a large conductor and its exhaust plume into a sufficiently large region of high-intensity electric field [see also Krider, Christian, et al., 2006, and the references therein; Mazur et al., 1984; and Moreau et al., 1992] and that strikes to aircraft typically occur at altitudes between 1 and 7 km. They also state that triggering occurs “in an ambient electric field typically near 50 kV/m...” and that “the aircraft extremities provide the region of high electric field needed to initiate a lightning discharge by enhancing the ambient electric field to breakdown values,  $3 \times 10^3$  kV/m near sea level and about half that value at 6 km altitude.” [Note: In the following analyses, we will use these electric field values as initial guides and sanity checks for our estimates of the ambient fields that are required for each RLV concept vehicle to initiate and propagate a lightning leader.]

Today many aircraft are constructed using advanced composite materials, which are much less conductive than a metal such as aluminum, and use one or more embedded layers of conductive materials or screens to minimize the effects of lightning currents. This technology increases the sensitivity to lightning because it reduces the shielding to transient currents and electromagnetic fields at the same time as manufacturers are increasing the use of low-voltage electronics, which are more susceptible to these transients. It will be important to determine if composites (or any other nonmetallic materials) are used in the construction of reusable launch vehicles (RLVs), because if so, it will dramatically increase their susceptibility to the effects of any electrical discharges such as lightning.

### 1.2.2 Triggered Lightning

Detailed study of the triggering phenomena (as well as other important aspects of lightning) has been facilitated by the application of rocket-triggering technology [St. Privat D’Allier Group, 1985; Newman, 1958, 1967; Brook et al., 1961; Laroche et al., 1989b; Willett et al., 1999; Lalande et al., 2002].

Considerable information is available on the phenomenology of positive leaders that are initiated by small rockets lifting a grounded wire aloft, including currents measured at the base of the triggering wires and the electric-field changes at the ground that are produced by these currents (e.g., Laroche et al., 1988; Lalande et al., 1998; 2002] together with their propagation velocities and other interesting optical characteristics [Idone, 1992; Idone and Orville, 1988]. Very briefly, during the first few hundred meters of propagation, positive leaders normally produce fast and slowly rising currents with peak values of several tens of amperes and average values of a few amperes, and they propagate upward at speeds ranging from a few times  $10^4$  to a few times  $10^5$  m/s. Unfortunately, the physical

conditions required to initiate and propagate a viable positive leader, especially from a spacecraft with a significant exhaust plume, are not well understood (see sections 1.2.3 and 2.6).

There are at least three conditions that must be satisfied in order to initiate and propagate a positive leader.

First, “breakdown” must occur in a small volume of air near the surface of the triggering object in order to produce free electrons in sufficient quantities to carry an electric current. This means that at normal temperatures and pressures, the local electric field must reach a value near 3.0 MV/m, and when this occurs, a phenomenon called “glow corona” is produced.

Second, the current in the corona region must be amplified to the point where positive streamers develop. These streamers propagate outward from the breakdown region, and further heat a small volume of air that is termed the “stem,” where the positive-leader channel initially forms.

Third, the *ambient* field must be large enough over a sufficiently large volume of space that the tip of the positive leader, once initiated, will continue to propagate and grow (i.e., the potential at the tip will remain large enough relative to the local ambient potential to sustain propagation). This last condition is what we will refer to as “leader viability.”

### 1.2.3 Triggering Models

We now briefly review four possible models for predicting the viability of a positive leader, and hence a lower bound on the triggering conditions for classical rocket-triggered lightning. (In this section, we will consider triggering only at altitudes near the surface, i.e., at standard temperature and pressure [STP]. Triggering at higher altitudes will be considered in section 2.6.3.)

Two simple models are the following:

1. A leader could become viable when the magnitude of the ambient field is larger than the longitudinal field that is found in long, laboratory arcs that carry the same current as a lightning leader, i.e., a few kilovolts per meter at arc currents of a few amperes [Larsson, 2002; Larsson et al., 2005]. This is probably a necessary condition, but it is certainly not sufficient because all violations will not be large enough to produce triggering.
2. It has also been suggested that triggering could occur when the potential “spanned” by the triggering wire exceeds about 3.5 MV. This might be called a “constant-potential-spanned” criterion, but it is too simplistic, especially when compared to two more sophisticated models of leader development that cannot be discussed in detail here without introducing unnecessary complexity.

The two additional models have been described by Aleksandrov et al. [2005], based on work by Bazelyan and Raizer [2000], and Lalande et al. [2002], who give a comparable formula, but for a very different physical model. As discussed in detail by Krider et al. [2006, section 3.1.2], the data of Willett et al. [1999] agrees reasonably well with both of these models, which gives little to recommend one over the other. Nevertheless, we believe the Bazelyan and Raizer model is safer—i.e., it predicts a smaller triggering field for a conductor of any specified length in the size range that is relevant for RLVs, and this model will be used in this study. Clearly, however, more work is needed on the basic triggering models and their validation.

### 1.3 Possible Solutions

There are two obvious solutions to the problem of triggered lightning—vehicle hardening and avoidance.

#### 1.3.1 Vehicle Hardening

All commercial passenger aircraft are required by the FAA to be “hardened” to withstand lightning strikes because such events cannot be entirely avoided. That this hardening has been successful is demonstrated by the fact that such aircraft are struck frequently (about once every 3,000 flight hours) but generally sustain only minor damage. The main reason that serious damage or destruction are relatively rare is undoubtedly that passenger aircraft have traditionally been constructed almost entirely out of aluminum skin and structural elements, which are excellent conductors of electricity. Nevertheless, careful attention is given to electrical bonding between the various metal parts, to the use of adequate metal thickness over fuel tanks and, in other sensitive areas, to the correct mounting and protection of electrical fixtures such as lights and antennas, and to numerous other details.

Composite materials are known to be highly vulnerable to physical damage by lightning (“direct effects”) and also to provide little or no shielding for internal electronic components against the associated electrical transients (“indirect effects”). Where such materials must be used for their lighter weight or transparency to electromagnetic waves, conducting foil or mesh, diverter strips, and other techniques have been developed to guide lightning currents harmlessly over the external surfaces.

Test standards and techniques are well developed to validate the various hardening technologies. Current test standards are outlined briefly by Rakov and Uman [2003, section 10.5], and the whole subject of lightning protection for aircraft has been described by Fisher et al. [1999]. Here we will assume that the cost and weight penalties associated with vehicle hardening will not be acceptable for RLVs.

#### 1.3.2 Lightning Avoidance

For vehicles that are not hardened, avoidance remains the only option. Either in situ measurements of the cloud electric field,  $E$ , or cloud-based rules can enable RLVs to avoid situations in which strikes by triggered (or natural) lightning are likely. These two approaches to avoidance are described further in the following sections.

In situ measurements of the ambient electrostatic field that is produced by any cloud that is near the flight path is undoubtedly the best way to determine whether that cloud poses a lightning hazard to any particular RLV. This is because most clouds do not give a clear indication to any known remote-sensing technique (e.g., morphology or radar reflectivity) of whether or not they are highly electrified. (Notable exceptions are cumulonimbus clouds and any clouds that are producing natural lightning.)

Some types of clouds, such as “thick clouds” and “thunderstorm debris clouds” (as defined in the current LFCC), are statistically known to constitute a hazard in a relatively small percentage of cases. Thus, in the absence of direct measurements, these clouds should be avoided, even though avoidance may produce unnecessary launch delays and scrubs. In such cases, an in situ measurement capability could eliminate false alarms and maximize launch availability, without compromising safety. Unfortunately, the only appropriate method of obtaining in situ electric field measurements—a high-performance aircraft instrumented with five or more field mills (an Airborne Field Mill, or ABFM, system)—is expensive and both technically and operationally difficult.

The existing LFCC are examples of avoidance criteria that are cloud-based [Federal Register, Vol. 71, No. 165/Friday, August 25, 2006/Rules and Regulations]. Although the present LFCC are believed to be very safe, these rules were developed for vehicles with large orbital boosters, such as the Titan and the space shuttle, and they do produce false alarms and reduce launch availability. Nevertheless, we believe the LFCC should be applied to smaller vehicles, such as the RLVs of interest here, until an operational ABFM or new ABFM experiments and/or further statistical analyses of existing ABFM data enable some of the LFCC to be tailored to smaller vehicles.

Note that the most important of the LFCC, *whether an operational ABFM is used or not*, are:

1. Avoid all clouds that are producing any type of natural lightning
2. Avoid cumulus clouds that may become electrified in just a few minutes and could rapidly create conditions for natural (or triggered) lightning.

Note also that measurements of surface electric fields using a Ground-Based Field-Mill system (GBFM, as opposed to an ABFM) are incorporated into certain of these LFCC, where they create added safety (by detecting additional hazards) and reduce false alarms (due to the conservative nature of cloud-based rules). Note also that a GBFM is not a substitute for an ABFM because of the electrical charges that can accumulate in screening layers near the ground or at the cloud boundaries, even if the GBFM system has the necessary areal extent and sensitivity for the clouds of interest.



## 2. The Current Study

Here lightning avoidance by RLVs and specifically by the four concept vehicles that are described in section 2.1 below is reviewed. The existing literature on the measurement of the cloud electric field,  $E$ , aloft in support of space launches has been reviewed by Krider, Willett, et al. (2006; section 2.3.2.1), leading to the conclusion that an ABFM, or similar platform, is the only suitable tool for simultaneously maximizing safety and launch availability. Here we discuss risk avoidance in lieu of an operational ABFM.

Two points should be noted about the proposed RLVs:

1. Because they are smaller and have less powerful engines than ICBM-type boosters, it is to be expected that their lightning-triggering thresholds expressed in terms of the ambient electric field will be correspondingly higher. Given our present incomplete understanding of the physics of triggering and the difficulty of measuring or inferring the ambient fields aloft, however, it will be difficult to exploit this advantage.
2. Because some of the suborbital RLVs may be piloted, hence not required to carry remote-destruct systems, use relatively nontoxic fuels, will operate in remote areas, will not impact public safety or third-party property, and are expected to require good visibility for the duration of their flights, the FAA might allow their operators more discretion than is given to the operators of large orbital boosters by the Federal Ranges.

### 2.1 Four Representative Suborbital Vehicle Concepts

In order to determine the electric fields that could trigger lightning to suborbital vehicles, the specific vehicle and trajectory characteristics must be known. As this information is difficult to obtain or is unavailable from the various suborbital vehicle companies, four representative suborbital vehicle configurations were developed that closely resemble currently proposed suborbital vehicle concepts. The four representative vehicles are:

1. Horizontal takeoff and landing vehicle with jet engines and rocket engines. This vehicle takes off using jet engines and proceeds to an airborne launch point, where it then climbs to apogee using rocket power and is powered to or glides to a landing on a runway.
2. Ferried and horizontal landing vehicle with rocket engines (referred to as “Air Launch vehicle”). The vehicle is carried aloft by a carrier aircraft to the drop point, where it is released and climbs to apogee using rocket power, and glides to a landing on a runway.
3. Horizontal takeoff and landing vehicle with rocket engines. This vehicle takes off using rocket engines, climbs to apogee using rocket power, and glides to a landing on a runway.
4. Vertical takeoff and landing vehicle with rocket engines. This vehicle takes off vertically using rocket engines, coasts to apogee, and lands by rocket-powered descent.

### **2.1.1 Horizontal Takeoff with Jet and Rocket Engines Representative Vehicle**

The Horizontal Takeoff with Jet and Rocket Engines vehicle is designed to take off from the airport of origin using jet engines to climb to approximately 20,000 to 30,000 ft. At that altitude, the rocket engines ignite to begin the suborbital trajectory. After rocket engine burn-out, the vehicle coasts to the 100 km altitude, and then reenters the atmosphere. The vehicle then either relights its jet engines for a powered landing or glides back to the airport of origin for an unpowered landing. The vehicle is controlled by a single pilot who controls the vehicle during all portions of the flight, including emergency situations. The vehicle also carries up to three passengers during the flight. The gross takeoff weight of the vehicle is 18,000 lb, with a vehicle length of 40.0 ft and a wingspan of 25.0 ft, as presented in Figure 2-1.

### **2.1.2 Air Launch Representative Vehicle**

The air launch vehicle is designed to be carried on the back of an aircraft to approximately 40,000 to 50,000 ft. At that altitude, the vehicle separates from the aircraft, and the rocket engines light off to begin the suborbital trajectory. After rocket engine burn-out, the vehicle coasts to the 100 km altitude, then reenters the atmosphere, and glides back to the airport of origin for an unpowered landing. The vehicle is controlled by a single pilot during all portions of the flight, including emergency situations, and carries up to two passengers. The gross weight of the vehicle is 9,103 lb, with a vehicle length of 21.1 ft, and a wingspan of 14.4 ft, as presented in Figure 2-2.

### **2.1.3 Horizontal Takeoff with Rocket Engines Representative Vehicle**

The Horizontal Takeoff with Rocket Engines vehicle is designed to take off from the airport of origin using two of its four rocket engines. Once clear of the runway, at an altitude of approximately 1 nm, the remaining two rocket engines light off to begin the suborbital trajectory. After rocket engine burn-out, the vehicle coasts to the 100 km altitude, reenters the atmosphere, and then glides back to the airport of origin for an unpowered landing. The vehicle is controlled by a single pilot during all portions of the flight, including emergency situations, and carries up to two passengers. The gross takeoff weight of the vehicle is 13,276 lb with a vehicle length of 24.3 ft and a wingspan of 17.0 ft, as presented in Figure 2-3.

### **2.1.4 Vertical Takeoff and Landing Representative Vehicle**

The Vertical Takeoff and Landing vehicle is a single-stage vehicle that launches using rocket engines. After rocket engine burn-out, the vehicle coasts to the 100 km altitude, reenters the atmosphere, where the vehicle's engines relight for a powered vertical landing at a downrange site. The vehicle is controlled by a single pilot and carries up to two passengers. The gross takeoff weight of the vehicle is 10,579 lb with a vehicle length of 22.2 ft and a diameter is 5.0 ft, as presented in Figure 2-4.



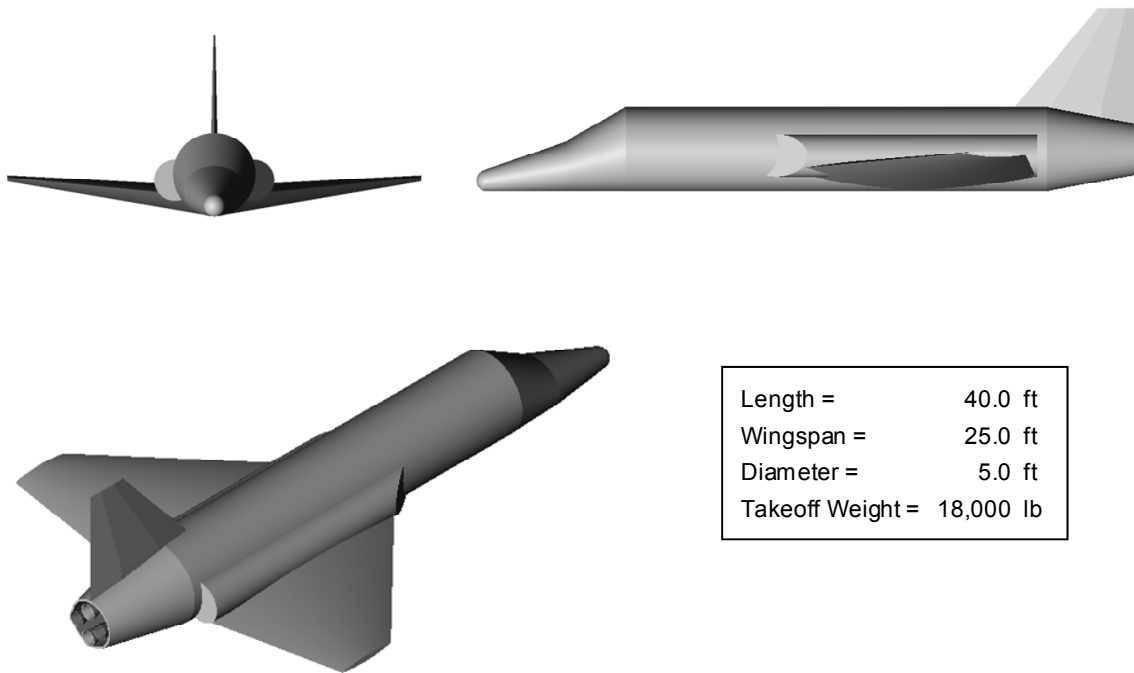


Figure 2-1. Horizontal takeoff with jet and rocket engines representative vehicle.

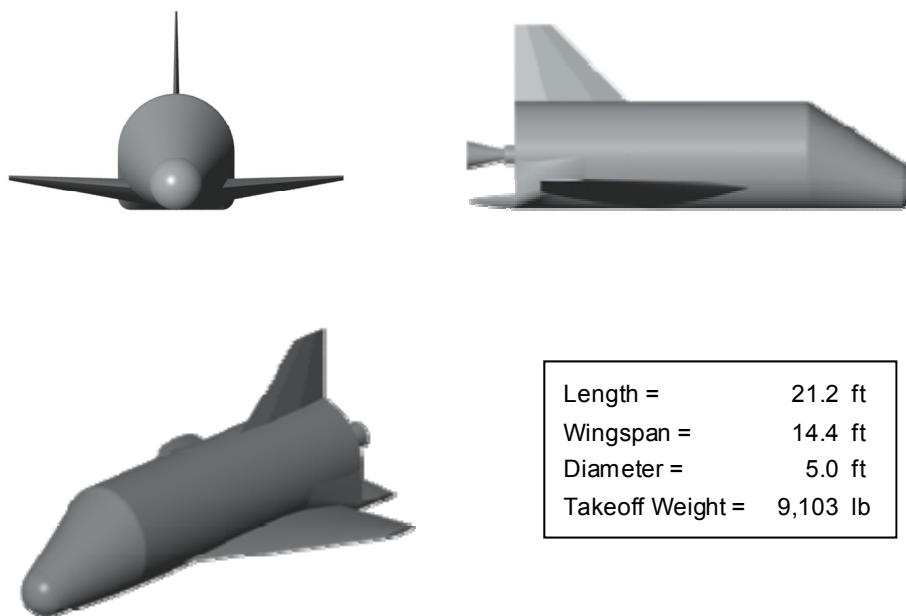


Figure 2-2. Air launch representative vehicle.

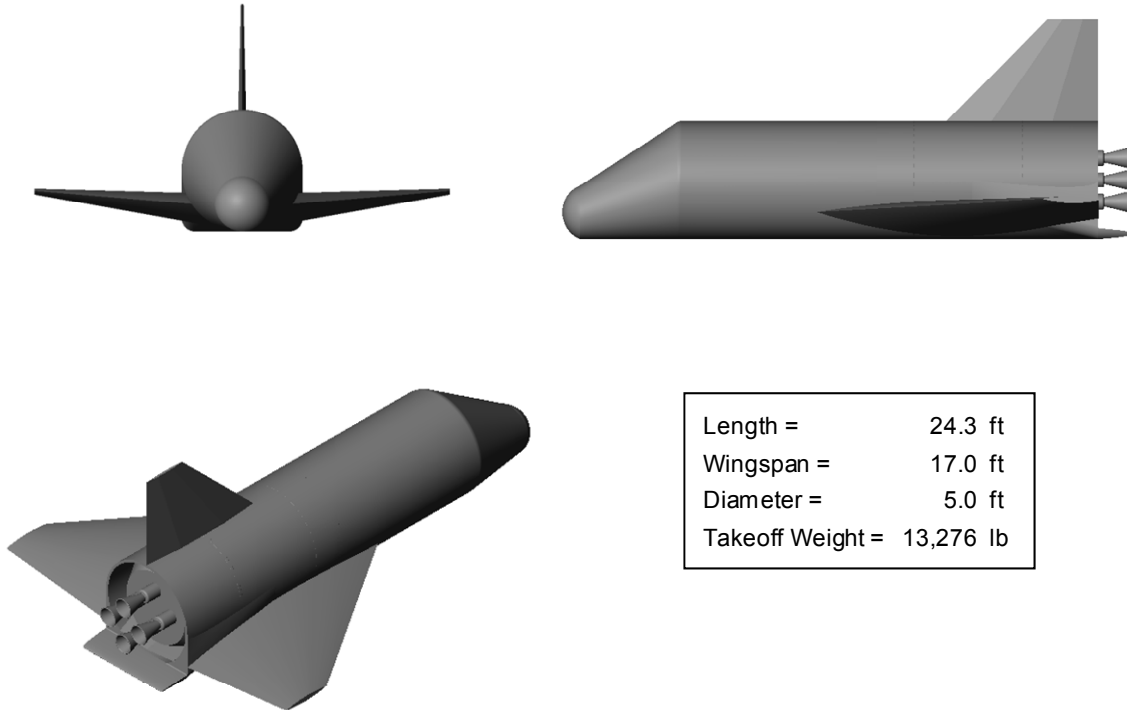


Figure 2-3. Horizontal takeoff with rocket engines representative vehicle.

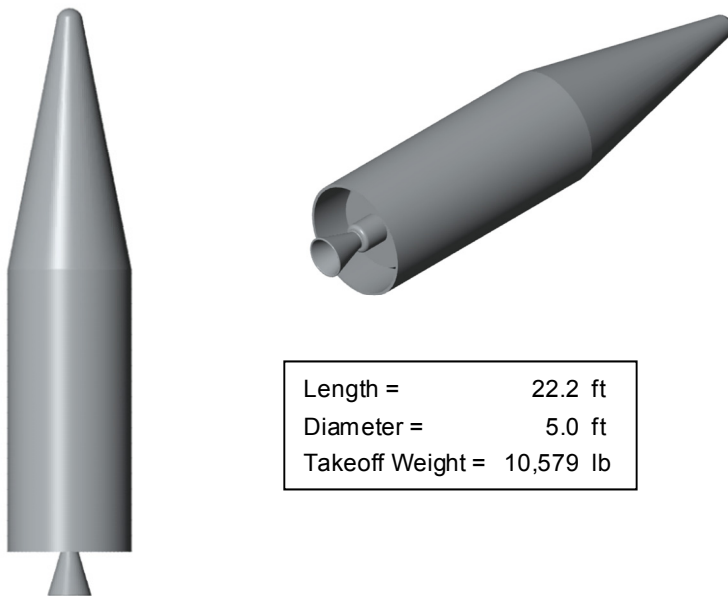


Figure 2-4. Vertical takeoff and landing representative vehicle.

Table 2-1 presents additional information on each of the four vehicles, as required to perform triggered lightning analyses.

Table 2-1. Representative Vehicle Design Information

Vehicle Number	1	2	3	4
Vehicle Type	HTHL w/Jet Engines	Air Launch	HTHL w/Rocket Engines	VTVL
Vehicle Length	40.0 ft	21.2 ft	24.3 ft	22.2 ft
Vehicle Wingspan	25.0 ft	14.4 ft	17.0 ft	N/A
Vehicle Diameter	5.0 ft	5.0 ft	5.0 ft	5.0 ft
Nose Radius of Curvature	1.7 ft	4.2 ft	4.2 ft	2.0 ft
Vehicle Gross Weight	18,000 lb	9,103 lb	13,276 lb	10,579 lb
Fuel Type	JP-1 and RP-1	Rubber	RP-1	RP-1
Oxidizer Type	Liquid Oxygen	Nitrous Oxide	Liquid Oxygen	Hydrogen Peroxide
Rocket Sea Level Thrust (total)	23,800 lb	10,500 lb	13,300 lb	14,300 lb
Engine Firing Altitude	24,000 ft	50,000 ft	0 ft	0 ft
Engine Burn-out Altitude	150,000 ft	173,000 ft	144,000 ft	125,000 ft
Rocket Burn Time	74.4 sec	96.7 sec	145.1 sec	110.0 sec
Total Flight Time	1537.4 sec (25.6 min)	973.8 sec (16.2 min)	914.7 sec (15.2 min)	600 sec (10 min)
Furthest Distance from Takeoff Site	36 nmi	28 nmi	12 nmi	4 nmi

## 2.2 Spaceports

For this analysis, four spaceports were evaluated: Spaceport America in New Mexico, the Oklahoma Spaceport, the Mojave Air and Space Port in California, and the West Texas Spaceport.

### 2.2.1 Spaceport America

The State of New Mexico is developing Spaceport America (SA) near Upham, New Mexico, approximately 45 miles north of Las Cruces and 30 miles east of Truth or Consequences. This location is along the western boundary of the White Sands Missile Range and will benefit from the controlled airspace around the missile range. The spaceport will encompass a 27-square-mile site consisting of open, generally level, range land with an average elevation of 4,700 ft. The plans for the spaceport facility call for a launch complex, a landing strip and aviation complex, a payload assembly complex, a support facilities complex, and a system development complex.

The location of Spaceport America, and its proximity to the White Sands Missile Range, is presented in Figure 2-5.



Figure 2-5. Location of Spaceport America.

## 2.2.2 Oklahoma Spaceport

The Oklahoma Spaceport (OS) is located at Burns Flat, Oklahoma, approximately 100 miles west of Oklahoma City. The Oklahoma Spaceport encompasses approximately 3,000 acres and has two runways, 13,500 ft and 5,200 ft in length. The Spaceport has an operational control tower and an instrument landing system (ILS) capability that can support a full range of aircraft operations. The Spaceport has multiple commercial-size hangars that can accommodate multiple suborbital vehicle companies and has adequate access to air, ground, and rail transportation modes. The spaceport also has access to manufacturing facilities and the facilities of Oklahoma's Western Technology Center, and it will coordinate all suborbital flights from its Spaceport Operations Center.

The location of the Oklahoma Spaceport is presented in Figure 2-6.

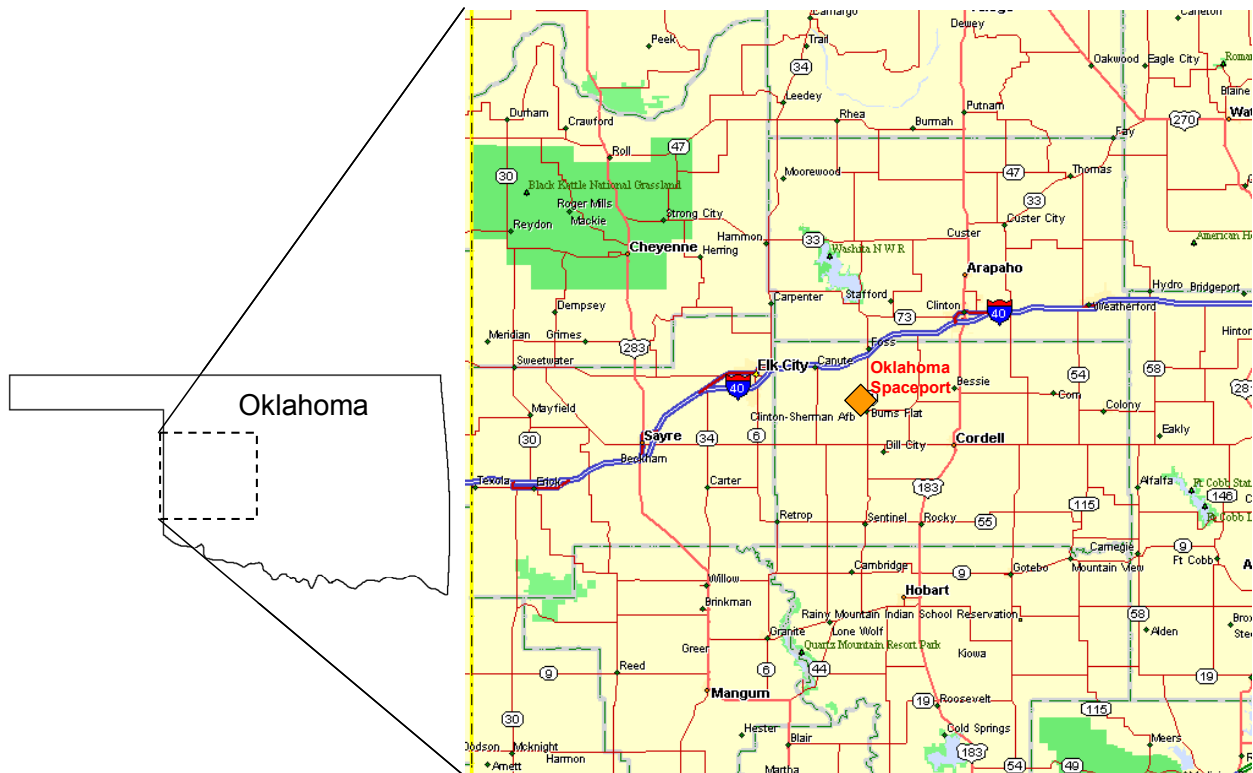


Figure 2-6. Location of Oklahoma Spaceport.

### 2.2.3 Mojave Air and Space Port

The Mojave Air and Space Port (MJSP) is located in the southeastern corner of Kern County, on the east side of the unincorporated town of Mojave, California. It encompasses approximately 3,000 acres and has three runways, at 9,502 ft, 7,050 ft, and 3,943 ft in length. The Mojave Airport can support a full range of aircraft operations. The airport serves as a civilian flight test center and is the location of the National Test Pilot School (NTPS), which operates various aircraft types, including high-performance jet aircraft, single- and twin-engine propeller aircraft, and helicopters. The Mojave Air and Space Port includes the terminal, an administrative building, hangars, offices, a maintenance shop, fuel services facilities, an industrial area located in the southern portion of the airfield, and rocket engine test stands located in the northern portion of the facility. The Mojave Air and Space Port required no airport modifications to accommodate the proposed launch of suborbital vehicles at the Mojave Airport.

The location of the Mojave Air and Space Port is presented in Figure 2-7.

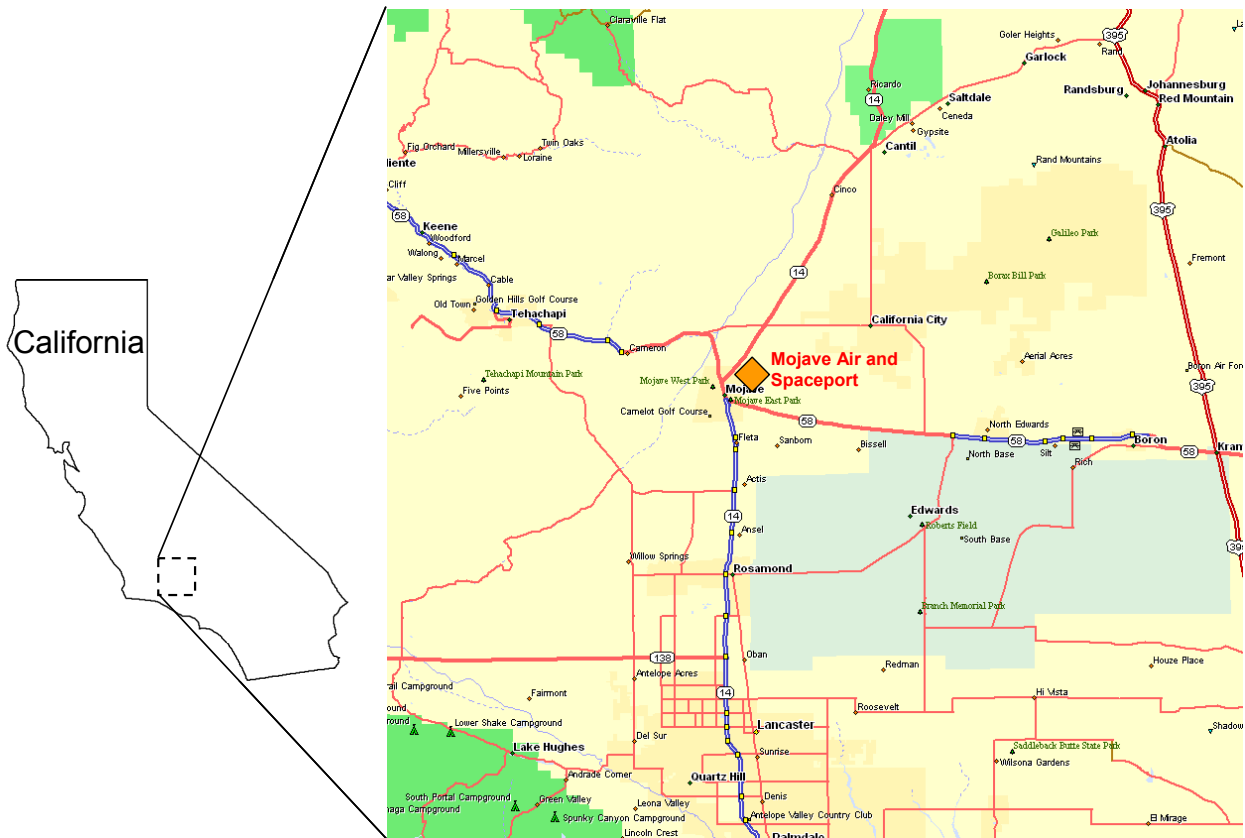


Figure 2-7. Location of Mojave Air and Space Port.

### 2.2.4 West Texas Spaceport

The West Texas Launch Site (WTLS) is located in Culbertson County, Texas, approximately 25 miles north of Van Horn, Texas. The spaceport will encompass a 75-square-mile site with an average elevation of 3,700 ft. The launch site lies within a larger, privately owned property known as the Corn Ranch. The plans for the spaceport facility call for a vehicle processing facility, a launch complex, a vehicle landing and recovery area, a spaceflight participant training facility, and other support facilities.

The location of the West Texas Spaceport is presented in Figure 2-8.

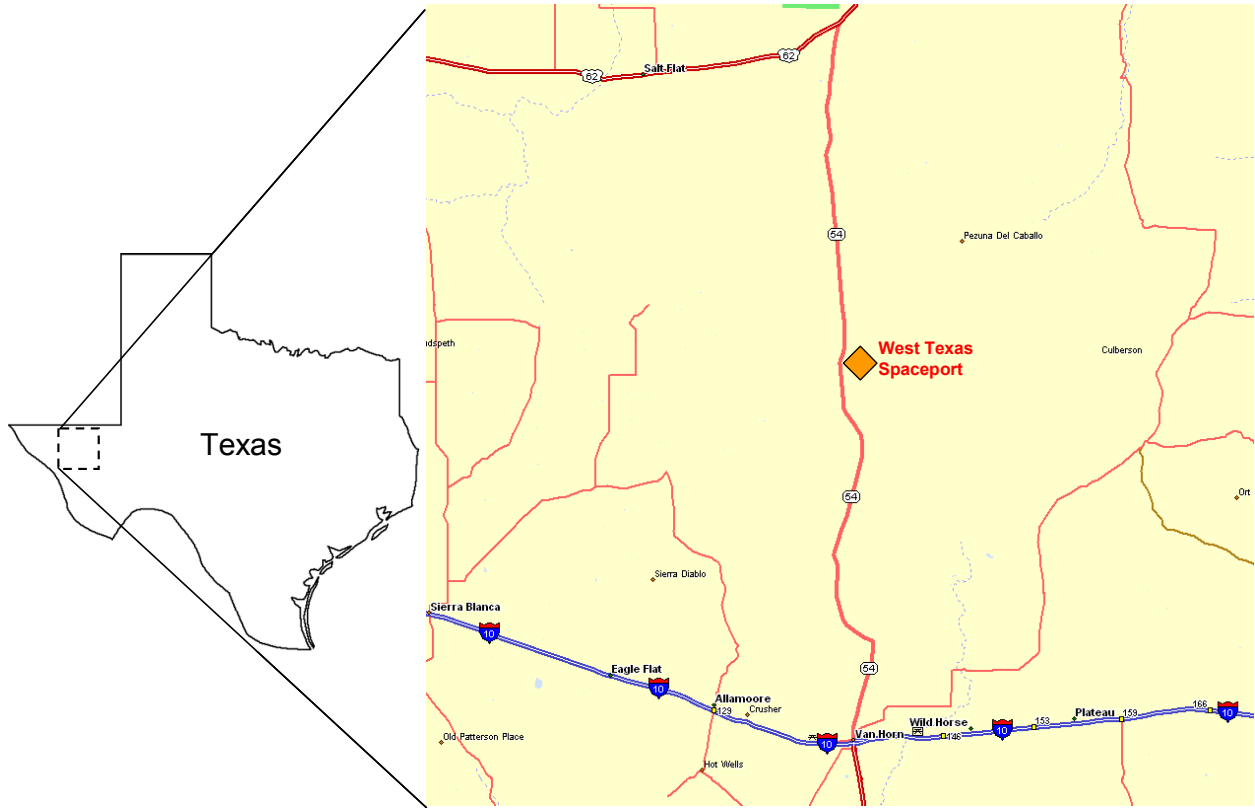


Figure 2-8. Location of West Texas Launch Site.

## 2.3 Hazards Associated with Natural and Triggered Lightning on Safety-Critical Systems and Recommended Mitigation Methods

### 2.3.1 Lightning Effects

The effects of lightning on flying vehicles are usually divided into two categories—“direct” and “indirect” (or “induced”).

#### 2.3.1.1 Direct Effects

Direct effects occur as a result of a lightning channel attaching to the vehicle and the current flowing through the surface and airframe and exiting the vehicle. Most of the damage occurs at the point(s) where the lightning channel contacts the surface and includes the heating, pitting, or melt-through of conducting materials or the puncturing or splintering of nonmetallic surfaces, such as radomes; burning holes in the skin; the welding or fusing of hinges and bearings; damage to antennas and/or lights; and rarely explosions due to the ignition of fuel vapors. Radomes are often equipped with metallic “diverter” strips to conduct any lightning currents directly to the metallic airframe in ways that will not damage the surface or interfere with radar or communications signals. Further details about the physics of direct effects are given in a series of papers by Larsson et al. [2000a, b], Larsson [2002], Broc et al. [2006], and Lago et al. [2006], and the methods of protecting aircraft from direct effects have been described by Fisher et al. [1999].

#### 2.3.1.2 Indirect Effects

Indirect effects include any momentary upsets or permanent damage caused by the transient voltages and currents that are induced by the “transformer action” of the lightning current during a direct attachment or a nearby discharge. Examples of the types of interference and outages that can be produced indirectly have been tabulated by Fisher et al. [1999], Rakov and Uman [2003], and Uman and Rakov [2003] and are reproduced here as Table 2-2. More details on the mechanisms of electromagnetic coupling are described in Fisher et al. [1999, Chapters 8, 9, 11, and 12].

On commercial aircraft, the direct effects of lightning strikes are usually minimal, but occasionally can be catastrophic. The reason for this is that commercial aircraft are designed and tested to withstand the large lightning currents and fast current rise times that are contained in selected lightning test standards [Fisher et al., 1999; Uman, 2008, Chapter 9]. At this point, it should be noted that since RLVs are not subjected to the same design and testing requirements that commercial aircraft are, we must assume that any direct interactions of an RLV with any type of lightning discharge will be a serious threat.

Table 2-2. Indirect Effects of 214 Lightning Strikes to Commercial Aircraft (Based on Fisher et al., 1999)

Incidents of indirect effects in commercial aircraft during 214 lightning strikes		
	Interference	Outage
HF communication set	—	5
VHF communication set	27	3
VOR receiver	5	2
Compass (all types)	22	9
Marker beacon	—	2
Weather radar	3	2
Instrument landing system	6	—



Automatic direction finder	6	7
Radar altimeter	6	—
Fuel flow gauge	2	—
Fuel quantity gauge	—	1
Engine rpm gauges	—	4
Engine exhaust gas temperature	—	2
Static air temperature gauge	1	—
Windshield heater	—	2
Flight director computer	1	—
Navigation light	—	1
AC generator tripoff	(6 instances of tripoff)	—
Autopilot	1	—

## 2.3.2 Vehicle Hardening

### 2.3.2.1 Direct Effects

Methods for protecting vehicles against the direct effects of lightning are discussed in chapter 6 of Fisher et al. [1999]. These include making all external conductors of sufficient thickness to prevent excessive heating or melt-through, carefully bonding different conductors to prevent potential differences from appearing within the airframe, and minimizing any arcing that might occur across all bonds, hinges, and joints. Particular attention should be paid to the fuel system and any gauge wiring. These should be designed so that there is minimum exposure to any lightning current and so that any potential differences that might be produced by lightning current flowing in the skin or airframe are minimal. All external antennas, navigation lights, etc., should be able to withstand a direct lightning strike.

For vehicles constructed out of composite materials, the use of diverter strips, foils, or embedded metallic mesh will reduce puncturing and explosive fracturing and will provide some shielding against indirect effects. The fuel system must be designed to withstand lightning currents.

### 2.3.2.2 Indirect Effects

Methods for protecting vehicles against the indirect (or induced) effects of lightning include many of those described in section 2.3.2.1 plus the application of enhanced shielding, bonding, surge protection, and circuit design in conjunction with the wiring [see chapters 14 to 17 in Fisher et al., 1999].

## 2.4 Instrumentation Survey

### 2.4.1 National Lightning Detection Network

The National Lightning Detection Network (NLDN) shows the location and progress of thunderstorms in the lower 48 states by detecting the electromagnetic radiation from cloud-to-ground lightning strokes. Data is acquired from 113 sensors and sent to a central processing location in Tucson, Arizona, operated by Vaisala, Inc. The processed data is transmitted via satellite to nearly 1,000 locations and can be used in real time by, for example, electric power companies, the petrochemical industry, fuel and chemical storage sites, TV stations, meteorologists, research facilities, and recreation parks [Orville, 2008; Krider et al., 1976]. The flash detection efficiency of

the NLDN network is 90 percent or better, the stroke detection efficiency is 60–80 percent, and the stroke location accuracy is 500-meter median error [Grogan, 2004]. The network of NLDN sensors provides complete coverage for the contiguous 48 states. Figure 2-9 shows the locations of the NLDN sensors that make up the network and how the network evolved over time [Cummins and Murphy, 2009].

The flash detection efficiency of the NLDN network is 90 percent or better, the stroke detection efficiency is 60–80 percent, and the stroke location accuracy is 500-meter median error.

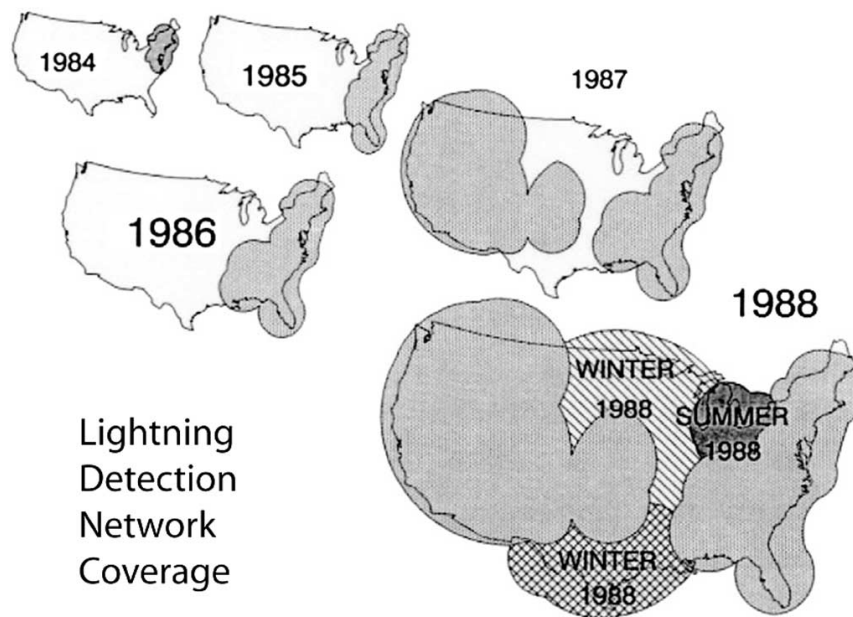


Figure 2-9. Coverage of NLDN sensors over the continental United States [Cummins and Murphy, 2009]. The network consists of 113 lightning sensors [Grogan, 2004].

### 2.4.2 Lightning Mapper Arrays (LMAs)

The LMA is a very-high-frequency time-of-arrival system developed at the New Mexico Institute of Mining and Technology (NMIMT) in the mid-to-late 1990s [Rison et al. 1999; Krehbiel et al., 2000]. Briefly, much of the broadband VHF radio “noise”—the relative timing of very short pulses radiated by lightning received at six or more LMA stations—is used to redundantly locate the source of these pulses. An important advantage of the LMA for our purposes is its capability of mapping the above-ground structure of both in-cloud (IC) and cloud-to-ground (CG) discharges. Thus it may be considered a “total-lightning” sensor. LMA networks have been operating more or less continuously out of the University of Oklahoma at Norman (UOK) since 2004, covering the Oklahoma Spaceport (OS), and out of the U.S. Army’s White Sands Missile Range (WSMR) since 2005, covering the New Mexico Spaceport (SA). No coverage is available for the California or Texas sites.

### 2.4.3 NEXRAD

A major part of the modernization of the National Weather Service (NWS) in the 1990s was the installation of a national network of Next Generation Radar (NEXRAD) [Weather Surveillance Radar-1988 Doppler (WSR-88D)] weather radars using a Doppler-pulse signal. They were adapted for weather applications through a cooperative effort by the NWS, the Federal Aviation Administration (FAA), and the Department of Defense. The system includes 121 radars installed at

NWS Weather Forecast Offices. The system is used to monitor and forecast severe storms and precipitation (including flash floods).

Figure 2-10 shows the coverage by the NEXRAD system. The coverage of the contiguous 48 states is nearly complete. Coverage includes the OS, SA, MJSP, and WTLS. A complete listing of sites for the U.S., including Alaska and Hawaii, are given in Appendix E and at <http://www.roc.noaa.gov>.

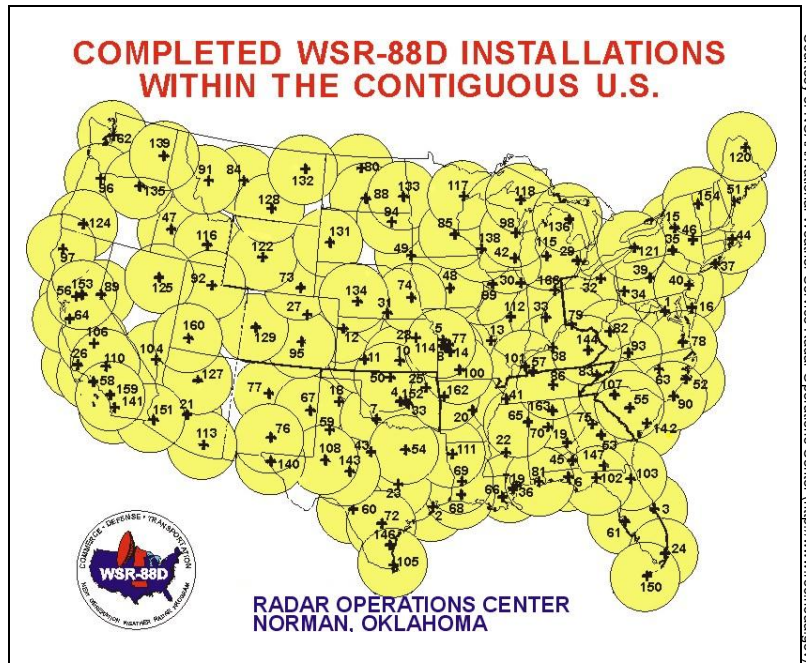


Figure 2-10. Location and coverage of NEXRAD (WSR-88D) radars for the continental U.S.

## 2.5 Alternative for Estimating the Frequency of Electrified Clouds That Do Not Produce Lightning

Krider et al. [2006] have reviewed the electrical structure of thunderclouds and the basic elements of cloud electrification. The processes that electrify clouds, and ultimately produce high electric fields and lightning, are thought to be non-inductive collisions between ice particles in the presence of supercooled water drops on a small spatial-scale, followed by a gravitational separation of particles of different sizes on a large-spatial scale. In cases where high electric fields have been observed in stratiform clouds, non-inductive ice-ice collisions in the presence of supercooled water drops may also have been involved [Krider et al., 2006]. Therefore, a necessary condition for a cloud to become highly electrified appears to be that it contains both supercooled water drops and ice particles in proximity, i.e., the cloud has a large mixed-phase region at subfreezing temperatures. Recent reviews of the microscale physics of ice surfaces and cloud electrification have been given by Dash et al. [2006], Saunders et al. [2006], and Saunders [2008].

It should be noted that the meteorological conditions that produce high electric fields in clouds are very similar to the conditions that present an in-flight icing hazard to aircraft [Gaviola and Fuertes, 1947; Sand et al., 1984; Politovich, 1989; and Bernstein et al., 1998] and that the problem of aircraft icing is most severe in mixed-phase clouds that contain both supercooled water drops and ice particles in proximity [Bernstein et al., 1997; 2007; Bernstein and LeBot, 2009, and the references therein]. Shupe et al. [2008] have reviewed ground-based methods for detecting mixed-phase clouds, and the advantages and disadvantages of each approach are noted in the references therein. The Current Icing

Potential (CIP) index has been developed for the FAA by the National Center for Atmospheric Research (NCAR) and quantifies the potential for clouds to produce icing on aircraft [Bernstein et al., 2005]. This index combines data from a number of sources (radars, aircraft, satellites, radiosondes, etc.) and applies the relevant physics to identify super-cooled water in clouds. Figure 2-11 and Figure 2-12 show that the CIP index is indeed highly correlated with clouds that produce natural cloud-to-ground lightning flashes in both New Mexico and Oklahoma (see also Figures A-7 and A-1). If it could be further demonstrated that the CIP index is also correlated with clouds that produce high electric fields in the absence of lightning, then this parameter could have wide application as a constraint in the LFCC. The CIP index would be particularly useful at launch sites that are not well supported by weather radars, ground-based electric field measurements, lightning mapping arrays, and the like.

The results of a correlation study are shown in Table 2-3. Results broken down by Spaceport are given in Appendix F. These results here in Table 2-3 and in Appendix F show a clear trend, with occurrence frequencies increasing (except for two minor deviations) with increasing CIP. For all months the occurrence frequency in the highest CIP bin greatly exceeds the occurrence frequency in the lowest bin. These results clearly indicate that CIP shows significant skill as an indicator of electrification. This index correlated with other information should be a useful operational product not only for natural lightning, but for triggered lightning as well.

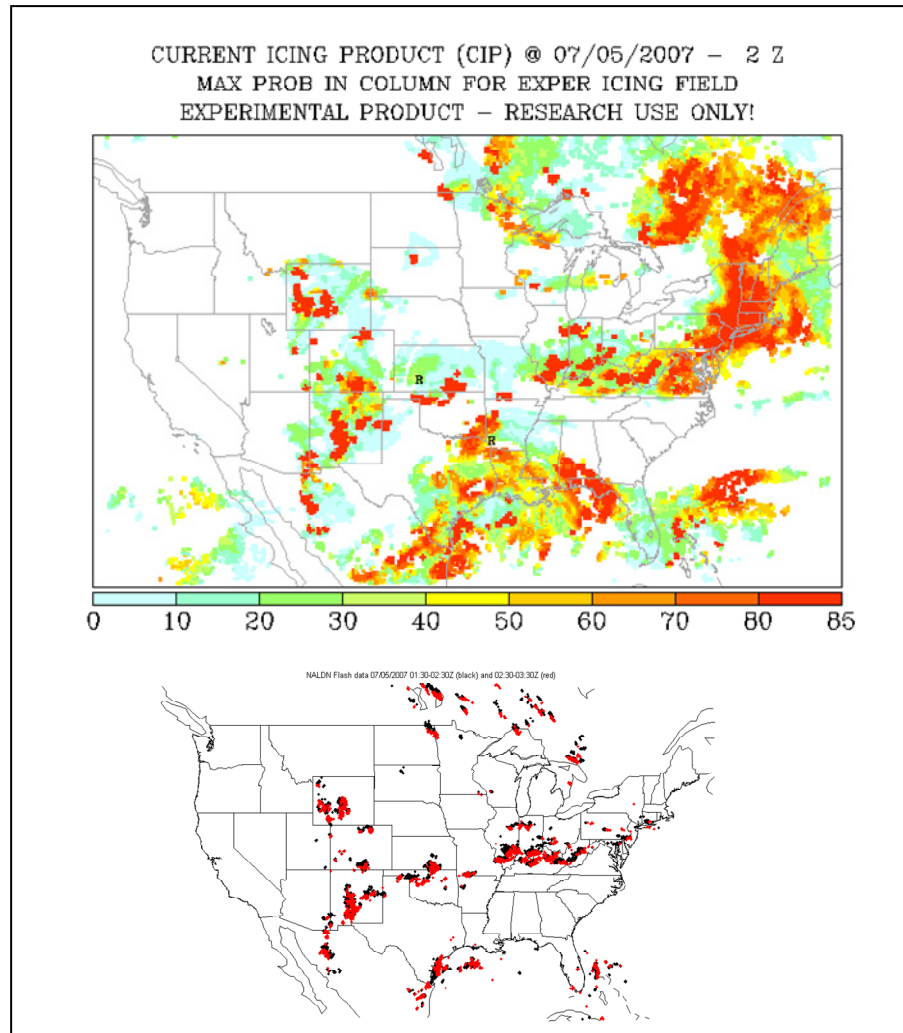


Figure 2-11. The Current Icing Product (CIP) at 2 UT on 5 July 2007 (upper panel) and CG lightning flashes (lower panel) detected by the National Lightning Detection Network (NLDN) during 1-hour intervals centered on the time of the CIP map (with permission). This data corresponds to the LMA data shown in Figure A-7 pertaining to SA.

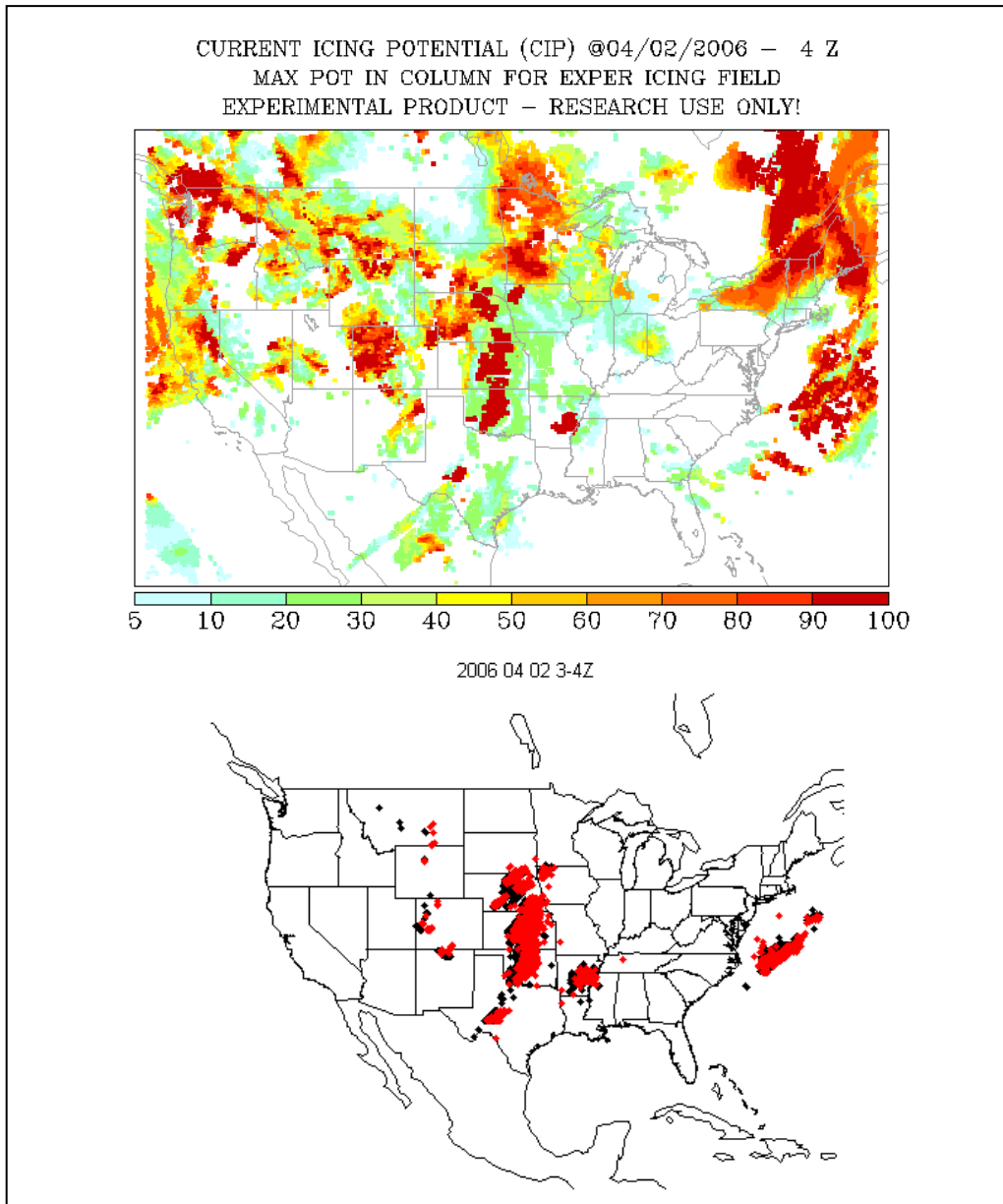


Figure 2-12. The Current Icing Product (CIP) at 2 UT on 2 April 2006 (upper panel) and CG lightning flashes (lower panel) detected by the National Lightning Detection Network (NLDN) during 1-hour intervals following the time of the CIP map. (With permission) This data corresponds to the LMA data shown in Figure A-1 pertaining to OS.

Table 2-3. The Variation of Lightning Occurrence in CIP Bins for Four Months over All Four Spaceports (MJSP, OS, SA, and WTLS).

**Lightning Occurrences < 100 km per Bin**

<b>Mo./Bin</b>	<b>0.2-0.4</b>	<b>0.4-0.6</b>	<b>0.6-0.8</b>	<b>0.8-1.0</b>
Jan	10	17	23	23
Apr	90	40	53	155
Jul	164	129	133	224
Oct	82	50	70	173
<b>Totals</b>	<b>346</b>	<b>236</b>	<b>279</b>	<b>575</b>

**Total CIP Determinations per Bin**

<b>Mo./Bin</b>	<b>0.2-0.4</b>	<b>0.4-0.6</b>	<b>0.6-0.8</b>	<b>0.8-1.0</b>
Jan	787	425	435	538
Apr	655	267	256	346
Jul	414	316	304	401
Oct	417	264	250	364
<b>Totals</b>	<b>2273</b>	<b>1272</b>	<b>1245</b>	<b>1649</b>

**Occurrence Frequencies**

<b>Mo./Bin</b>	<b>0.2-0.4</b>	<b>0.4-0.6</b>	<b>0.6-0.8</b>	<b>0.8-1.0</b>
Jan	0.01	0.04	0.05	0.04
Apr	0.14	0.15	0.21	0.45
Jul	0.40	0.41	0.44	0.56
Oct	0.20	0.19	0.28	0.48
<b>Totals</b>	<b>0.15</b>	<b>0.19</b>	<b>0.22</b>	<b>0.35</b>

## 2.6 Estimate Quantitative Triggering Conditions

### 2.6.1 Threshold Electric Field Environment for Triggering Lightning

The threshold electric field for triggering lightning is relevant primarily to an in situ measurement of  $E$  and only secondarily for the present, radar-based LFCC [see Krider et al., 2006, Appendix C, and section 2.5.2]. Application of the LFCC to RLVs (which are smaller vehicles and presumably have higher electric field thresholds) flying at mid-latitude, continental launch sites introduces two difficulties. The first is that the radar vs. field relationship (on which the anvil rules and the proposed debris-cloud rule in Appendix C are based) was developed for quasi-maritime, subtropical anvils and might not be valid for anvils that develop in a continental air mass that contains a different aerosol and/or humidity profile. This question should be considered further by experts in cloud physics.

Second, if the existing ABFM dataset (on which the proposed anvil and debris-cloud rules were based) is found to be applicable in other geographical locations and weather regimes, then an extreme-value statistical analysis, like that performed to develop the LFCC for large launch vehicles in Florida, will need to be repeated in order to quantify the radar parameters that correspond to higher electric field thresholds [Dye et al., 2006; Merceret et al. 2008].

Notwithstanding these difficulties, our approach to the triggering conditions here follows that of Krider et al. [2006, section 3.1], as outlined below. First a model is adopted for the triggering conditions by the rocket-and-grounded-wire technique. Then these triggering conditions are scaled to the altitudes and flight speeds of interest. Finally, the electrical effective length of each vehicle of interest (corresponding to the length of the grounded triggering wire in Eq. 2-1, below) is estimated. This effective length can be strongly influenced by the electrical effects of the vehicle's exhaust plume. New material has been developed with respect to both the altitude dependence of these triggering conditions (see detailed discussion by Krider et al. [2006, section 3.1.3]) and the electrical effects of exhaust plumes (see detailed discussion in the report by Krider et al. [2006, sections 3.1.5.3 and 3.1.5.4]) that will be presented in the corresponding sections below.

### 2.6.2 Models of Positive-Leader Viability

As outlined in section 1.2.3, Krider et al. [2006, section 3.1.2] selected the model of Bazelyan and Raizer [2000]. Bazelyan and Raizer [2000, p. 139] and Aleksandrov et al. [2005] have found that the minimum ambient field for triggering by small rockets trailing a grounded wire is

$$E_0 \approx 3.7 \times 10^5 H^{-3/5} \quad (2-1)$$

given a grounded wire of length  $H$ . This formula predicts that the ambient field required to trigger lightning decreases nonlinearly as the electrical effective length of the triggering object increases.

### 2.6.3 Altitude (Density) Dependence of Triggering

A new analysis of the dependence of positive-leader-viability conditions on atmospheric pressure by Bazelyan et al. (2007) has predicted that the conditions for continued propagation of a positive leader (which we have taken as the primary determinant of the triggering conditions) may be nearly independent of atmospheric pressure (altitude). Although this would be a welcome result (the triggering-field thresholds would not decrease rapidly with increasing altitude, as we previously assumed), the assumptions and theoretical manipulations used to obtain it were both uncertain and complex. Further, it has no direct experimental validation. To take the more conservative course, the Lightning Advisory Panel decided to use Paschen's Law (breakdown field inversely proportional to gas density) in its development of the new volume-averaged, height-integrated radar reflectivity (VAHIRR) criterion from the ABFM II results [Dye et al., 2006]. This decision is retained here from



Krider et al. [2006, section 3.1.3], with the understanding that this may have resulted in an underestimate of the triggering thresholds at altitudes well above the surface.

#### **2.6.4 Velocity Dependence of Triggering**

As previously discussed in detail by Krider et al. [2006, section 3.1.4], any velocity dependence of the triggering conditions is not believed to be relevant for present purposes.

#### **2.6.5 Modeling of Electrical Conduction in Plume Exhausts**

Our previous report on this topic (see Krider et al., 2006, sections 3.1.5.3 and 3.1.5.4) depended primarily on photographic and video measurements of the extent of the visible radiation from the incandescent particulates in the exhaust. At that time we had neither access to a model of plume conductivity, nor any real idea what conductivity level might correspond to the electrical extremity of the plume. A numerical plume model that is capable of predicting the conductivity distribution in the hot exhaust gases is described in section 2.6.5.1, and its results are used in subsequent sections. Then we ask what conductivity levels in exhaust plumes might be important for determining the effective electrical length of a vehicle in flight. Note that this is not the same problem as determining the radar cross section of a plume or the attenuation length for S-band communications. Our problem is much more similar to an electrostatic problem, because the ambient conductivity of the troposphere, in which our plume is acting as a conductor, is so low—typically less than  $10^{-12}$  s/m below an altitude of 10 km.

We will first use a dimensional argument to estimate the relevant conductivity levels for determining the electrical length of an exhaust plume. This argument will then be extended to a simple, 1½-dimensional calculation of the relaxation time of the potential (as opposed to the local electrical relaxation time) at the end of a uniform, motionless, conducting plume embedded in insulating air. Finally, we will explore the validity of our dimensional argument with an explicit 1-D, steady-state model of plume conduction, with variable conductivity but a uniform flow velocity. Then, in 2.6.5.7, recommendations are offered on how to make these crude estimates more realistic by developing a more complex, but relatively straightforward numerical model.

##### **2.6.5.1 Simulation with Plume Modeling Code**

The objective of the modeling study is an assessment of electrical conductivity in the plume of a rocket engine hypothesized to power a reusable, suborbital, FAA concept vehicle. Concept Vehicle #3 (“HTHL w/rocket engines”) employs two or four rocket engines of ~4,000 lbf thrust each over a range of tropospheric altitudes. The possible presence of sodium (Na) and/or potassium (K) contaminant in some chemical form in the engine’s Rocket Propellant 1 (RP-1) fuel, or liquid oxygen (LOX) oxidizer, has the potential to generate free electrons and/or ions in the exhaust plume, resulting in large conductivity levels.

A sequence of rocket engine nozzle and flow-field chemistry codes was used to estimate the generation and density of charged species and the resultant conductivity (mho/m) in the plume. The rocket engine was modeled as a scaled-down version of a typical large RP-1/LOX fueled engine. The hardware was scaled linearly to achieve 4,000 lbf thrust, while maintaining the nominal operating conditions of the large engine (e.g., chamber pressure). The oxidizer/fuel flow weight ratio was set to the concept value of 2.25. The model was run for a single engine of the 2–4 engine propulsion system of the concept vehicle. Depending on the geometrical arrangement of individual engines, the centerline conductivity and length of a multi-engine plume could be somewhat greater than that from the single-engine calculation.

The baseline engine performance and nozzle exit-plane conditions (e.g., neutral species abundances, temperature, pressure, flow speed, etc.) were modeled with a combustion chamber/nozzle computer code. Na and K contaminants were inserted in the form of NaCl and KCl at the nozzle exit plane of the calculation. Three levels of contaminant abundance were considered: 1, 5, and 25 ppm by weight of Na and the same simultaneous abundance by weight of K in the RP-1 fuel. Alternate chemical forms for exit-plane insertion of Na and K (e.g., NaO, NaOH, Na+Cl, Na<sup>+</sup>+Cl<sup>-</sup>, Na<sup>+</sup>+e<sup>-</sup>+Cl, etc.) had negligible impact on modeled plume conductivity levels. No soot, or other particulate, was included in the nozzle flow.

The plume flowfield downstream of the nozzle exit plane, including afterburning chemistry and the generation/destruction of ionic species, was modeled with a rocket plume flowfield/chemistry code employing an extensive neutral and ion chemistry reaction set. The flowfield code generates species properties and conductivity levels over a grid of three-dimensional locations in the plume. At its widest, the diameter of the single-engine plume was roughly an order of magnitude smaller than its length. Conductivity values down the centerline of the plume axis are of greatest interest.

The models were run for a representative range of conditions. Three points along the flight path were considered:

1. time (t)=50 s, altitude (H)=0.91 nmi, velocity (V)=715 ft/s
2. t=70 s, H=2.74 nmi, V=859 ft/s
3. t=85 s, H=5.05 nmi, V=1038 ft/s

Typical modeled plume centerline conductivities were  $10^{-1}$ – $10^{-2}$  mho/m over the first 5–6 m downstream of the nozzle and fell to  $10^{-5}$ – $10^{-6}$  mho/m as the plume cooled at a downstream distance of 15–25 m, depending on altitude. For all altitudes considered, the length of the highly conductive region of the plume was comparable to, or greater than, the length of the concept vehicle hardbody (i.e., rocket plane length = 6.4 m). The conductive plume length is related only coincidentally to the vehicle length and is driven by the engine thrust, vehicle speed, and altitude.

It should be noted that in many cases the mechanisms and rate constants of the ion-related reactions necessary for conductivity model calculations are not well known. The model calculations should be considered only best estimates. Uncertainties in mixing and chemistry rates will have the greatest impact on ion recombination processes in the cooling tail of the plume and consequently on the details of the rapid conductivity fall-off beyond a distance of 5–6 m. It is unlikely that modeled conductivities less than  $10^{-5}$ – $10^{-6}$  mho/m are meaningful. It should also be noted that the RP-1 fueled engines may produce soot, which is not included in the present chemistry/ion model and which could influence the conductivities.

### **2.6.5.2 Prior Research**

Prior literature on the electrical conductivity of rocket exhausts is extensive, but largely classified and directed primarily toward establishing the radio and radar signatures of ballistic missiles during launch and/or the attenuation of telemetry signals between those missiles and ground stations. Thus, this literature is mostly irrelevant for present purposes. The most relevant literature has been reviewed by Perala et al. [1994], a reference that remains the most comprehensive attempt to address the effects of the vehicle exhaust on the lightning-triggering problem. This work is discussed here in some detail. Earlier work includes Krider et al. [1974], who report spectroscopic measurements of exhaust temperature from the Saturn V booster, but do not address the relatively low conductivity levels of interest here; and Uman [1970, p. 9], who hints at our problem (“Below about 3500 feet, the exhaust can be considered an insulator... [electrical relaxation time] exceeds 1 second [conductivity about  $10^{-11}$  s/m] and the charge density is sufficiently small that only electric fields smaller than about

10 V/cm can be excluded from the interior of the exhaust”) but does not explain the origin or significance of this conclusion. Also noteworthy is the work of Heckscher [1972] and Heckscher and Pagliarulo [1973], who attempted to estimate the conductivity levels of interest here (see below) and to measure directly (with limited success) the conductivity of rocket exhausts during launch.

Perala et al. [1994] adopted an interesting, but ultimately unsatisfying, approach. They first assume (reasonable but apparently without experimental justification) that the trailing end of the conductive portion of an exhaust plume acts like a Kelvin water-dropper or flame potential equalizer. That is, any space charge that would normally accumulate at this location is carried away in the exhaust flow so that, at equilibrium, this point has zero longitudinal electric field and therefore is at the same electrostatic potential as the ambient air at roughly the same altitude. This point in the plume is defined by a “critical conductivity” that will be determined later in the context of a plume-chemistry model. Second, it is assumed that all of the (two-dimensional) exhaust volume bounded by the critical-conductivity contour acts as a perfect conductor that is electrically attached to the rocket body. With these assumptions, the electric field at the nose of the rocket can be calculated using electrostatic theory and is proportional to the magnitude of the ambient electric field in the longitudinal direction. (The rocket/plume conductor has a net charge that exactly cancels the longitudinal field that would be induced at the trailing edge of an uncharged conductor in the ambient field. The equal and opposite net charge on the plume is assumed to disappear downstream in the exhaust trail.)

The next steps taken by Perala et al. [1994] make use of two static test firings of small solid-rocket motors (described in their Appendix E), together with a numerical model of the chemistry of the exhaust-plume (described in their Appendix G), and these steps are considered even less reliable than the electrostatic model outlined above. First a motor test stand was insulated from the ground, and an electrostatic field was applied along its longitudinal axis, so that the effective resistance of a fixed length of the exhaust plume could be measured. The results were then compared to predictions of the plume-chemistry code [Pergament et al., 1993] and found to be far out of agreement. The code was therefore “refined” (the rapid hydration of positive ions and its effect on later recombination with unhydrated negative ions are included) to yield reasonable agreement between measurements and predictions. The modified plume code was then used to compute the two-dimensional geometry of various contours of the electrical conductivity (extending down to  $10^{-10}$  s/m) that was expected in the exhaust plume of the small rocket motors. A second static test was conducted to measure the charging of a motor in the presence of a known, fair-weather, atmospheric-electric field. These measurements were extrapolated to obtain an asymptotic motor voltage, which was then compared with predictions of the electrostatic model described above, based on the different geometries of the model conductivity contours. The contour that gives the best agreement was interpolated to be  $3 \times 10^{-10}$  s/m. This was taken to be the “critical conductivity” defined above and, therefore, the conductivity value that defines the “conducting extent” of the plume. Finally, the authors argue that this value should be essentially the same for larger rockets powered by different motors. Although the work of Perala et al. [1994] has many uncertainties, not the least of which is the plume-chemistry model that they use, it is interesting that we arrive at a similar estimate of the “critical conductivity” using two different approaches in sections 2.6.5.3 and 2.6.5.5 below.

Eriksen et al. [1991] outline an earlier version of the above scheme, which is of interest because it contains some of the ideas elaborated herein:

- A one-dimensional, time-dependent model of space-charge distribution along the length of an exhaust plume is discussed qualitatively, and its steady-state solution is sketched without being explicitly derived, as we have done in 2.6.5.3.
- A dimensional argument is used to equate electrical relaxation time to the ratio of a plume length and a rocket velocity, as is done in the next section.

The main difference between Eriksen's work and the new work described here is that the plume length scale used by Eriksen et al. [1991] is the downstream *thickness* of a transition region across which the longitudinal electric field is presumed to increase from near zero (inside conductive part of the plume) to near ambient (in the insulating part). This latter concept is incorporated into an iterative, electrostatic procedure for determining rocket net charge, similar to the electrostatic part of the calculation by Perala et al. [1994] (discussed above). A critical flaw in the calculation proposed by Eriksen et al. [1991], however, is that the thickness of the transition region is to be calculated from electrostatics, whereas in reality it is determined by the conductivity gradient and exhaust velocity.

Heckscher [1972] outlines an interesting method of estimating the conductivity level of interest. Although quite different from either the complex approach of Perala et al. [1994] (above) or the simple arguments presented below [sections 2.6.5.3 and 2.6.5.5], Heckscher's calculation is noteworthy for yielding similar results. He considers the initial stages of a launch and asks at what altitude the rocket electrically disconnects from ground, so that its potential can rise toward local ambient. This question is answered by balancing the current required to charge the rocket/plume combination (to hold it at ground potential as the vehicle gains altitude) against the current that can flow through the interface between plume and ground. Since both of these currents are proportional to the ambient field, the result is independent of it. This equation defines the critical conductivity level at ground level in the plume as a function of vehicle altitude and other geometrical factors. Estimates are given for Minuteman, Atlas, and Saturn vehicles in Heckscher's Figure 15, which range from about  $3 \times 10^{-11}$  to  $3 \times 10^{-9}$  s/m for altitudes ranging between about 30 m (for Atlas) and 500 m (for Minuteman), respectively.

Armed with the relevant conductivity range, Heckscher [1972] and Heckscher and Pagliarulo [1973] describe instrumentation for, and ground-based measurements of, conductivity in the fringes of exhaust plumes from Minuteman, Atlas, and Saturn vehicles shortly after liftoff. They find measured conductivity values comparable to their calculated critical values for vehicle altitudes in the range given above.

### **2.6.5.3 The Dimensional Argument**

As mentioned above, we are primarily concerned with the effects of an exhaust plume on the effective electrical dimensions of a vehicle in flight. The plume will be effective in this context to the extent that it can exclude the ambient electrostatic field on a time scale that is relevant for the plume kinematics. Very roughly, the electrical relaxation time (which controls the local decay of space charge by conduction) at any point in the plume must be shorter than the transit time of the material from the exhaust nozzles to that point in space. Since the relaxation time is determined entirely by the electrical conductivity of the material, this puts a lower bound on the conductivity of interest at each downstream location, thus indirectly determining the effective electrical length (given model predictions of the velocity and conductivity distributions in the plume).

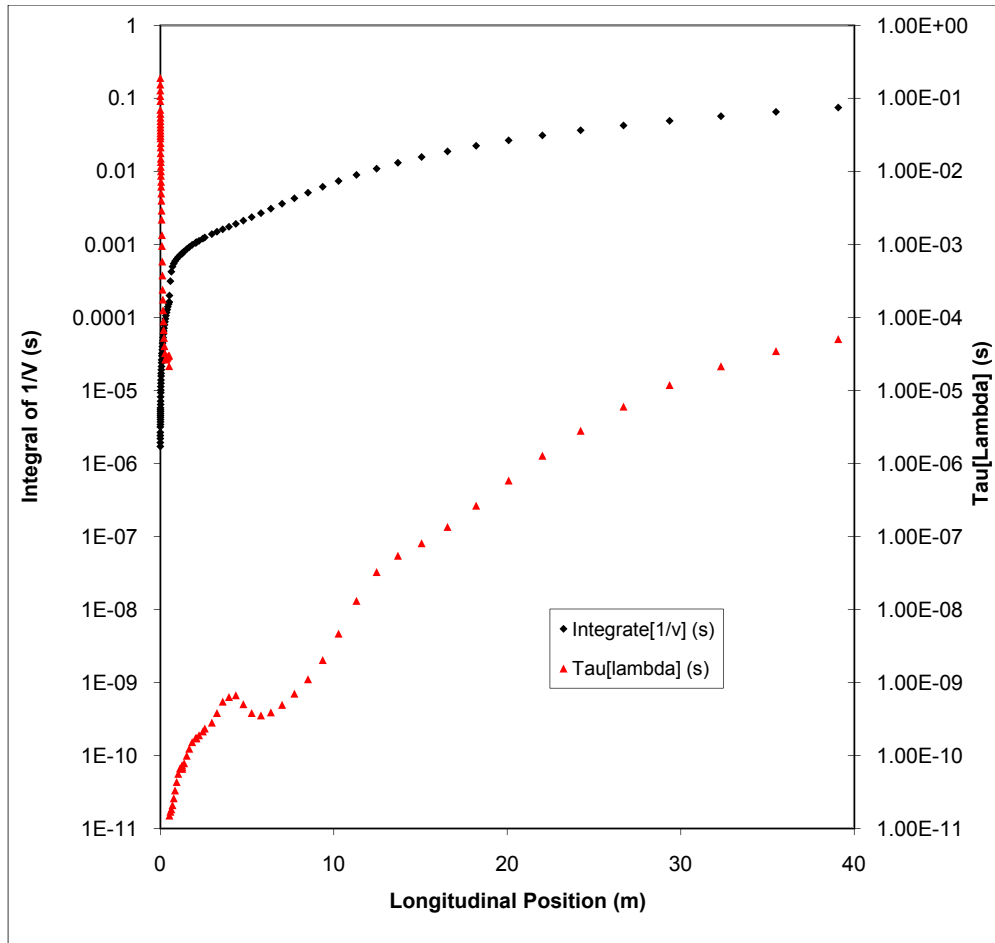


Figure 2-13. Plot of time of flight (Integral of  $1/v$ —the black diamonds) and electrical relaxation time ( $\text{Tau}[\lambda]$ —the red triangles) in an exhaust parcel vs. downstream distance, based on results from the model discussed in section 2.6.5.2 at a rocket altitude of 9.4 km and an alkali-metal concentration of 5 ppm.

A more physical way to look at the electrodynamics of the plume on the relevant time scales is to first imagine a completely static “plume,” with a conductivity that decreases radially and downstream from the exhaust nozzle, embedded in a uniform, longitudinal, electrostatic field in air with a uniform background conductivity. During the approach to equilibrium, space charge will build up on the conductivity gradients and exclude most of the field from the high-conductivity regions. (This is a simple calculation in the one-dimensional case, but not so simple in the more realistic, 2-D, cylindrically symmetric case.) Now consider what happens when the system is put into motion, with the vehicle traveling through the air and the plume flowing relative to both the vehicle and the ambient air. The steady-state, equilibrium space charge described above will be “blown away” to the extent that it cannot be replenished rapidly enough by conduction—a process governed by the electrical relaxation time. Again, a rough estimate of the electrical length of the plume is given by the downstream distance at which the relaxation time equals the transit time of exhaust gas from the nozzle to that point.

This concept could be refined with fully 2-D modeling, of course, and this is recommended below. Nevertheless, the current concept might be good enough for present purposes, depending on the accuracy of the available conductivity estimates. In any case, it suggests that the conductivities of concern to us will be much lower than those that are involved in estimating the radar cross section of the plume. As an example, suppose that a dynamical transit time from the nozzle to some point in the

plume is 0.1 s. That time-scale corresponds to a conductivity level of about  $9 \times 10^{-11}$  s/m, which is about 10,000 times greater than a typical background conductivity of surface air (or about 200 times greater than air at 10 km altitude). Notice that this crude estimate is comparable to those of Perala et al. [1994] ( $3 \times 10^{-10}$  s/m) and of Heckscher [1972] ( $3 \times 10^{-11}$  to  $3 \times 10^{-9}$  s/m), which are summarized above.

As a more concrete example, Figure 2-13 compares the time-of-flight from the exhaust nozzle to a point of interest, with the electrical relaxation time at the same point for different distances downstream from the nozzle, based on the plume model that was described in section 2.6.5.1. Notice that (except perhaps very close to the nozzle) the time-of-flight greatly exceeds the relaxation time at all locations within the domain of the calculation, which in turn suggests that the effective electrical length of this plume is much greater than 40 m. At greater distances downstream, the exhaust velocity should become constant (equal and opposite to the rocket velocity) so that the time-of-flight increases linearly, while the conductivity decreases (and the relaxation time increases) by several orders of magnitude until it approaches the value of ambient air, about  $6 \times 10^{-13}$  s/m (time constant around 15 s) at the same altitude. Thus one would expect the two curves to cross at some position further downstream.

#### 2.6.5.4 The 1½-Dimensional Calculation of Relaxation Time

The use of the electrical relaxation time (a strictly local parameter) in the above estimates is not altogether satisfying, because it does not take into account the dimensions of the plume, hence its electrical resistance and capacitance per unit length. A simple way to investigate the effects of these parameters is to consider electrical conduction in a uniform, stationary cylinder whose cross section is much smaller than its length. With the additional caveat that the conductivity within the cylinder is much larger than that of the ambient air, this is analogous to the familiar, time-dependent problem of heat flow in an insulated, thermally conducting rod that is driven from one end. For the initial conditions, we can assume that the voltage distribution,  $V(z,0)$ , along the rod/plume is linear at time,  $t = 0$ , as a result of a uniform, ambient, electric field,  $E_0$ —in other words, the plume is initially invisible electrically. With the plume grounded at one end (at the exhaust nozzle,  $z = 0$ ), we can solve for the voltage at the other (downstream or insulated) end at  $z = H$ , as a function of time,  $V(H, t)$ . Over time, the voltage throughout the plume will approach ground potential at a rate determined by the resistance per unit length,  $R_1$  (based on the internal conductivity and cross-section area), and the capacitance per unit length,  $C_1$  (based on the dimensions alone). If we can find the value of uniform internal conductivity for which the downstream end of the rod/plume approaches ground potential on the same time scale as the time-of-flight for an exhaust parcel to reach that end, as proposed in the dimensional argument above, then we have an estimate of the relevant conductivity level.

The governing partial-differential equation for this problem is

$$\frac{\partial^2 V}{\partial z^2} = R_1 C_1 \frac{\partial V}{\partial t}, \quad 0 \leq z \leq H, \quad 0 \leq t \quad (2-2)$$

with the initial and boundary conditions

$$V(z,0) \equiv -E_0 z, \quad V(0,t) \equiv 0, \quad \left. \frac{\partial V}{\partial z} \right|_{H,t} \equiv 0 \quad (2-3)$$

The complete solution of (2-3) and (2-4) can be written as an infinite sum that simplifies at  $z = H$  to

$$V(H,t) = -\frac{8HE_0}{\pi^2} \sum_{n \text{ odd}} \frac{1}{n^2} \exp\left[-\left(\frac{\pi n}{2H}\right)^2 \frac{t}{R_1 C_1}\right] \quad (2-4)$$

At  $t = 0$  (2-4) becomes simply

$$V(H,0) = -\frac{8HE_0}{\pi^2} \sum_{n \text{ odd}} \frac{1}{n^2} \quad (2-5)$$

Since the infinite sum in (2-5) equals  $\pi^2/8 \approx 1.23$  (ignoring the dimensional coefficient), the first term is by far the largest, constituting 81 percent of the total. Thus we can approximate the initial behavior of  $V(H,t)$  quite well by a simple exponential with time constant  $\tau_0 = 4H^2 R_1 C_1 / \pi^2$ .

In order to evaluate this time constant, we need to know the resistance and capacitance per unit length in the plume. The former is easily written for a conducting cylinder:

$$R_1 = \frac{4}{\lambda_0 \pi d^2} \quad (2-6)$$

in ohms/m, where  $\lambda_0$  is the conductivity of the material and  $d$  is its diameter. The capacitance per unit length is a more difficult parameter, however, because it depends on where “ground” is assumed to be. For our present purposes, we will use an approximate formula that has been derived for a thin, vertical cylinder extending upward from height,  $H$ , to height,  $2H$ , (in other words, of total length,  $H$ ) above an infinite, horizontal, conducting, ground plane [see Terman [1943, section 2, Equation 134 and Table 30],

$$C_1 \approx \frac{24.1 \times 10^{-12}}{\log_{10}(2H/d) - 0.207} \quad (2-7)$$

in F/m. Thus, the time-constant (in seconds) is

$$\tau_0 \approx \frac{12.5 \times 10^{-12}}{\log_{10}(2H/d) - 0.207} \frac{1}{\lambda_0} \frac{H^2}{d^2} \quad (2-8)$$

Now, if we assume that the diameter/length ratio of the plume is 1/10 (as suggested by results from the model described in section 2.6.5.1) and that the internal conductivity is  $10^{-6}$  s/m and uniform (approximately the model-predicted conductivity 15 to 30 m downstream in the plume, depending on its altitude and alkali-metal content). These values imply that the electrical time constant near the downstream end of the plume is roughly  $\tau_0 \approx 10^{-3}$  s. This value is about two orders of magnitude longer than the simple electrical relaxation time corresponding to the assumed conductivity—a result of the extra time that is required to charge the capacitance of the relatively large plume surface area through the resistance of the relatively small plume cross section. Nevertheless,  $\tau_0$  is almost two orders of magnitude shorter than the parcel time-of-flight to a point 30 m downstream from the nozzle. This result suggests that the effective electrical length of the plume is much longer than 30 m, or to put it another way, that the critical conductivity level is closer to  $10^{-8}$  s/m than the modeled  $10^{-6}$  s/m.

### 2.6.5.5 The 1-Dimensional Model of Charge Advection

The simple model in the previous section contains no charge advection. Although it does offer a more realistic estimate of an electrical time scale in the plume, it still depends on crude, time-of-flight estimates of a comparable kinematic time scale. A complete, two-dimensional calculation that incorporates both electrical conduction in the presence of non-uniform conductivity and the mechanical motion of the space charge that develops on the conductivity gradients in a non-uniform flow field is clearly beyond the scope of this study. Nevertheless, we have explored the interactions between a spatially varying conductivity and charge advection in a 1-D setting.

First, the governing equations for a 2-D, time-dependent plume model are derived for use later in our recommendations (see section 4.4). These equations will then be simplified for the 1-D, steady-state problem that is of interest here.

We begin with Maxwell's equations, where we have already assumed  $\mathbf{D} = \epsilon_0 \mathbf{E}$  and  $\partial \mathbf{B} / \partial t \approx 0$  (which can be called the "quasi-static" approximation) in the following:

$$\nabla \times \mathbf{H} = \mathbf{J} + \epsilon_0 \frac{\partial \mathbf{E}}{\partial t} \quad (2-9)$$

$$\nabla \times \mathbf{E} = 0 \quad (2-10)$$

$$\epsilon_0 \nabla \cdot \mathbf{E} = \rho \quad (2-11)$$

Here  $\mathbf{J}$  is the vector electric current density,  $\epsilon_0 = 8.85 \times 10^{-12}$  F/m is the dielectric permittivity of free space,  $\mathbf{E}$  is vector electric field, and  $\rho$  is volume density of space-charge. Since the divergence of any curl is identically zero, Eq. (2-9) can be combined with Eq. (2-11) to get the following charge-conservation equation:

$$\frac{\partial \rho}{\partial t} = -\nabla \cdot \mathbf{J} \quad (2-12)$$

In our situation, the total electric current density is due to the vector sum of the conduction current density plus the current density produced by the mechanical motion of  $\rho$  (or the "convection-current" density):

$$\mathbf{J} = \lambda \mathbf{E} + \rho \mathbf{v} \quad (2-13)$$

where  $\lambda$  is conductivity and  $\mathbf{v}$  is the velocity of the plume material. Equations (2-10), (2-11), (2-12), and (2-13) are the equations that govern the charge or electric-field distribution in the plume.

Inserting (2-13) into (2-12) results in an equation that we will use below:

$$\frac{\partial \rho}{\partial t} = -\nabla \cdot (\lambda \mathbf{E} + \rho \mathbf{v}) \quad (2-14)$$

Assuming incompressible flow for simplicity (invalid near the exhaust nozzle, of course), and again using Eq. (2-11), we can more clearly see the following physical processes at work in our plume:



$$\frac{\partial \rho}{\partial t} = -\mathbf{E} \cdot \nabla \lambda - \left( \frac{\lambda}{\varepsilon_0} \right) \rho - \mathbf{v} \cdot \nabla \rho \quad (2-15)$$

Basically, space charge accumulates as a result of electrical conduction parallel to the electric field as a result of the conductivity gradient, decays with the local electrical relaxation time, and advects with the material flow. Note that the first term on the RHS, which we will call the “accumulation term,” is the source of all *net* space charge in the plume (unless the rocket engine itself actively transfers charge from the rocket to the exhaust).

Now assuming that the conductivity and the longitudinal component of the exhaust velocity,  $w$ , both depend only on the downstream distance,  $z$ , from the nozzle, we can set all time-derivatives to zero, and forbid any radial or tangential components or variability in the electric field or velocity. Under these very simplified conditions, Eq. (2-11) in conjunction with Eq. (2-14), can be integrated once over  $z$  to get a first-order, ordinary differential equation with nonconstant coefficients that describes the longitudinal component of the electric field,  $E_z$ :

$$\varepsilon_0 w(z) \frac{dE_z}{dz} + \lambda(z) E_z = J_0 \quad (2-16)$$

(Note that the major simplification here results, not from our steady-state assumption, but from reducing the dimensionality from three or two, to one. This obviates the need to use Eq. (2-2) and allows Eq. (2-6)—or more precisely, its predecessor, the divergence of Eq. (2-1)—to be integrated immediately over  $z$ .) For the present calculations, we will set  $w(z) \equiv w_0$ , a constant. This is a logical consequence of incompressible flow in one dimension, but it is by no means necessary to solve the 1-D problem. For convenience, we will also assume an explicit form for the conductivity a function of  $z$ :

$$\lambda(z) \equiv \lambda_\infty + \lambda_0 e^{-z/L} \quad (2-17)$$

where  $\lambda_\infty$  is the ambient conductivity, when  $z \rightarrow \infty$ , and  $\lambda_0$  is essentially the (presumed much larger) conductivity at the nozzle exit,  $z = 0$ .  $J_0 = \lambda_0 E_0 = \lambda_\infty E_\infty$  is the uniform total current density passing through the domain, where the subscripts on  $E$  have the same meaning as those on  $\lambda$ , and the equalities result from the assumption that there is no space charge at either end of the domain to be advected. The first equality ( $J_0 = \lambda_0 E_0$ ) also serves as the initial condition on  $E_z(0)$ .

Equation (2-8) can then be made nondimensional by introducing the following scaled variables:

$$\left. \begin{aligned} z' &\equiv z/L \\ E'(z') &\equiv E_z(z)/E_0 \\ \tau'(z') &\equiv \frac{\lambda_0}{\varepsilon_0} \tau_\lambda(z) \end{aligned} \right\} \quad (2-18)$$

where  $\tau_\lambda(z) \equiv \varepsilon_0/\lambda(z)$  is the local electrical relaxation time (used only for reference). Notice that the spatial scale,  $L$ , is defined by the e-folding length of the conductivity in Eq. (2-17). Notice also that we have used values at the nozzle exit as our scaling constants, so that  $E'(0) = \tau'(0) = 1$ . The following dimensionless parameters can also be introduced:

$$\left. \begin{aligned} W &\equiv \frac{\varepsilon_0}{\lambda_\infty} \frac{w_0}{L} \\ \Lambda &= \frac{\lambda_\infty}{\lambda_0} \end{aligned} \right\} \quad (2-19)$$

W can be thought of as a speed parameter (a proxy for  $w_0$ , the longitudinal plume velocity) or as the ratio of an electrical time scale,  $\varepsilon_0/\lambda_\infty$ , to a convective time scale,  $w_0/L$ . (Note: In our definition of W, we have deliberately used  $\lambda_\infty$  instead of  $\lambda_0$  for the conductivity scaling so that W will be independent of  $\Lambda$ .) Given our assumptions about the values of conductivity, we expect  $\Lambda \ll 1$ . Inserting Eq. (2-18) and Eq. (2-19) into Eq. (2-16), we get the following equation in terms of nondimensional variables:

$$\Lambda W \frac{dE'}{dz'} + \Lambda E' + e^{-z'} E' = 1 \quad (2-20)$$

with the initial condition,  $E'(0) = 1$ .

Figure 2-14 shows a numerical solution of (2-20) when  $W = 2270$  and  $\Lambda = 1/100,000$ . This value of W was chosen to represent a case where  $w = 400$  m/s,  $L = 2.6$  m, and  $\lambda_\infty = 6 \times 10^{-13}$  s/m, estimated from the plume-model solution when the rocket altitude is 9.4 km and the alkali-metal concentration is 5 ppm, as in Figure 2-13. The value of  $\Lambda$  is essentially arbitrary, as we will see later; but it does determine the vertical scale of the plot, because  $E_\infty/E_0 = \lambda_0/\lambda_\infty$ . The red curve in Figure 2-14 is the dimensionless solution of Eq. (2-20) for  $E'(z')$ . The green curve is  $\tau'(z')$ , which is completely determined by  $\lambda(z)$  and is shown because of its equivalence to the solution for  $w \rightarrow 0$ . In this limit, the uniformity of total current guarantees that  $E(z) = J_0/\lambda(z)$ . The cyan curve is the limiting form of the solution for  $\lambda(z) \rightarrow \lambda_\infty$ . In this limit, there is no conductivity gradient, and the space charge inside each parcel decays with the electrical-relaxation time of the ambient air,  $\tau_\lambda(\infty) \equiv \varepsilon_0/\lambda_\infty$ , as it drifts downstream at velocity  $w$ . Integrating the charge profile once over  $z$  gives the corresponding  $E_z(z)$ .

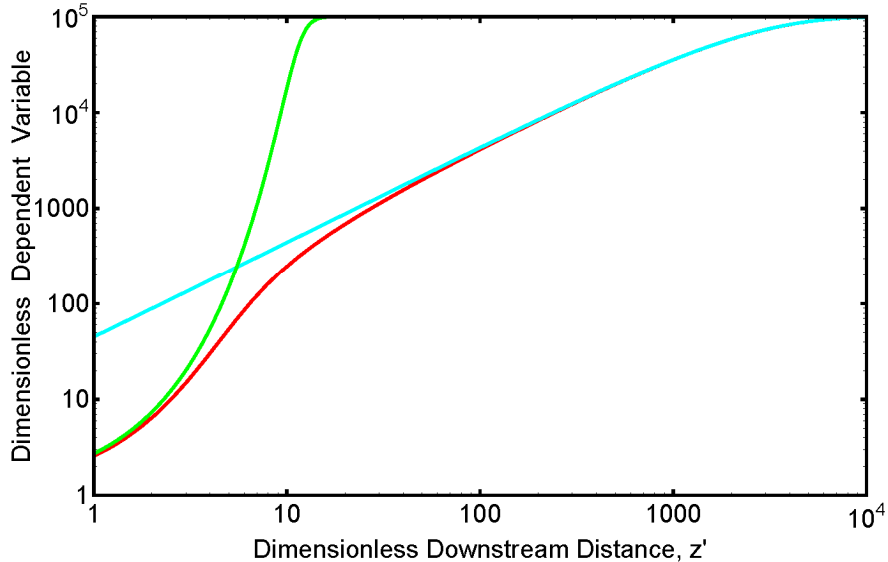


Figure 2-14. Nondimensional numerical results for  $W = 2270$  and  $\Lambda = 1/100,000$ . Solutions of Eq. (2-20) for  $E'(z')$  [red curve],  $\tau'(z')$  [green curve], and the limiting form of the solution for  $\lambda(z) \rightarrow \lambda_\infty$  [cyan curve] are shown as functions of the dimensionless downstream position,  $z'$ .

Two features of Figure 2-14 are noteworthy:

1. The values of  $E'(z')$ —the red curve—tend to approach  $\tau'(z')$ —the green curve—at small  $z'$  because the conductivity is larger (and  $\tau'$  is smaller) there, which means electrical conduction is more important than mechanical transport. This is also the region where space charge tends to accumulate (at least initially) because the gradient in conductivity is highest. Not surprisingly,  $E'(z')$  follows  $\tau'(z')$  more closely as either  $\Lambda$  or  $W$  decreases.
2.  $E'(z')$  approaches the uniform-conductivity limit—the cyan curve—at large  $z'$  because both the conductivity and its gradient are smaller (i.e.,  $\tau'$  is larger and more uniform) there, which means that charge accumulation is less important relative to advection. Also as expected,  $E'(z')$  follows this limit more closely as either  $\Lambda$  or  $W$  increases.

The latter behavior indicates an important shortcoming of the 1-D model. Since uniform conductivity implies that any space charge in a parcel simply decays with the relatively long, ambient electrical relaxation time, any charge that is blown out of the accumulation region (where the conductivity gradient is high) can travel a long distance downstream. But because there can be no radial “fringing” of the electric field in one dimension, all of this space charge contributes directly to the longitudinal electric field through the 1-D version of Eq. (2-2). This in turn produces a large field change that extends over a long distance downstream (roughly,  $z'$  between 10 and 10,000 in Figure 2-14). The implied strong shielding of the ambient field (e.g., only 0.65 percent of ambient at  $z' = 20$  in this case) is certainly not an accurate representation of the true situation in 2-D.

Table 2-4. Seven Related Tables of Numerical Results Extracted from Solutions of Eq. (2-20) for Various Parameter Combinations (see text)

$z'_x$ :	$W$		
$\Lambda$	22.7	227	2270
1.0E-04			2.5
1.0E-05	12.0	8.3	5.7
1.0E-08			13.0

$\tau'(z'_x)$ :	$W$		
$\Lambda$	22.7	227	2270
1.0E-04			1.20E+01
1.0E-05	4.00E+04	3.70E+03	2.50E+02
1.0E-08			5.60E+05

$\tau'(\infty)/\tau'(z'_x)$ :	$W$		
$\Lambda$	22.7	227	2270
1.0E-04			833.3
1.0E-05	2.5	27.0	400.0
1.0E-08			178.6

$L/w[s]$ :	$W$		
$\Lambda$	22.7	227	2270
1.0E-04			6.5E-03
1.0E-05	6.5E-01	6.5E-02	6.5E-03
1.0E-08			6.5E-03

$z_x/w[s]$ :	$W$		
$\Lambda$	22.7	227	2270
1.0E-04			1.6E-02
1.0E-05	7.8E+00	5.4E-01	3.7E-02
1.0E-08			8.4E-02

$\tau_\lambda(z_x)[s]:$	$W$		
$\Lambda$	22.7	227	2270
1.0E-04			1.8E-02
1.0E-05	5.9E+00	5.5E-01	3.7E-02
1.0E-08			8.3E-02

$(z_x/w)/\tau_\lambda(z_x):$	$W$		
$\Lambda$	22.7	227	2270
1.0E-04			0.92
1.0E-05	1.32	0.99	1.00
1.0E-08			1.02

Nevertheless, other aspects of the 1-D model results may well be meaningful. For example, the deviation of  $E'(z')$  from  $\tau'(z')$  with increasing  $z'$  (above  $z' \sim 3$  in Figure 2-14) implies that mechanical transport is beginning to overwhelm conductive charge accumulation in this region – basically, the accumulated space charge is being blown away from the conductivity gradient that is producing it. If we take the point at which  $\tau'(z')$  (the green curve) crosses the cyan curve ( $z_x' = 5.7$  in this case) as a measure of this downstream distance, we can tabulate the results for several combinations of parameter values.

The first two blocks of Table 2-4 show values of  $z_x'$  and  $\tau'(z_x')$ , respectively, for several combinations of the parameters,  $W$  (ranging from 22.7 to 2270 by columns) and  $\Lambda$  (ranging from  $10^{-4}$  to  $10^{-8}$  by rows), as determined from graphs like Figure 2-14. Based on these values, and assuming  $\tau_\lambda(\infty) = 15$  s (based on  $\lambda_\infty = 6 \times 10^{-13}$  s/m, as stated above), we have computed several ratios and dimensional values that are listed in the subsequent blocks of the table:

1.  $\tau'(\infty)/\tau'(z_x')$  shows that the conductivity ratio between  $z_x$  and  $\infty$  varies approximately in proportion to  $W$  but is quite insensitive to  $\Lambda$ , which validates our earlier claim that  $\Lambda$  is somewhat arbitrary. In other words, the maximum plume conductivity (near the nozzle) does not affect the conductivity level, relative to ambient, at which the space charge is “blown away from” the conductivity gradient. In fact, this level appears to be only a few orders of magnitude larger than the ambient level.
2. The next two blocks show two convective time scales (in seconds),  $L/w[s]$  and  $z_x/w[s]$ , respectively, that are based on the conductivity e-folding length and on the “empirical”  $z_x$ , respectively. The latter is the time scale referred to in the dimensional argument given in section 2.6.5.3. Notice that both scales vary primarily with  $W$  and that their ratio,  $z_x'$ , is always greater than unity but is relatively insensitive to variations in the parameters.
3. The next-to-last block of the table shows  $\tau_\lambda(z_x)[s]$ , the electrical relaxation time (in seconds) at the downstream position where the space charge is “blown away from” the conductivity gradient. This has also been referred to in the dimensional argument in section 2.6.5.3, and the values depend primarily on  $W$  but are relatively insensitive to  $\Lambda$ .
4. Finally, the last block of the table compares the two time scales referred to in our dimensional argument (section 2.6.5.3) and given in the previous two blocks.  $(z_x/w)/\tau_\lambda(z_x)$  is the ratio of the convective time scale based on  $z_x$  to the electrical relaxation time at the same downstream distance. Remarkably, this ratio is near unity for all parameter combinations that were computed!

The above results of the 1-D model calculations appear to validate the dimensional argument given in section 2.6.5.3. Therefore, in the absence of a more realistic numerical model, it is reasonable to use that simple argument to estimate the effective conducting length of a rocket exhaust plume. This 1-D

model also suggests that the conductivity level that determines the downstream end of the plume will be only a few orders of magnitude above ambient, the actual deviation depending primarily on the exhaust velocity.

#### **2.6.5.6 Conclusions from Dimensional Analysis and Simple Modeling**

We have seen above that the critical conductivity threshold that determines the electrical effective length of the exhaust plume is much lower than might be expected—probably only a few orders of magnitude above the ambient value. This is certainly much lower than the conductivity to be expected in the incandescent part of the plume (the length of which has been used here to estimate the electrical effective length) and is also much lower than any of the results of the model described in section 2.6.5.1. If this conclusion is validated by more complete modeling and/or experiment, then the actual effective length of RLV exhaust plumes may be much greater than the estimates used herein. This would make the overall electrical length of the vehicles during boost phase longer, which would, in turn, decrease their triggering thresholds and make the triggering of a discharge more likely. Considerable caution is therefore warranted in the use of these results.

#### **2.6.5.7 Recommendations for Future Modeling**

At least three important tasks remain to be accomplished before we can fully understand the role of the exhaust plume in determining the effective electrical length of a launch vehicle. From the point of view of this section, and because it is the easiest of the remaining tasks, we strongly recommend developing a fully two-dimensional, steady-state model of the electric-field distribution in a hypothetical exhaust plume. In other words, one or more realistic, two-dimensional conductivity and velocity distributions should be *assumed*, and then two-dimensional, time-independent versions of Eqs. (2-10) to (2-13) should be solved in the presence of a uniform, ambient, electric field that is oriented parallel to the longitudinal axis of the plume. Such an extension of the 1-D model (described in section 2.4.5.4) to more realistic, 2-D scenarios would facilitate a credible determination of the critical conductivity level. (Later, the possible role in charge transport of particulates in the exhaust stream could be explored, if that is warranted.)

Once the critical conductivity level and its dependence on the vehicle velocity and plume geometry are understood better, the next (and much more difficult) challenge will be to construct a realistic chemical/dynamical model that can *predict* the conductivity distribution in exhaust plumes of various types (solid fuel, hybrid, liquid fuel) and thrust magnitudes. A key aspect of such a chemical/dynamical model would be its capability to credibly predict plume conductivity values at least as low as  $10^{-11}$  s/m so that it could provide useful input to the 2-D electrical model proposed above. Such a model should not have to be classified, since it would be of little or no use in booster signature recognition. If the higher-conductivity portions of the plume, which probably *would* remain classified, turned out to be at all relevant to our problem, then one of the classified models might be used to initialize the proposed, low-conductivity model. Based on the results of sample calculations with the plume model that has been described in section 2.6.5.1, however, it is not clear that the low-conductivity portions of the plume are significantly affected by the free-electron concentration in the high-conductivity portions.

Finally, one or more in-flight and/or static tests should be performed to validate the predictions of both models outlined above. Unfortunately, even static testing (which might be sufficient, given adequate electrical diagnostics) would be a relatively expensive undertaking, as outlined briefly by Krider et al. [2006, end of section 3.1.5.3]; nevertheless, it would be foolhardy to base launch constraints on triggering conditions that have been estimated from untested models.

## 2.6.6 Triggering Conditions

The following material has been covered by Krider et al. [2006], but for convenience, it is repeated here in summarized form. The threshold electric-field required for triggering has been estimated for each of the concept RLVs at two altitudes, 0 and 10 km, both during boost phase (with the exhaust plume) and during landing (without the plume). Table 2-5 compares these thresholds and compares them with similar estimates for the Titan IV. Triggering conditions during the glide phase have not been given for the Concept 4 vehicle because this vehicle is designed to land vertically, decelerating first with a parachute and then with its rocket motor. Thus, the exhaust plume may play a role during landing as well as during launch.

Although the field thresholds in Table 2-5 are quite uncertain in absolute terms, they should be reasonably comparable between vehicles at the same altitude. Thus, they do provide a quantitative basis for the following three conclusions:

1. For vehicles that are designed for unpowered horizontal landings (Concept vehicles 1, 2, and 3), there is a significant increase in triggering threshold (or, qualitatively, a reduction in the likelihood of lightning strikes) during the glide phase of the flight.
2. During the glide phase, these concept RLVs have higher triggering thresholds than those of medium-sized aircraft (which have been measured to be on the order of 45 kV/m at 4–5 km altitudes).
3. Not surprisingly, each concept RLV has much higher triggering fields than the Titan IV. This is typical for large, orbital boosters that the current LFCC have been designed to address.

Although Concept 1, the largest vehicle, has an appreciably lower triggering threshold as compared to the other concepts, during boost phase they are all comparable to the triggered-lightning threshold of medium-sized aircraft. This conclusion is highly uncertain because conventional aircraft do not have electrically significant exhaust plumes and, consequently, are not strictly comparable to space vehicles during the boost phase:

Table 2-5. Estimated Triggering Fields

Vehicle	Boost Phase		Glide Phase	
	Surface, kV/m	10 km, kV/m	Surface, kV/m	10 km, kV/m
Concept 1	60	20	125	42
Concept 2	93	31	182	61
Concept 3	83	28	169	56
Concept 4	79	26	—	—
Titan IV	16	5	—	—

Two words of caution are warranted here in light of the discussion in sections 2.6.3 and 2.6.5 above. The triggering thresholds presented in Table 2-5 and used in the remainder of this report might be underestimated (biased in the conservative direction) by the continued use of Paschen's law, in the face of the new Russian prediction that they may actually be independent of pressure. On the other hand, in our opinion these triggering thresholds are likely to be overestimated (biased in the risky direction) by the continued use of plume electrical effective lengths from Krider et al. [2006, sections 3.1.5.3 and 3.1.5.4], in view of the above finding that the critical conductivity is probably much lower than would be found at the extremity of the incandescent extent of the plume. Until further theory and/or experimentation has been done to validate (or invalidate) the assumptions that went into

Table 2-5, considerable caution is therefore recommended before applying our conclusions quantitatively in any safety-critical situation.

## 2.7 Lightning Climatology

In Krider et al. [2006] a climatological study was performed for two commercial launch sites in Oklahoma (the Oklahoma Spaceport) and New Mexico (Spaceport America). Frequency of natural lightning, percentage of cloud cover, and cloud top temperatures were analyzed to determine the risk of natural or triggered lightning to anticipated suborbital launch activity at these sites. Diurnal and seasonal variability of natural cloud-to-ground lightning at the spaceports was compared to existing federal launch ranges at Cape Canaveral Air Force Station (CCAFS) in Florida, and Vandenberg Air Force Base (VAFB) in California in order to assess relative lightning risk. This study extends the climatology to include the Mojave Air and Space Port (MJSP) and the West Texas Launch Site (WTLS). The frequency of natural lightning and the occurrence of lightning versus cloud type and cloud top temperature versus cloud type were analyzed to help assess the risk of natural or triggered lightning at these sites.

Data from a nearly 15-year lightning climatology study [Schaub, 1996] of all cloud-to-ground lightning strikes detected by the National Lightning Detection Network (NLDN) within a 100 km radius from the latitude and longitude coordinates in Table 2-6 were collected. The climatology study includes periods before and after the NLDN system upgrade in 1995. Only periods after the upgrade were selected for further analysis. LMA data is discussed in section 2.7.4.

Cloud data from the Cloud Depiction and Forecast System Version 2 (CDFS2) [Zamiska and Giese, 1996] was used to investigate the relationship between the occurrence of convective clouds and lightning and the applicability of cloud-based LFCC. CDFS2 is a global cloud analysis product that uses sensor data from the Defense Meteorological Satellite Program (DMSP). It identifies clouds by types, percent coverage, and top and base heights for up to four layers.

Some LFCCs involve temperature criteria. Thus temperatures from the European Center for Medium Range Weather Forecasting (ECMWF) global analysis model grid were associated with each cloud type.

The following analysis uses data from the NLDN, CDFS2, and ECMWF databases. While the data can give the locations and times that clouds and lightning were observed, it cannot establish that a particular cloud generated lightning. This is because the CDFS2 data gives summary data (coverage) for an element of area (tile) and does not resolve individual clouds. The temperatures were obtained from a global analysis model and cannot be expected to exactly represent the actual temperatures within a cloud.

Table 2-6. Site Coordinates and Cloud-to-Ground Lightning Occurrence within 100 km

	<b>SA</b>	<b>OS</b>	<b>MJSP</b>	<b>WTLS</b>	<b>CCAFS</b>	<b>VAFB</b>
<b>Lat</b>	35.3 N	32.8 N	35.1 N	31.4 N	28.4 N	34.7N
<b>Lon</b>	99.2 W	107 W	118.2 W	104.8 W	80.6 W	120.5W
<b>1993–2007 Total</b>	2257424	2180357	85568	2458170	2979456	13682

Figure 2-15 is a map of the average annual area-density of cloud-to-ground lightning flashes over the continental U.S. based on U.S. National Lightning Detection Network (NLDN) data for the years 1997 to 2007. Units are flashes per square kilometer per year. The locations of the spaceports are

indicated with stars. All spaceports except MJSP are located in or near regions of significant lightning activity. The statistics are averaged over all seasons, and seasonal variation induced by flow regimes (such as the Southwest Monsoon) interacting with local topography can give a geographical distribution of activity during the summer months with large values of flash density shifted toward the sites in New Mexico and west Texas. Both of these regions come under the influence of the Southwest Monsoon during summer months and are located near significant topographical features. The Oklahoma site has neither influence. The site in southern California is near significant topography and comes under the influence of a regional summer monsoon; as a result summertime lightning activity in its vicinity is not negligible, though much less than for the New Mexico and west Texas sites. This is seen in the succeeding figures.

Figures 2-16 through 2-20 show the frequency of lightning occurrence for the day of year based on hourly NLDN data for the sites listed in Table 2-6 (except for VAFB, where lightning occurrence is minimal). The values plotted are the percentage of hours with lightning over the 15-year length of the data set.

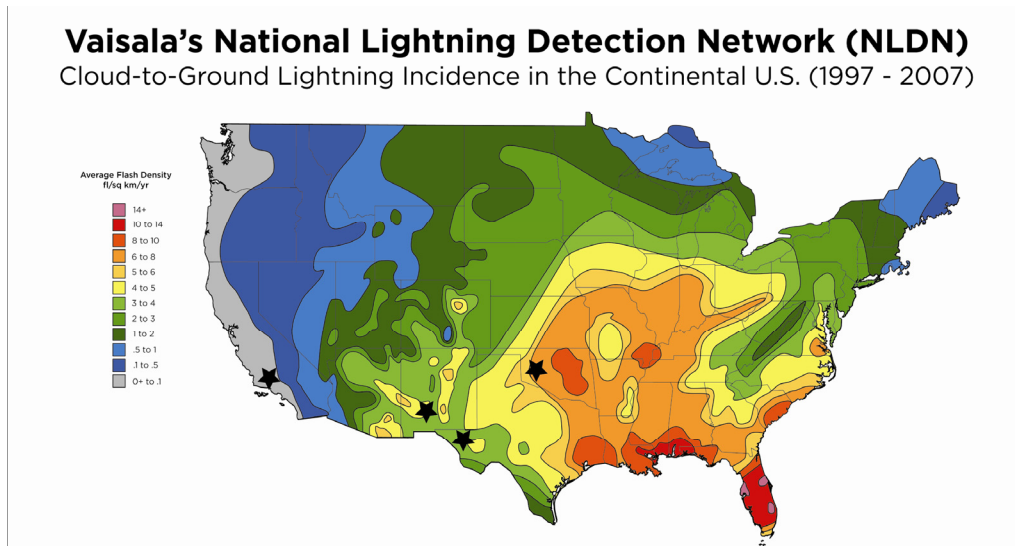


Figure 2-15. Average annual area-density of cloud-to-ground lightning flashes based on NLDN data for the years 1997 to 2007. Units are flashes per square kilometer per year. Stars indicate spaceport locations [With permission from Vaisala].



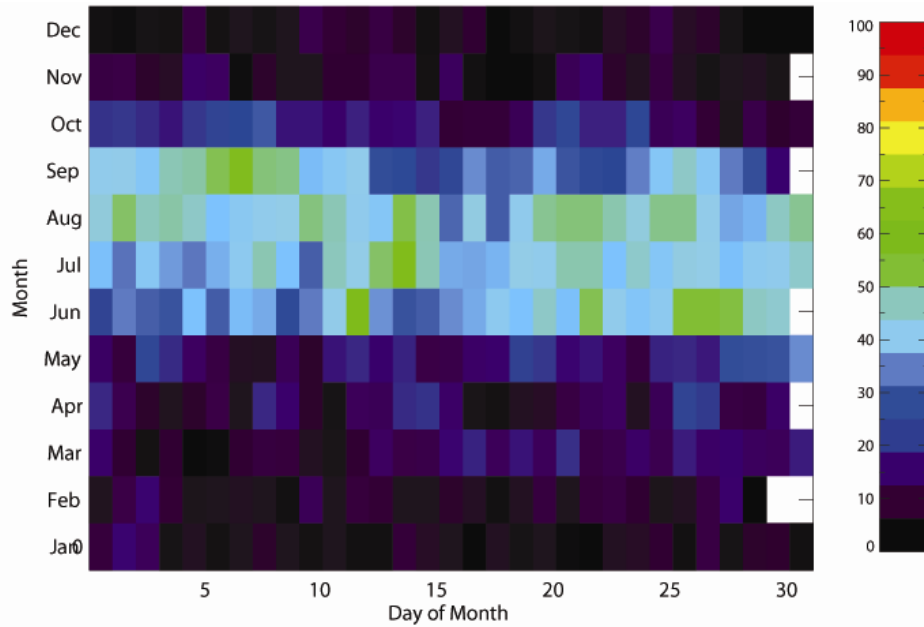


Figure 2-16. The number of hours of lightning versus month and day-of-month for CCAFS. The values plotted are the percentage of hours with lightning over the 15-year length of the data set. The white areas on the right indicate where data does not exist because the length of the month in question is less than 31 days.

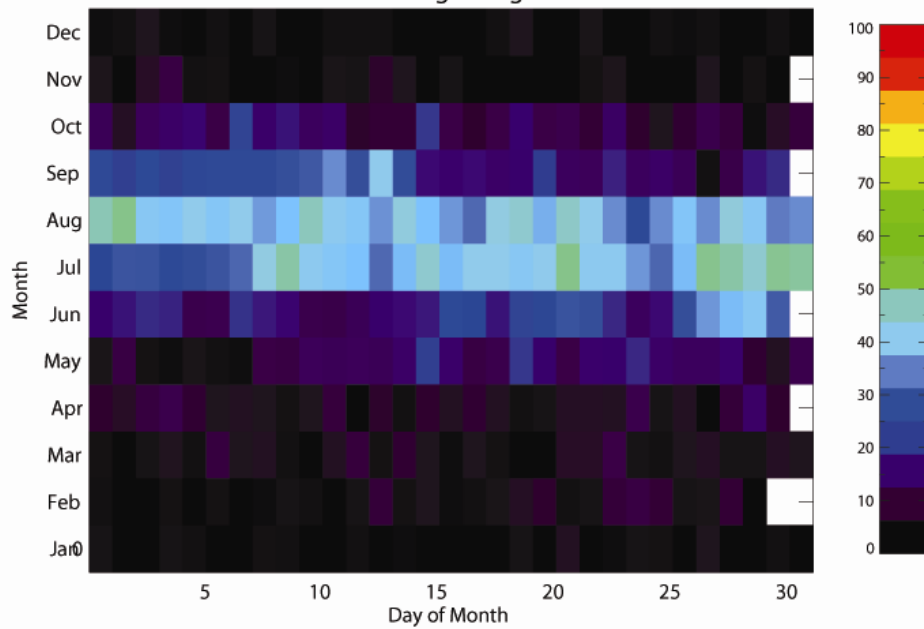


Figure 2-17. Same as Figure 2-15 except for SA.

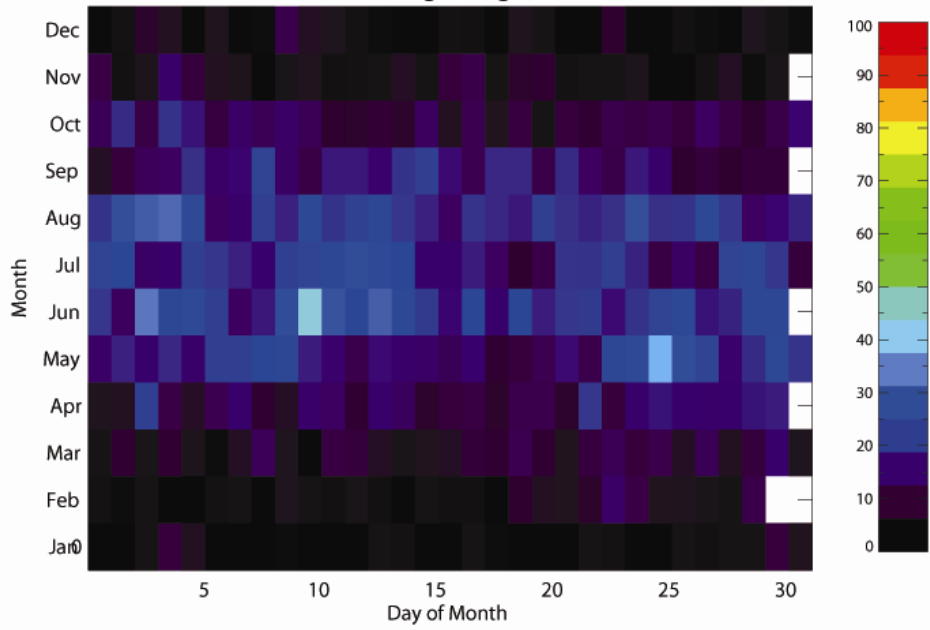


Figure 2-18. Same as Figure 2-15 except for OS.

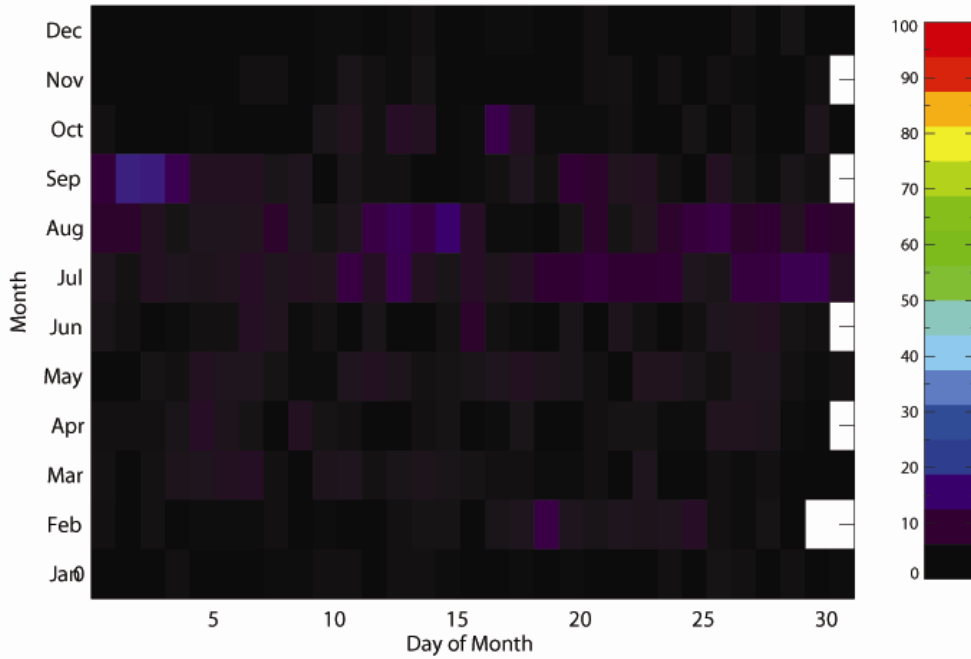


Figure 2-19. Same as Figure 2-15 except for MJSP.

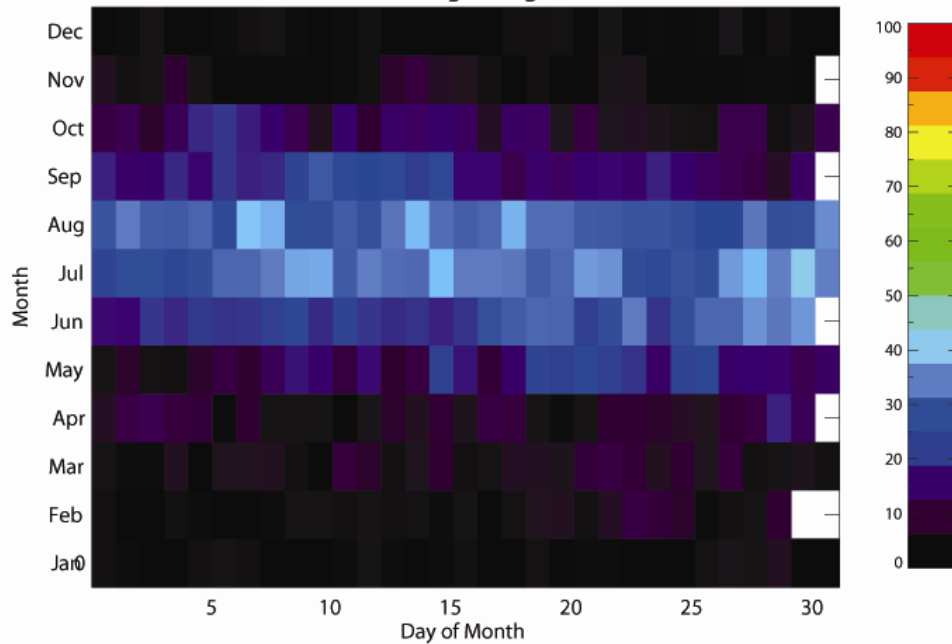


Figure 2-20. Same as Figure 2-15 except for WTLS.

The CCAFS and VAFB sites represent the extremes for natural lightning activity, with CCAFS being the most active and VAFB (not shown) the least active. The natural lightning threat at CCAFS is known to be large, while that at VAFB is virtually nonexistent. Locations that are similar to CCAFS have a large natural lightning risk during the lightning-prone months, while those that are VAFB-like have little or no natural lightning risk. The spaceport that is most like CCAFS is Spaceport America. During the months of peak activity (June through September) occurrence frequencies are less, but not greatly so. Activity for WTLS and OS is somewhat less than that for SA, but still appear to be significant. The main difference between WTLS and OS is the somewhat longer season at OS (commencing in April rather than May). Activity at MJSP is similar to that at VAFB. The differences between sites are further quantified below.

### 2.7.1 Likelihood of Lightning-free Days

The climatology of naturally occurring cloud-to-ground lightning at all six sites was examined for seasonal and diurnal variability (Tables 2-7 and 2-8). Vandenberg is shown likely to be lightning free year-round.

The natural lightning seasons at the four spaceport sites are on par with or shorter than that for Cape Canaveral, the most lightning-prone existing launch site. Even though SA had a shorter lightning season than OS, it experienced twice the number of lightning strikes and for more hours per day (in season) as OS did.

Table 2-7. Approximate Number of Days with Greater Than Indicated Chance of Lightning within 100 km

Site	Approx. DOY Range >20%	Approx. Date Range >20%	Approx. DOY Range >40%	Approx Date Range >40%
VAFB	No significant activity	No significant activity	No significant activity	No significant activity
CCAFS	150-275	Late May/Early Jun – Late Sep/Early Oct	175-250	Late Jun – Early Sep
OS	150-240	Late May/Early Jun – Late Sep/Early Oct	No significant activity	No significant activity
SA	160-260	Mid Jun to Mid Sep	190-240	Mid July – late Aug
MJSP	No significant activity	No significant activity	No significant activity	No significant activity
WTLS	150-260	Late May/Early Jun – Mid Sep	No significant activity	No significant activity

Table 2-8. Times of Minimum and Maximum Probability of Naturally Occurring Lightning in July within 100 km

Site	Min (Universal Time)	Min (Local Time)	Occurrence Frequency	Max (Universal Time)	Max (Local Time)	Occurrence Frequency
CCAFS	1200	0500	15	1900	1400	90
SA	1300–1700	0600–1000	0	2400	1700	75
OS	15–18	9–12	0	2200	1600	15
MJSP	1800	1000	0	2400	1600	30
WTLS	1000–1200	0400–600	0	2200	1600	50

NOTE: VAFB is omitted because it is nearly lightning free in July.

### 2.7.2 Temperatures within Clouds

Some of the cloud-based LFCC are based on cloud microphysical properties. Cloud electrification peaks where water and ice are both present, around  $-10^{\circ}\text{C}$ . Existing cloud-based LFCC also specify that the flight path must not come within 0, 5, or 10 nautical miles of cumulus clouds with cloud tops higher than the  $-5^{\circ}\text{C}$ ,  $-10^{\circ}\text{C}$ , and  $-20^{\circ}\text{C}$  isotherms, respectively. Since the CDFS2 dataset does not give cloud temperature information, incorporation of a third database was required. The ECMWF global analysis model grid was used to provide cloud top temperatures

The data at the tiles containing MJSP and WTLS were vertically interpolated to obtain the isotherm geopotential heights for  $5^{\circ}\text{C}$ ,  $-5^{\circ}\text{C}$ ,  $-10^{\circ}\text{C}$ , and  $-20^{\circ}\text{C}$  (red, green, aqua, blue lines) (Figures 2-21 and 2-22).

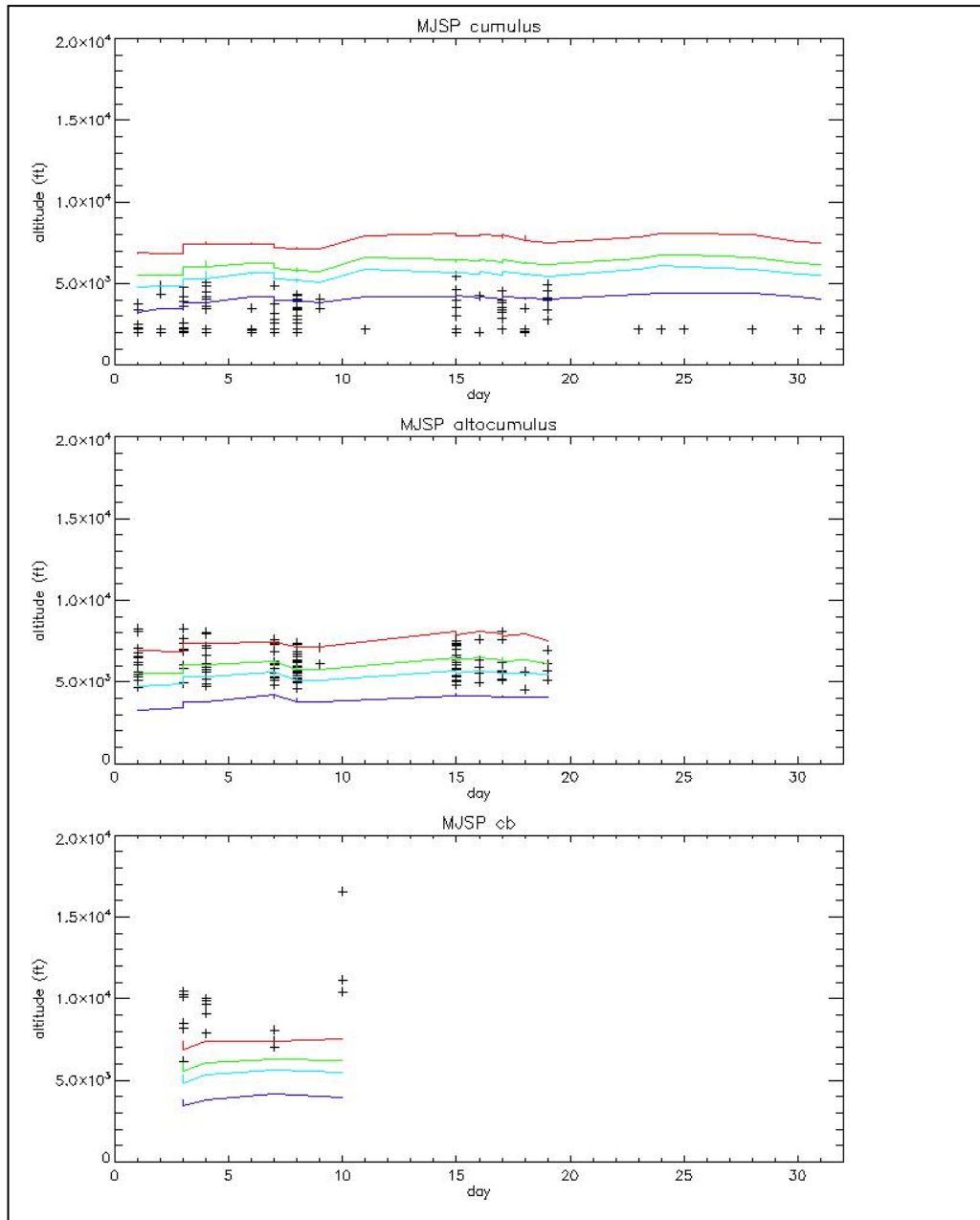


Figure 2-21. Cloud top heights for selected cloud types are shown in black (+). Isotherm heights for 5, -5, -10, and -20°C are shown in red, green, aqua, and blue, respectively, MJSP. Data is for July 2004. The symbol “cb” in the title of the bottom panel refers to cumulonimbus.

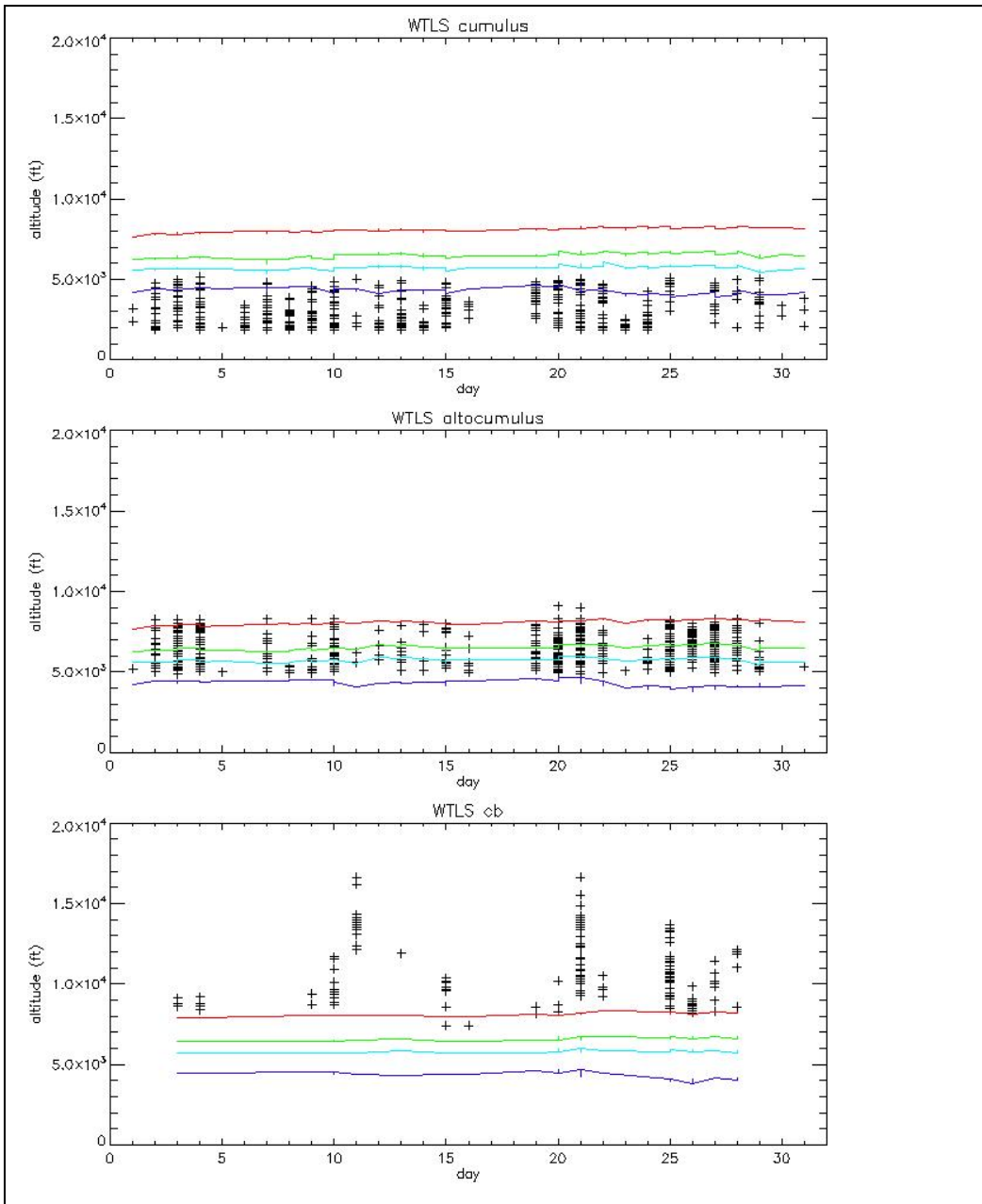


Figure 2-22. Cloud top heights for selected cloud types are shown in black (+). Isotherm heights for 5, -5, -10, and -20°C are shown in red, green, aqua, and blue, respectively, for WTLS. Data is for July 2004. The symbol “cb” in the title of the bottom panel refers to cumulonimbus.

### 2.7.3 Natural-Lightning Statistics from Analysis of LMA Data

The purpose of developing statistics on natural lightning over the spaceports is to estimate the occurrence frequency of conditions in which an RLV might be struck during flight. It must be remembered, however, that most lightning strikes to flying vehicles are “triggered” by the passage of the vehicle through a high-ambient-field region, not simply by intercepted natural lightning. Although strikes are clearly a danger wherever natural lightning is occurring, triggering is also known to occur in clouds that are not producing natural lightning. Therefore the present statistics can place only a lower bound on the risk of lightning strikes.

Two datasets are available with which to estimate natural-lightning statistics at geographic locations of interest. The NLDN locates the ground strike points of most cloud-to-ground (CG) discharges within the continental United States. The NLDN does not report intra-cloud (IC) discharges. Data from the NLDN has been obtained for all four of the spaceports in this study and is analyzed elsewhere. A small but growing number of LMAs have also been installed at locations of high interest around the country. The LMA gives three-dimensional maps of virtually all lightning (both CG and IC) within close proximity to its array. It is LMA data that is the subject of this section.

### **2.7.3.1 The Lightning Mapping Array**

The LMA system was developed at the New Mexico Institute of Mining and Technology (NMIMT) in the mid-to-late 1990s and has been described by Rison et al. [1999] and Krehbiel et al. [2000]. The LMA is a very-high-frequency (VHF) time-of-arrival (TOA) system, based on earlier work by Maier et al. [1995] and Lennon and Poehler [1982] at the Kennedy Space Center and by Proctor [1971] in South Africa. Briefly, much of the broadband VHF radio “noise” radiated by lightning is composed of irregular sequences of numerous, very short pulses. The relative timing of any such pulse, received at six or more LMA stations, is used to redundantly locate the “source” of this pulse in three-dimensional space. The calculation of a source location is done with a least-squares approach in which a reduced chi-squared value indicates the degree to which the TOA measurements from all reporting sensors are mutually consistent. Much of the spatial-temporal development of a lightning discharge can thus be built up from sequences of individual sources so located. The major innovation in the LMA is the use of GPS timing at each station, which permits remote stations to be connected to a base station by relatively low-bandwidth communication links.

An important advantage of the LMA for our purposes is its capability of mapping the above-ground structure of both IC and CG discharges. Thus it may be considered a “total-lightning” sensor. Although the LMA is inherently a short-range system, we are fortunate that LMA networks have been operating more or less continuously out of the University of Oklahoma at Norman (UOK) since 2004, covering the Oklahoma Spaceport, and out of the U.S. Army’s White Sands Missile Range (WSMR) since 2005, covering the New Mexico spaceport. So-called “processed, decimated” (or “real-time”) data from these two networks has been kindly made available to us on DVDs by Prof. Bill Rison of NMIMT, with permission from the system owners, Prof. Don MacGorman of UOK, and Terry Huck of the WSMR. This data contains source locations that were processed and displayed in real time at the base stations. Thus, they include only a fraction of the 12,500 sources that the LMA is theoretically capable of locating. (To achieve higher source-location rates, the raw data from all of the stations may be recorded locally and then processed later off-site.) This decimated data is used here to estimate the climatology of natural lightning at these two spaceports.

NMIMT has developed excellent software, called Extensible Markup Language for Analysis (“XLMA”), for the display and analysis of processed LMA data. This software plots the location and time of every computed LMA source point in plan view, in two vertical cross sections, and in time series. For example, Figure 2-23 shows a large meso-scale convective complex (MCC) over Norman, OK. XLMA also contains its own “flash algorithm” and several other useful analysis features.

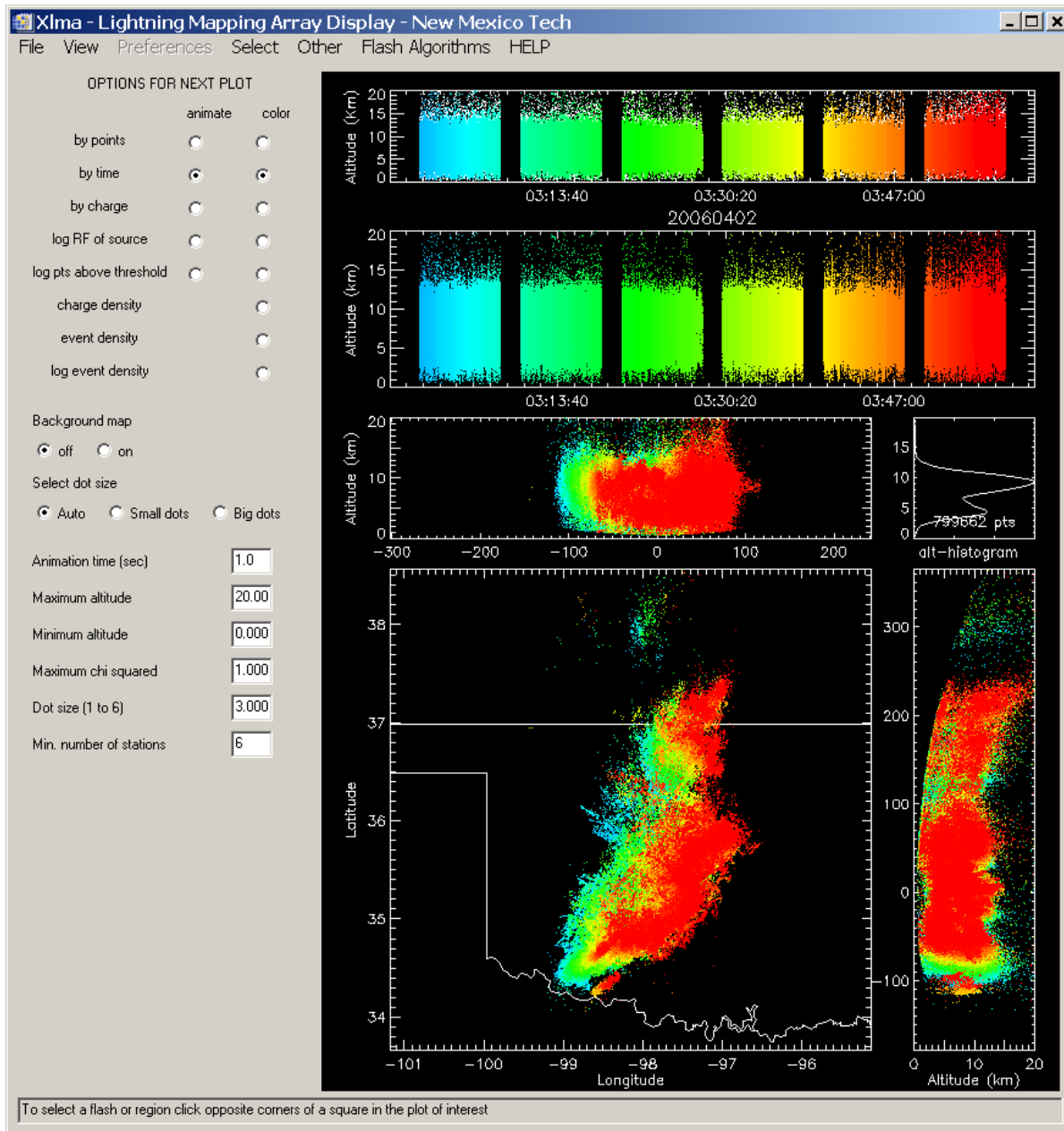


Figure 2-23. XLMA display of a large MCC passing over Norman, OK, showing all source points (reduced chi-squared  $\leq 1.0$ ) within range of the Oklahoma LMA during the hour after 0300 UT on April 2, 2006 (20060402). The upper two strips are time series of source altitude. (The distinction between them will become evident in subsequent figures.) The lower left panel is a plan view, in this case showing all detected lightning. To its right is a latitude-altitude projection (*both* scales in km in this case) and above it is a longitude-altitude projection (*both* scales in km in this case). (In these projections latitude and longitude refer to distances in the N-S and E-W directions, respectively. These distances may be demarcated either in degrees of latitude/longitude or in km. Which convention is used will be obvious.) An altitude histogram is also included (vertical scale always in km), showing the total number of sources plotted. Each source point is color-coded according to time within the hour in each panel. For unknown reasons this particular hour of data has two-minute gaps every ten minutes.



### 2.7.3.2 Details of Analysis Procedure

Even for identical networks, there would be at least two significant problems in obtaining comparable LMA statistics for the Oklahoma and New Mexico sites. First and foremost, detection efficiency is a strong function of range, with the Oklahoma Spaceport being twice as far (about 130 km—see Figure A-3 in Appendix A) from the center of the University of Oklahoma (UOK) network at Norman as the New Mexico Spaceport is from the center of the White Sands network (about 65 km—see Figure A-9 in Appendix A). To a lesser extent, detection efficiency is also a function of lightning rate, which will vary from day to day, as well as between the two networks, because of the considerable “dead time” of the real-time data processing during which each individual source is detected and located.

The “dead-time” situation can be more clearly explained with reference to some details of the signal recording and processing. Individual LMA stations currently record the strongest VHF plus (above threshold) during each successive 80  $\mu$ s time window for offline processing. Due to restrictions in channel bandwidth and processing power for the real-time data, however, only the strongest pulse within five consecutive 80  $\mu$ s windows is sent back to the base station for processing. Thus, the realtime system can locate at most 2,500 sources per second (as opposed to a maximum of 12,500 pulses with post processing of the full-bandwidth data). Lightning in the region of interest may therefore be eclipsed by a very active storm elsewhere within the domain of the network.

A second problem in obtaining comparable statistics is that natural and man-made noise, on the one hand, and incorrectly located sources from lightning outside the region of interest (also considered “noise”), on the other, can be mistaken for lightning overhead. Both the noise level and the prevalence of nearby storms can be expected to differ from network to network. For both of these reasons, simply counting LMA sources per hour, per unit area, will produce serious biases.

The conventional alternative to source counting is “flash” counting, which is based on the physical concept of a lightning flash [e.g., Rakov and Uman, 2003, section 1.2]. Individual flashes can usually be distinguished from one another by a combination of time and position, at least during relatively low lightning rates. However, for the Oklahoma Spaceport, which is located on the fringes of the UOK LMA network’s 2-D coverage, conventional “flash algorithms” (see Murphy [2006] for a good overview) are not expected to work well. For this reason we defined and counted “lightning events” as follows:

It was decided to count these “lightning events” (defined below) within 80×80 km squares centered on the coordinates of each spaceport (see Table 2-9). Squares oriented E-W/N-S are convenient, since they are easy to define approximately in terms of latitude/longitude, which is how the LMA source locations are reported. It was also decided to focus on 1-hour time intervals, which could easily be combined later into hour-of-day and month-of-year averages. Initially, lists were generated of individual hours during which lightning occurred over each spaceport. Lists have been correlated with NLDN data as discussed elsewhere (see section 2.7.34).

Table 2-9. Spaceport Coordinates for Purpose of Centering 80×80 km Squares

Network	N. Latitude	E. Longitude
UOK	35.3	-99.2
WSMR	32.8	-107.0

Following a suggestion by Martin J. Murphy [Vaisala Inc. Tucson, personal communication], the 80×80 km squares mentioned above were each divided symmetrically into four 40×40 km squares. Within each of these smaller squares LMA sources were counted in each 4 s time interval for which

data was available. Each 4 s interval having five or more sources located within one of these smaller squares was defined as a “lightning event.” Such lightning events were then summed over the four squares and over all 4 s intervals in each hour of each day for the duration of the dataset. (The individual event counts in each 40×40 km box were also preserved in the hourly lists mentioned above, although this finer spatial resolution has not been exploited to date.) “Lightning event” average rates were then derived from these hourly counts for each spaceport.

The rationale behind the above choices of box size and time interval is as follows: Individual thunderstorm cells have typical linear dimensions of 10 km or less [e.g., MacGorman and Rust, 1998, section 7.1.1(ii)] (although lightning in “super-cell” storms or in MCCs can be much more horizontally extensive—see below), and individual lightning flashes have typical time durations of 1 s or less [e.g., Rakov and Uman, 2003, Tables 1.1 and 9.1]. The intent in choosing spatial areas and temporal intervals roughly four times larger than these typical dimensions was to avoid splitting too many physical flashes between more than one square or time interval (overcounting), while at the same time avoiding the lumping of too many individual flashes together (undercounting). The required minimum number of sources, five, was chosen primarily to minimize the counting of “noise,” but also in an effort to maximize the counting of actual flashes, which we observed to comprise typically tens to hundreds of sources. Noise was further minimized by imposing a fairly strict limit on the reduced chi-squared for each accepted source. (The reduced chi-squared limits used here were 2.0 in New Mexico but only 1.0 in Oklahoma, where the locations were generally more robust.) Thus we arrived at a statistic (lightning events per hour per km<sup>2</sup>) that was roughly comparable to flash rate, but was much more easily determined from the data and should be relatively insensitive to source-detection efficiency.

Another layer of conservatism can be added by preserving only the binary information of whether or not an individual hour had any lightning events over a given spaceport (anywhere in the corresponding 80×80 km square). This, plus the conservative “noise” thresholds described above, should eliminate virtually all overcounting and detection-efficiency biases while missing very little real lightning. This “hours-with-lightning” statistic was also converted into hour-of-day and month-of-year averages for each spaceport.

To make statistical sense out of the lightning-event and hours-with-lightning averages, one must know how many hours the corresponding LMA system was operational during each hour of each day in each month (see Figures A-11 and A-12 in Appendix A). To make statistical sense out of the list of all hours with lightning events—for example, in correlations with cloud-to-ground flash counts from the NLDN (Appendix A.2)—one also needs to know which individual hours and which entire days are missing from the dataset. This information has been organized into a list of missing hours and a list of missing days for each network. Overall, the New Mexico LMA system was operational for 52 percent of the hours during the nominal three years for which we have data, 2005 to 2007, while the Oklahoma LMA system was operational for 84 percent of the hours during the three years, 2004 to 2006.

Relative to the above-described time intervals of missing data, it should be noted that these lists are not exhaustive. Within any given hour that has a non-empty file (hence, is counted as an hour of operational data), there is generally no way to tell from the data format whether or not the respective LMA system was running properly during that entire hour. During intense storms with nearly continuous lightning (as often occurs in Oklahoma) data gaps do occasionally appear and are obvious in the XLMA plots (see, for example, Figure 2-23). We have made no effort to detect such gaps here, however, primarily because any such detection would be storm dependent and could not be done during most hours.

### 2.7.3.3 “Lightning Event” Validation

For short intervals during several individual storms over each spaceport, the present “lightning events” have been compared to sample plots and to lists of lightning “flashes” made using the XLMA software. An example of the output of this software was given in Figure 2-23. The details of this analysis are given in Appendix A.

The following conclusions were reached:

- No case was found in which a “lightning event” was reported at a spaceport when no identifiable lightning was displayed over the corresponding 40×40 km square by the XLMA software. In other words, the events counted here are real lightning (or at least branches of larger flashes that extended over the spaceport), not noise. (See the separate comparison to NLDN flashes discussed below, however, for some caveats.)
- No case was found in which significant lightning over a spaceport was missed by our “lightning event” algorithm. (We did notice one case where the first “flash” in a storm over SA, which comprised only 5 source points within a very short time interval when using the generous reduced-chi-squared maximum of 5.0—the XLMA default value—was rejected with the tighter threshold that we eventually selected. Later flashes in this storm were detected, however.)
- The “flash” counts given by the XLMA software (using NMIMT default parameters) correspond roughly to the “lightning event” counts in our software, although event counts could be varied appreciably by using different, but apparently reasonable, values of minimum source count (currently five) and reduced-chi-squared threshold. It appears that our 40×40 km boxes and 4 s intervals are appropriate for minimizing simultaneously the overcounting (due to one flash spanning more than one box or time interval) and the undercounting (because more than one flash occurs in the same box and interval).
- As mentioned above, the preferred values for these parameters are a minimum source count of five (per 40×40 km box and 4 s time interval) at both sites and a reduced-chi-squared threshold of either 1.0 for the Oklahoma Spaceport or 2.0 for SA. It was found that we could use the smaller reduced-chi-squared threshold in Oklahoma without losing too many sources (relative to our original choice of 3.0), but the same small threshold in New Mexico resulted in weeding out almost half of the sources over the spaceport. (We do not currently have an explanation for the greater sensitivity to reduced-chi-squared threshold at SA, but we can report that decreasing this threshold from 3.0 to 1.0 makes little or no change in the morphology of lightning flashes there, as displayed in the corresponding XLMA plots.) Doubling the minimum source count to 10 also reduces the “event” counts, but not greatly.
- The structure and detail of the flashes over SA are captured very well in the XLMA displays, whereas those over the Oklahoma Spaceport (which is considerably further from the network) are “muddier.” Nevertheless, there appears to be little doubt that the Oklahoma LMA system is giving a good plan view of lightning over that spaceport, albeit with relatively poor altitude resolution. No sign was detected of the radial “smearing” of flashes over the Oklahoma Spaceport that we had initially feared.

#### **2.7.3.4 Additional “Lightning Event” Validation: Comparison with NLDN Data**

The NLDN analysis reported in section 2.7.3.4 also yielded a list of hours with lightning over the same two 80×80 km squares as used for the LMA analysis herein. In general, there was good agreement between lists from the two lightning-detection systems, although there were some discrepancies. Many individual hours—even entire days—of data were missing from the LMA dataset for reasons unknown. Also, there was no way to determine from the available LMA dataset whether that system was operational during the entirety of any hour for which it yielded a data file (e.g., Figure 2-23). Finally the NLDN data pertains only to CG strikes, whereas the LMA data pertains to both IC and CG strikes. Therefore a comparison between the two data sets can shed some light on the efficiency of NLDN data while assessing the effect of missing (or possibly missing) LMA data. The details of this analysis are given in Appendix A.

Based on the above examples, the following modifications can be made to the tentative conclusions listed in the section above:

- A few cases of LMA aircraft tracks (tracks due to aircraft electrification) were found to produce apparent lightning events in the absence of any real lightning. Such cases appear to be relatively rare and, in any case, seem likely to represent a potential electrostatic hazard that should probably be avoided by flight operations.
- A few cases were found of the “smearing” of mislocated sources into the spaceport area from more distant storms to the west in Oklahoma. Again, bogus “lightning events” due to such smearing appear relatively rare and, given the prevailing meteorology of the region, are likely to be followed shortly by real lightning as the storms move rapidly eastward into the spaceport area.
- There is some indication that the NLDN might be missing some ground strikes in the vicinity of SA. If true, this might be due to terrain shadowing where the terrain shields detectors from signals arriving from certain azimuths, but our data alone cannot confirm or deny this hypothesis.

#### **2.7.3.5 Statistical Analysis and Results**

Approximately three-year data sets were obtained for SA (July through October 2005; 2006 except for January and February; and 2007 only through early October) from the White Sands Missile Range and for the Oklahoma Spaceport (from early February 2004, essentially continuously through 2006) from the University of Oklahoma. Analysis of the “lightning-event” and “hours-with-lightning” statistics have resulted in the following plots and summary statistics.

Several overview graphics are presented in the form of two-dimensional “rainbow” plots, with month of year shown on the vertical axis (January through December represented by 1–12) and Universal-time hour of day on the horizontal axis (1–24). The color of each month/hour cell of these 2-D arrays represents the magnitude of the variable in question on a linear scale, increasing from violet through red (as in a spectrum of white light) across the data range stated in each graph title. The following rainbow plots are provided for each spaceport:

1. Operational hours for the data system, summed over the three years of operation for each hour of each month of the year (“Hours per Hour each Month”)—maximum possible, approximately 90—which shows that the highest data coverage in New Mexico (Figure 2-24) was during the summer months and that there was much more uniform and complete coverage throughout the year in Oklahoma (Figure 2-25).

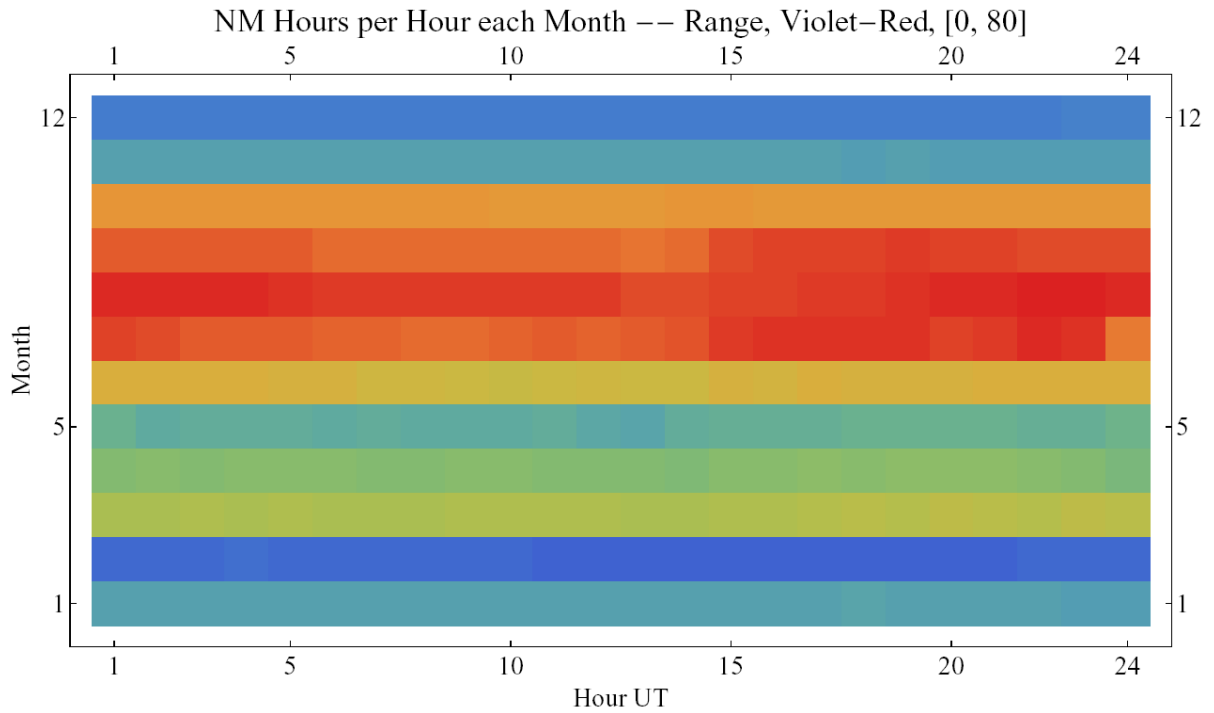


Figure 2-24. "Rainbow plot," as described in the text, of the operating hours of the New Mexico LMA over the years 2005 through 2007.

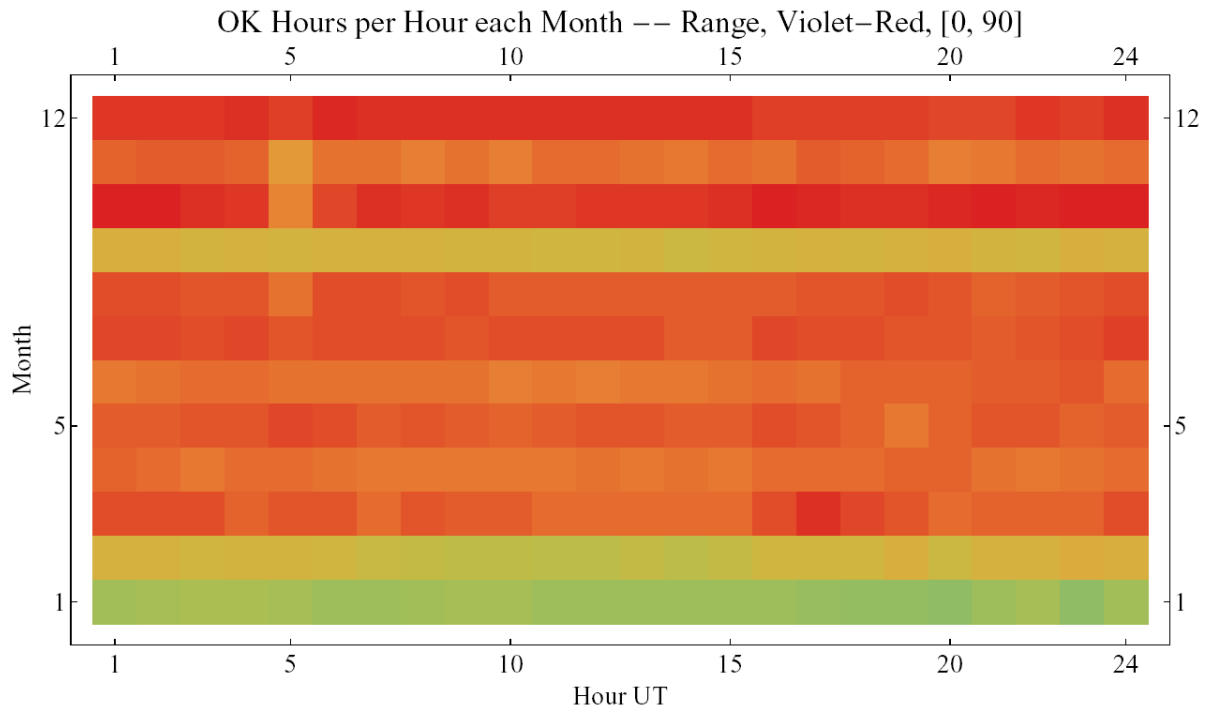


Figure 2-25. Similar to Figure 2-24, but for the Oklahoma LMA over the years 2004 through 2006.

2. Rate of “lightning events” per unit time and horizontal area (“Events/Hour/km<sup>2</sup>”), normalized by the number of system operating hours in the same hour of that month (see above) and by the chosen detection area (6400 km<sup>2</sup>). In Figure 2-26 one sees that the peak lightning activity in New Mexico occurs near 5 PM MST (midnight UT) in the mid-summer. (There is also the suggestion of a weak secondary maximum around 5 AM MST (noon UT) during October.) In Figure 2-27 the peak lightning activity in Oklahoma occurs near 11 PM CST (0500 UT— notably later than in New Mexico) in the early summer. There is also the suggestion of a weak secondary maximum in the early afternoon CST (late in the UT day), this time during March.
3. Rate of hours-with-lightning per unit time (“Hours with Lightning per Day”)—maximum possible, 24—the more conservative statistic that counts only the hours with one or more “lightning events” each hour of each month, again normalized by system operation time. This looks pretty similar to “Events/Hour/km<sup>2</sup>,” both in New Mexico (Figure 2-28) and in Oklahoma (Figure 2-29), although a few differences (notably the suggestion of a bimodal diurnal variation in Oklahoma) might be considered significant.

Regarding item 3 above, we note with skepticism that the overall fraction of operating hours having lightning during the nominal three years of data was 9.4 percent in New Mexico, whereas this fraction was only 4.7 percent in Oklahoma—roughly half as much. The fraction for New Mexico is definitely biased high, however, since the overall fraction of missing-data hours there during these three years was 48 percent, mostly occurring during the winter and spring when lightning rates were low. This may be compared to only 16 percent missing hours in Oklahoma, whose absolute annual lightning rates should therefore be much less biased. Of course this same bias will show up in the overall absolute lightning-event rate for New Mexico—item 2 above. Thus, although the diurnal and seasonal variations indicated in the above figures may be taken as representative (to the extent that a three-year time series can be representative of climate in general), these absolute annual lightning rates may not be.

One can attempt to remedy this defect, and obtain a less biased comparison of annual-average lightning rates between the two sites, by taking the hourly-average lightning rates themselves (the values in the individual month/hour cells in Figures 2-26 through 2-29) and averaging them over all 288 such entries in the year (as opposed to dividing the total number of lightning events or hours-with-lightning by the total number of operating hours, as in the preceding paragraph). This results in the comparisons in Table 2-10.

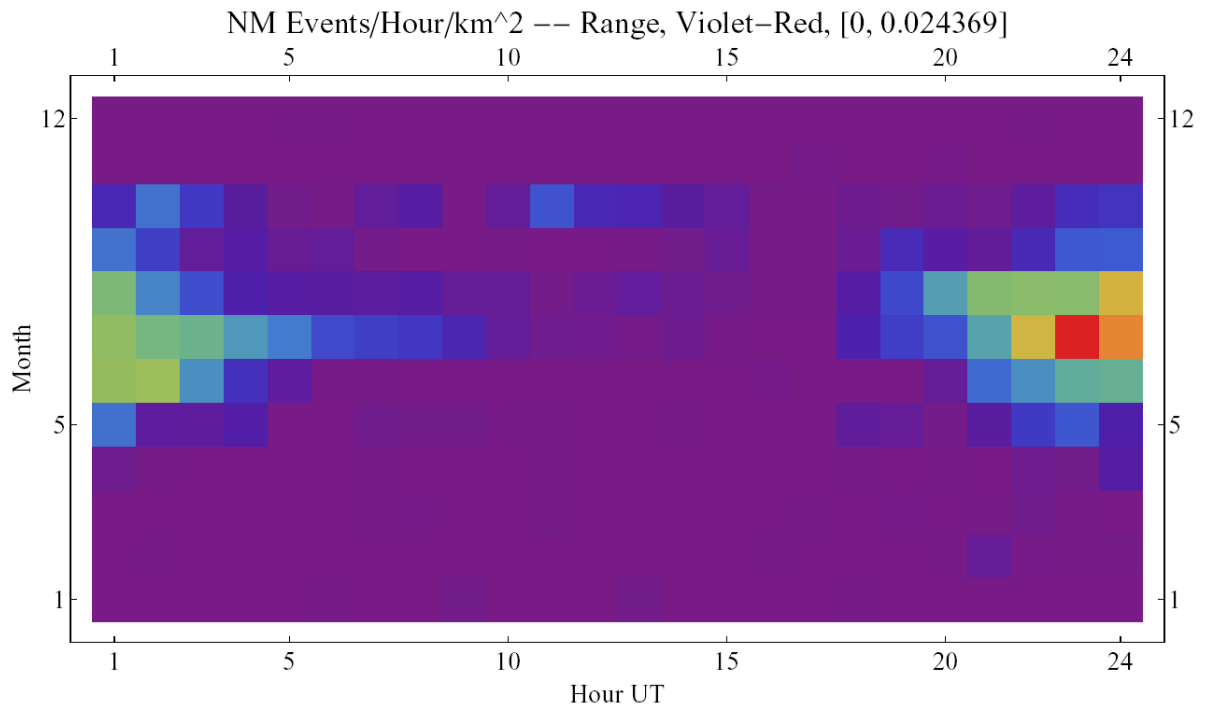


Figure 2-26. "Rainbow plot" of the "lightning-event" rate at the SA over the years 2005 through 2007.

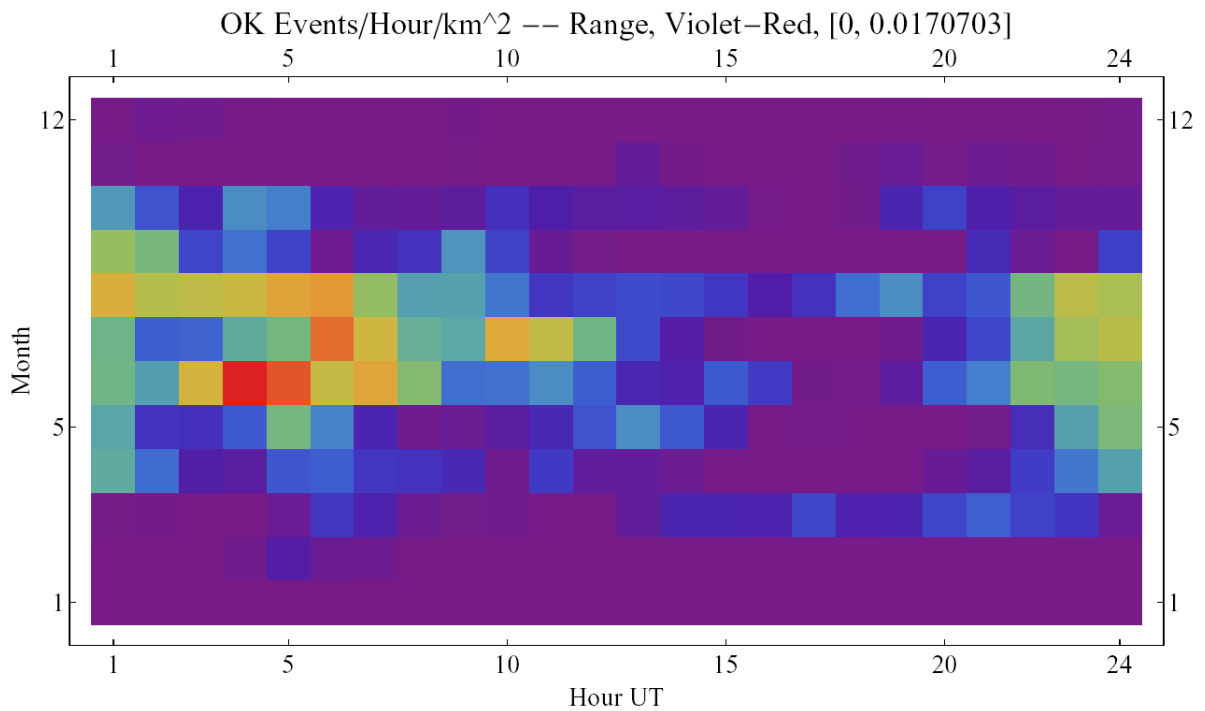


Figure 2-27. Similar to Figure 2-26, but for the Oklahoma LMA over the years 2004 through 2006.

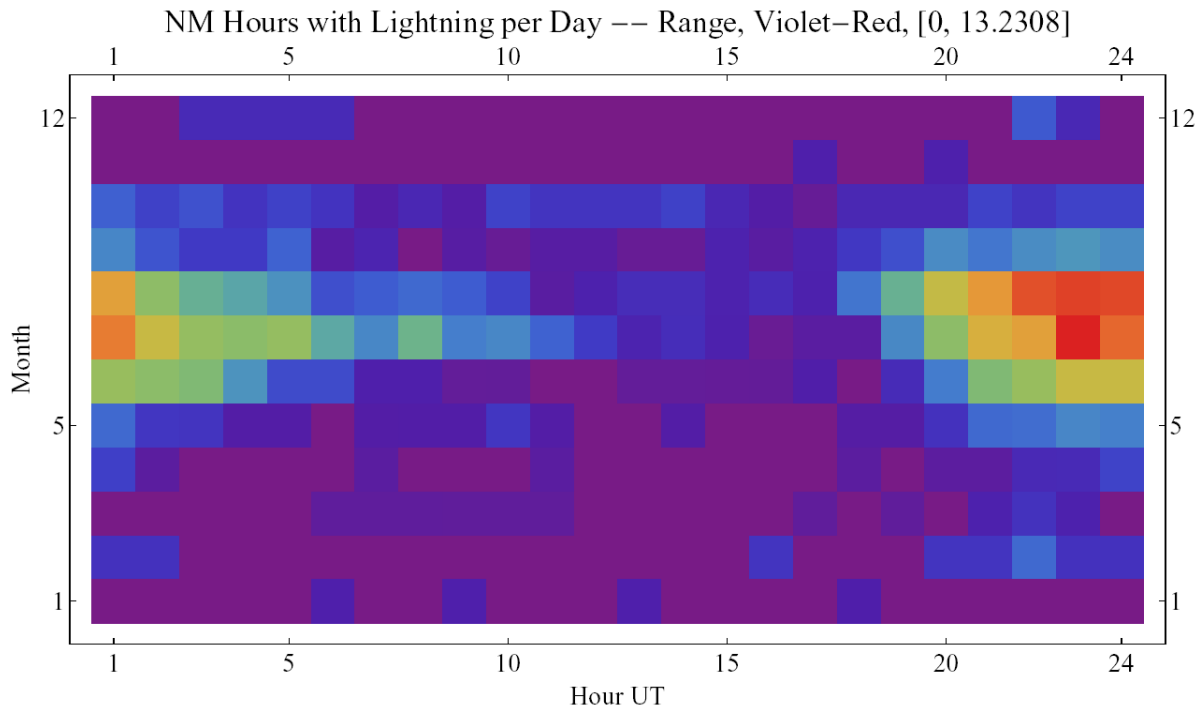


Figure 2-28. "Rainbow plot" of the "hours-with-lightning" rate at SA over the years 2005 through 2007. Compare to Figure 2-26.

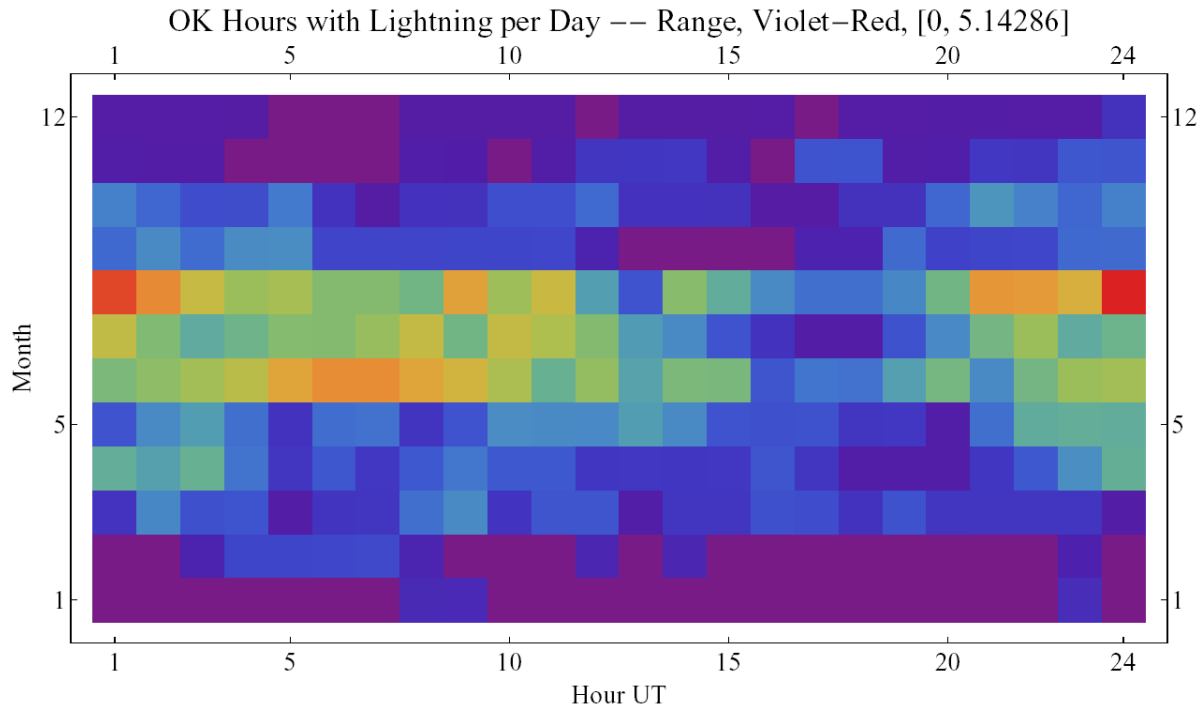


Figure 2-29. Similar to Figure 2-28, but for the Oklahoma LMA over the years 2004 through 2006. Compare to Figure 2-27.



Table 2-10. Effect of Bias Correction on the Annual-Average Rates

Statistic	Correction	
	None	Bias Removed
NM events/hr/km <sup>2</sup>	0.0021	0.0014
OK events/hr/km <sup>2</sup>	0.0024	0.0022
NM % hrs w/ltnng	9.4	6.7
OK % hrs w/ltnng	4.7	4.5

After correction, we find that the annual lightning-event rate is substantially smaller, but that the hours-with-lightning rate is about 50 percent larger in New Mexico than the corresponding rate in Oklahoma. That is, Oklahoma storms tend to have more lightning per unit area and time than New Mexico storms, even though the latter are more frequent when averaged over the year.

The bottom line is that the overall probability of an hour with lightning is almost 7 percent at SA, compared to between 4 and 5 percent at the Oklahoma Spaceport. The peak probabilities are much higher, of course: 55 percent in New Mexico at 1600 MST (2300 UT) in July and 21 percent in Oklahoma at midnight UT in August, as can be seen from Figures 2-28 and 2-29, respectively. The peak event rates are also much higher than the annual averages in the above tables, of course: 0.024 events/hr/km<sup>2</sup> in New Mexico, also at 1600 MST in July, and 0.017 events/hr/km<sup>2</sup> in Oklahoma, this time at 2100 MST (0400 UT) in June, as can be seen from Figures 2-26 and 2-27, respectively.

The absolute magnitudes of the diurnal variations of the two lightning rates, averaged over the year, are also reduced by this same bias-correction approach, again much more so in New Mexico than in Oklahoma. Perhaps surprisingly, however, the *shapes* of these diurnal variations are not significantly affected by the bias. Of course, neither the seasonal variations, averaged over the day, nor the diurnal variations averaged only over a given month or season, are significantly affected. (The hours of operation of the two systems have no significant diurnal variation, nor do they vary much within a given month or season. The main operational variations occur between seasons.)

Regarding the diurnal and seasonal variations of the two lightning rates, Figures 2-30 through 2-39 plot these as one-dimensional graphs vs. hour of day (averaged over the year and bias corrected) and month of year (averaged over the day) at the two sites. Also shown are the diurnal variations for October in New Mexico and for March in Oklahoma, which appear in these limited “climatologies” to have different patterns from those of the summer months (which dominate both annually averaged diurnal variations).

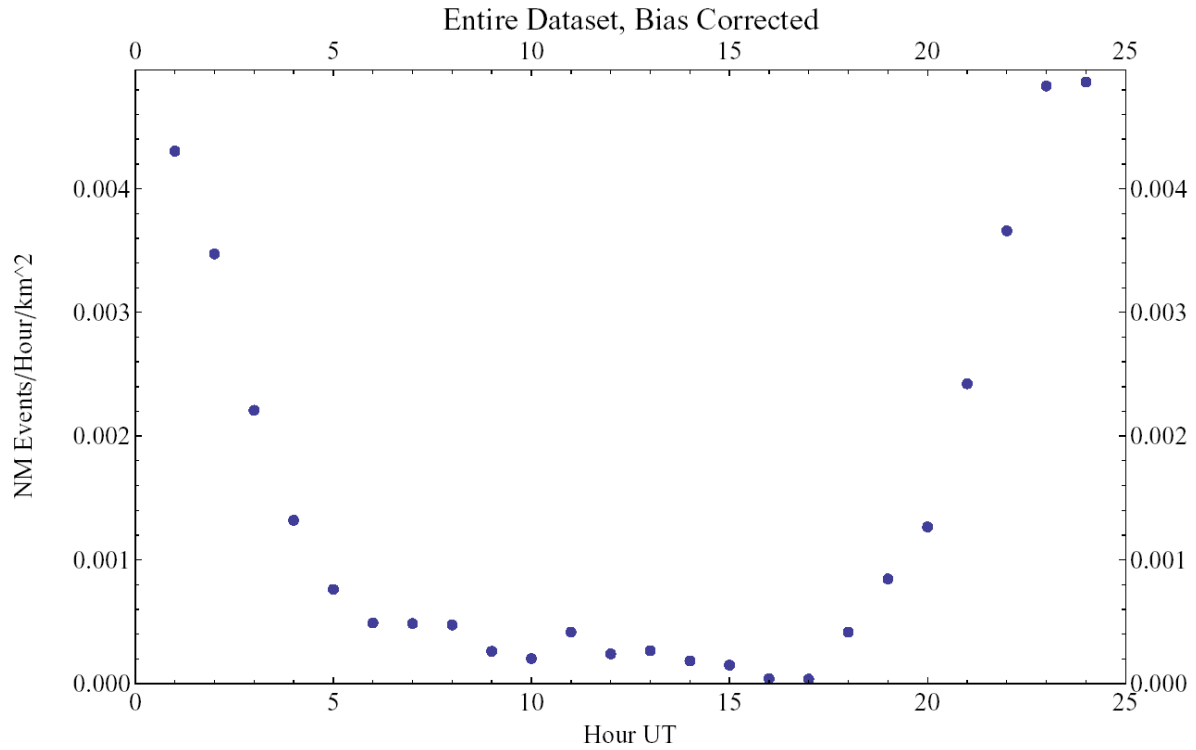


Figure 2-30. Bias-corrected (see text) diurnal variation of the “lightning-event” rate at SA.

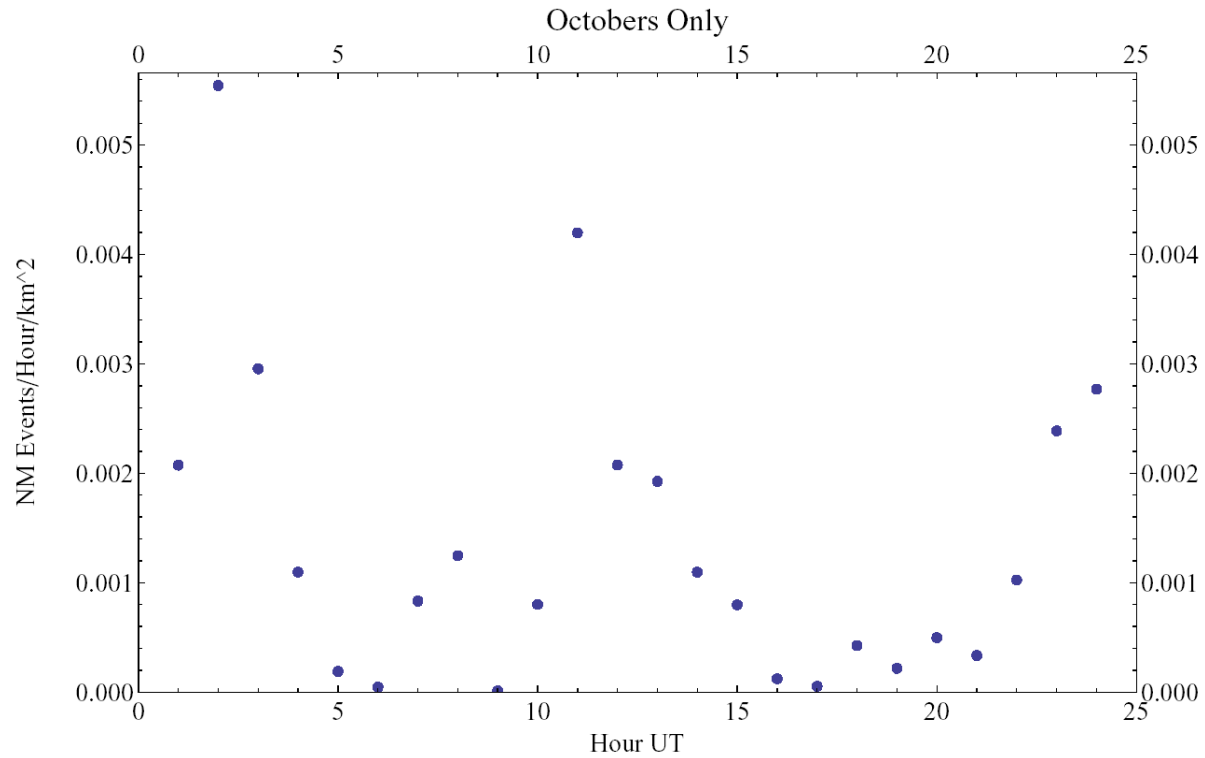


Figure 2-31. Octobers-only diurnal variation of the “lightning-event” rate at SA. Compare to Figure 2-30.

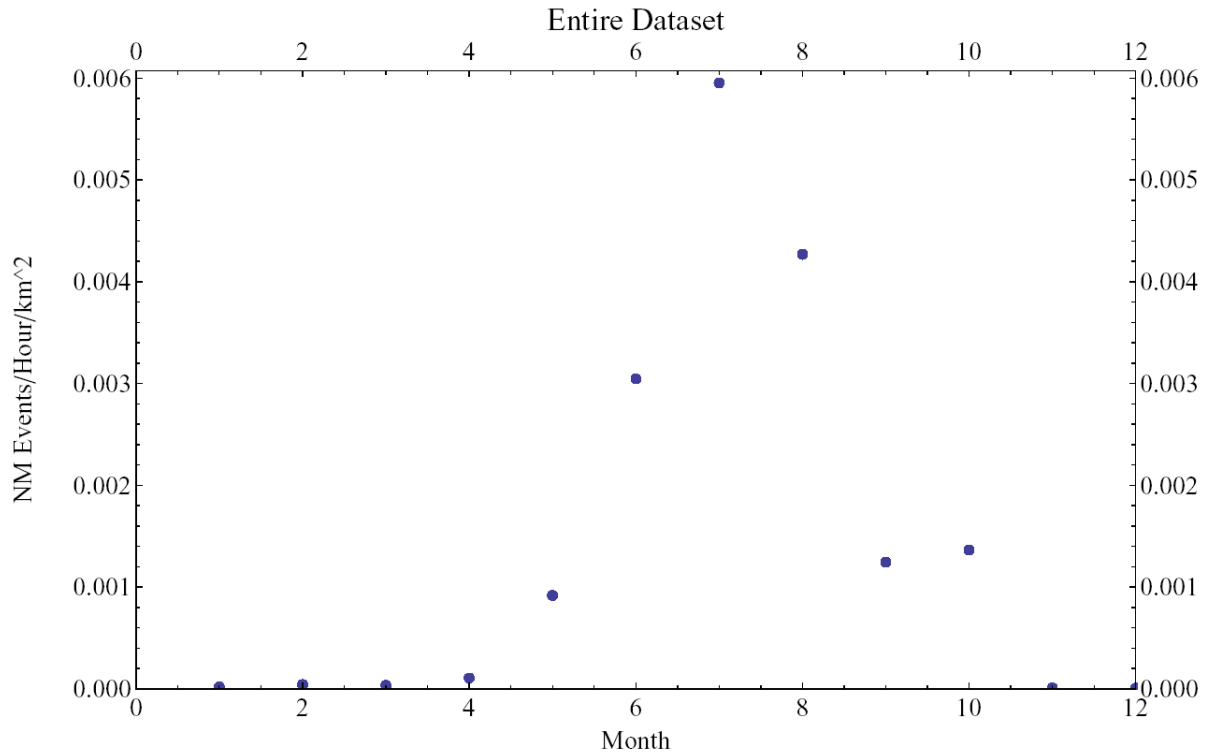


Figure 2-32. Seasonal variation of the “lightning-event” rate at SA.

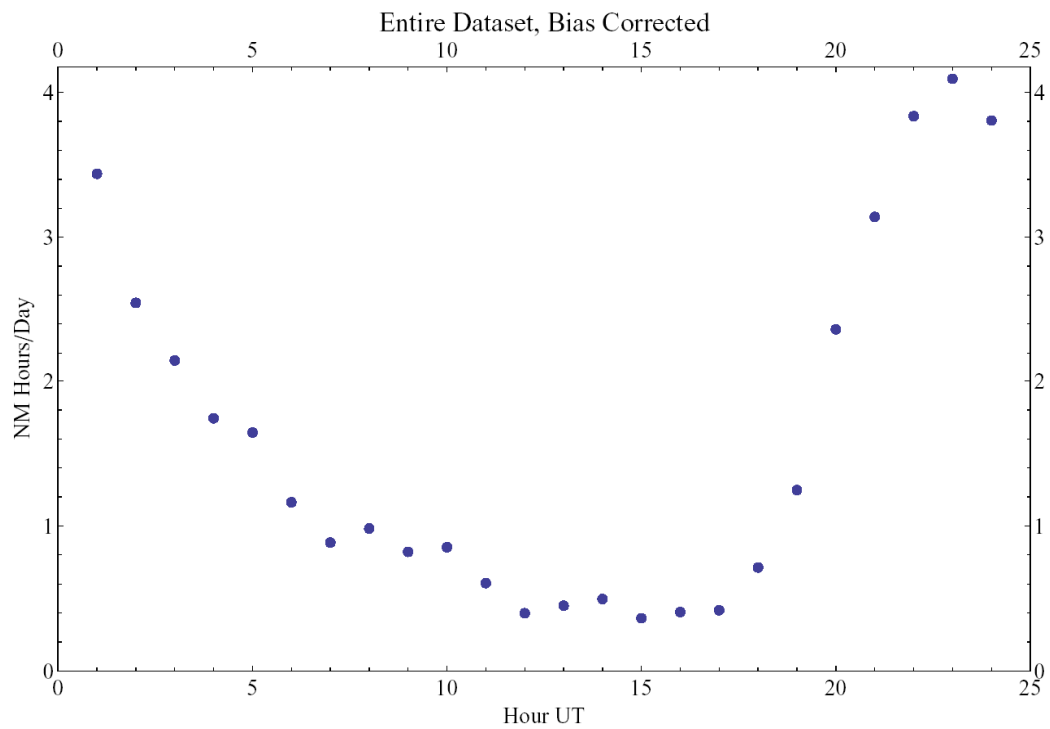


Figure 2-33. Bias-corrected diurnal variation of the “hours-with-lightning” rate at SA. Compare to Figure 2-30.

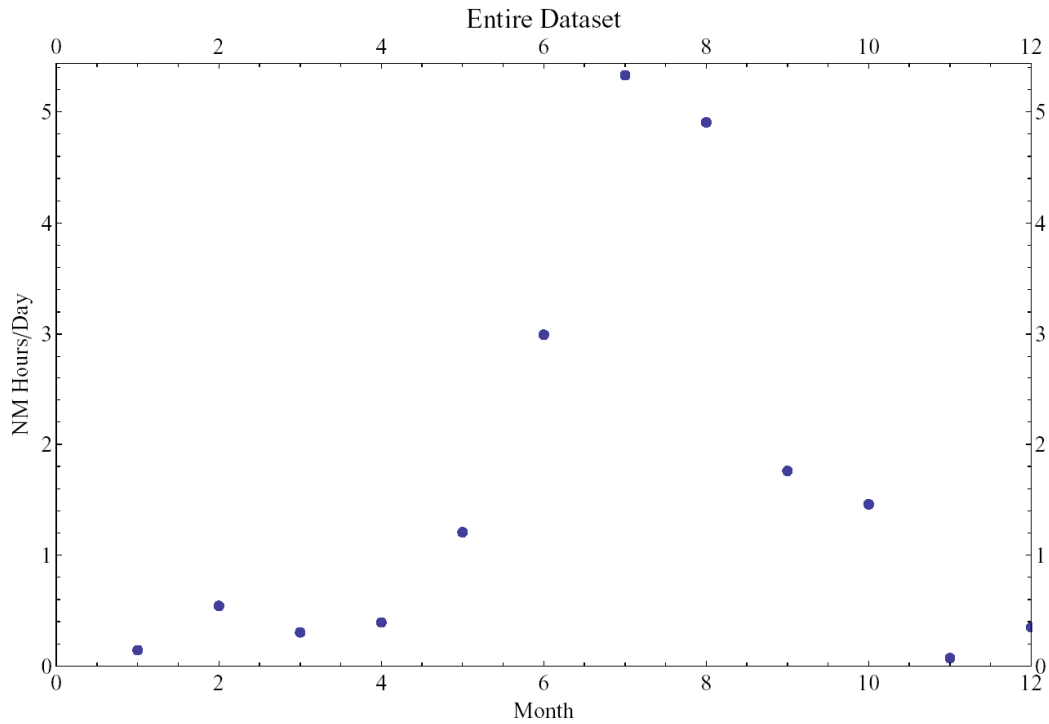


Figure 2-34. Seasonal variation of the “hours-with-lightning” rate at SA. Compare to Figure 2-32.

In New Mexico we see similar diurnal variations in both the lightning-event rate (Figure 2-30) and the hours-with-lightning rate (Figure 2-33), having a single peak just before 5 PM MST (midnight UT), except perhaps in the fall (see Figure 2-31). The seasonal variations (Figures 2-32 and 2-34) are also similar, with a single peak in July.

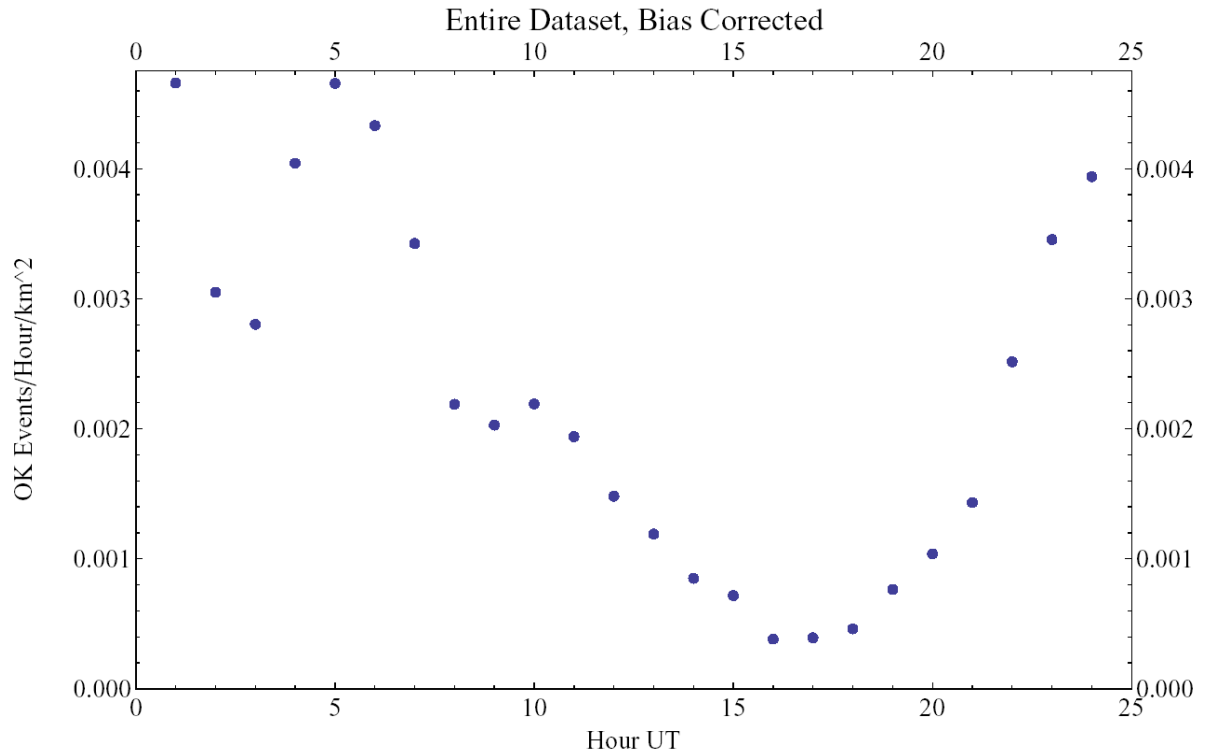


Figure 2-35. Similar to Figure 2-32, but for the Oklahoma Spaceport.

In Oklahoma the two diurnal variations appear to be different. That of lightning-event rate (Figure 2-35) is more ragged, potentially having three peaks at 1800, 2200, and 0300 MST (at 0100, 0500, and 1000 UT), respectively. Taking the hours-with-lightning rate (Figure 2-37) as potentially more representative, we find a diurnal variation that has lower relative amplitude than that in New Mexico and has two peaks, 6 PM CST (midnight UT ) and 0300 CST (0900 UT ), except perhaps in the early spring—see Figure 2-36. The seasonal variations (Figures 2-37 and 2-39) are similar, however, with a broad peak in June-July-August that might actually be two closely spaced peaks, June and August.

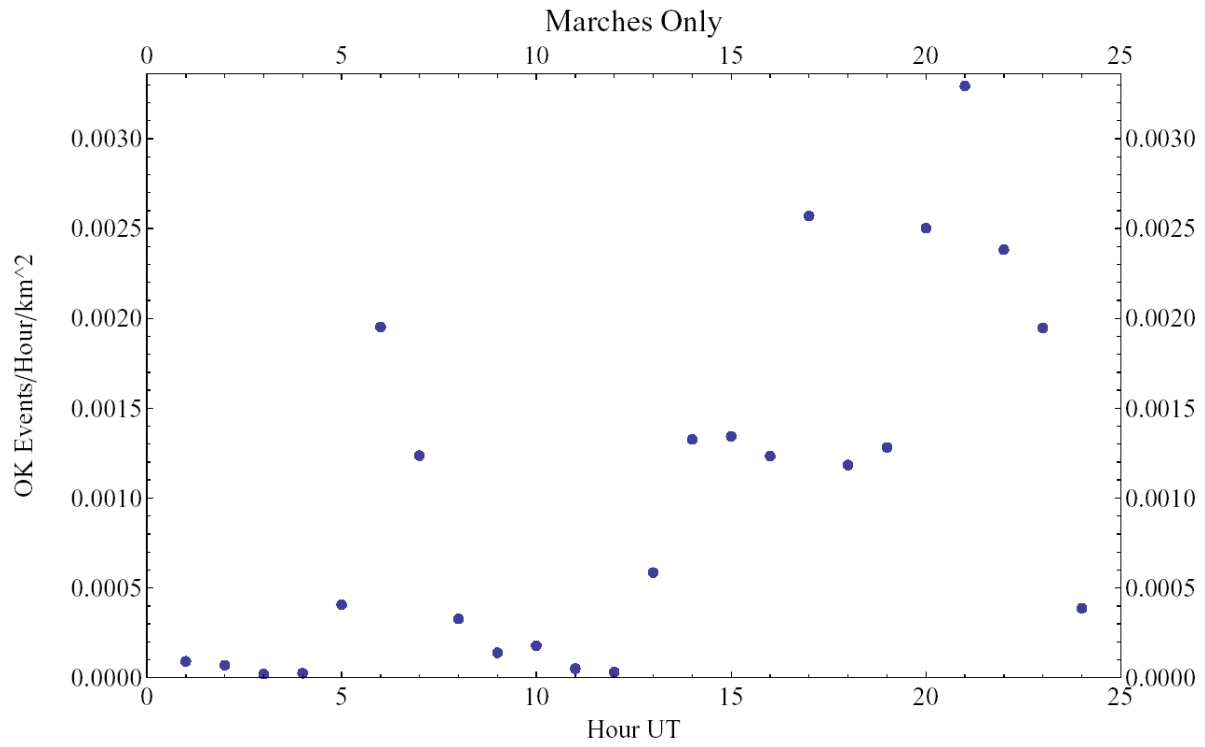


Figure 2-36. Similar to Figure 2-31, but for March and the Oklahoma Spaceport. Compare to Figure 2-37.

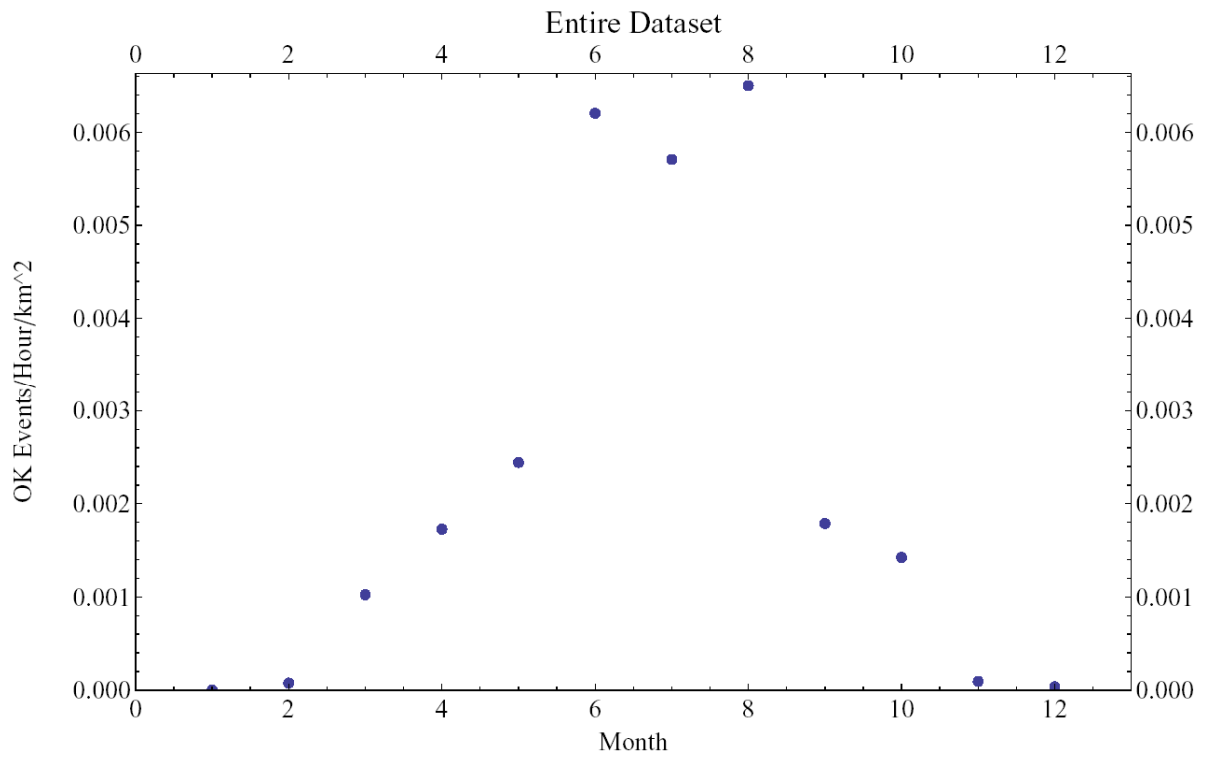


Figure 2-37. Similar to Figure 2-32, but for the Oklahoma Spaceport.

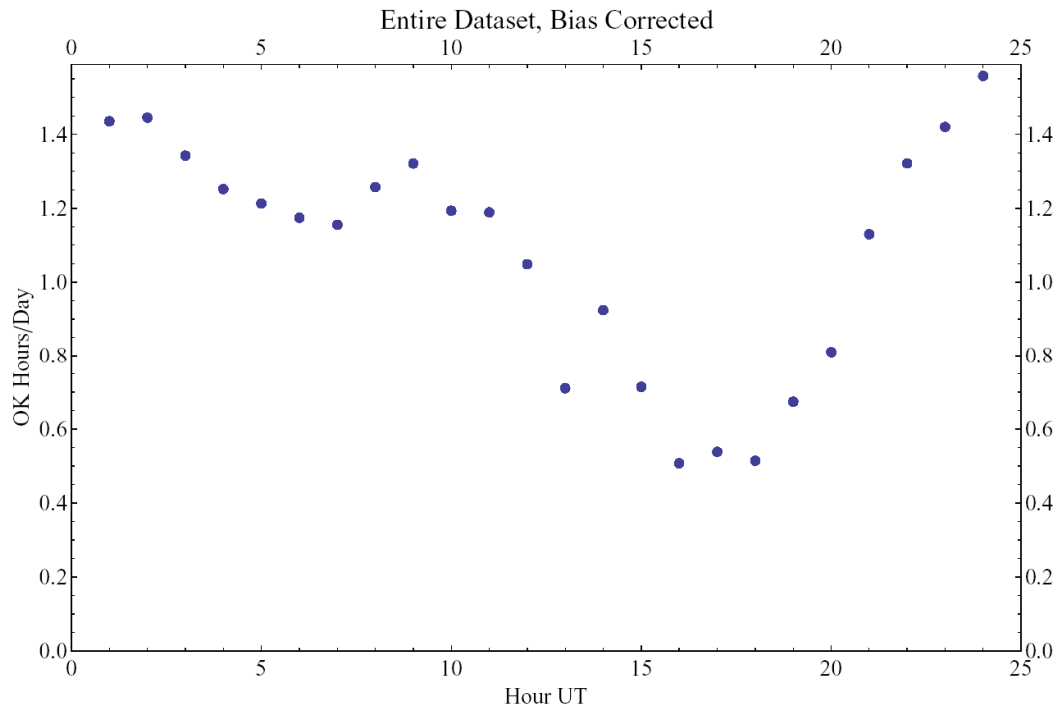


Figure 2-38. Similar to Figure 2-30, but for the Oklahoma Spaceport. Compare to Figure 2-35.

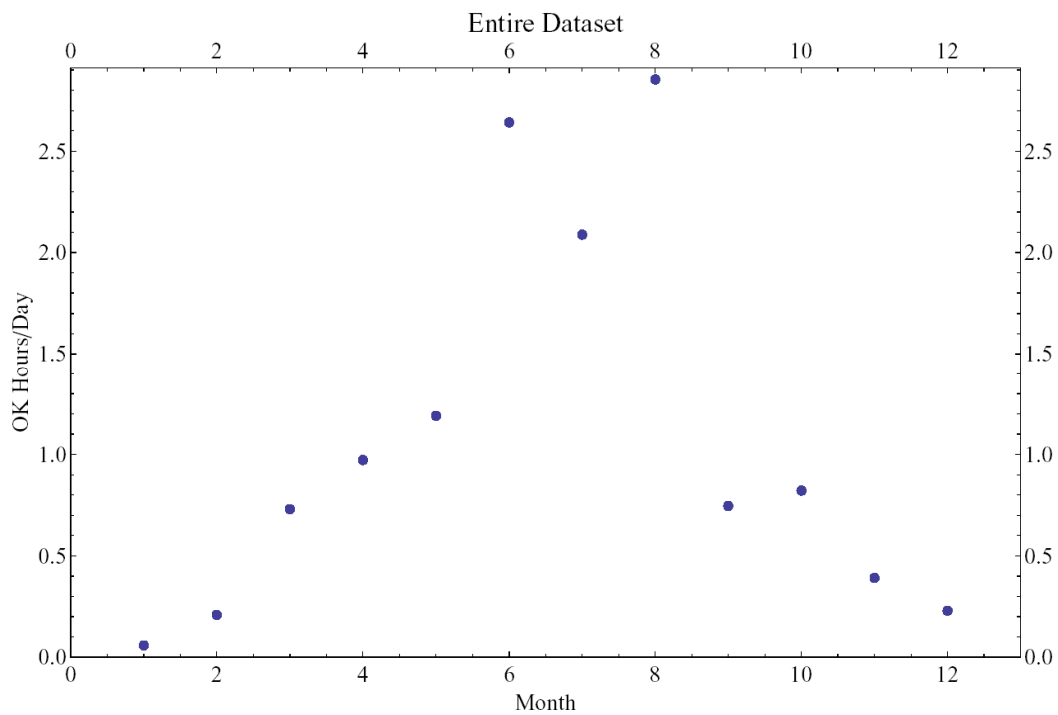


Figure 2-39. Similar to Figure 2-34, but for the Oklahoma Spaceport. Compare to Figure 2-37.

## 2.7.4 Summary of Lightning and Cloud Climatology

A nearly 15-year climatology study of naturally occurring cloud-to-ground lightning strikes showed that SA experiences significantly more lightning strikes overall than OS. However, year-to-year variability is high, and cloud-to-ground data from July 2004 indicated twice the number of lightning strikes at the proposed OS than at the proposed SA.

The launch sites at OS and SA are more than 20 percent likely to experience lightning for seasons spanning 120 and 90 days a year, respectively. The main lightning season begins at the end of May and lasts through early September in Oklahoma. In New Mexico, it begins in mid-June and lasts until early October.

## 2.8 Quantitative Risk Assessment

This section summarizes the extent to which a comprehensive risk assessment for the four concept RLVs at the four spaceports has been achieved and outlines the additional information and analyses that seem necessary to meet this challenge. By “comprehensive risk assessment,” we mean a computation of the diurnal and seasonal probability that any particular vehicle will trigger lightning during a particular flight at any particular spaceport, if it is launched without regard to current weather conditions. The following steps have been taken toward such a result:

The frequency of natural cloud-to-ground lightning has been determined from NLDN data, both diurnally and seasonally, in the vicinity of each spaceport. Noting that intra-cloud lightning (which is disregarded by the NLDN) constitutes the majority of natural lightning; this frequency gives a *lower bound* on the violation frequency of the LFCC natural-lightning rule. (See Appendix A.2, however, for evidence that few hours with LMA lightning were missed by the NLDN dataset.) The resulting statistics are summarized in section 2.7.1.

The frequencies of violations of certain of the cloud-based LFCC have also been estimated from our database of clouds, lightning, and temperatures for the various sites, as described in section 2.8.1. These statistics constitute an important new step toward a comprehensive risk assessment that is used in section 2.8.3 below.

To make the connection between the LFCC-violation frequencies and the triggering conditions (summarized in section 2.8.1), one needs the probability of occurrence of the relevant electric-field magnitudes in clouds that violate the various LFCC. We have analyzed data provided by Marshall Space Flight Center (MSFC) from the ABFM I campaign to obtain these probabilities, which have then been used in combination with the LFCC violation frequencies from section 2.8.1 to estimate the desired triggering probabilities. These data and calculations are described in detail in section 2.8.3.

### 2.8.1 Estimated Probability of LFCC Violations

Using our cloud, temperature, and lightning database and the scheme described in Appendix D, the probability of a violation for each rule was evaluated for each rule, spaceport, and representative month (January, April, July, and October). This data is combined with electric field data from the ABFM I campaign to calculate risk (see section 2.8.3). The calculation of risk is performed in a manner that is consistent with the way violations were recorded during the ABFM I campaign. During the campaign only the dominant rule violation was recorded. Dominance was not necessarily ordered in terms of hazard, but reflected the target conditions for the campaign (mostly layered clouds). An index that reflects the ordering used by MSFC to assign the dominant rule to a data collection (cloud penetration) was developed. For consistency that index is used in this section as well.



The Rule Violation Priority Category that was used by MSFC in the ABFM I re-analysis, in part determined by the classification scheme used during the original experiment, was as follows [Dr. Douglas Mach, NASA/MSFC, and Launa Maier, NASA/KSC, personal communications, 2009]:

- Detached Anvil (added rule, no contemporary rule existed)
- Lightning/Cumulonimbus/Attached Anvil (contemporaneous Rule A and/or B4)
- Towering Cumulus with top above  $-20^{\circ}\text{C}$  (Rule B3)
- Large Cumulus with top between  $-10$  and  $-20^{\circ}\text{C}$  (Rule B2)
- Modest Cumulus with top between  $+5$  and  $-10^{\circ}\text{C}$  (Rule B1)
- Debris Cloud (Rule F)
- Disturbed Weather (Rule E)
- Thick Cloud Layer (Rule D)

The application of this hierarchy, which is repeated at the end of Appendix D, to our climatological dataset is discussed further in section 2.8.3.2.

Table 2-11 shows the occurrence frequency for each rule violation obtained from our cloud, lightning, and temperature data sets. The data are averaged over all hours, representative months (January, April, July, and October), and the five years common to the data sets (2003 to 2005, inclusive). The most frequent rule violations are for Category 2 (lightning/cumulonimbus/attached anvil) and Category 5 (modest cumulus). The least common violations are Category 3 (large cumulus) and Category 6 (debris clouds). The paucity of Category 3 violations is most likely due to the fact that most cumulus clouds meeting the height (temperature) criterion would be classified as cumulonimbus by the cloud identification scheme used to infer cloud type from satellite data.

Occurrence statistics by site show that SA is the site most apt to show a violation and is comparable to CCAFS. Among the Spaceports MJSP is the least likely to show a violation.

Table 2-11. Average Occurrence Frequency of Rule Violations by NASA/MSFC Priority Category over All Hours, Months (Jan, April, Jul, Oct) and Years

Site	NASA Rule Violation Priority Category (Percent)							
	1	2	3	4	5	6	7	8
CCAFS	0.37	8.01	0.00	0.23	3.00	0.06	0.32	0.27
SA	0.45	7.17	0.12	2.06	6.62	0.14	0.06	0.07
OS	0.20	7.73	0.01	0.19	5.24	0.06	0.20	0.00
WTLS	0.27	7.74	0.02	0.40	6.23	0.10	0.16	0.07
MJSP	0.05	4.49	0.35	1.93	9.90	0.01	0.03	0.08
VAFB	0.01	2.47	0.01	0.19	4.49	0.00	0.20	0.18

Statistics by site and by month averaged over all hours and by hour averaged over all months are shown in Appendix G. The results are summarized here. The categories with the largest occurrence frequencies are 2 (lightning/attached anvil/lightning), 4 (moderate cumulus), and 5 (small cumulus). These categories frequently exceed 10 percent, where the remaining categories never exceed 3 percent and typically do not exceed 1–2 percent. Among the most frequently occurring categories 2 and 5 may dominate, but not 4. All of these categories are related to convective clouds and peak in the afternoon and evening hours. Whether category 2 or 4 dominates depends on site and season. At all sites except MJSP category 2 dominates in summer. At MJSP there is approximate parity between categories 2 and 5. Category 5 is dominant in the spring and fall at MJSP and in the winter and spring at VAFB.

## **2.8.2 Estimated Triggering Conditions**

To estimate risk it is necessary to apply triggering conditions for each of the concept vehicles. Triggering conditions, in terms of ambient electric-field thresholds, have been estimated for each of the concept RLVs and given in Table 2-5.

These field thresholds are quite uncertain in absolute terms, but they should be reasonably comparable between vehicles at the same altitude. Thus, they provide a quantitative basis for the following conclusions:

- For vehicles that are designed for unpowered horizontal landings (Concept vehicles 1, 2, and 3), there is a significant increase in triggering threshold (qualitatively, a reduction in triggering likelihood) during the glide phase of the flight.
- During the glide phase, these concept RLVs have higher triggering thresholds than medium-sized aircraft (which have been measured to be on the order of 45 kV/m at 4–5 km altitudes).
- Not surprisingly, all of these concept RLVs have much higher triggering fields than the Titan IV does (which is typical of large orbital boosters for which the current LFCC were designed).

Although the largest vehicle (Concept 1) has an appreciably lower triggering threshold than the others do, during boost phase all of them appear to be roughly comparable to medium-sized aircraft. This conclusion is less certain than the others because conventional aircraft do not have electrically significant exhaust plumes and, consequently, are not strictly comparable to space vehicles during the boost phase.

## **2.8.3 Estimated Probability of Triggered Lightning**

The triggering fields given in Table 2-5 constitute a quantitative metric that may be compared among vehicles. A higher triggering field corresponds to a lower likelihood of triggered lightning, all other circumstances being equal. Note, however, that a given field threshold cannot be translated directly into a probability of triggering. Triggering probability depends primarily on the weather into which a vehicle flies. We address this meteorological question in two steps.

### **2.8.3.1 Triggering-Field Exceedence Probabilities vs. LFCC**

First we examine a re-analysis of ABFM I data that has been provided by MSFC to determine the probability of exceeding our estimated triggering fields for the various vehicles during violations of each of the possible LFCC. The ABFM I re-analysis was accomplished for us by Dr. Douglas Mach of MSFC and is described in detail in Appendix B. In particular, this appendix gives cumulative probability distributions of electric-field intensity measured during flights into conditions that violate

each LFCC. The numerical tables that we actually used in our calculations were provided by MSFC on a CD-ROM.

Before proceeding, it must be recognized that the ABFM I data was obtained exclusively in Florida, from a maritime and/or semicontinental, subtropical climate. Although this is the only data available for our application (excepting only the ABFM II data, which suffer from these same limitations), it may be misleading or outright inapplicable to the continental, midlatitude climates of the commercial spaceports of interest. There are several reasons that limit the applicability of these data to an inference of risk, including the lower water-vapor mixing ratios, higher aerosol concentrations, and different aerosol size and composition spectra typical of continental sites, likely resulting very different drop- and ice-crystal-size spectra in the clouds. These characteristics, together with the higher vertical velocities typically observed in continental cumuli, could result in quite different electrification profiles in the various cloud types of interest to the LFCC.

The first “Airborne Field Mill” experiment (ABFM I) was carried out at the Kennedy Space Center (KSC) by scientists from MSFC and KSC, using a Learjet 28/29 operated by NASA LARC, during the summers of 1990 and 1991 and the winters of 1991 and 1992. The resulting dataset has been summarized for our purposes in Appendix B. During that experiment the lightning launch-commit criteria were much simpler than those now in use at the Eastern Range (essentially identical to proposed LFCC in Appendix C). The then-current rules are stated in Appendix B.4. They comprised a Lightning Rule, a four-section Cumulus Clouds Rule, a Surface Electric Fields Rule, a Thick Cloud Layers Rule, a Disturbed Weather Rule, and a Debris Clouds Rule. We will refer to these now-obsolete rules as the “LCC,” as they were called at the time, to distinguish them from the current LFCC. Although broadly similar, these LCC did not include separate Anvil Rules, had more conservative standoff distances from anvils and debris clouds, and lacked any radar-based exceptions like the “VAHIRR” exceptions to the current Anvil and Debris Cloud Rules.

There are several other features of the ABFM I re-analysis that influence its use herein:

- Because there was discussion at the time of treating detached anvils as a distinct class of debris cloud (although the concept of a detached anvil was not added to the LCC until April 1995), any detached anvil clouds were noted in the flight logs, and passes that mentioned them have been logged as detached-anvil violations for purposes of the re-analysis.
- Each pass was associated with only one “dominant” rule violation. For example, a given case might have simultaneously violated the Debris Clouds, Disturbed Weather, and Thick Cloud Layers Rules but would have been reported only as a violation of the Debris Clouds Rule. This reporting characteristic of the re-analysis was governed by an implicit rule-violation hierarchy that is detailed below.
- Violations of the Surface Electric Fields Rule were not individually catalogued because of ex post facto data-access problems and because “nearly all of the penetrations had some other rule violation, and they were classified by the other rules violated” [Appendix B.4.f].

Point 2 above made it impossible to use the scheme for calculating triggering probabilities that was illustrated by Equation 8, section 3.4.4 of Krider et al. [2006] because that equation assumes a knowledge of the probability that *no* hazardous fields occur during violations of each individual rule, *independent* of the state of the other rules. The ABFM I re-analysis, on the other hand, has reported one, and only one, rule violation for each pass, implying that the rule violations in this dataset are mutually exclusive.

In more specific detail, our exceedence probabilities have been determined as follows. We first selected what are believed to be the most appropriate of MSFC’s “Cumulative Probability

Distribution” (CPD) tables for each LCC violation. That is, for rules that require significant standoff distances (5 to 10 nm in A/B4, B3, B2, and F), we used the tables designated “all data runs,” which are presumed to include both actual penetrations and cloud fly-bys to determine standoff conditions. For the other LCC (Anvil, B1, E, and D), on the other hand, we used the CPD tables designated “cloud penetrations only.”

We also chose to use MSFC’s CPDs for field *magnitude*, called “ $E_{MAX}$ ” in Appendix B, as opposed to the vertical component only, called “ $E_Z$ .” (Each of these statistics was computed from the maximum value of the corresponding variable during each pass, although Appendix B does not make that clear. Further, there is a typographical error in Figure 6 of Appendix B, where the label on the horizontal axis should read “ $E_Z/E_{MAX}$ ” instead of its inverse.) This latter choice is controversial to the extent that the  $x$ -component of the field (along the flight direction) could become significantly contaminated by aircraft charge during cloud penetrations, generally leading to an overestimate of  $E_{MAX}$ , especially at the lower field magnitudes, whereas  $E_Z$  was not believed to suffer from such contamination. Appendix B points to evidence of this contamination with respect to the B1 statistics. Nevertheless, we chose to use  $E_{MAX}$  (which is always  $\geq E_Z$ ) in order to err on the conservative side.

Another factor that modifies the exceedence probabilities used herein is the effective altitude that we have ascribed to each rule violation. This is because of the presumed altitude scaling of the triggering threshold in proportion to atmospheric density, as summarized in section 2.6.3. In order to simplify the calculation of triggering probabilities while minimizing the introduction of additional uncertainties and maintaining conservatism, we have chosen to assign an approximate altitude or temperature level and the corresponding relative atmospheric density (based on the U.S. Standard Atmosphere 1976) to each LLCC violation, as shown in Table 2-12.

Table 2-12. Effective Relative Air Densities Assigned to the Various Rule Violations

<b>Rule Violation</b>	<b>Altitude (km)</b>	<b>Temperature (°C)</b>	<b>Relative Air Density</b>
1. Detached Anvil	10.0	-50	0.338
2. Lightning/Cumulonimbus/ Attached Anvil (A/B4)	10.0	-50	0.338
3. Towering Cumulus (B3) top above -20°C	5.5	-20	0.569
4. Large Cumulus (B2) top between -10 and -20°C	5.5	-20	0.569
5. Modest Cumulus (B1) top between +5 and -10°C	3.5*	0	0.705
6. Debris Cloud (F)	3.5*	0	0.705
7. Disturbed Weather (E) extends above 0°C	3.5*	0	0.705
8. Thick Cloud Layer (D) any part between 0 and -20°C	5.5	-20	0.569

\*The nominal altitude of the freezing level (and the corresponding relative air density) was adjusted from the Standard Atmosphere value of 2.5 km to conservatively account for the geographic distribution of spaceports and for seasonal variations.

Based on the relative air density values in Table 2-12, the selected CPD tables were themselves scaled to the corresponding altitudes by multiplying all field magnitudes in each table by the applicable relative-air density. This is equivalent to dividing the surface-field thresholds for each vehicle by the correct relative air density for each LCC, but it is easier and results in a consistent set of exceedence probabilities for use with all vehicles and spaceports.

Finally, CPD values corresponding to the surface triggering thresholds of the various vehicles that are given in Table 2-5 were looked up by interpolation in the scaled probability distributions. Triggering, or field-threshold-exceedence, probability equals one minus interpolated CPD. The surface triggering thresholds could be used directly, of course, because the CPD tables had already been scaled to the appropriate altitudes, as explained immediately above with respect to Table 2-12. This last step resulted in the matrix of exceedence probabilities given in Table 2-13. We will refer to individual values in this table as “partial triggering probabilities,” since each such value gives only the contribution to overall triggering probability due to the violation of a given rule. More will be said about this table in section 2.9.3 below.

It must be noted that some of the LLCC involve standoff distances and this was included in the calculation of violation probabilities (Table 2-11). The ABFM electric field data on the other hand refer to a combination of mostly cloud penetrations plus some fly-bys. Thus combining the probabilities of LLCC violations with the probabilities of encountering threshold fields based on the ABFM data gives estimates that are probably upper bounds for the probabilities of encountering such fields for LLCC that involve standoffs.

Table 2-13. Partial Triggering Probabilities for Each Combination of Vehicle Concept and Rule Violation. (Values Scaled According to Effective Relative Air Densities in Table 2-11)

<b>Vehicle\Rule:</b>	<b>1. Anvil</b>	<b>2. A/B4</b>	<b>3. B3</b>	<b>4. B2</b>	<b>5. B1</b>	<b>6. F</b>	<b>6. E</b>	<b>8. D</b>
Titan IV Boost	0.289	0.691	0.668	0.076	0.002	0.201	0.249	0.050
Concept 1 Boost	0.102	0.415	0.278	0.000	0.000	0.034	0.045	0.004
Concept 2 Boost	0.049	0.283	0.097	0.000	0.000	0.004	0.010	0.000
Concept 3 Boost	0.069	0.319	0.134	0.000	0.000	0.013	0.034	0.001
Concept 4 Boost	0.073	0.328	0.143	0.000	0.000	0.015	0.035	0.001
Concept 1 Glide	0.012	0.185	0.028	0.000	0.000	0.000	0.004	0.000
Concept 2 Glide	0.000	0.048	0.010	0.000	0.000	0.000	0.000	0.000
Concept 3 Glide	0.003	0.071	0.014	0.000	0.000	0.000	0.001	0.000

### 2.8.3.2 Application of Climatological LCC-Violation Frequencies

The second step in the calculation of triggering probability is to combine appropriately the set of exceedence probabilities for each vehicle and violation that are described in section 2.8.4.1 with the set of occurrence frequencies of each LCC violation for the various spaceports, hours of day, and seasons, from section 2.8.2. In order to use these exceedence probabilities, we had to develop climatological rule-violation frequencies that were based on the same requirement of mutually exclusive rule violations and that used the same hierarchy for assigning any given observation (which often violated more than one of the LCC) to a single rule.

Using the hierarchy list defined in section 2.8.1 and Appendix D, the rule-violation assessment for each hour of data at each spaceport, developed in section 2.8.2, has been re-classified, whenever multiple rules were deemed to be violated, by selecting only the lowest-numbered of these multiple violations from the list. Thus each rule violation was made mutually exclusive, presumably in the same manner as had been done in the ABFM I re-analysis itself. The rule-violation frequencies that have been calculated from these re-classified assessments are therefore appropriate for use with the exceedence probabilities determined from Appendix B. To obtain the overall triggering probability for a given vehicle, spaceport, and climatological time period, one simply sums the product of the individual triggering-threshold exceedence probability (or “partial triggering probability”) and the corresponding climatological violation frequency over all of the LCC. In symbols similar to those

used in Equation 8, section 3.4.4 of Krider et al. [2006], the overall triggering probability,  $P_{jkl}$ , for vehicle  $j$ , climatological period  $k$ , and spaceport  $l$  is given by

$$P_{jkl} = \sum_1^8 p_{ji} f_{ikl} \quad (2-20)$$

where  $f_{ikl}$  is the frequency of rule violation  $i$  at climatological period  $k$  and spaceport  $l$ , and  $p_{ji}$  is the probability of exceeding the triggering threshold of vehicle  $j$  for the same rule violation. The numerical matrix of partial triggering probabilities,  $p_{ij}$ , has already been given in Table 2-12.

### 2.8.3.3 Numerical Results

There are several ways to display the overall triggering probabilities that have been computed from Eq. 2-20. Recall that each of these probabilities represents the chance of triggering lightning by a given vehicle if launched during a given climatological period from a given spaceport, without regard to current weather conditions. Here we have not associated any particular group of vehicles with any individual spaceport, but treated them all as interchangeable. The Titan IV vehicle during boost phase (with its conducting plume) has been included for comparison purposes, as have the Federal Ranges at Cape Canaveral and at Vandenberg. Each of the concept vehicles that is intended to land in an unpowered glide is shown both during boost and during the glide phase.

The simplest (and least informative) way of displaying these results is as annual averages vs. vehicle and spaceport. Such a comparison is shown graphically in Figure 2-40, with the different spaceports evenly spaced along the x-axis (ranked in descending order of triggering probability) and the various vehicles shown as lines of different colors, solid for the boost phase and broken for the glide phase. A two-decade semilogarithmic plot is given to better illustrate the variability. The corresponding probability matrix is given in tabular form as Table 2-14.

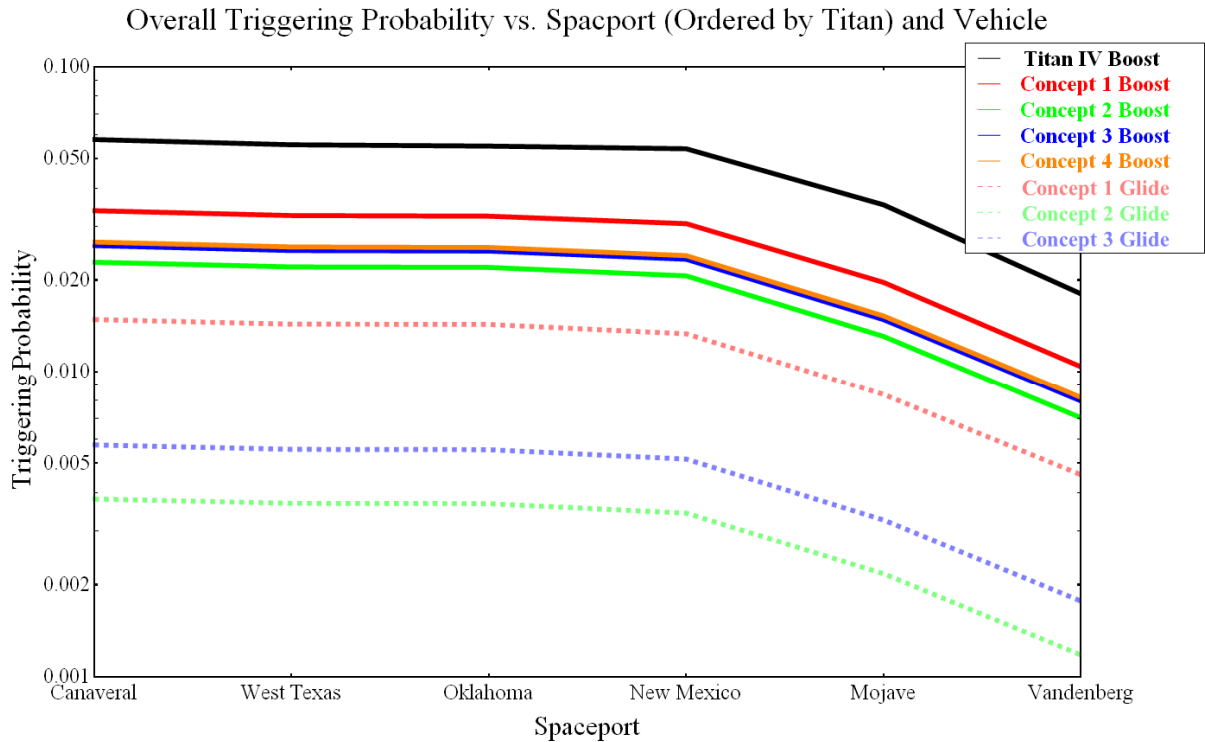


Figure 2-40. Overall triggering probabilities (annual average) by vehicle and spaceport.

Figure 2-40 clearly shows that triggering probabilities for the various vehicles track one another more or less (although not precisely) in proportion across the different spaceports. Therefore, we concentrate only on the vehicle at greatest risk—Concept 1 Boost—from here on. Notice that even the largest of the relevant annual probabilities is quite small. On average Concept 1 Boost can be expected to trigger lightning roughly 3.3 percent of the time if launched from the West Texas Spaceport. This is not the whole story, however.

Table 2-14. Overall Triggering Probabilities (Annual Average) by Vehicle and Spaceport

Vehicle: Spaceport	Titan IV Boost	Concept 1 Boost	Concept 2 Boost	Concept 3 Boost	Concept 4 Boost	Concept 1 Glide	Concept 2 Glide	Concept 3 Glide
Canaveral	0.0577	0.0338	0.0229	0.0259	0.0266	0.0148	0.0038	0.0057
West Texas	0.0555	0.0325	0.0221	0.0250	0.0257	0.0143	0.0037	0.0055
Oklahoma	0.0549	0.0324	0.0220	0.0249	0.0256	0.0143	0.0037	0.0055
New Mexico	0.0538	0.0306	0.0206	0.0234	0.0240	0.0133	0.0034	0.0052
Mojave	0.0353	0.0196	0.0131	0.0148	0.0153	0.0084	0.0022	0.0033
Vandenberg	0.0180	0.0104	0.0070	0.0080	0.0082	0.0046	0.0012	0.0018

Moving to the opposite extreme, we now examine the triggering probabilities for Concept 1 Boost during each hour of the day in each season. Recall that section 2.8.1 reported LCC-violation climatologies for only four representative months: January, April, July, and October. If we select the month and hour with the maximum triggering probability for Concept 1 Boost at each spaceport, we get the numbers in Table 2-15. Notice that, of the relevant spaceports, New Mexico has the highest maximum probability—nearly 17 percent—at 1700 MDT in July, whereas Mojave has the lowest—only 2 percent—at 1900 PST in January.

Table 2-15. Maximum Hourly Triggering Probability for Concept 1 Boost at the Various Spaceports, Ranked in Descending Order, and the Month and UT Hour in Which that Maximum Occurs. (The overall values from Table 2-13 are also shown for comparison)

<b>Spaceport</b>	<b>Overall</b>	<b>Maximum</b>	<b>Month</b>	<b>Hour (UT)</b>
Canaveral	0.034	0.166	Jul	23
New Mexico	0.031	0.143	Jul	3
West Texas	0.033	0.125	Jul	22
Oklahoma	0.032	0.077	Apr	4
Mojave	0.020	0.066	Jan	3
Vandenberg	0.010	0.038	Jan	22

Because the seasonal and diurnal variations can be quite different among geographic regions, parts (a) through (f) of Figure 2-41 show the hourly data for all six spaceports, all on the same vertical scale.

Interesting things to note from these six figures, in addition to the large differences in hourly triggering probability across spaceports, are the following: Although the Eastern Range, New Mexico Spaceport, and West Texas Spaceport all have their maxima in summer afternoon/evening (local time), the Oklahoma Spaceport has its maximum in spring late evening, and the Western Range (such as it is) and the Mojave Spaceport have their maxima in winter afternoons/evenings. The first three of these sites, which have the largest maxima, also have the greatest diurnal and annual variations, presumably because most of their storms are driven by local convection (see section 2.8.1 for a breakdown of the relevant LCC violations).

Finally, we show as examples the diurnal variation (averaged over all seasons) and the seasonal variation (averaged over all days of the month) for all vehicles at the New Mexico Spaceport in Figures 2-42 and 2-43.



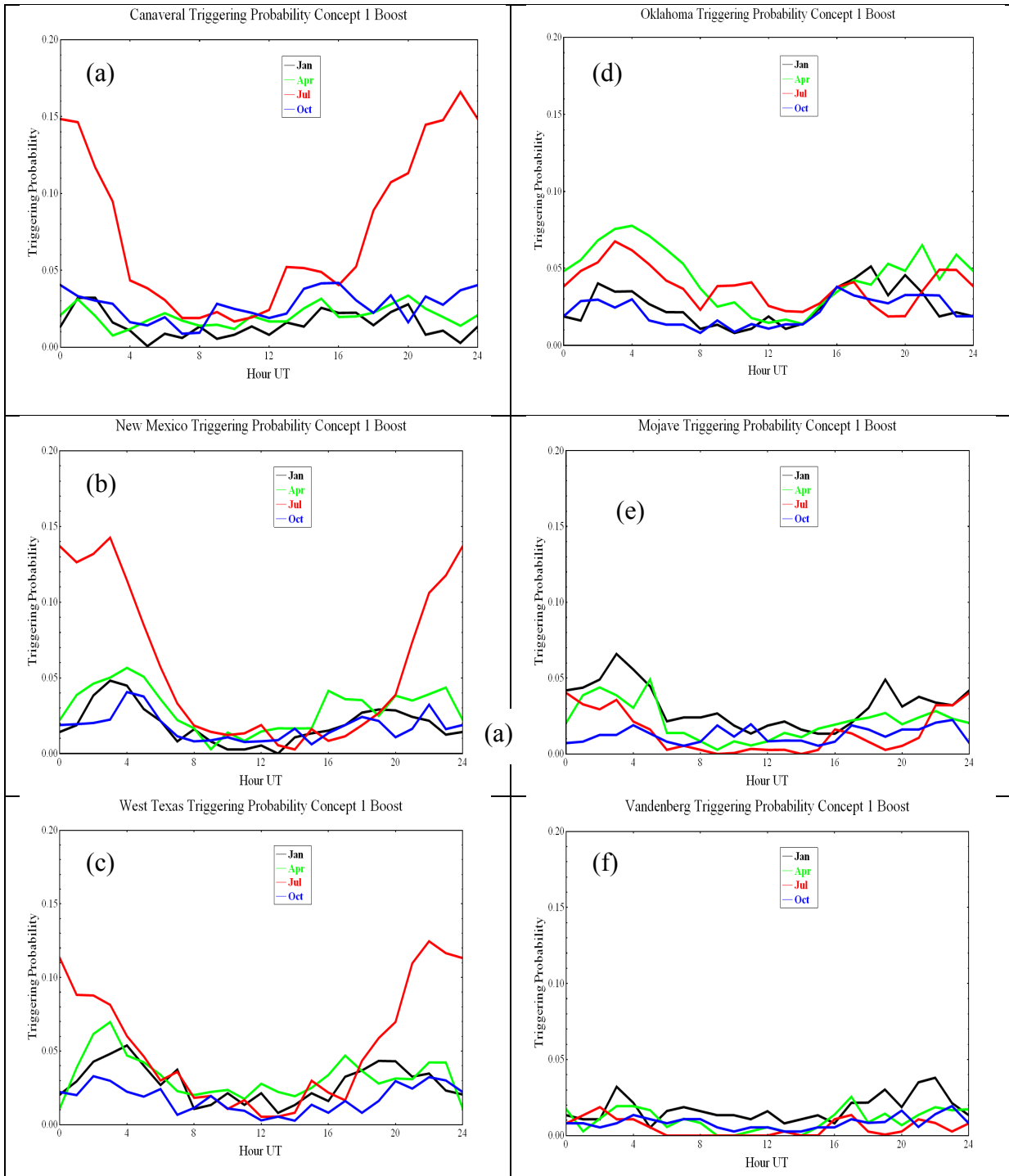


Figure 2-41. (a) Hourly triggering probability of Concept 1 boost for all hours and seasons at the Eastern Range (EST is UT - 5 hr.); (b) Similar to (a) at the New Mexico Spaceport (MST is UT - 7 hr); (c) Similar to (a) at the West Texas Spaceport (MST is UT - 7 hr); (d) Similar to (a) at the Oklahoma Spaceport (CST is UT - 6 hr); (e) Similar to (a) at the Mojave Spaceport (PST is UT - 8 hr); (f) Similar to (a) at the Western Range (PST is UT - 8 hr).

### New Mexico Diurnal Triggering Probability

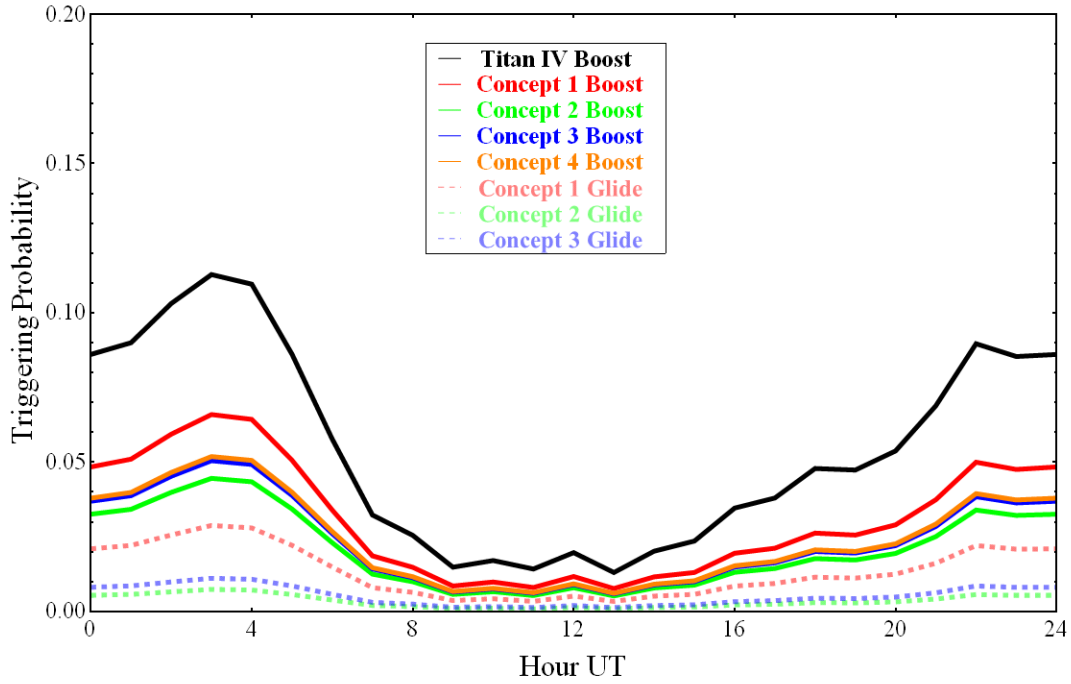


Figure 2-42. Average diurnal variation of triggering probability for all vehicles at SA.

### New Mexico Seasonal Triggering Probability

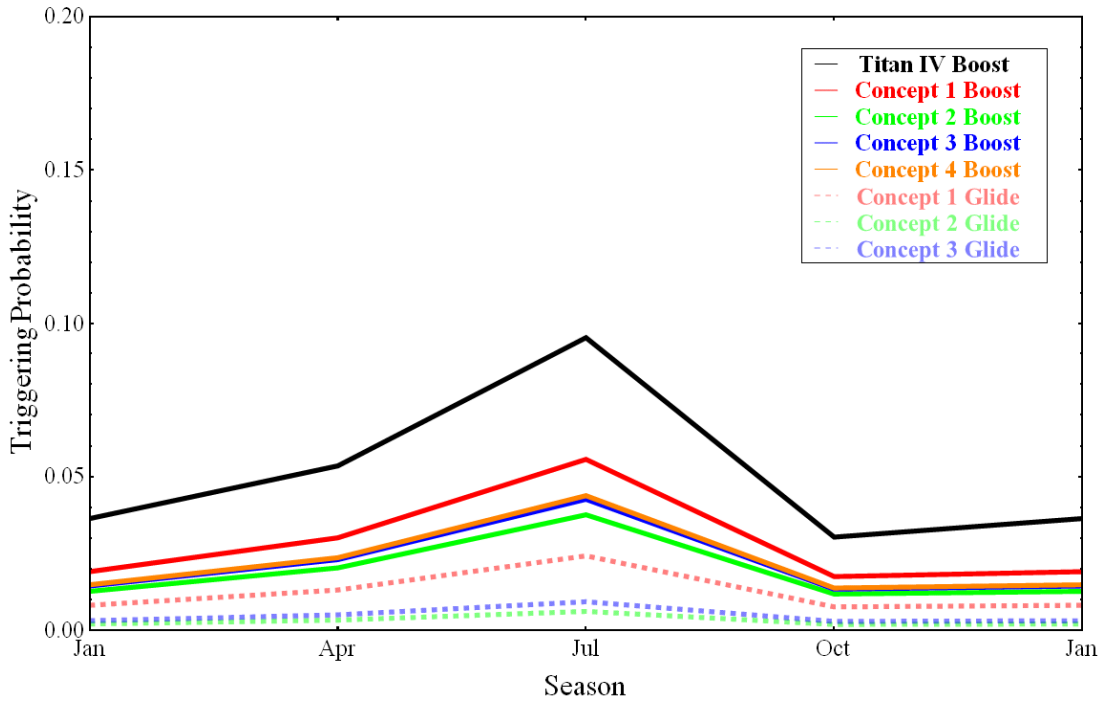


Figure 2-43. Average seasonal variation of triggering probability for all vehicles at SA.

## 2.9 Relevancy of Existing LFCC to Proposed RLV Concepts

Based on recent work on cloud electrification and the analysis of the ABFM data presented here it is possible to comment on the relevancy of the existing LFCC to RLV concept vehicles.

### 2.9.1 Cloud Electrification

Krider et al. [2006] have given an overview of what is known today about the electrical structure of thunderclouds and the mechanisms of cloud electrification. A more recent review of the physics of ice surfaces (including microscale electrification mechanisms) has been given by Dash et al. [2006], and recent surveys of laboratory experiments on cloud electrification have been published by Saunders et al. [2006] and Saunders [2008]. At this point, it is clear that we still need to obtain more information about the microphysical, electrical, and dynamical structure of thunderclouds before we can make further evaluations of the non-inductive, ice-ice collision mechanism (coupled with precipitation), the detailed physics that underlies this process, and other possible mechanisms. Among the parameters that we are still lacking are the number of ice-ice collisions per unit volume, the liquid water content (LWC), and the temperatures in the relevant regions of thunderclouds; the sizes of the ice crystals and collision velocities in these regions; and what charges are present on the ice crystals, water drops, and precipitation particles inside the cloud (all as a function of size). Several experiments are currently underway both in the laboratory and in nature to learn more about the electrical structure of clouds, the mechanisms of electrification, and the possible effects of lightning on both of these factors.

### 2.9.2 FAA Lightning Flight Commit Criteria (LFCC)

The FAA Natural and Triggered Lightning Flight Commit Criteria (LFCC), modeled after the Air Force and NASA Lightning Launch Commit Criteria (LLCC) are designed to protect the public from lightning hazards on expendable launch vehicles during launch. The LFCCs are found in Appendix C together with the Definitions. This version of the LFCC was approved by the USAF/NASA Lightning Advisory Panel (LAP) in October of 2008. They differ notably from the existing FAA LFCCs in that radar-based revisions to the anvil and debris rules have been proposed. The revisions take into account data from the ABFM II campaign [Dye et al., 2004b]. It should be noted in Appendix C that the definitions are given first because they are an integral part of the LFCC, and the logic and wording of the LFCC depend in a critical way on these definitions. It should also be noted that each of the LFCC requires *clear and convincing evidence* to trained weather personnel that its constraints are *not violated*. Under some conditions, trained weather personnel can make a clear and convincing determination that the LFCC are not violated based on visual observations alone. However, if the weather personnel have access to additional information such as measurements from weather radar, lightning sensors, electric field mills, and/or aircraft, and this information is within the criteria outlined in the LFCC, it would allow a launch to take place where a visual observation alone would not.

For further details, the reader can consult the Titan Program [1988], Krider et al. [1999], Dye et al. [2006], and Willett et al. [2006], Federal Register, Vol. 71, No. 165, August 25, 2006 /Rules and Regulations].

### 2.9.3 Risk Assessment Based on ABFM I Data

In section 2.8.3.1 a matrix of “partial triggering probabilities” was presented as Table 2-13, in terms of launch vehicle and LCC violation. These partial probabilities express the likelihood that a given vehicle will trigger lightning when violating a specified LCC. They were derived only from:

- ABFM I cumulative-probability distributions of measured field intensity in conditions that violated the various LCC.
- Our estimated lightning-triggering thresholds at surface conditions for the various vehicles of interest.
- Our assumptions about the approximate altitudes (consequently, the air densities) applicable to these LCC, and about the dependence of triggering field on air density.

They should therefore be independent of spaceport, subject to the caveats in section 2.8.3.1. A glance at this table reveals the presence of many zero or near-zero values. For Figure 2-44 we have first sorted the columns of the table (the LCC violations) in descending order of partial triggering probability for the Titan IV vehicle. The different LCC violations are evenly spaced along the x-axis, and the partial probabilities for the various vehicles are shown as broken lines of different colors. A four-decade semilogarithmic plot is given to better illustrate the range of variability.

Before drawing any important conclusions from this figure and its associated table, it is wise to remember the many sources of uncertainty in the numbers, including especially:

- Significant theoretical and experimental uncertainties both in the triggering conditions themselves and in their dependence on altitude [see sections 2.6.2 and 2.6.3 and references therein].
- Major uncertainties in the electrical effects of the exhaust plumes that are assumed to increase the electrical effective lengths of the vehicles during boost phase [see section 2.6.5].
- Potential inapplicability of the ABFM I dataset to the commercial spaceports of interest [see section 2.8.3.1].

In addition to these major sources of error, there are less serious statistical uncertainties, such as the relatively small sample size of the ABFM I dataset used to determine our cumulative probability distributions of electric fields in the various LCC violations [see Appendix B], and the relatively crude techniques that we have used to estimate LCC-violation frequencies from satellite and other meteorological data for the spaceports in question [see section 2.8.1]. Given the unknown, but presumably high, statistical confidence levels required by the FAA for safe RLV operations, it is difficult to overemphasize the effect of all the uncertainties involved in the creation of Figure 2-44.

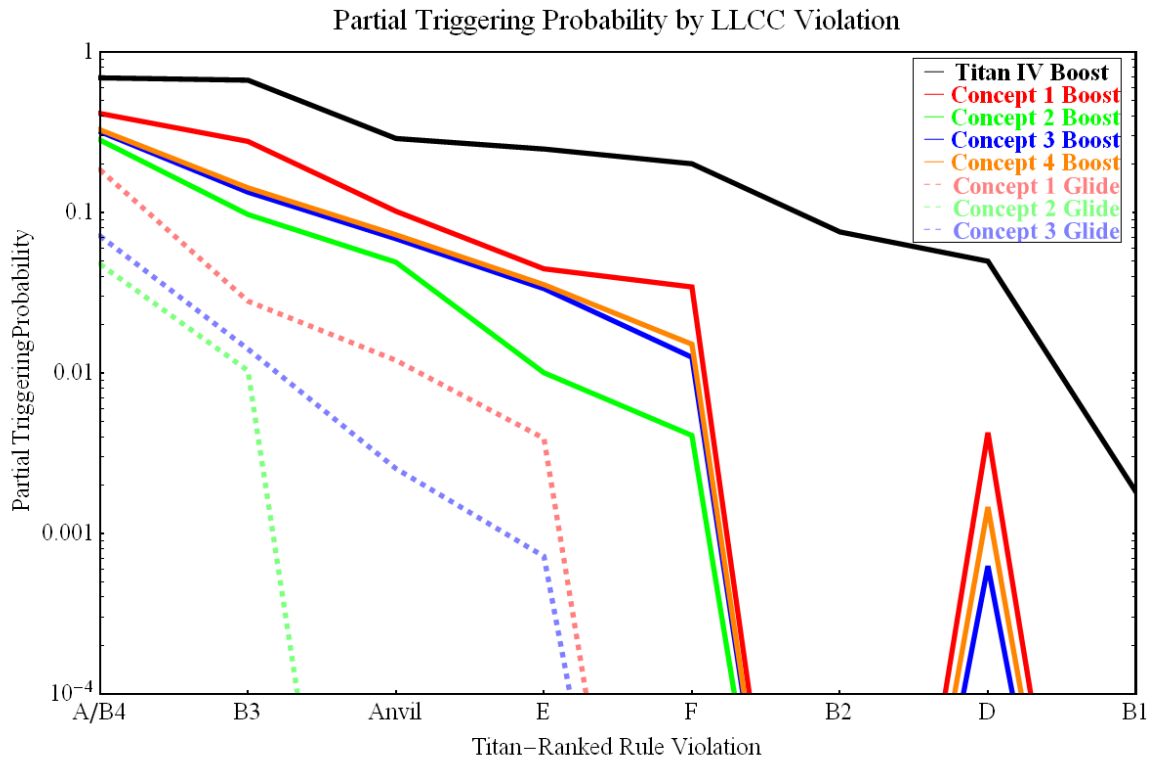


Figure 2-44. Partial triggering probabilities for the various vehicles, plotted against the various possible LCC violations on a semilogarithmic scale. Where the broken lines disappear off the bottom of the graph, these probabilities are too small to distinguish from zero.

Figure 2-44 is striking for several reasons. Most obvious and important is the prediction that the partial triggering probabilities due to Lightning/Cumulonimbus/Attached Anvil (A/B4) violations are relatively large for all vehicles considered, making the observance of these rules vital to flight safety. [The partial probabilities due to all violations except perhaps Modest Cumulus (B1) are significant for Titan, but that is of limited interest in the present context.] It also appears that the partial probabilities for most violations [excepting only Large Cumulus (B2) and Modest Cumulus (B1)], are significant for all RLVs during boost phase; although those for Thick Cloud Layer (D) violations may be small enough to be insignificant in three of those cases and are negligible for Concept 2 Boost. For the three RLVs that glide to an unpowered landing, violations of at least half of the rules [Debris Cloud (F), Large Cumulus (B2), Thick Cloud Layer (D), and Modest Cumulus (B1)] are probably harmless during descent; and for some of these vehicles, Detached Anvil and Disturbed Weather (E) violations may be relatively or completely safe. Not surprisingly, the Concept 2 vehicle is predicted to experience the least hazard, both during boost and during glide, because of its relatively small size and low engine power [see Table 2-1].



### **3. Recommended Lightning Flight Rules**

Because the risk is based on the analysis of fields associated with the lightning rules for small and moderate cumulus clouds, we recommend that these rules be relaxed subject to a rigorous statistical analysis suited to infrequently occurring events (e.g., extreme value analysis). Also, because these rules refer to clouds that can undergo rapid development the rules should be relaxed only when collateral data (e.g., CIP indices) indicates little potential for growth.





## **4. Recommendations for the Future**

### **4.1 Statistical Analysis of Existing Data to Better Determine LLCC and LFCC Applicability to RLVs**

In section 2.8 we have made use of a statistical re-analysis of ABFM I data by MSFC to estimate the probability of triggering due to various LCC violations. There is another dataset from the ABFM II experiment [Dye and Lewis, 2004b] that could also be re-analyzed to yield more accurate electric-field statistics for both anvil clouds and debris clouds, also in the Florida area. It would be productive to make use of these data, which is readily available.

### **4.2 Current Icing Potential (CIP)**

Monitor all types of lightning (both cloud-to-ground and intra-cloud) at each launch site. (Note that the detection and location of intra-cloud lightning may require the installation of additional equipment at each site.) This should be done before beginning RLV operations, to the extent possible using the sensors presently installed, both to better quantify the effects of lightning on launch availability vs. time of day, season, etc., and to find any new or unexpected behavior at those locations.

### **4.3 Instrumentation**

A fully instrumented and staffed site would include

- Instrumentation, such as field mills suitable to detect significant enhancements or polarity reversals in the normal fair-weather field at the ground, should be installed near each launch site to aid in the avoidance of unexpected hazards during all future RLV operations.
- Trained weather observers, with access to both lightning data from either a local LMA (preferred) or a realtime feed from the NLDN and radar data from either a dedicated weather radar (preferred) or a realtime feed from the nearest NEXRAD, are required to identify cloud types, measure cloud heights and thicknesses, monitor radar reflectivities and verify the modified LFCC during all future RLV operations at each launch site.

### **4.4 Quantification of Electric-field Triggering Conditions and Effects of Vehicle Plumes**

- Continue both theoretical and experimental efforts to quantify the electric-field triggering conditions and the effects of the vehicle exhaust plumes in order to obtain more accurate, altitude-dependent triggering thresholds for the various RLVs. Specific topics in need of further research include experimental and/or theoretical determinations are: What is the true relationship between effective electrical length and triggering threshold?
- What is the true altitude dependence of the triggering threshold for any given vehicle?
- How does the exhaust plume actually affect the triggering process?
- Is the focus on positive-leader viability fully justified?

We believe that the greatest opportunity for progress toward understanding the triggering conditions currently lies in two areas, as summarized at the end of section 2.6.6. First, a much better understanding of the effects of exhaust plumes is needed (see section 2.6.5.7). Second, a much more accurate knowledge of the effects of altitude (atmospheric density) is required (see section 2.6.3). Specific recommendations in these two areas are given in the following subsections.

## **4.5 Numerical Calculation of the Critical Conductivity Magnitude in Exhaust Plumes**

### **4.5.1 Construct a Model of Plume-Conductivity Distributions Valid Near this Critical Magnitude**

The next, and significantly more difficult, step in determining the plume effects would be to develop a plume-chemistry and -dynamics model that is valid out to the low-conductivity extremities of the plume (at least as low as  $10^{-11}$  S/m). As indicated in section 2.6.5.7, such a code should not need to be classified, although it might require initialization by one of the classified models. In addition to incorporating low-temperature ion chemistry, this code would need to include ion-attachment equations like those mentioned at the end of the previous section to account for the effects of particulates. (The Aerospace Corporation has experts with access to the appropriate plume codes.) The output of such a model could then be used as input to the strictly electrical solution described above, although it might be best to incorporate those electrical equations within this new model itself.

### **4.5.2 Validate These Critical-Conductivity Models Experimentally**

As recommended at the end of section 2.6.5.1, one or more experiments should be conducted on an insulated static-test stand to measure the actual conductivity distributions in, and electrical behavior of, exhaust plumes from the engine types under consideration here. Without such experimental validation, it would not be prudent to depend on results of the above-mentioned modeling for the LFCC.

### **4.5.3 Conduct Experiments to Validate Existing Modeling of the Altitude Dependence**

It has been noted that uncertainty about the altitude dependence of the triggering conditions is comparable, in our estimation, to uncertainty about the plume electrical effects of triggering thresholds for the various RLVs. The model predictions of Bazelyan et al. (2007) on altitude dependence of positive-leader viability, mentioned in section 2.6.3, are judged to be too uncertain to form the basis for a relaxation of the LFCC. Experimental validation, not only of several of the individual steps in their theoretical work, but especially of the *actual* altitude dependence of the triggering conditions, is badly needed. Such experimental validation could be pursued in several ways, including:

- The launching of electric-field-sounding rockets, followed by grounded-wire triggering rockets from a high-altitude site [e.g., Willett et al., 1999].
- The firing of triggering rockets from an aircraft instrumented to measure the ambient field and flying at different altitudes.

Although vitally important to a full understanding of the triggering conditions, this would be a difficult and expensive undertaking.

## **4.6 ABFM System to Provide Measurements of Electric Field Aloft in Support of RLV Operations**

Consider further the feasibility of an ABFM system to provide measurements of the electric field in and around clouds in support of RLV operations.

## 5. Acronyms and Abbreviations

ABFM	Airborne Field Mill
Ac	altocumulus
AF	Air Force
AFB	Air Force Base
AFCCC	Air Force Combat Climatology Center
AEDC	Arnold Engineering Development Center (Tullahoma)
AIAA	American Institute of Aeronautics and Astronautics
As	altostratus
AST	Office of Commercial Space Transportation
Cb	cumulonimbus
CCAFS	Cape Canaveral Air Force Station, Florida
Cc	cirrocumulus
CDFS2	Cloud Depiction and Forecast System V2
CFR	Code of Federal Regulations
CG	cloud-to-ground
Ci	cirrus
CIP	current icing potential
cm	centimeter
CONUS	Continental United States
COTR	Contracting Officer's Technical Representative
Cs	cirrostratus
CST	Central Standard Time
Cu	cumulus
CVC	current-voltage characteristic
dBZ	Radar reflectivity units
DC	direct current
°C	degrees Centigrade
DMSP	Defense Meteorological Satellite Program
DOT	Department of Transportation
DOY	day of year
$\Delta E$	change in electric field
$E$	electric field
ECMWF	European Center for Medium Range Weather Forecasting
FAA	Federal Aviation Administration
ft	foot
GBFM	Ground-Based Field Mill
HTHL	horizontal takeoff horizontal landing
IC	intracloud
ILS	instrument landing system
IR	infrared
ISCCP	International Satellite Cloud Climatology Project
JP-1	Fuel Oil Number 1, Kerosene
K	degrees Kelvin
km	kilometer
KSC	Kennedy Space Center (NASA)
kV	kilovolt
lb	pound
lbf	pound force
LDAR	Lightning Detection and Ranging

LFCC	Proposed FAA natural and triggered lightning flight commit criteria (FAA)
LLC	limited liability company
LLCC	Lightning Launch Commit Criteria (AF)
LLJ	low-level jet
LLL	liquid-like layer
LMA	lightning mapping array
LOX	liquid oxygen
LT	local time
LWC	liquid water content
MHz	megahertz
MJSP	Mojave Air and Space Port
m	meter
MCC	mesoscale convective complex
MCS	mesoscale convective system
$\mu$ A	microampere
MJSP	Mojave Air and Space Port
MSFC	Marshall Space Flight Center (NASA)
MST	Mountain Standard Time
MV	megavolt
NASA	National Aeronautics and Space Administration
nmi	nautical mile
NCAR	National Center for Atmospheric Research
NEXRAD	Next generation radar
NLDN	National Lightning Detection Network
NMIMT	New Mexico Institute of Mining and Technology
NTPS	National Test Pilot School
NWS	National Weather Service
Ns	nimbostratus
OS	Oklahoma Spaceport
O <sub>2</sub>	molecular oxygen
ONERA	<i>Office National d'Études et de Recherches Aéronautiques</i> (French Aeronautics and Space Research Center)
RF	radio frequency
RLV	reusable launch vehicle
RMS	root mean square
RP-1	Rocket Propellant 1 (standard kerosene rocket fuel, MIL-P-25576)
RPV	remotely piloted vehicle
SA	Spaceport America
s	second
Sc	stratocumulus
sec	second
SRB	solid rocket booster
St	stratus
STP	standard temperature and pressure
TOA	time of arrival
UCAR	University Corporation for Atmospheric Research
UHF	Ultra High Frequency (300–3000 MHz; 1 m – 10 cm)
USAF	United States Air Force
UT	Universal Time
VAFB	Vandenberg Air Force Base

VAHIRR	volume-averaged, height-integrated radar reflectivity
VHF	very high frequency
VTVL	vertical takeoff vertical landing
WSMR	White Sands Missile Range
WSR-88D	Weather Surveillance Radar-1988 Doppler
WTLS	West Texas Launch Site
XMLA	Extensible Markup Language for Analysis



## 6. References

- Aleksandrov, N. L., E. M. Bazelyan, and Yu P. Raizer. "Initiation and Development of First Lightning Leader: The Effects of Coronae and Position of Lightning Origin." *Atmospheric Research* 76 (2005): 307–329, doi:10.1016/j.atmosres.2004.11.007.
- Avila, E. E., C. P. R. Saunders, H. Bax-Norman, and N. E. Castellano. "Charge Sign Reversal in Ice Particle-graupel Collisions." *Geophys. Res. Lett.* 32 (2005): L01801, doi:10.1029/2004GL020761.
- Bailey, J. C., and R. V. Anderson. *Experimental Calibration of a Vector Electric Field Meter Measurement System on an Aircraft*. Memorandum Report 5900, Naval Research Laboratory, Washington, D.C., March 13, 1987.
- Baker, M. B., A. M. Blyth, H. J. Christian, J. Latham, K. L. Miller, and A. M. Gadian. *Atmos. Res.* 51 (1999): 221–236.
- Baker, M. B., and J. G. Dash. "Charge Transfer in Thunderstorms and the Surface Melting of Ice." *J. Crystal Growth* 97 (1989): 770–776.
- Baker, M. B., E. R. Jayarantne, J. Latham, and C. P. Saunders. "The Influence of Diffusional Growth Rates on the Charge Transfer Accompanying Rebounding Collisions Between Ice Crystals and Soft Hailstones." *Quart. J. Roy. Meteorol. Soc.* 113 (1987): 1193–1215.
- Baker, M. B., H. J. Christian, and J. Latham. "A Computational Study of the Relationships Linking Lightning Frequency and Other Thundercloud Parameters." *Quart. J. Roy. Meteorol. Soc.* 121 (1995): 1525–1548.
- Barnes, A. A. Jr., and J. I. Metcalf. *Summary of the Triggered Lightning Workshop Held at Cape Canaveral AFS, Florida*. AFGL Technical Memorandum No. 151, 17–19 February 1988.
- Bateman, M. G., D. M. Mach, S. Lewis, J. E. Dye, E. Defer, C. A. Grainger, P. T. Willis, H. J. Christian, and F. J. Merceret. "Comparison of in Situ Electric Field and Radar Derived Parameters for Stratiform Clouds in Central Florida." In *Proceedings of the 12th International Conference on Atmospheric Electricity*, Versailles, France, International Commission on Atmospheric Electricity, 9–13 June 2003.
- Bazelyan, E. M., and Yu P. Raizer. *Lightning Physics and Lightning Protection*. Bristol: Institute of Physics Publishing, 2000. 325 pp.
- Bazelyan, E. M., and Yu P. Raizer. *Spark Discharge*. Boca Raton: CRC Press, 1998. 294 pp.
- Bazelyan, E. M., N. L. Aleksandrov, Yu P. Raizer, and A. M. Konchakov. "The Effect of Air Density on Atmospheric Electric Fields Required for Lightning Initiation from a Long Airborne Object." *Atmospheric Research* 86 (2007): 126–138, doi:10.1016/j.atmosres.2007.04.001.
- Bernstein, B. C., and C. LeBot. "An Inferred Climatology of Icing Conditions Aloft, Including Supercooled Large Drops. Part II: Europe, Asia and the Globe." *J. Meteorol. Clim.* 48 (2009): 1503–1526.
- Bernstein, B. C., C. A. Wolff, and F. McDonough. "An Inferred Climatology of Icing Conditions Aloft, Including Supercooled Large Drops. Part I: Canada and the Continental United States." *J. Appl. Met. and Clim.* 46 (2007): 1857–1877.

- Bernstein, B. C., F. McDonough, M. K. Politovich, B. G. Brown, T. P. Ratvasky, D. R. Miller, C. A. Wolff, and G. Cumming. "Current Icing Potential: Algorithm Development and Comparison with Aircraft Observations." *J. Appl. Met.* 44 (2005): 969–985.
- Bernstein, B. C., T. A. Omeron, F. McDonough, and M. K. Polotovich. "The Relationship Between Aircraft Icing and Synoptic-Scale Weather Conditions." *Weather and Forecasting* 12 (1997): 742–762.
- Bernstein, B. C., T. A. Omeron, M. K. Politovich, and F. McDonough. "Surface Weather Features Associated with Freezing Precipitation and Severe In-flight Aircraft Icing." *Atmos. Res.* 46 (1998): 57–74.
- Black, R., and J. Hallett. "The Mystery of Cloud Electrification." *American Scientist* 86 (6) (Nov–Dec 1998).
- Boccippio, D. J., D. J. Heckman, and S. J. Goodman. "A Diagnostic Analysis of the Kennedy Space Center LDAR Network 1. Data Characteristics." *J. Geophys. Res.* 106 (D5) (2001a): 4769–4786.
- Boccippio, D. J., D. J. Heckman, and S. J. Goodman. "A Diagnostic Analysis of the Kennedy Space Center LDAR Network 2. Cross-sensor Studies." *J. Geophys. Res.* 106 (D5) (2001b): 4787–4796.
- Bondiou, A., and I. Gallimberti. "Theoretical Modeling of the Development of Positive Sparks in Long Gaps." *J. Phys. D* 27 (1994): 1252–1266.
- Boulay, J. L., J. P. Moreau, A. Asselineau, and P. L. Rustan. "Analysis of Recent In-flight Lightning Measurements on Different Aircraft." Paper presented at the Aerospace and Ground Conference on Lightning and Static Electricity, Oklahoma City, April 19–22, 1988.
- Broc, A., P. Lalande, E. Montreui, J-P Moreau, A. Delannoy, A. Larsson, and P. Laroche. "A Lightning Swept Stroke Model: A Valuable Tool to Investigate the Lightning Strike to Aircraft." *Aerospace Science and Technology* 10 no. 8 (2006): 700–708. doi:10.1016/j.ast.2005.10.008
- Brook, M., C. R. Holmes, and C. B. Moore. "Lightning and Rockets: Some Implications of the Apollo 12 Lightning Event." *Naval Research Reviews* 23(4) (1970): 1–17.
- Brook, M., G. Armstrong, R. P. H. Winder, B. Vonnegut, and C. B. Moore. "Artificial Initiation of Lightning Discharges." *J. Geophys. Res.* 66 (1961): 3967–3969.
- Brooks, I. M., and C. P. R. Saunders. "Thunderstorm Charging: Laboratory Experiments Clarified." *Atmos. Res.* 39 (1995): 263–273.
- Brown, K. A., P. R. Krehbiel, C. B. Moore, and G. N. Sargent. "Electrical Screening Layers Around Charged Clouds." *J. Geophys. Res.* 76 (1971): 2825–2835.
- Byrne, G. J., A. A. Few, and M. E. Weber. "Altitude Thickness and Charge Concentration of Charge Regions of Four Thunderstorms During TRIP 81, Based on in Situ Balloon Electric Field Measurements." *Geophys. Res. Lett.* 10 (1983): 39–42.
- Byrne, G. J., A. A. Few, and M. F. Stewart. "Electric Field Measurements Within a Severe Thunderstorm Anvil." *J. Geophys. Res.* 94 (1989): 6297–6307.
- Christian, H. J., V. Mazur, B. D. Fisher, L. H. Ruhnke, K. Crouch, and R. P. Perala. "The Atlas/Centaur Lightning Strike Incident." *J. Geophys. Res.* 94 (D11) 13 (1989): 169–13,177.



- Clothiaux, E. E., T. P. Ackerman, G. G. Mace, K. P. Moran, R. T. Marchand, M. A. Miller, and B. E. Martner. "Objective Determination of Cloud Heights and Radar Reflectivities Using a Combination of Active Remote Sensors at the ARM CART Sites." *J. Applied Meteorology* 39 (May 2000): 645–665.
- Cohen, I. Bernard. "The Kite, the Sentry Box, and the Lightning Rod." Chap. 6 in *Benjamin Franklin's Science*. Cambridge: Harvard Univ. Press, 1990.
- Cummins, K. L., and M. J. Murphy. "An Overview of Lightning Locating Systems: History, Techniques, and Data Uses, with an In-depth Look at the U.S. NLDN." *IEEE Trans. Electromagn. Compat.* 51 (2009): 499–518.
- Dash, J. G., A. W. Rempel, and J. S. Wettlaufer. "The Physics of Premelted Ice and Its Geophysical Consequences." *Rev. Mod. Physics* 78 (2006): 1–47.
- Dash, J. G., B. L. Mason, and J. S. Wettlaufer. "Theory of Charge and Mass Transfer in Ice-Ice Collisions." *J. Geophys. Res.* 106, (D17) (2001): 20,395–20,402.
- Davydenko, S. S., E. A. Mareev, T. C. Marshall, and M. Stolzenburg. "On the Calculation of Electric Fields and Currents of Mesoscale Convective Systems." *J. Geophys. Res.* 109 (2004): D11103, doi:10.1029/2003JD003832.
- Dawson, G. A., and W. P. Winn. "A Model for Streamer Propagation." *Z. Phys.* 183 (1965): 159–171.
- Drake, J. C. "Electrification Accompanying the Melting of Ice Particles." *Quart. J. Roy. Meteorol. Soc.* 94 (1968): 176–191.
- Dye, J. E., and S. Lewis. *Summary of the Final Report to NASA KSC on the Airborne Field Mill Project*. (ABFM) Under NASA Grant NAG10-284, June 4, 2004a.
- Dye, J. E., and S. Lewis. *Final Report to NASA KSC on the Airborne Field Mill Project*. (ABFM) Under NASA Grant NAG10-284, June 4, 2004b.  
[http://box.mmm.ucar.edu/abfm/webpage/Reports/FinalReport\\_0604.pdf](http://box.mmm.ucar.edu/abfm/webpage/Reports/FinalReport_0604.pdf)
- Dye, J. E., J. J. Jones, A. J. Weinheimer, and W. P. Winn. "Observations Within Two Regions of Charge During Initial Thunderstorm Electrification." *Quart. J. Roy. Meteorol. Soc.* 114 (1988): 1271–1290.
- Dye, J. E., J. J. Jones, A. J. Weinheimer, and W. P. Winn. "Reply to Comments by C. B. Moore and B. Vonnegut: Further Analysis of Two Regions of Charge During Initial Thunderstorm Electrification." *Quart. J. Roy. Meteorol. Soc.* 118 (1992): 401–412.
- Dye, J. E., M. Bateman, D. Mach, H. J. Christian, C. A. Grainger, H. C. Koons, E. P. Krider, F. J. Merceret, and J. C. Willett. "The Scientific Basis for a Radar-based, Lightning Launch Commit Criteria for Anvil Clouds." Paper No. 8.7, presented at the 12th Conference on Aviation, Range, and Aerospace Meteorology (ARAM), Atlanta, Georgia, January 29–February 2, 2006.
- Edels, H., and E. Graffmann. "Time Constant Measurements of High Pressure Arc Columns." *Z. Phys.* 228 (1969): 396–415.
- Ely, B. L., and R. E. Orville. "High Percentage of Positive Lightning Along the USA West Coast." *Geophys. Res. Lett.* 32 (2005).

Eriksen, F. J., T. H. Rudolph, and R. A. Perala. "The Effects of the Exhaust Plume on the Lightning Triggering Conditions for Launch Vehicles." In International Aerospace and Ground Conference on Lightning and Static Electricity (NASA Conf. Pub. 3106, Vol. I), Cocoa Beach, FL, April 16–18, pp. 65-1 through 65-10, 1991.

Farrell, W. M., R. A. Goldberg, R. J. Blakeslee, M. D. Desch, J. G. Houser, J. D. Mitchell, C. L. Crosky, D. M. Mach, and J. C. Bailey. "ACES: A Unique Platform for Electrodynamic Studies of Upward Currents into the Middle Atmosphere." In *Proceedings of the 12th International Conference on Atmospheric Electricity*, Versailles, France, International Commission on Atmospheric Electricity, 9–13 June 2003.

Fisher, B. D., M. R. Phillips, and L. M. Maier. "Joint NASA/USAF Airborne Field Mill Program—Operation and Safety Considerations During Flights of a Lear 28 Airplane in Adverse Weather." AIAA-92-4093, paper presented at the 6th Biennial Flight Test Conference, Hilton Head I., SC, American Institute of Aeronautics and Astronautics, August 24–26, 1992.

Fisher, F. A., J. A. Plumer, and R. A. Perala. *Lightning Protection of Aircraft*. Pittsfield, MA: Lightning Technologies, Inc., 10 Downing Parkway, 1999. 499 pp.

Freund, J. E. *Modern Elementary Statistics*. 3rd ed. Englewood Cliffs, NJ: Prentice-Hall, Inc., 1967. pp. 432.

Gallimberti, I., G. Bacchiega, A. Bondiou-Clergerie, and P. Lalande. "Fundamental Processes in Long Air Gap Discharges." *C. R. Physique* 3 (2002): 1335–1359.

Gaviola, E., and F. A. Fuertes. "Hail Formation, Vertical Currents, and Icing of Aircraft." *J. Met.* 4 (1947): 116–120.

Grogan, M. J. "Report on the 2002–2003 U.S. NLDN System-wide Upgrade." *Vaisala news* 165 (2004): 4–8.

Harrison, H. T. *United Air Line Turbojet Experience with Electrical Discharges*. UAL Meteorological Circular, no. 57, 1965.

Hays, R. B., and R. G. Roble. "A Quasi-static Model of Atmospheric Electricity: 1. The Lower Atmosphere." *J. Geophys. Res.* 84 (1979): 3291–3305.

Heckscher, J. L. "Measured Electrical Parameters and the Effective Length of Rocket Exhaust Plumes." In *Proceedings, AFSC 1972 Science & Engineering Symposium*, Vol. II, AFSC-TR-72-005, 17–19 October 1972.

Heckscher, J. L., and R. P. Pagliarulo. *Measurement of Ionic Conductivity and Temperature in the Apollo 15 Plume*. AFCRL-TR-73-0124, 26 Feb. 1973.

Helsdon, J. H., S. Gattaleeradapan, R. D. Farley, and C. C. Waits. "An Examination of the Convective Charging Hypothesis: Charge Structure, Electric Fields, and Maxwell Currents." *J. Geophys. Res.* 107, (D22) (2002): ACL 9-1 to ACL 9-26. doi:10.1029/2001JD001495.

Helsdon, J. H., W. A. Wojcik, and R. D. Farley. "An Examination of Thunderstorm-charging Mechanisms Using a Two-dimensional Storm Electrification Model." *J. Geophys. Res.* 106, (D1) (2001): 1165–1192.

Holle, R. L., M. Murphy, and R. E. Lopez. "Distances and Times Between Cloud-to-Ground Flashes in a Storm." Paper 103-79KMI, presented at the International Conference on Lightning and Static Electricity, Blackpool, U.K., September 2003.

Holle, R. L., R. E. López, and C. Zimmermann. "Updated Recommendations for Lightning Safety—1998." *Bull. Am. Meteorol. Soc.* 80 (1999): 2035–2041.

Holzer, R. E., and D. S. Saxon. "Distribution of Electrical Conduction Currents in the Vicinity of Thunderstorms." *J. Geophys. Res.* 57 (1952): 207–216.

Idone, V. P. "The Luminous Development of Florida Triggered Lightning." *Res. Lett. Atmos. Electr.* 12 (1992): 23–28.

Idone, V. P., and R. E. Orville. "Channel Tortuosity Variations in Florida Triggered Lightning." *Geophys. Res. Lett.* 15 (1988): 645–648.

Imyanitov, I. M., Ye V. Chubarina, and Ya M. Shvarts. *Electricity of Clouds*. NASA Technical Translation. NASA TT F-718, 122 pp, February 1972.

Jacobson, E. A., and E. P. Krider. "Electrostatic Field Changes Produced by Florida Lightning." *J. Atmos. Sci.* 33 (1976): 103–117.

Jayaratne, E. R., C. P. R. Saunders, and J. Hallett. "Laboratory Studies of the Charging of Soft Hail During Ice Crystal Interactions." *Quart. J. Roy. Meteorol. Soc.* 109 (1983): 609–630.

Jones, J. J., W. P. Winn, and F. Han. "Electric Field Measurements with an Airplane: Problems Caused by Emitted Charge." *J. Geophys. Res.* 98 (1993): 5235–5244.

Kasemir, H. W. "The Thunderstorm as a Generator in a Global Electric Circuit" (in German). *Z. Geophys.* 25 (1959): 33–64.

King, L. A. *The Voltage Gradient in the Free-burning Arc in Air or Nitrogen*. British Electrical and Allied Industries Research Association Report G/XT172. Surrey, England: Leatherhead, 1961.

Koshak, W. J., and E. P. Krider. "Analysis of Lightning Field Changes During Active Florida Thunderstorms." *J. Geophys. Res.* 94 (1989): 1165–1186.

Koshak, W. J., D. M. Mach, H. J. Christian, and M. F. Stewart. Forthcoming. "A Mathematical Method for Retrieving Storm Electric Fields from Aircraft Field Mill Data." *J. Oceanic and Atmosph. Tech.* (2005): in preparation.

Koshak, W. J., J. C. Bailey, H. J. Christian, and D. M. Mach. "Aircraft Electric Field Measurements: Calibration and Ambient Field Retrieval." *J. Geophys. Res.* 99 (1994): 22,781–22,792.

Kositsky, J., K. L. Giori, R. A. Maffione, D. H. Cronin, J. E. Nanevicz, and R. Harris-Hobbs. *Airborne Field Mill (ABFM) System Calibration Report*. PIIN No. F04701-90-C-0023, The Aerospace Corporation, El Segundo, CA, January 1991.

Krehbiel, P. R. "The Electrical Structure of Thunderstorms." Chap. 8 in *The Earth's Electrical Environment*. Washington, DC: National Academy Press, 1986.

Krehbiel, P. R., M. Brook, and R. A. McCrory. "An Analysis of the Charge Structure of Lightning Discharges to Ground." *J. Geophys. Res.* 84 (1979): 2432–2456.

- Krehbiel, P. R., R. J. Thomas, W. Rison, T. Hamlin, J. Harlin, and M. Davis. "GPS-based Mapping System Reveals Lightning Inside Storms." *Eos Trans. AGU* 81(3), 21, 2000.
- Krehbiel, P. R., R. J. Thomas, W. Rison, T. Hamlin, J. Harlin, and M. Davis. "Lightning Mapping Observations in Central Oklahoma." *Eos* (January 2000): 21–25.
- Krider, E. P. "Electric Field Changes and the Cloud Electrical Structure." *J. Geophys. Res.* 94 (1989): 13145–13149.
- Krider, E. P., H. C. Koons, R. L. Walterscheid, W. D. Rust, and J. C. Willett. *Natural and Triggered Lightning Launch Commit Criteria (LCC)*, SMC-TR-99-20, Aerospace Report TR-99(1413)-1, Air Force Materiel Command, Space and Missile Systems Center, Los Angeles, CA, 15 January 1999.
- Krider, E. P., H. J. Christian, J. E. Dye, H. C. Koons, J. Madura, F. Merceret, W. D. Rust, R. L. Walterscheid, and J. C. Willett. "Natural and Triggered Lightning Launch Commit Criteria." Paper No. 8.3, presented at the 12th Conference on Aviation, Range, and Aerospace Meteorology (ARAM), Atlanta, Georgia, January 29–February 2, 2006.
- Krider, E. P., J. C. Willett, G. S. Peng, F. S. Simmons, G. W. Law, and R. W. Seibold. *Triggered Lightning Risk Assessment for Reusable Launch Vehicles at the Southwest Regional and Oklahoma Spaceports*, Aerospace Report No. ATR-2006(5195)-130, Volpe National Transportation Systems Center U.S. Department of Transportation Contract No. DTRS57-99-D-00062, January 2006.
- Krider, E. P., R. C. Noggle, and M. A. Uman. "A Gated, Wide-band Magnetic Direction Finder for Lightning Return Strokes." *J. Appl. Meteor.* 15 (1976): 301–306.
- Krider, E. P., R. C. Noggle, M. A. Uman, and R. E. Orville. "Lightning and Apollo 17/Saturn V Exhaust Plume." *J. Spacecraft* 11(2) (1974): 72–75.
- Labaree, L. W., et al., eds. *The Papers of Benjamin Franklin*. Yale University Press, Vol. 5, 1962. p. 69.
- Lago, F., J. J. Gonzalez, P. Freton, F. Uhlig, N. Lucius, and G. P. Piau. "A Numerical Modelling of an Electric Arc and Its Interaction with the Anode: Part III. Application to the Interaction of a Lightning Strike and an Aircraft in Flight." *J. Phys. D: Appl. Phys.* 39 (2006): 2294–2310.
- Lalande, P., A. Bondiou-Clergerie, G. Bacchiega, and I. Gallimberti. "Observations and Modeling of Lightning Leaders." *C. R. Physique* 3 (2002): 1375–1392.
- Lalande, P., A. Bondiou-Clergerie, P. Laroche, A. Eybert-Bérard, J. P. Berlandis, B. Bador, A. Bonamy, M. A. Uman, and V. A. Rakov. "Leader Properties Determined with Triggered Lightning Techniques." *J. Geophys. Res.* 103 (1998): 14,109–14,115.
- Lalande, P., and A. Bondiou-Clergerie. *Collection and Analysis of Available In-flight Measurement of Lightning Strikes to Aircraft*. Report AI-95-SC.204-RE/210-D2.1, ONERA (France) Transport Research and Technological Development Program DG VII, 24 February 1997.
- Laroche, P., A. Bondiou, A. Eybert-Bérard, L. Barret, J. P. Berlandis, G. Terrier, and W. Jafferis. "Lightning Flashes Triggered in Altitude by the Rocket and Wire Technique." Paper presented at the International Conference on Lightning and Static Electricity, University of Bath, UK, September 26–28, 1989b.

- Laroche, P., A. Delannoy, and H. Le Court de Béru. "Electrostatic Field Conditions on an Aircraft Stricken by Lightning." Paper presented at the International Conference on Lightning and Static Electricity, University of Bath, UK, September 26–28, 1989a.
- Laroche, P., A. Eybert-Bérard, L. Barret, and J. P. Berlandis. "Observations of Preliminary Discharges Initiating Flashes Triggered by the Rocket and Wire Technique." Paper presented at the 8th International Conference on Atmospheric Electricity, Uppsala, Sweden, 13–16 June 1988.
- Larsson, A. "The Interaction Between a Lightning Flash and an Aircraft in Flight." *Comptes Rendus Physique* 3, issue 10 (2002): 1423–1444.
- Larsson, A., A. Delannoy, and P. Lalande. "Voltage Drop Along a Lightning Channel During Strikes to Aircraft." *Atmospheric Research* 76, issues 1–4 (July–August 2005): 377–385.  
doi:10.1016/j.atmosres.2004.11.033
- Larsson, A., P. Lalande, A. Bondiou-Clergerie, and A. Delannoy. "The Lightning Swept Stroke Along an Aircraft in Flight. Part I: Thermodynamic and Electric Properties of Lightning Arc Channels." *J. Phys. D: Appl. Phys.* 33 (2000): 1866–1875.
- Larsson, A., P. Lalande, and A. Bondiou-Clergerie. "The Lightning Swept Stroke Along an Aircraft in Flight. Part II: Numerical Simulations of the Complete Process." *J. Phys. D: Appl. Phys.* 33 (2000): 1876–1883.
- Latham, D. "Lightning Flashes from a Prescribed Fire-induced Cloud." *J. Geophys. Res.* 96 (D9) (1991): 17,151–17,157.
- Latham, D. J. "Anode Column Behavior of Long Vertical Air Arcs at Atmospheric Pressure." *IEEE Trans. Plasma Sci.* PS-14 (1986): 220–227.
- Latham, J. "The Electrification of Thunderstorms." *Quart. J. Roy. Meteorol. Soc.* 107 (1981): 277–298.
- Launch Vehicle Lightning/Atmospheric Electrical Constraints Post-Atlas/Centaur 67 Incident.* TOR-0088(3441-45)-2, The Aerospace Corporation, El Segundo, CA, 31 August 1988.
- Lennon, C. L., and H. A. Poehler. "Lightning Detection and Ranging." *Aeronautics and Astronautics* (March 1982): 29–31.
- Lightning Review Committee. *Launch Vehicle Lightning/Atmospheric Electrical Constraints Post-Atlas/Centaur 67 Incident.* TOR-0088(3441-45)-2, The Aerospace Corporation, El Segundo, CA, 31 August 1988.
- MacGorman, D. R., and W. D. Rust. *The Electrical Nature of Storms.* Oxford University Press, 1998. 422 pp.
- Mach, D. *Reanalysis of the ABFM-I Dataset Final Report*, Marshall Space Flight Center Final Report for Interagency Agreement No. DTRT57-08-X-70053 between Volpe Center, the FAA Office of the Associate, 2009.
- Mach, D. M., and W. J. Koshak. "General Matrix Inversion Technique for the Calibration of Electric Field Sensor Arrays on Aircraft Platforms." In *Proceedings of the 12th International Conference on Atmospheric Electricity*, Versailles, France, International Commission on Atmospheric Electricity, 9–13 June 2003.

- Maier, L. M., and E. P. Krider. "The Charges That Are Deposited by Cloud-to-ground Lightning in Florida." *J. Geophys. Res.* 91 (1986): 13,275–13,289.
- Maier, L., C. Lennon, T. Britt, and S. Schaefer. "LDAR System Performance and Analysis." In *Proceedings of the International Conference on Cloud Physics*, Am. Met. Soc., Boston, MA, Dallas, TX, Jan. 1995.
- Marshall, T. Comment on "'Spider' Lightning in Intracloud and Positive Cloud-to-ground Flashes" by Vladislav Mazur, Xuan-Min Shao, and Paul R. Krehbiel. *J. Geophys. Res.* 105 (D6) (2000): 7397–7399.
- Marshall, T. C., and B. Lin. "Electricity in Dying Thunderstorms." *J. Geophys. Res.* 97 (D9) (1992): 9913–9918.
- Marshall, T. C., and W. D. Rust. "Two Types of Vertical Electrical Structures in Stratiform Precipitation Regions of Mesoscale Convective Regions." *Bull. Am. Meteorol. Soc.* 78 (11) (1993): 2159–2170.
- Marshall, T. C., M. Stolzenburg, W. D. Rust, E. R. Williams, and R. Boldi. "Positive Charge in the Stratiform Cloud of a Mesoscale Convective System." *J. Geophys. Res.* 106 (D1) (2001): 1157–1163.
- Marshall, T. C., W. D. Rust, W. P. Winn, and K. E. Gilbert. "Electrical Structure in Two Thunderstorm Anvil Clouds." *J. Geophys. Res.* 94 (D2) (1989): 2171–2181.
- Mason, B. J. "The Electrification of Clouds." Chap. 9 in *The Physics of Clouds*. 2nd ed. Oxford: Clarendon, 1971.
- Mason, B. L., and J. G. Dash. "Charge and Mass Transfer in Ice-ice Collisions: Experimental Observations of a Mechanism in Thunderstorm Electrification." *J. Geophys. Res.* 105, (D8) (2000): 10,185–10,192.
- Mason, J. "The Generation of Electric Charges and Fields in Thunderstorms." *Proc. Roy. Soc. London* A415 (1988): 303–315.
- Mazur, V. "A Physical Model of Lightning Initiation on Aircraft in Thunderstorms." *J. Geophys. Res.* 94 (1989b): 3326–3340.
- Mazur, V., B. D. Fisher, and J. C. Gerlach. "Lightning Strikes to an Airplane in a Thunderstorm." *J. Aircraft* 21 (1984): 607–611.
- Mazur, V., X-M. Shao, and P. R. Krehbiel. "'Spider' Lightning in Intracloud and Positive Cloud-to-ground Flashes." *J. Geophys. Res.* 103 (1988): 19,811–19,822.
- McNamara, T. M. "The Horizontal Extent of Cloud-to-ground Lightning over the Kennedy Space Center." M.S. thesis, Air Force Institute of Technology, Wright-Patterson AFB, Ohio, 2002. AFIT/GM/ENP/02M-06.
- Merceret, F. J., J. G. Ward, D. M. Mach, M. G. Bateman, and J. E. Dye. "On the Magnitude of the Electric Field Near Thunderstorm-associated Clouds." *J. Appl. Meteorol., Clim.*, 47 (2008): 240–248.
- Mo, Q., A. E. Ebner, P. Fleischhacker, and W. P. Winn. "Electric Field Measurements with an Airplane: A Solution to Problems Caused by Emitted Charge." *J. Geophys. Res.* 103 (1998): 17,163–17,173.

Moore, C. B., and B. Vonnegut. "Comments on 'Observations of Two Regions of Charge During Initial Thunderstorm Electrification' by J. E. Dye, J. J. Jones, A. J. Weinheimer, and W. P. Winn (July 1988, 114, 1271–1290)." *Quart. J. Roy. Meteorol. Soc.* 118 (1992): 395–400.

Moore, C. B., G. D. Aulich, and W. Rison. "Measurements of Lightning Rod Responses to Nearby Strikes." *Geophys. Res. Lett.* 27 (2000): 1487–1490.

Moreau, J.-P., J.-C. Alliot, and V. Mazur. "Aircraft Lightning Initiation and Interception From in Situ Electric Measurements and Fast Video Observations." *J. Geophys. Res.* 97(D14) (1992): 15,903–15,912.

Morse, P. M., and H. Feshbach. *Methods of Theoretical Physics*, Vol. 2, p. 1284. New York, NY: McGraw-Hill, 1953.

Murphy, M. J. "When Flash Algorithms Go Bad." 19th International Lightning Detection Conference, Tucson, AZ, 24–25 April 2006.

Murphy, M. J., and R. L. Holle. "A Warning Method for Cloud-to-ground Lightning Based on Total Lightning and Radar Information." Preprints, paper LDM-36, 2005. International Conference on Lightning and Static Electricity, Seattle, Washington, 19–23 September 2005.

Murphy, M. J., E. P. Krider, and M. W. Maier. "Lightning Charge Analyses in Small Convection and Precipitation Experiment (CaPE) Storms." *J. Geophys. Res.* 101 (D23) (1996): 29,615–29,626.

Nanevicz, J. E., and G. R. Hilbers. *Environment Titan Vehicle Electrostatic*. Air Force Avionics Laboratory, AFAL-TR-73-170, Wright-Patterson AFB, Ohio, 1973.

NAS. *The Earth's Electrical Environment*. Washington, D.C.: National Academy Press, 1986.

Naud, C. M., J-P Muller, and E. E. Clothiaux. "Comparison Between Active Sensor and Radiosonde Cloud Boundaries over the ARM Southern Great Plains Site." *J. Geophys. Res.* 108(D4) (2003): 4140.

Naud, C. M., J-P Muller, M. Haeffelin, Y. Morille, and A. Delaval. "Assessment of MISR and MODIS Cloud Top Heights Through Inter-comparison with a Back-scattering Lidar at SIRTa." *Geophys. Res. Lett.* 31 (2004): L04114.

Nelson, L. A. "Synthesis of 3-dimensional Lightning Data and Weather Radar Data to Determine the Distance that Naturally Occurring Lightning Travels from Thunderstorms." M.S. thesis, Air Force Institute of Technology, Wright-Patterson AFB, Ohio, (2002): AFIT/GM/ENP/02M-07.

Newman, M. M. "Lightning Discharge Channel Characteristics and Related Atmospherics." In *Recent Advances in Atmospheric Electricity* 475–484. Edited by L. G. Smith. New York: Pergamon Press, 1958.

Newman, M. M., J. R. Stahmann, J. D. Robb, E. A. Lewis, S. G. Martin, and S. V. Zinn. "Triggered Lightning Strokes at Very Close Range." *J. Geophys. Res.* 72 (1967): 4761–4764.

Orville R. E. "Development of the National Lightning Detection Network." *Bull. Amer. Meteor. Soc.* 89 (2008): 180–190.

Panel on Meteorological Support for Space Operations. *Meteorological Support for Space Operations, Review and Recommendations*. Washington, DC: National Academy Press, 1988. 77 pp.

Peng, G. S. "An Analysis of Lightning Risk and Convective Cloud Cover for Two Proposed Commercial Spaceport Sites." Paper 8.10, presented at the 12th Conference on Aviation, Range, and Aerospace Meteorology (ARAM), Atlanta, GA, February 1, 2006.

Perala, R. A., T. H. Rudolph, D. A. Steffen, G. J. Rigden, and H. S. Weigel IV. *A Model for Predicting the Triggering of Lightning by Launch Vehicles*. Denver, CO: Electromagnetic Applications, Inc., 1994. EMA-93-R-035.

Pergament, H. S., T. R. Hvidock, and M. A. Najarian. "Electrical Conductivity of Solid Propellant Rocket Plumes." PST TR-20, Propulsion Science and Technology, Inc., Princeton, NJ, 1993 (included as Appendix G in Perala et al. [1994]).

Phelps, C. T., and R. F. Griffiths. "Dependence of Positive Corona Streamer Propagation on Air Pressure and Water Vapor Content." *J. Appl. Phys.* 47 (1976): 2929–2934.

Politovich, M. K. "Aircraft Icing Caused by Large Super-Cooled Droplets." *J. Appl. Met.* 28 (1989): 856–868.

Proctor, D. E. "A Hyperbolic System for Obtaining VHF Radio Pictures of Lightning." *J. Geophys. Res.* 76 (1971): 1478–1489.

Raizer, Yu P. *Gas Discharge Physics*. Berlin: Springer-Verlag, 1991. 449 pp.

Rakov, V. A., and M. A. Uman. *Lightning Physics and Effects*. Cambridge University Press, 2003. 687 pp.

Reynolds, S. E., M. Brook, and M. F. Gourley. "Thunderstorm Charge Separation." *J. Meteorol.* 14 (1957): 426–436.

Rison, W., R. J. Thomas, P. R. Krehbiel, T. Hamlin, and J. Harlin. "A GPS-based Three-dimensional Lightning Mapping System: Initial Observations in Central New Mexico." *Geophys. Res. Lett.* 26 (1999): 3573–3576.

Roeder, W. P., J. E. Sardonía, S. C. Jacobs, M. S. Hinson, A. A. Guiffrida, and J. T. Madura. "Lightning Launch Commit Criteria at the Eastern Range/Kennedy Space Center." Paper presented at the 37th AIAA Aerospace Sciences Meeting and Exhibit, January 11–14, 1999. AIAA-99-0890.

Rust, W. D., and D. R. MacGorman. "Possibly Inverted-polarity Electrical Structures in Thunderstorms." *Geophys. Res. Lett.* 29 (12) (2002): 12-1 to 12-4.

Rust, W. D., and R. J. Trapp. "Initial Balloon Soundings of the Electric Field in Winter Nimbostratus Clouds in the USA." *Geophys. Res. Lett.* 29 (20) (2002): 20-1 to 20-4.

Sand, W. R., W. A. Cooper, M. K. Politovich, and D. L. Veal. "Icing Conditions Encountered by a Research Aircraft." *J. Climate Appl. Meteor.* 23 (1984): 1427–1440.

Saunders, C. P. R. "Charge Separation Mechanisms in Clouds." *Sp. Sci. Rev.* 137 (2008): 335–353.

Saunders, C. P. R. "Thunderstorm Electrification." *Weather* 43 (1988): 318–324.

Saunders, C. P. R., H. Bax-Norman, C. Emersic, E. E. Avila, and N. E. Castellano. "Laboratory Studies of the Effect of Cloud Conditions on Graupel/crystal Charge Transfer in Thunderstorm Electrification." *Q. J. Roy. Meteorol. Soc.* 132 (2006): 2653–2673.



- Saunders, C. P. R., W. D. Keith, and R. P. Mitzeva. "The Effect of Liquid Water on Thunderstorm Charging." *J. Geophys. Res.* 96 (1991): 11007–11017.
- Schaub, W. R. Jr. *Lightning Climatology for Holloman AFB, New Mexico*. Air Force Combat Climatology Center Report AFCCC/TN-96/005. March 1996b.
- Schaub, W. R. Jr. *Nationwide Lightning Climatology*. Air Force Combat Climatology Center Report. AFCCC/TN-96/002. Feb. 1996a.
- Schonland, B. F. J. *The Flight of Thunderbolts*. Oxford: Clarendon, 1950. p. 22.
- Schuur, T. J., B. F. Smull, W. D. Rust, and T. C. Marshall. "Electrical and Kinematic Structure of the Stratiform Precipitation Region Trailing an Oklahoma Squall Line." *J. Atmos. Sci.* 48 (6) (1991): 825–842.
- Scott, R. D., P. R. Krehbiel, and W. Rison. "The Use of Simultaneous Horizontal and Vertical Transmissions for Dual-polarization Radar Meteorological Observations." *J. Atmos. Ocean. Tech.* 18 (2001): 629–648.
- Shepherd, T. R., W. D. Rust, and T. C. Marshall. "Electric Fields and Charges Near 0°C in Stratiform Clouds." *Mon. Wea. Rev.* 124 (1996): 919–938.
- Shupe, M. D., J. S. Daniel, G. De Boer, E. W. Elantorta, P. Kollias, C. N. Long, E. P. Luke, D. D. Turner, and J. Verlinde. "A Focus on Mixed-phase Clouds: The Status of Ground-based Observational Methods." *Bull. Am. Meteorol. Soc.* 89 (2008): 1549–1562.
- Simmons, F. S. *Rocket Exhaust Plume Phenomenology*. The Aerospace Press and American Institute of Aeronautics and Astronautics, ISBN 1-884989-08-X. 2000.
- Simpson, G. "Atmospheric Electricity During Disturbed Weather." *Geophysical Memoirs* No. 84, Vol. 4 (1949): Meteorological Office, London, 51 pp.
- Smythe, W. R. *Static and Dynamic Electricity*. 3rd ed. New York: McGraw-Hill Book Company, 1968. 623 pp.
- Standler, R. B., and W. P. Winn. "Effects of Coronae on Electric Fields Beneath Thunderstorms." *Quart. J. Roy. Meteorol. Soc.* 105 (1979): 285–302.
- Stolzenburg, M., and T. C. Marshall. "Two Simultaneous Charge Structures in Thunderstorm Convection." *J. Geophys. Res.* 107, D18 (2002): ACL 5-1 – ACL 5-12.
- Stolzenburg, M., T. C. Marshall, and W. D. Rust. "Serial Soundings of Electric Field Through a Mesoscale Convective System." *J. Geophys. Res.* 106 (D12) (2001): 12371–12380.
- Stolzenburg, M., T. C. Marshall, W. D. Rust, and B. F. Smull. "Horizontal Distribution of Electrical and Meteorological Conditions across the Stratiform Region of a Mesoscale Convective System." *Mon. Wea. Rev.* 122 (1994): 1777–1797.
- Stolzenburg, M., W. D. Rust, B. F. Smull, and T. C. Marshall. "Electrical Structure in Thunderstorm Convective Regions: 1. Mesoscale Convective Systems." *J. Geophys. Res.* 103 (1998a): 14,059–14,078.

Stolzenburg, M., W. D. Rust, B. F. Smull, and T. C. Marshall. "Electrical Structure in Thunderstorm Convective Regions: 2. Isolated Storms." *J. Geophys. Res.* 103 (1998b): 14,079–14,096.

Stolzenburg, M., W. D. Rust, B. F. Smull, and T. C. Marshall. "Electrical Structure in Thunderstorm Convective Regions: 3. Synthesis." *J. Geophys. Res.* 103 (1998c): 14,097–14,108.

St. Privat D'Allier Group. "Artificially Triggered Lightning in France." Applications: possibilities, limitations paper presented at the 6th Symposium on Electromagnetic Compatibility, Zurich, 5–7 March 1985.

Szymanski, E. W., S. J. Szymanski, C. R. Holmes, and C. B. Moore. "An Observation of a Precipitation Echo Intensification Associated with Lightning." *J. Geophys. Res.* 85 (C4) (1980): 1951–1953.

Takahashi, T. "Riming Electrification as a Charge Generation Mechanism in Thunderstorms." *J. Atmos. Sci.* 35 (1978): 1536–1548.

Takahashi, T., and K. Miyawaki. "Reexamination of Riming Electrification in a Wind Tunnel." *J. Atmos. Sci.* 59 (2002): 1018–1025.

Terman, F. E. *Radio Engineers' Handbook*. New York: McGraw-Hill Book Company, 1019 pp., 1943.

Thomas, R. J., P. R. Krehbiel, W. Rison, S. J. Hunyady, W. P. Winn, T. Hamlin, and J. Harlin. "Accuracy of the Lightning Mapping Array." *J. Geophys. Res.* 109 (2004): (D14207, doi:10.1029/2004JD004549).

Thomas, R. J., P. R. Krehbiel, W. Rison, T. Hamlin, J. Harlin, and D. Shown. "Observations of VHF Source Powers Radiated by Lightning." *Geophys. Res. Lett.* 28 (2001): 143–146.

Titan Programs. *Launch Vehicle Lightning/atmospheric Electrical Constraints Post-Atlas/Centaur 67 Incident*. TOR-0088(3441-45)-2, The Aerospace Corporation, 1988.

Uman, M. A., *Electrical Breakdown in the Apollo 12/Saturn V First Stage Exhaust*. 70-9C8-HIVOL-R1, Westinghouse Research Lab., Pittsburgh, PA, 1970.

Uman, M. A. *The Lightning Discharge*. Orlando: Academic Press, 1987. 377 pp.

Uman, M. A. *The Art and Science of Lightning Protection*, Cambridge Univ. Press, 2008. 240 pp.

Uman, M. A., and E. P. Krider. "Naturally and Artificially Initiated Lightning." *Science* 246, (1989): 457–464.

Uman, M. A., and V. A. Rakov. "The Interaction of Lightning with Airborne Vehicles." *Prog. in Aerospace Sciences* 39 (2003): 61–81.

Vonnegut, B. "How the External Currents Flowing to a Thundercloud Influence its Electrification." *Ann. Geophysicae* 9 (1991): 34–36.

Vonnegut, B., D. J. Latham, C. B. Moore, and S. J. Hunyady. *J. Geophys. Res.* 100 (D3) (1995): 5037–5050.

Willett, J. C., and A. A. Barnes Jr. *Feasibility Analysis for Measuring Electric Field Aloft*. Unpublished report prepared for the Weather Integrated Product Team, Range Standardization and Automation Program, 2 June 2000.

Willett, J. C., D. A. Davis, and P. Laroche. "An Experimental Study of Positive Leaders Initiating Rocket-triggered Lightning." *Atmospheric Research* 51 (1999): 189–219.

Willett, J. C., E. P. Krider, G. S. Peng, F. S. Simmons, G. W. Law, R. W. Seibold, and K. Shelton-Mur. "Triggered Lightning Risk Assessment for Reusable Launch Vehicles at the Southwest Regional and Oklahoma Spaceports." Paper 8.9, presented at the 12th Conference on Aviation, Range, and Aerospace Meteorology (ARAM), Atlanta, Georgia, January 29 – February 2, 2006.

Williams, E. R. "The Electrification of Thunderstorms." *Scientific American* 259 (1988): 88–99.

Williams, E. R. "The Tripole Structure of Thunderstorms." *J. Geophys. Res.* 94 (1989): 13,151–13,167.

Williams, E. R., R. Zhang, and J. P. Rydock. "Mixed-phase Microphysics and Cloud Electrification." *J. Atmos. Sci.* 48 (1991): 2195–2203.

Wilson, C. T. R. "Investigations on Lightning Discharges and on the Electric Field of Thunderstorms." *Phil. Trans. Roy. Soc. London* A221 (1920): 73–115.

Winn, W. P. "Aircraft Measurement of Electric Field: Self Calibration." *J. Geophys. Res.* 98 (1993): 7351–7365.

Workman, E. J., and R. E. Holzer. *A Preliminary Investigation of the Electrical Structure of Thunderstorms*. NACA Tech. Note 850, National Advisory Committee for Aeronautics, Washington, DC, 1942.

Workman, E. J., and R. E. Holzer. "Quantities of Charge Transfers in Lightning Discharges." *Phys. Rev.* 55, 2nd ser. (1939): 598.

Zamiska, A., and P. Giese. *RTNeph AFCCC Climatic Database Users Handbook No. 1*. Air Force Combat Climatology Center Report USAFETAC/UH-86/001. Sept. 1986 (Revised Nov. 1996).

Ziegler, C. L., and D. R. MacGorman. "Observed Lightning Morphology Relative to Modeled Space Charge and Electric Field Distributions in a Tornadic Storm." *J. Atmos. Sci.* 51 (1994): 833–851.

Ziegler, C. L., D. R. MacGorman, J. E. Dye, and P. S. Ray. "A Model Evaluation of Noninductive Graupel-ice Charging in the Early Electrification of a Mountain Thunderstorm." *J. Geophys. Res.* 96 (1991): 12,833–12,855.



## Appendix A. Lightning Mapper Array Event Validation

NMIMT has developed excellent software, called “XLMA,” for the display and analysis of processed LMA data. This software plots the location and time of every computed LMA source point in plan view, in two vertical cross sections, and in time series. For example, Figure A-1 shows a large meso-scale convective complex (MCC) over Norman, OK. XLMA also contains its own “flash algorithm” and several other useful analysis features.

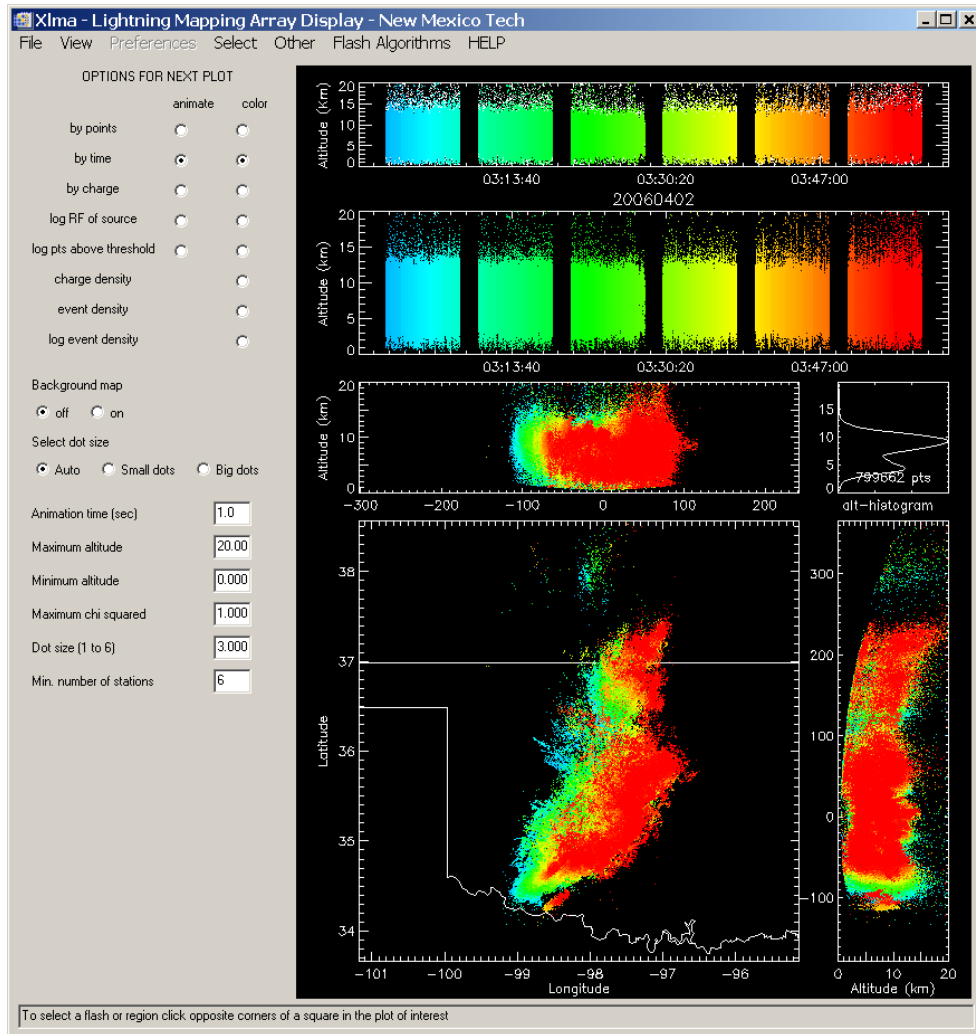


Figure A-1. XLMA display of a large MCC passing over Norman, OK.

Figure A-1 shows all source points (reduced chi-squared  $\leq 1.0$ ) within range of the Oklahoma LMA during the hour after 0300 UT on April 2, 2006 (20060402). The two upper strips are time series of source altitude. (The distinction between them will become evident in subsequent figures.) The lower left panel is a plan view, in this case showing all detected lightning. To its right is a latitude-altitude projection, and above it is a longitude-altitude projection. An altitude histogram is also included, showing the total number of sources plotted. Each source point is color-coded according to time within the hour in each panel. For unknown reasons this particular hour of data has 2-minute gaps every 10 minutes. (Here, latitude and longitude refer to distances in the longitudinal and latitudinal directions, respectively. Henceforward latitude and longitude may refer to either actual latitude or longitude or to distances in the latitudinal and longitudinal directions. Which convention is used will be obvious.)

## A.1 Lightning Event Validation

For short intervals during several individual storms over each spaceport, the present “lightning events” have been compared to sample plots and to lists of lightning “flashes” made using the XLMA software. We look first at lightning examples over the Oklahoma Spaceport. Figure A-2 shows a zoomed view of the MCC of Figure A-1, in which our 80×80 km square (NW and SE corners at [N. latitude (degrees), E. longitude (degrees)] = [35.66, -99.64] and [34.94, -98.76], respectively) lies in the upper left-hand corner of the plan view, occupying somewhat less than one-quarter of the plot. (The scale of the plot was chosen so as to include all of the stations of the UOK LMA array, although they are invisible beneath the numerous lightning locations in this plot. See Figure A-3 for another plot with identical scales but less lightning, allowing the stations to be seen clearly.)

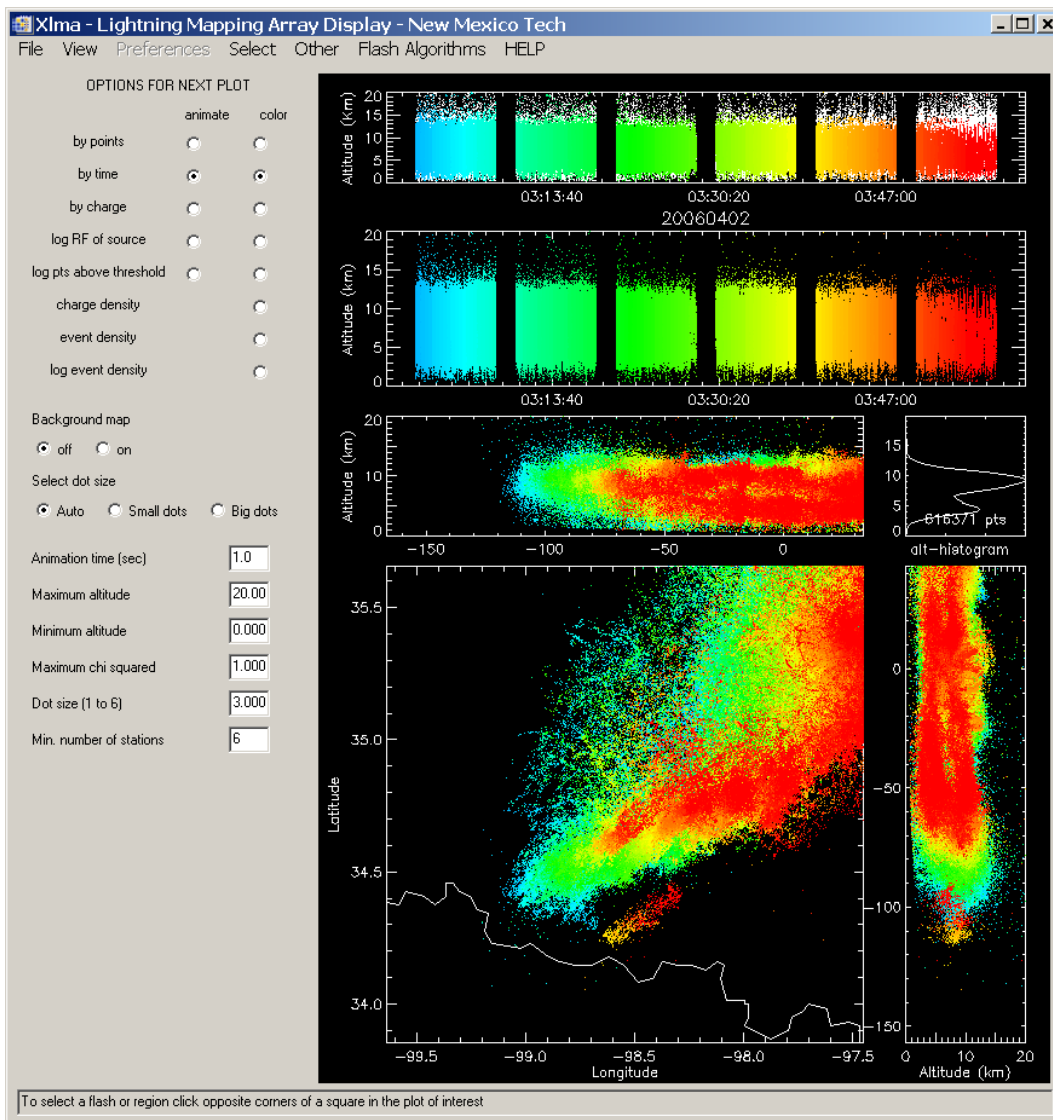


Figure A-2. Similar to Figure A-1 except zoomed in so that the Oklahoma Spaceport lies in the upper left-hand corner. Note here that some of the sources plotted in the upper time series are white, indicating that these points in the data file have been excluded by the reduced boundaries of the plan view.

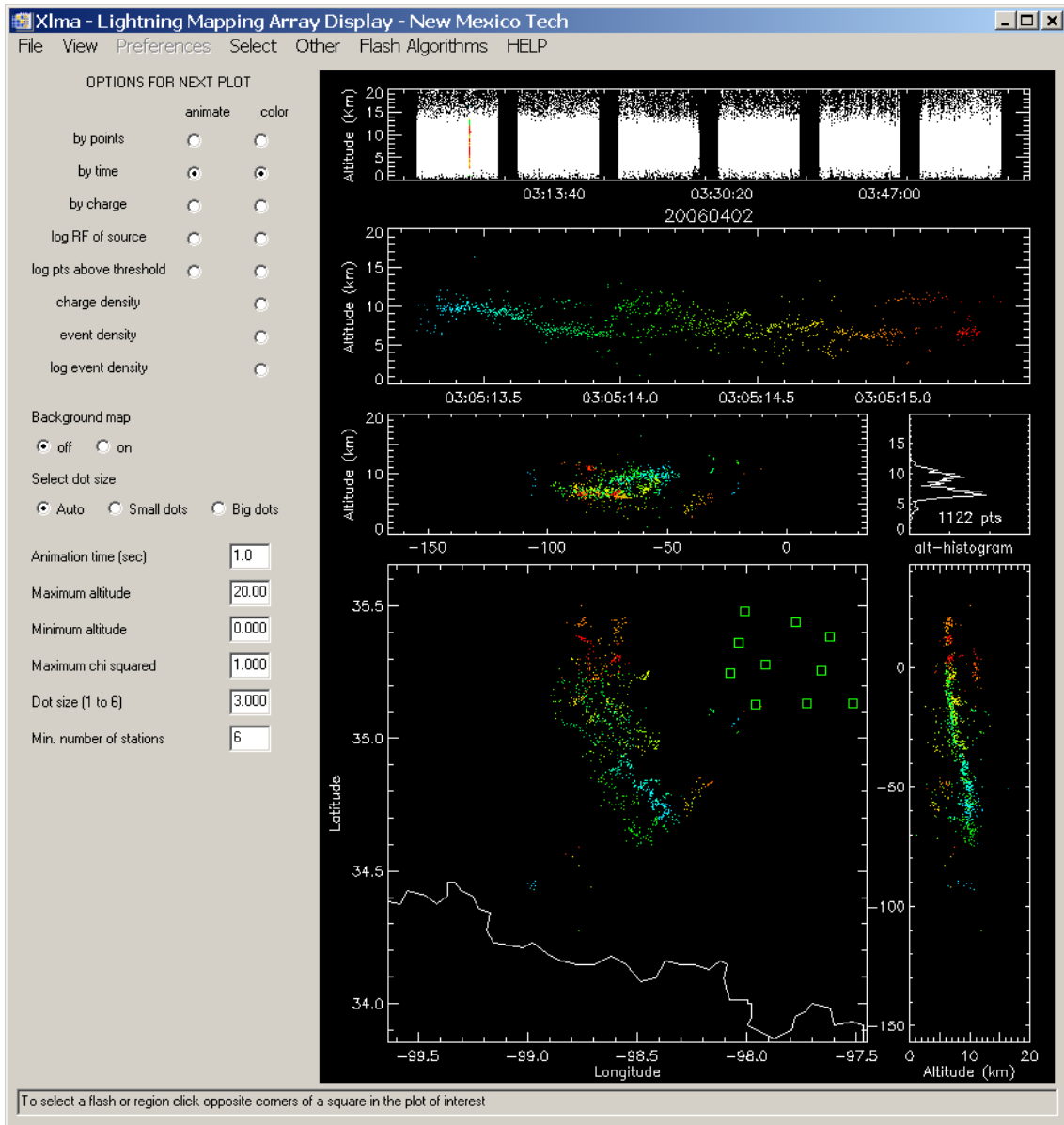


Figure A-3. Similar to Figure A-2 but with a much-reduced time window. The network station locations are now visible as green boxes in the upper right of the plan view. Note that the time interval of the plot is shown in color in the upper time series, points not plotted in the other panels being shown in white, and that the lower time series now shows an expanded view of the time interval of interest, with the color coding expanded accordingly.

Figure A-3 shows the same region as Figure A-2, but with a much-reduced time window that includes a single, large lightning flash that lasts about 2 s. This is an example of the very extensive discharges that can occur in the trailing stratiform region of an MCC. Although this flash is well outside the network proper, even extending into our 80×80 km area over the spaceport, the geometry of the flash appears to be rendered in considerable detail, and there still seems to be useful altitude information. (See also Figure A-6.) As shown in Figure A-4, the extremities of this flash entered two of our 40×40 km quadrants during the 4 s interval from 03:05:12 to 03:05:16, producing two credible “lightning events.”

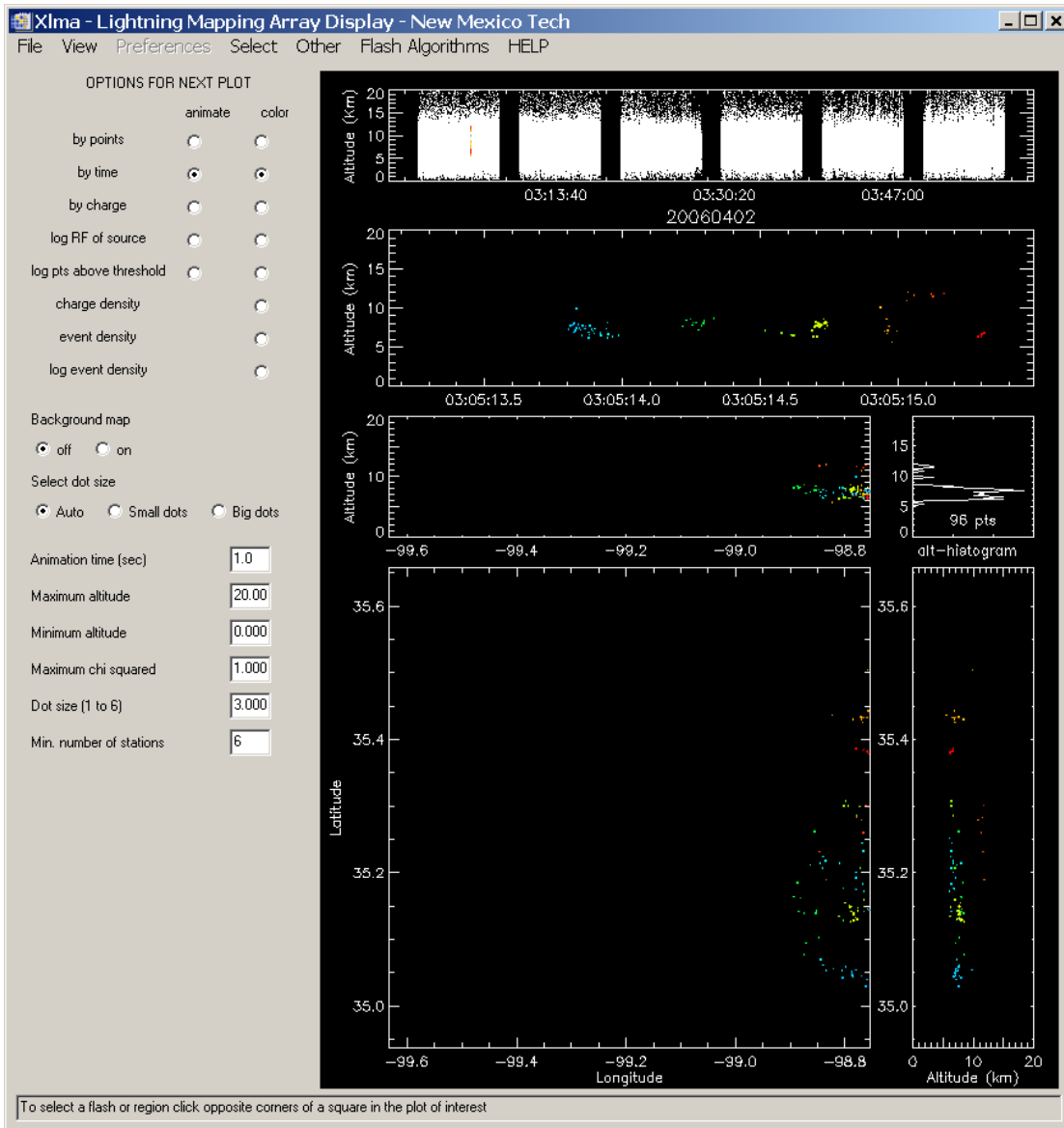


Figure A-4. Similar to Figure A-3, but with the spatial domain reduced further to encompass only our 80×80 km area over the spaceport.

During this hour we looked at how the number of the “lightning events” produced by such large flashes extending into the spaceport area depended on key detection parameters. For example, with the required number of sources equal to five (our chosen value) and a reduced-chi-squared threshold of 3.0, we found source points within our 80×80 km square during 25 four-second time intervals, producing a total of 19 lightning events (counting each 40×40 km quadrant separately but weeding out cases with fewer than five sources). Increasing the required number of sources to 10 and reducing the reduced-chi-squared threshold to 1.0 (our chosen value for Oklahoma) decreased the number of “active” time intervals by 18 percent to 21 and the number of lightning events by 32 percent to 13. In a similar hour during an unrelated storm at the same spaceport, these decreases were 7 percent and 18 percent, respectively. During the 1 minute shown in Figure A-5, when the MCC of Figure A-2 was passing directly over the spaceport, however, the same decreases were only 0 percent and 2 percent, suggesting that the lightning-events statistic is more robust for flashes centered over the spaceport area. For the entire year, 2006, the same parameter changes reduced the total number of accepted



sources (over the whole domain of the network, dependent only on the reduced-chi-squared threshold) by 18 percent, the total number of lightning events by 19 percent, but the total number of hours with lightning over the spaceport area by only 10 percent. None of these variations can be considered indicative of extreme uncertainties in our statistics. They also support the expectation that hours-with-lightning is a more robust statistic than lightning events.

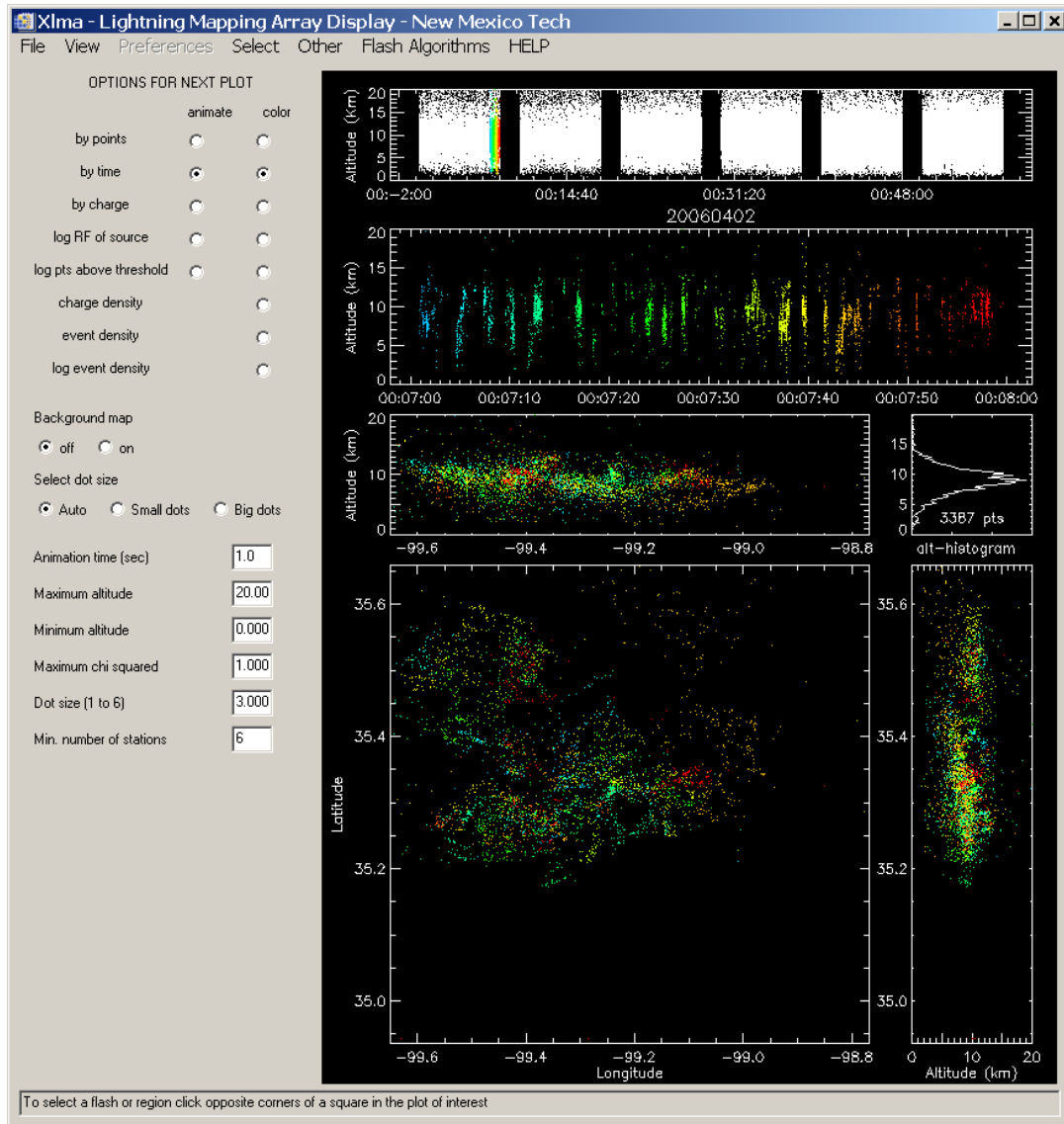


Figure A-5. Similar to Figure A-4, but for a 1-minute period about 3 hours earlier in the life of this MCC.

Figure A-5 shows 1 minute of data from the same MCC 3 hours earlier, when it was passing over the spaceport, still developing, and much less active. At this even-longer distance from the network, where the detection efficiency and location accuracy of the LMA are undoubtedly much reduced, individual flashes still seem to be rendered fairly well. See, for example, the single large flash from this interval that is illustrated in Figure A-6 and that produced two credible lightning events.

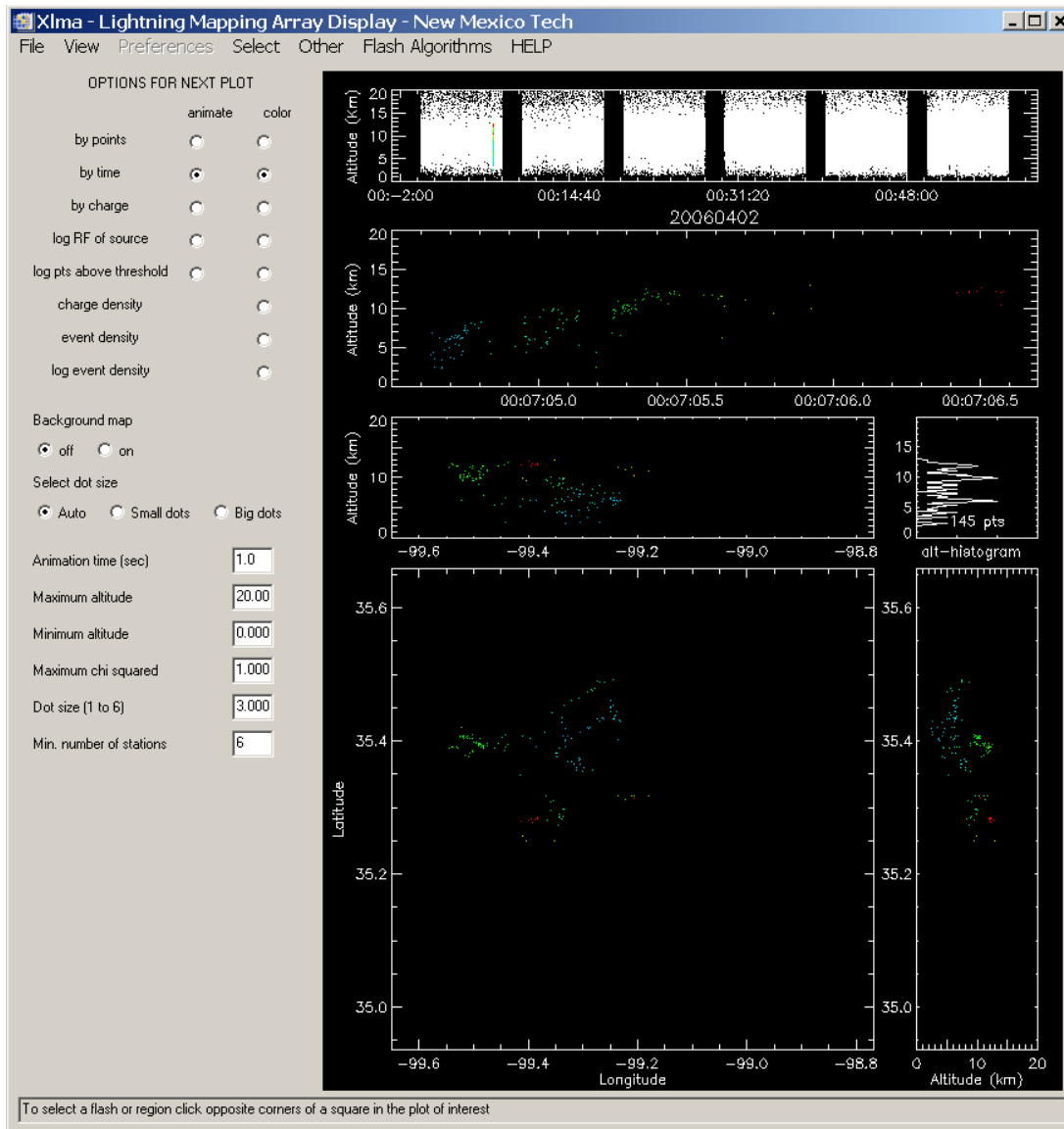


Figure A-6. Similar to Figure A-5, but showing only a single flash from that 1-minute interval.

Next we turn to lightning examples over SA in New Mexico. Figure A-7 shows a large complex of air-mass storms within range of the WSMR LMA. Evident here, much more so than in Figure A-1, is the expected radial “smearing” of lightning at large ranges from the network. The smearing is worst to the north because the network stations are strung out N-S in a relatively narrow E-W distribution. (See Figure A-9 for a better illustration of the station locations.) This configuration may be compared to the UOK LMA network (see Figure A-3), which is more or less circular. Because of the WSMR network configuration, as well as its proximity, we will see that lightning over SA is mapped much more accurately, at least in the horizontal, than lightning over the Oklahoma Spaceport.

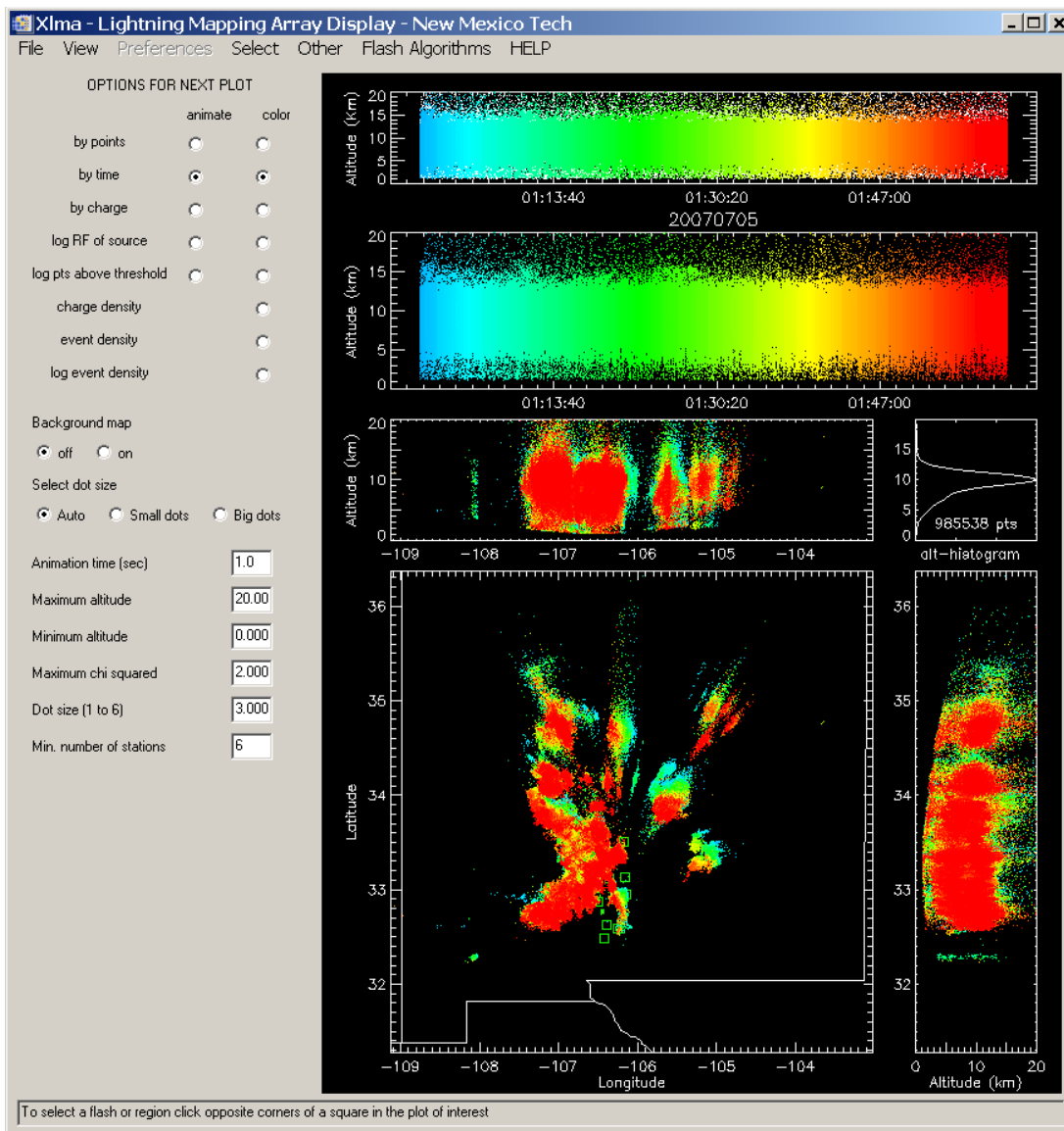


Figure A-7. Similar to Figure A-1, but for a large group of air-mass thunderstorms within range of the New Mexico LMA during the hour after 0100 UT on July 5, 2007. In this case, the reduced chi-squared threshold is 2.0. This is a more typical hour with no noticeable data gaps.

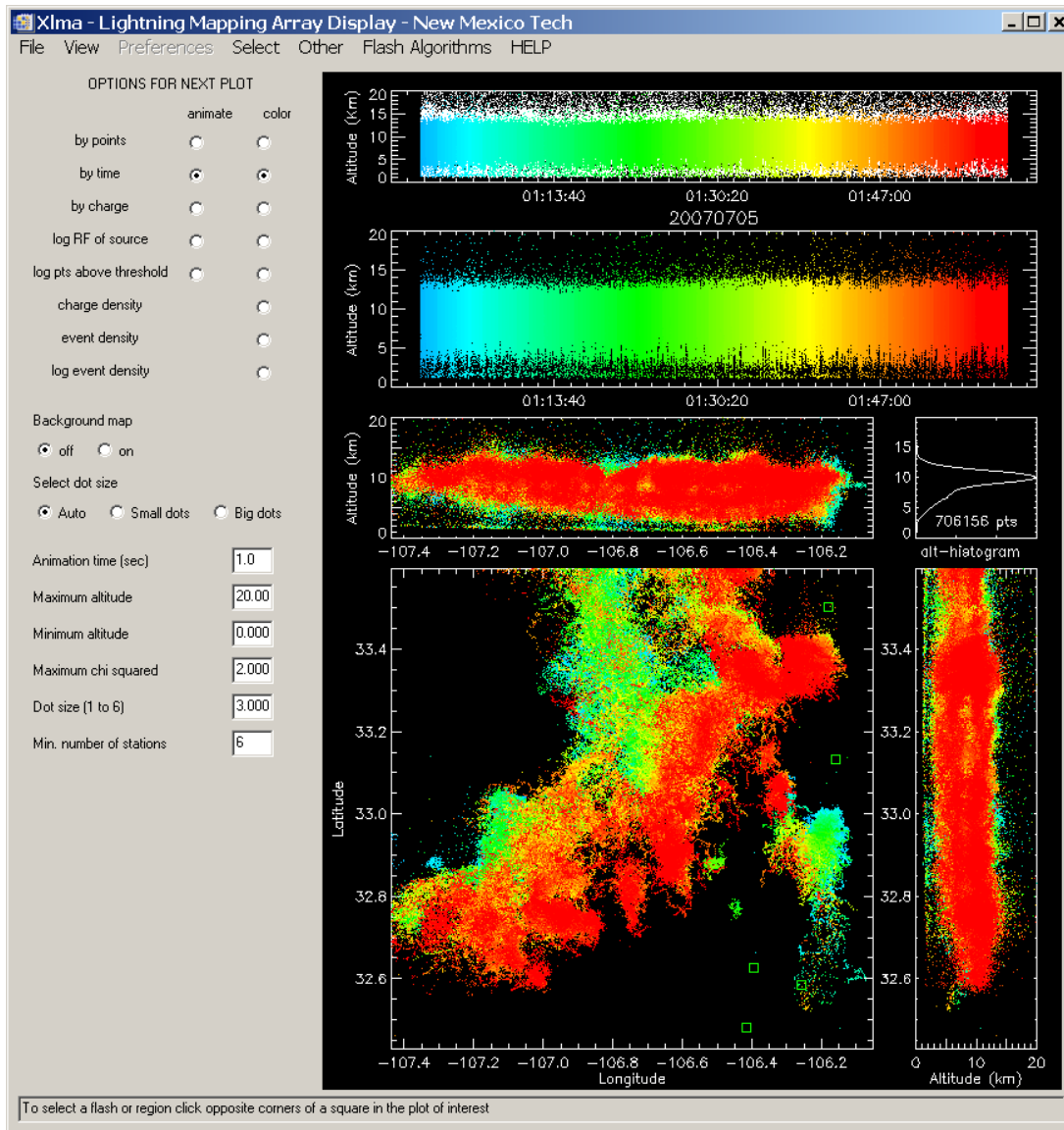


Figure A-8. Similar to Figure A-2, but for the data shown in Figure A-7. In this case, however, the spaceport area lies in the lower left-hand corner of the plan view.

Figure A-8 shows the same data, zoomed in so that our  $80 \times 80$  km square (SW and NE corners at [N. latitude (degrees), E. longitude (degrees)] = [32.44, -107.43] and [33.16, -106.57], respectively) lies in the lower left-hand corner of the plot, occupying somewhat more than one-quarter of the plot. Again, the display is scaled so that all of the network stations are within the viewing area, although they cannot all be seen. Again, see Figure A-9 for a better illustration.

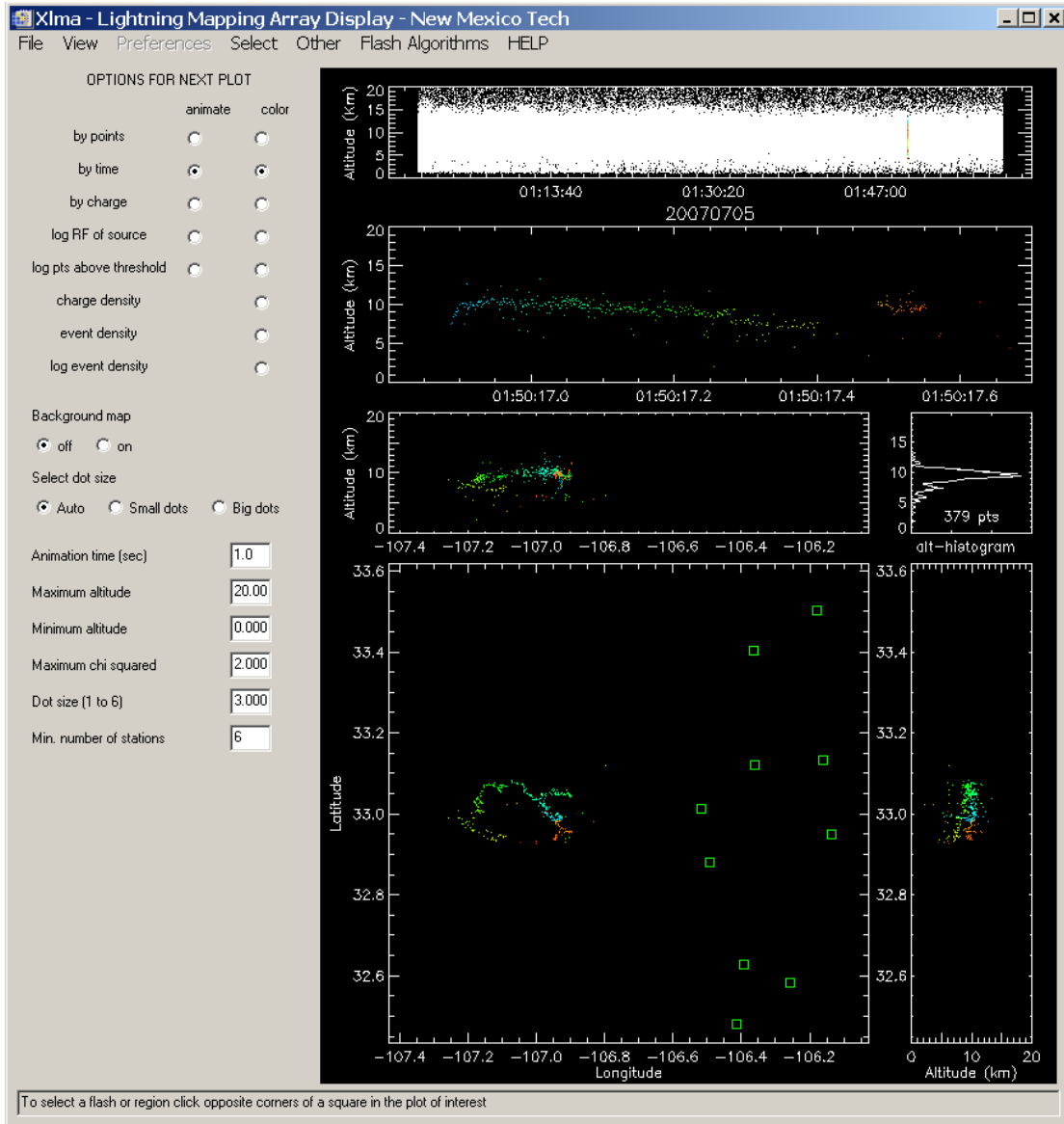


Figure A-9. Similar to Figure A-8, but for a single lightning flash over the spaceport.

Figure A-9 shows a single lightning flash on the same spatial scales as in Figure A-8, so that the station locations are evident. Notice here and in Figure A-10 (which shows the same flash over the spaceport area alone) that, although significantly smaller in horizontal extent and/or temporal duration, this flash over SA is rendered in considerably sharper detail than are those in Figures 3 and 6 over the Oklahoma Spaceport. This is because of both the proximity of the flash to the WSMR LMA and the almost three times greater N-S extent of the NM network itself.

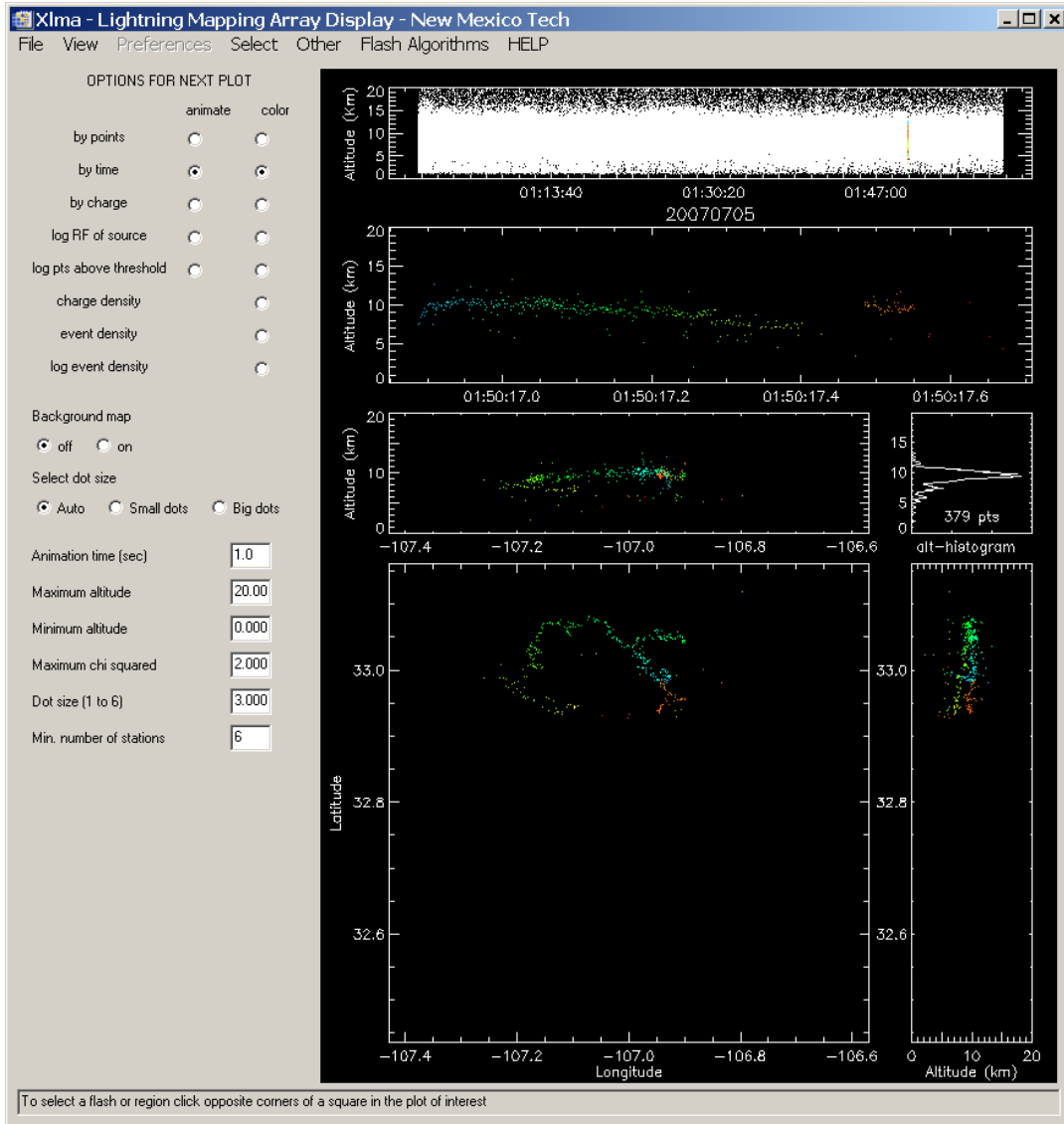


Figure A-10. Similar to Figure A-4, in which the spaceport area occupies the entire plan view, but for the flash shown in Figure A-9.

During the last minute of this very active hour of data over SA we again looked at the dependence of lightning events on the key detection parameters. For example, with the required number of sources equal to five (our chosen value) and a reduced-chi-squared threshold of 3.0, we found source points within our 80×80 km square during 15 four-second time intervals, producing a total of 44 lightning events. Increasing the required number of sources to 10 and reducing the reduced-chi-squared threshold to 1.0 (*lower* than our chosen value of 2.0 for New Mexico; see below) decreased the number of “active” time intervals not at all and the number of lightning events by only 7 percent to 41. During an unrelated hour over the same spaceport, however, these decreases were 16 percent and 13 percent, respectively. For the entire year, 2007, the same parameter changes reduced the total number of accepted sources by a dramatic 45 percent, the total number of lightning events by 22 percent, and the total number of hours with lightning over the spaceport area by only 11 percent.

In spite of the relatively modest reductions of lightning events and hours-with-lightning reported here, the unexpectedly large reduction in total accepted sources (45 percent) motivated an examination of the dependence of accepted sources on the reduced-chi-squared threshold during hour 0100 UT of

day 20070705. Decreasing the reduced-chi-squared threshold from 5.0 to 3.0 decreased the number of accepted sources over the spaceport area by only 7 percent. A reduction from 5.0 to 2.0 translated to a decrease of 15 percent, however, and a reduction from 5.0 to 1.0 reduced the source count by 42 percent. These results motivated us to choose a reduced-chi-squared threshold of 2.0 for New Mexico, as opposed to the value of 1.0 chosen for Oklahoma.

Finally, our numbers of lightning events were also compared with flash counts by the NMIMT “flash algorithm” in a few of the above cases. The default parameters in the XLMA program were used for this purpose, except that flashes of fewer than five source points were ignored. In general, we found that the NMIMT algorithm produced more events than our algorithm did, primarily because it tended to break up large discharges that we would have manually identified as single flashes into two or more flashes. Nevertheless, the agreement was within a factor of two over the Oklahoma Spaceport and considerably better than that over SA.

Based on these and other comparisons, we arrived at the following conclusions:

- No case was found in which a lightning event was reported at a spaceport when no identifiable lightning was displayed over the corresponding 40×40 km square by the XLMA software. In other words, the events counted here are real lightning (or at least branches of larger flashes that extended over the spaceport), not noise. (See the separate comparison to NLDN flashes discussed below, however, for some caveats.)
- No case was found in which significant lightning over a spaceport was missed by our lightning event algorithm. (We did notice one case where the first “flash” in a storm over SA was rejected with the tighter threshold that we eventually selected. This flash comprised only five source points within a very short time interval when using the generous reduced-chi-squared maximum of 5.0—the XLMA default value. Later flashes in this storm were detected, however.)
- The “flash” counts given by the XLMA software (using NMIMT default parameters) correspond roughly to the “lightning event” counts in our software, although event counts could be varied appreciably by using different, but apparently reasonable, values of minimum source count (currently five) and reduced-chi-squared threshold. It appears that our 40×40 km boxes and 4 s intervals are appropriate for minimizing simultaneously the overcounting (due to one flash spanning more than one box or time interval) and the undercounting (because more than one flash occurs in the same box and interval).
- As mentioned above, the preferred values for these parameters are a minimum source count of five (per 40×40 km box and 4 s time interval) at both sites and a reduced-chi-squared threshold of either 1.0 for the Oklahoma Spaceport or 2.0 for Spaceport America. It was found that we could get away with the smaller reduced-chi-squared threshold in Oklahoma without losing too many sources (relative to our original choice of 3.0), but the same small threshold in New Mexico resulted in weeding out almost half of the sources over the spaceport. (We do not currently have an explanation for the greater sensitivity to reduced-chi-squared threshold at Spaceport America, but we can report that decreasing this threshold from 3.0 to 1.0 makes little or no difference in the morphology of lightning flashes there, as displayed in the corresponding XLMA plots.) Doubling the minimum source count to 10 also reduces the event counts, but not greatly.
- The structure and detail of the flashes over Spaceport America are captured very well in the XLMA displays, whereas those over the Oklahoma Spaceport (which is considerably further from the network) are “muddier.” Nevertheless, there appears to be little doubt that the Oklahoma LMA system is giving a good plan view of lightning over that spaceport, albeit

with relatively poor altitude resolution. No sign was detected of the radial “smearing” of flashes over the Oklahoma Spaceport that we had initially feared.

## A.2 Additional “Lightning Event” Validation: Comparison with NLDN Data

The NLDN analysis reported in section 2.7 also yielded a list of hours with lightning over the same two 80×80 km squares as used for the LMA analysis herein. In general, there was good agreement between lists from the two lightning-detection systems, although there were some discrepancies, as illustrated in Figures A-11 and A-12. As discussed above, many individual hours—even entire days—of data were missing from the LMA dataset for reasons unknown to us. This probably explains the missing red boxes around some of the black crosses in these two figures. As also noted, there was no way to determine from the available LMA dataset whether that system was operational during the entirety of any hour for which it yielded a data file (e.g., Figure A-1). For these reasons we look below only at hours for which there were LMA lightning events without any NLDN flashes over the spaceports (empty red boxes in the example figures). For Oklahoma, out of 1,043 hours with LMA lightning events, only 36 hours (3.5 percent) had no NLDN flashes. For New Mexico, out of 1,265 hours with LMA, there were 100 (7.9 percent) without NLDN. As we shall see below, there is some indication that the larger fraction of missing NLDN in New Mexico might be meaningful.

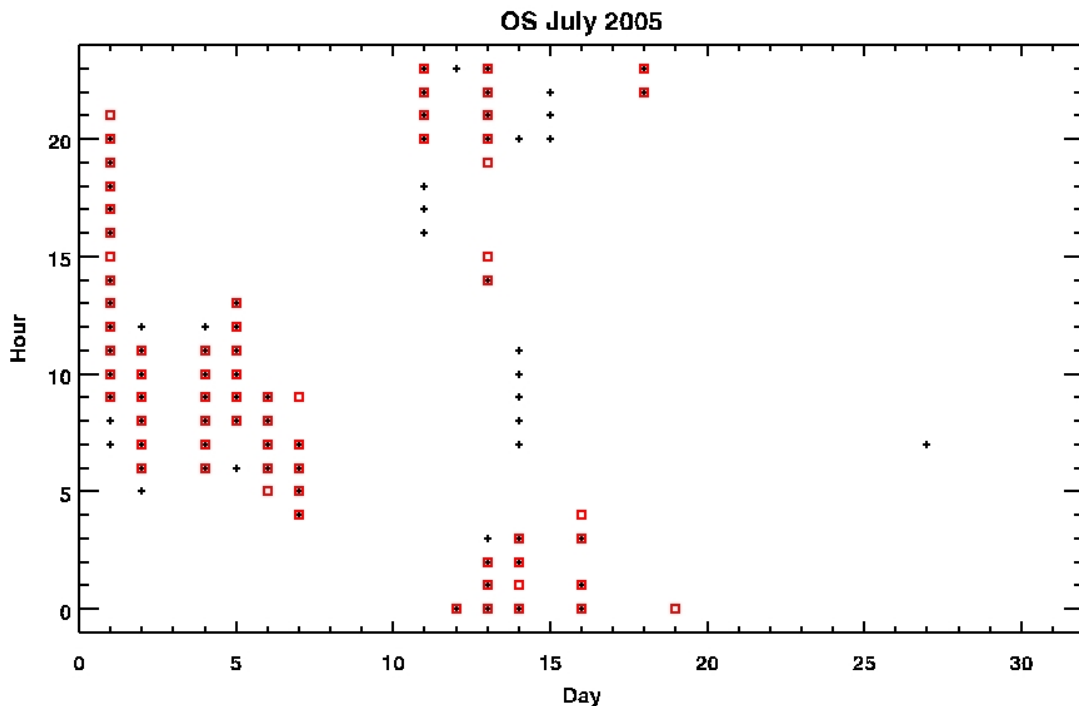


Figure A-11. Hours with LMA lightning events (red boxes) and/or NLDN flashes (black crosses) during the month of July 2005 over the Oklahoma Spaceport.



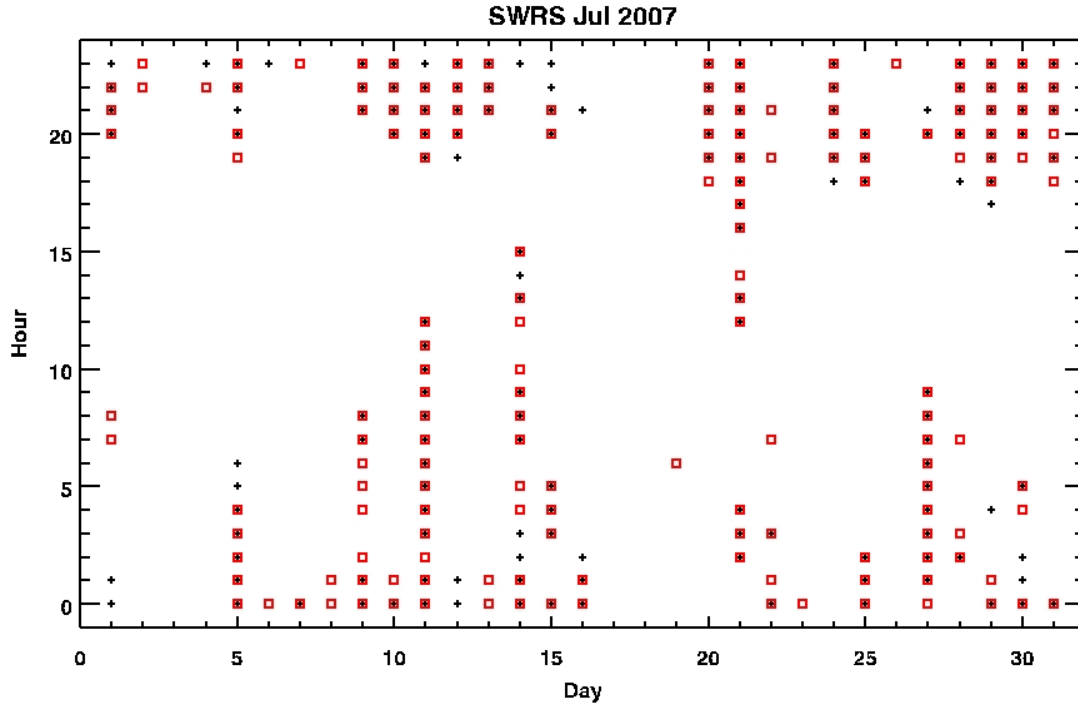


Figure A-12. Similar to Figure A-11 for July 2007 over the SA.

We examined in detail several of these anomalous cases from both spaceports. (In selecting hours to examine, we were forced to avoid files from the years 2004 and 2005 in Oklahoma because their abbreviated data headers were not compatible with our Windows version of the XLMA software. This fact, plus the smaller overall number of such cases from Oklahoma, resulted in our looking at more examples from New Mexico—seven in all—than from Oklahoma—only five.) We concentrated on hours having more than a few lightning events, especially in isolated storms or near the beginning or ending of larger storms (as judged from the complete lightning-event listings) because we were expecting to find mostly IC flashes or the in-cloud fringes of horizontally extensive flashes that may or may not have produced CG strikes *outside* our 80×80 km boxes. As we will see below, some of the cases that we checked were caused by apparent aircraft tracks—no real lightning activity at all. Others resulted from radial “smearing” of source locations from more distant storms, still others appeared to match our expectations, and a few represented small storms over the Spaceport America from which it was difficult to believe that no CG strikes emerged.

An LMA “aircraft track” is known to be produced when an airplane (or even the space shuttle) flies through ice clouds under the right conditions. It is assumed that particle impaction on suitable surfaces charges the vehicle, or portions thereof, to the extent that corona or small sparks radiate VHF pulses of sufficient amplitude to trigger the LMA system. Examples of this from both Oklahoma and New Mexico are shown in Figures A-13 and A-14.

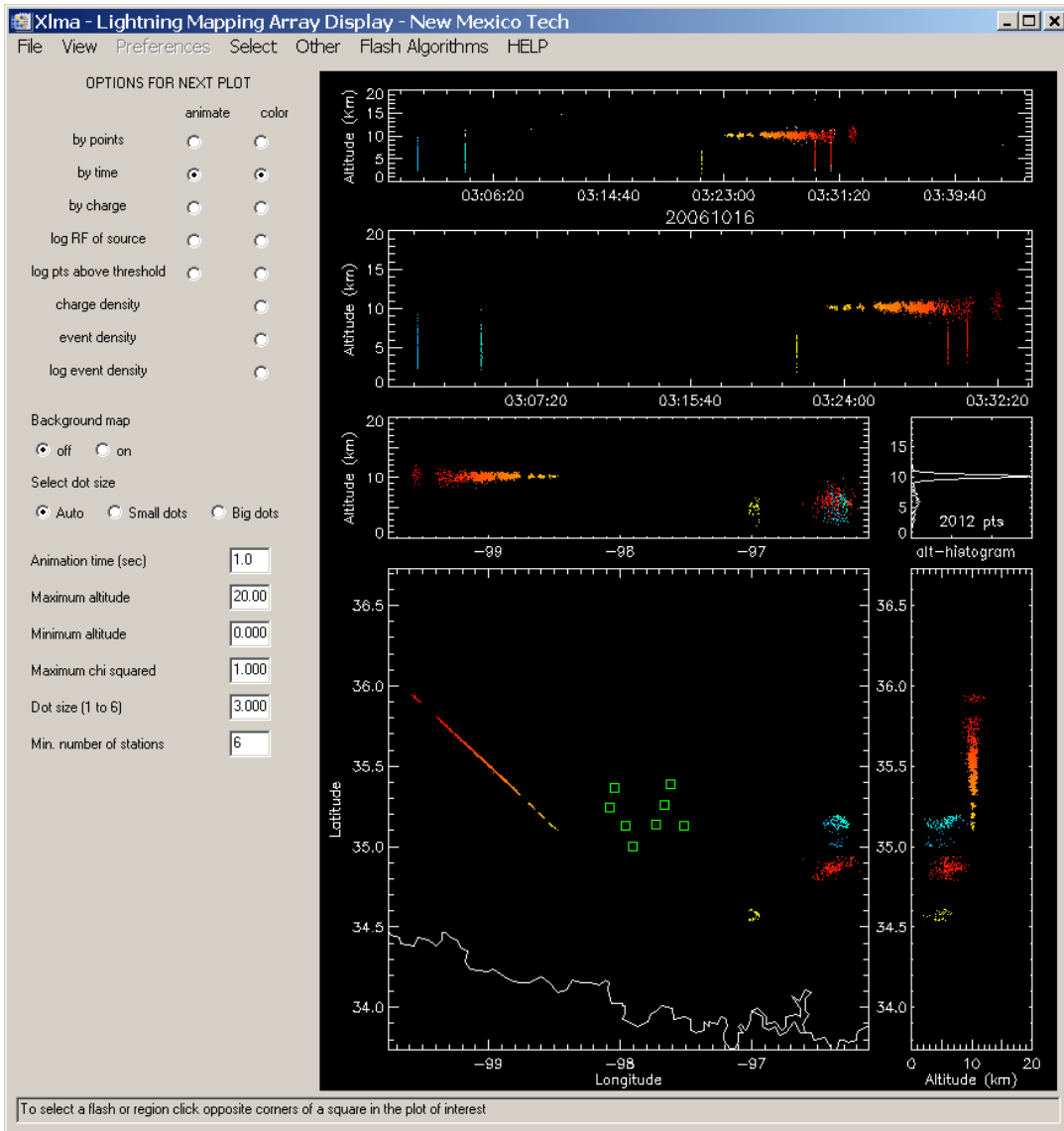


Figure A-13. XLMA view of the Oklahoma network and vicinity shows an aircraft track in the left center. The middle part of this track passes over the northeast quadrant of our 80×80 km spaceport box and is misidentified a series of lightning events. A few small storms are producing natural lightning in the middle left of the field.

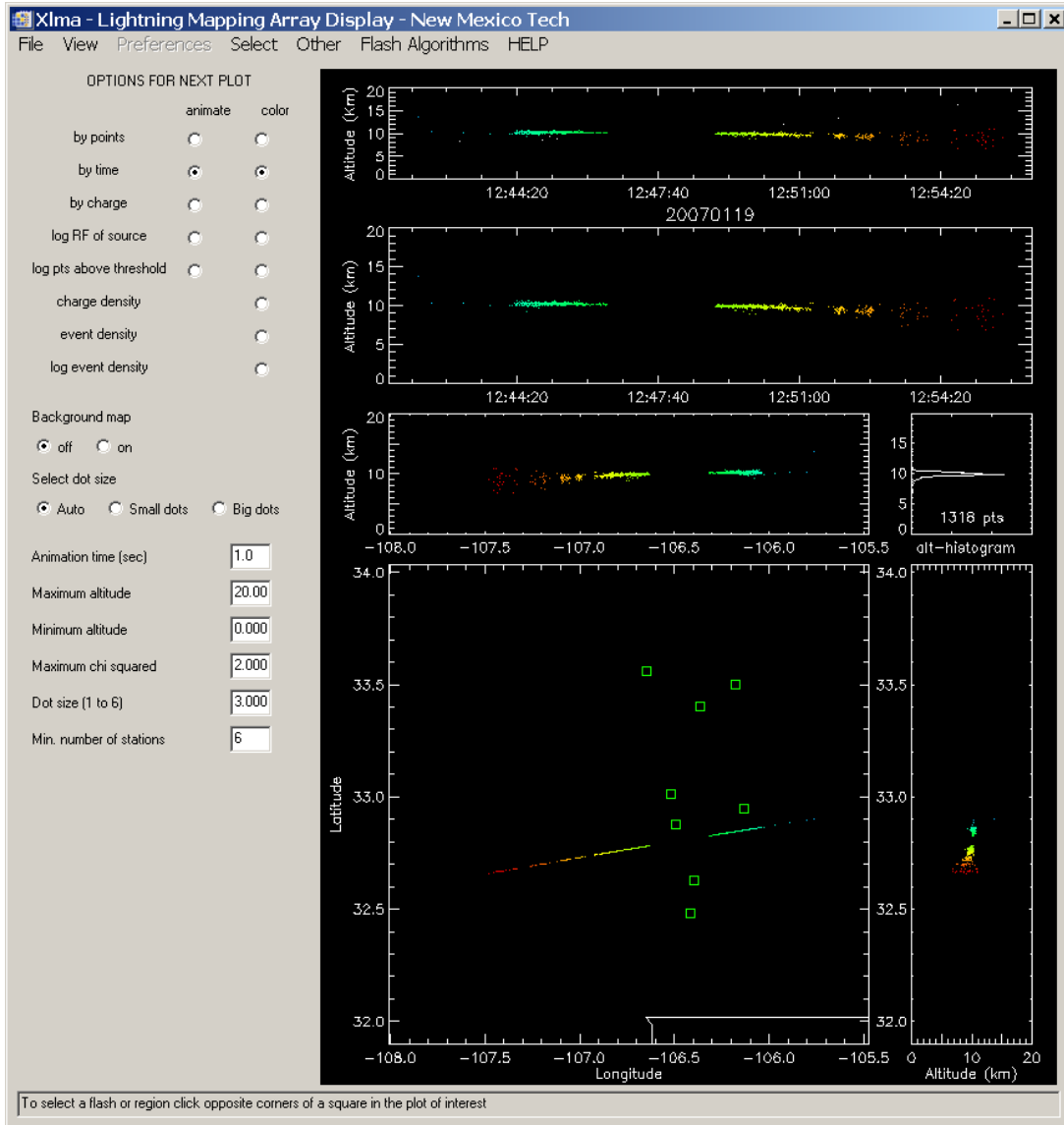


Figure A-14. Similar to Figure A-13 for the New Mexico network. No natural lightning is visible in this figure.

Figure A-15 shows an example of the smearing of distant sources across the Oklahoma Spaceport. In this case a storm to the west of the spaceport (and very far from the LMA network) has scattered just enough mislocated sources across the west side of the spaceport area to produce several bogus lightning events. We found no similar examples at Spaceport America, probably because of its location not far to the west of the long north-south array of LMA stations.

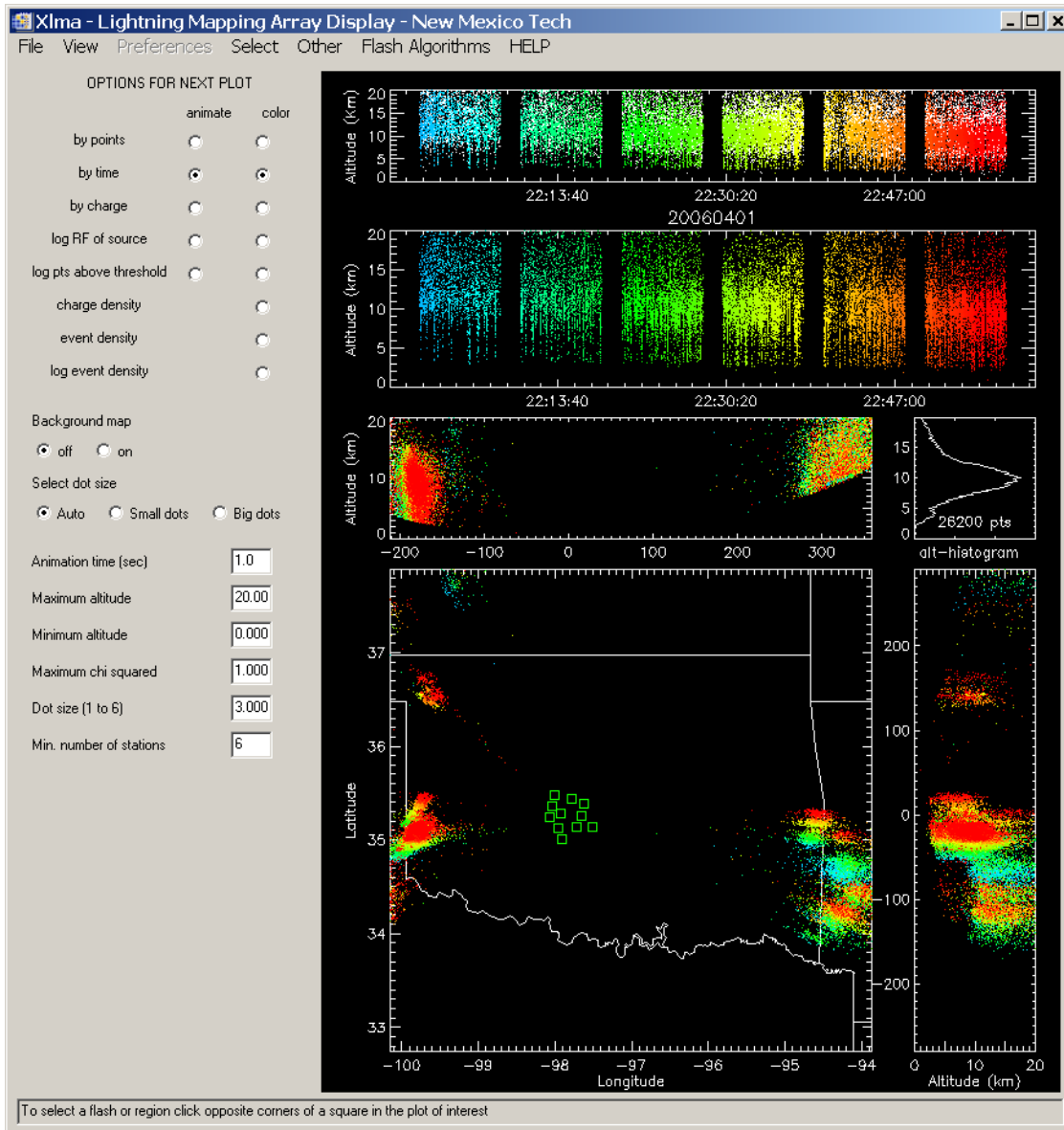


Figure A-15. This Oklahoma example shows relatively distant storms to the W and NW of the network. A few poorly located source points spread radially inward toward the spaceport (a square with corners at [35.66 N, -99.64 E] and [34.94 N, -98.76 E], not explicitly shown).

Next we show 2 hours of data that illustrates both our expectations (IC flashes or in-cloud fringes of large flashes) and possible examples of “terrain shadowing.” Both of these data hours are chosen from New Mexico because it is easier to interpret lightning morphology when it is located closer to the LMA network and because no clear-cut examples of terrain shadowing were found in the Oklahoma plains. Figure A-16 shows an overview of the first hour of interest, with a small storm extending out of the northern edge of the nominal spaceport area (left center of this image) and a much larger storm with its northern fringes extending into the southern edge of the spaceport. Figure A-17 shows only the spaceport area itself for the same hour.

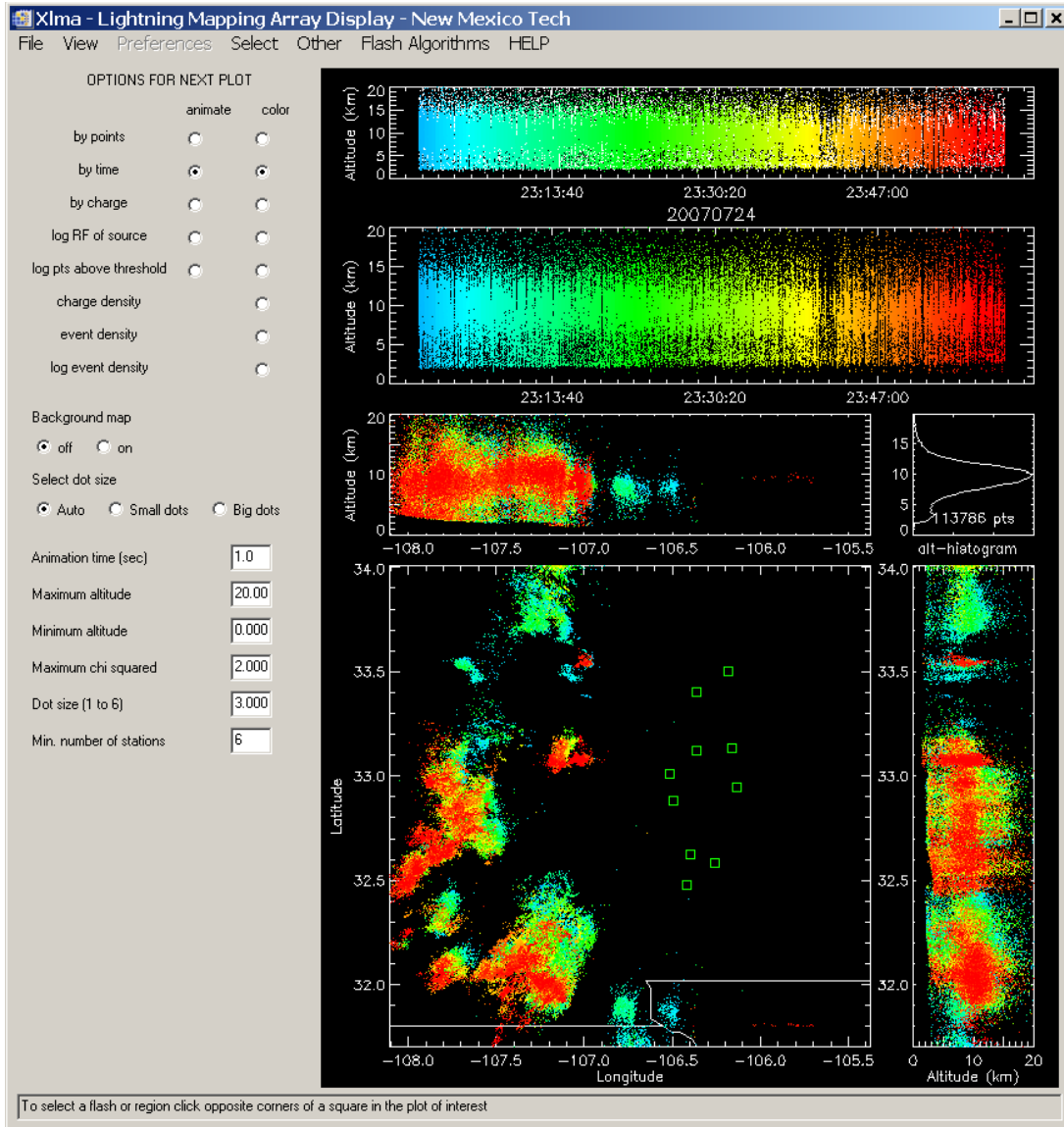


Figure A-16. One hour of LMA data from the New Mexico network. The nominal spaceport area (a square with corners at [33.16 N, -107.43 E] and [32.44 N, -106.57 E], not explicitly shown) is located left of center.

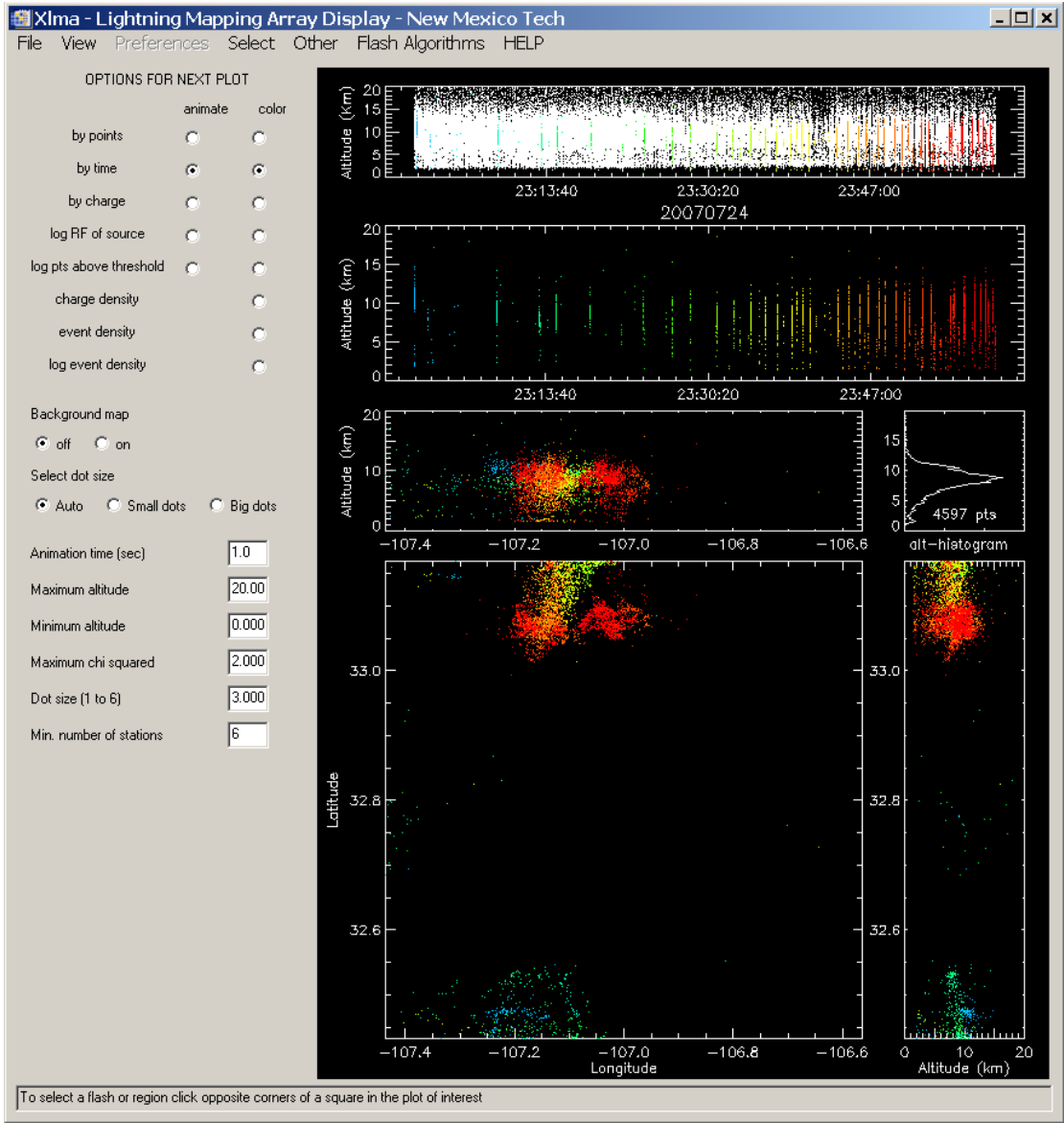


Figure A-17. Similar to Figure A-16 but showing only our 80×80 km box centered on SA encompassing most of the northern storm but only the northern fringe of the southern storm.

Zooming in on the northern fringe of the southern storm in Figure A-18, we see that a few horizontally extensive flashes appeared to project only their northernmost in-cloud extremities over the spaceport. Figure A-20 shows one of these flashes in detail, illustrating how the LMA might correctly report a lightning event over the spaceport area without there being any ground strikes in the same area for the NLDN to report.

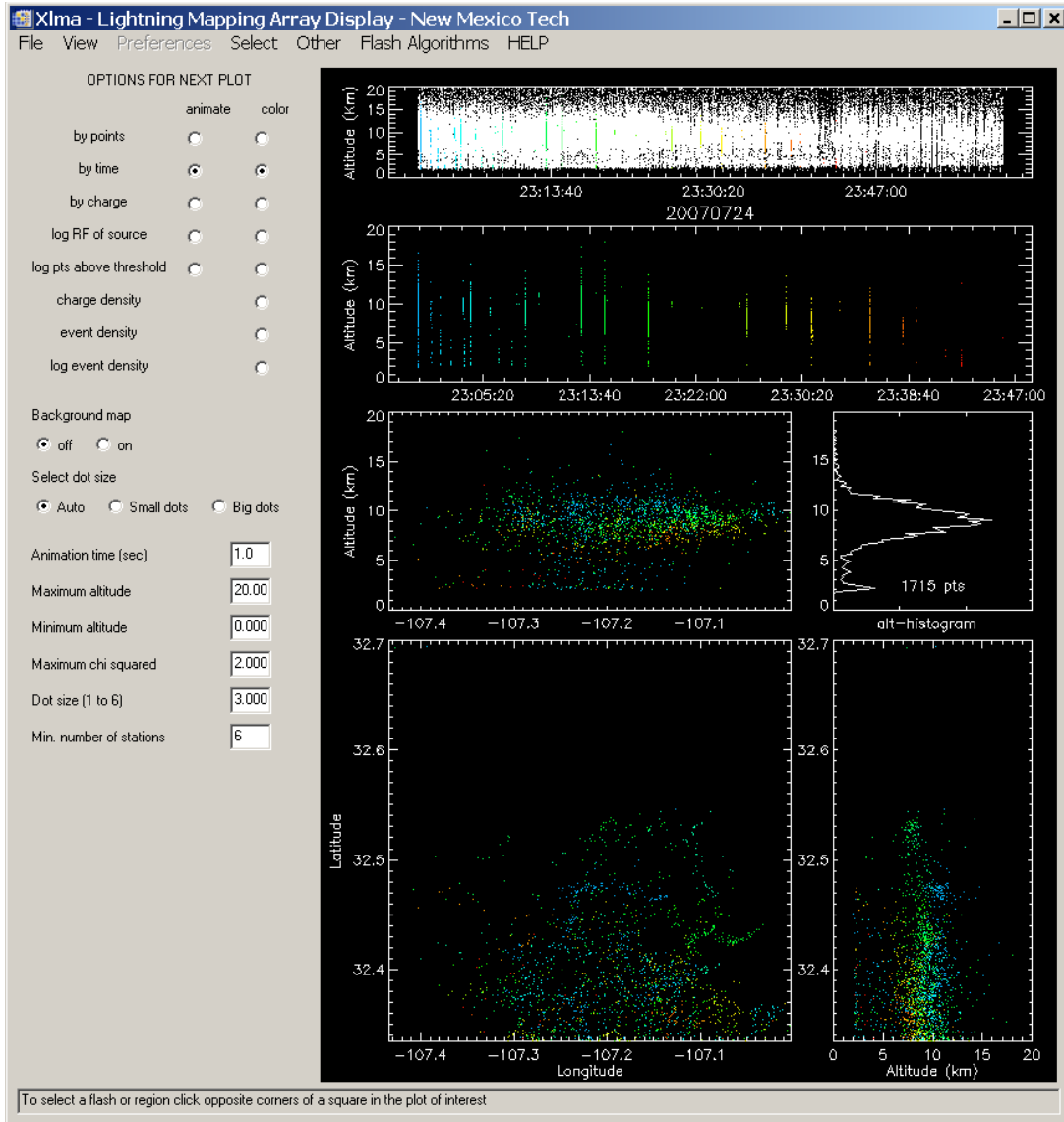


Figure A-18. A magnification of the storm of Figure A-17. Note that this image extends well below the southern boundary of the nominal spaceport area, which is located at latitude 32.44 N.

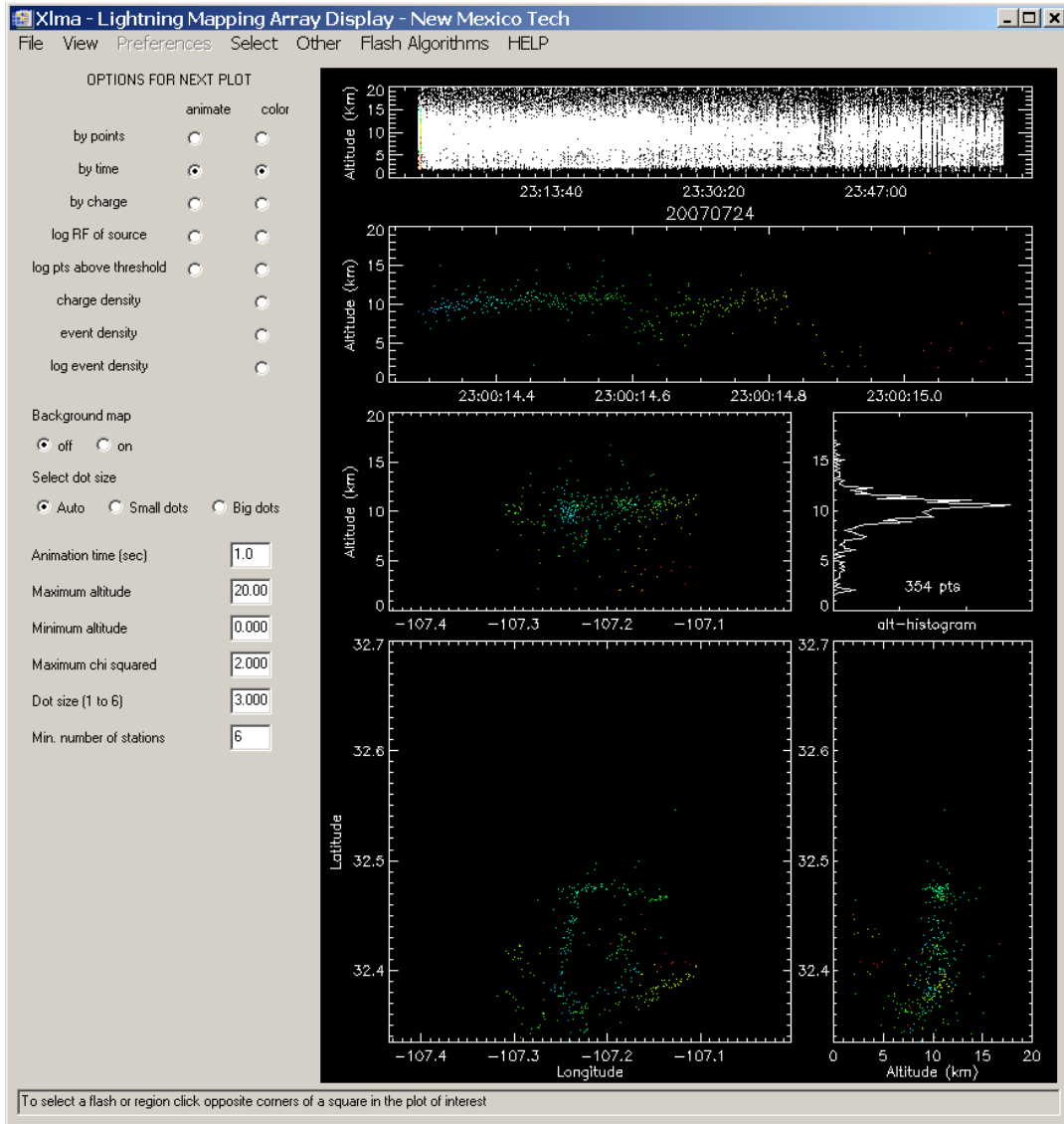


Figure A-19. The same horizontal area as Figure A-18, showing just one large flash, which may have sent a return stroke to ground just outside the southern boundary of the spaceport box.

Next we zoom in on the northern storm of Figure A-19. Figure A-20 shows its complete activity during the hour in question, while Figure A-21 examines a single flash in detail. No matter how this particular flash is categorized, it is hard to believe that none of the 30-odd flashes in this storm produced a ground strike within the spaceport area.



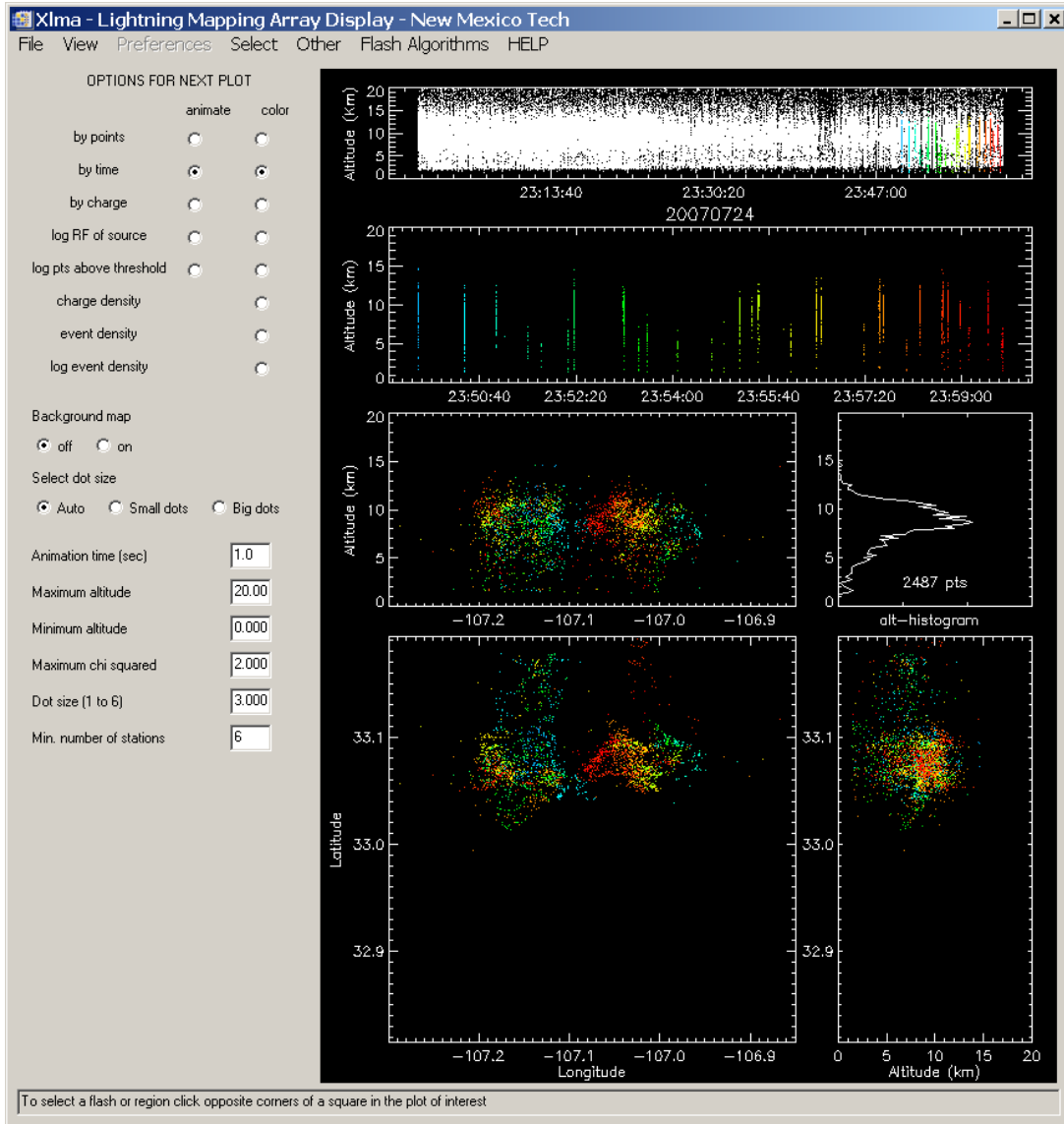


Figure A-20. A magnification of the northern storm of Figure A-18. Note that this image extends somewhat above the northern boundary of the nominal spaceport area, which is located at latitude 33.16 N.

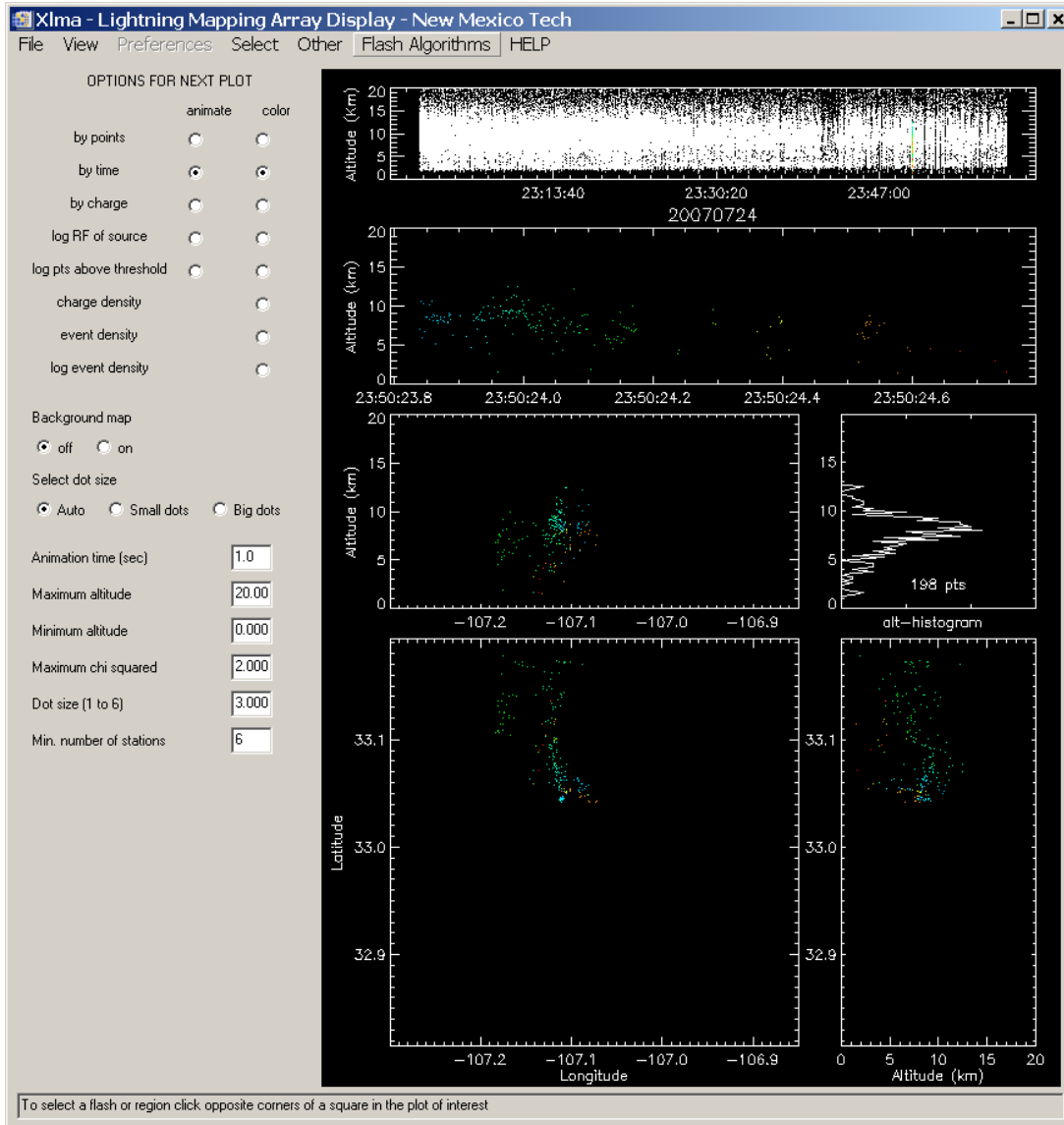


Figure A-21. The same horizontal area as Figure A-20, showing one flash that may well have sent one or more return strokes to ground inside the nominal spaceport area.

Figure A-22 shows only the nominal spaceport area for the second hour of interest, during which three small storms were active in the area. (There were other small storms scattered throughout the region, but all were well outside of our 80×80 km box.) This case gives both some excellent examples of IC discharges (which probably did not put down return strokes) and our best indication that the NLDN missed some return strokes over the spaceport, perhaps because of terrain shadowing.

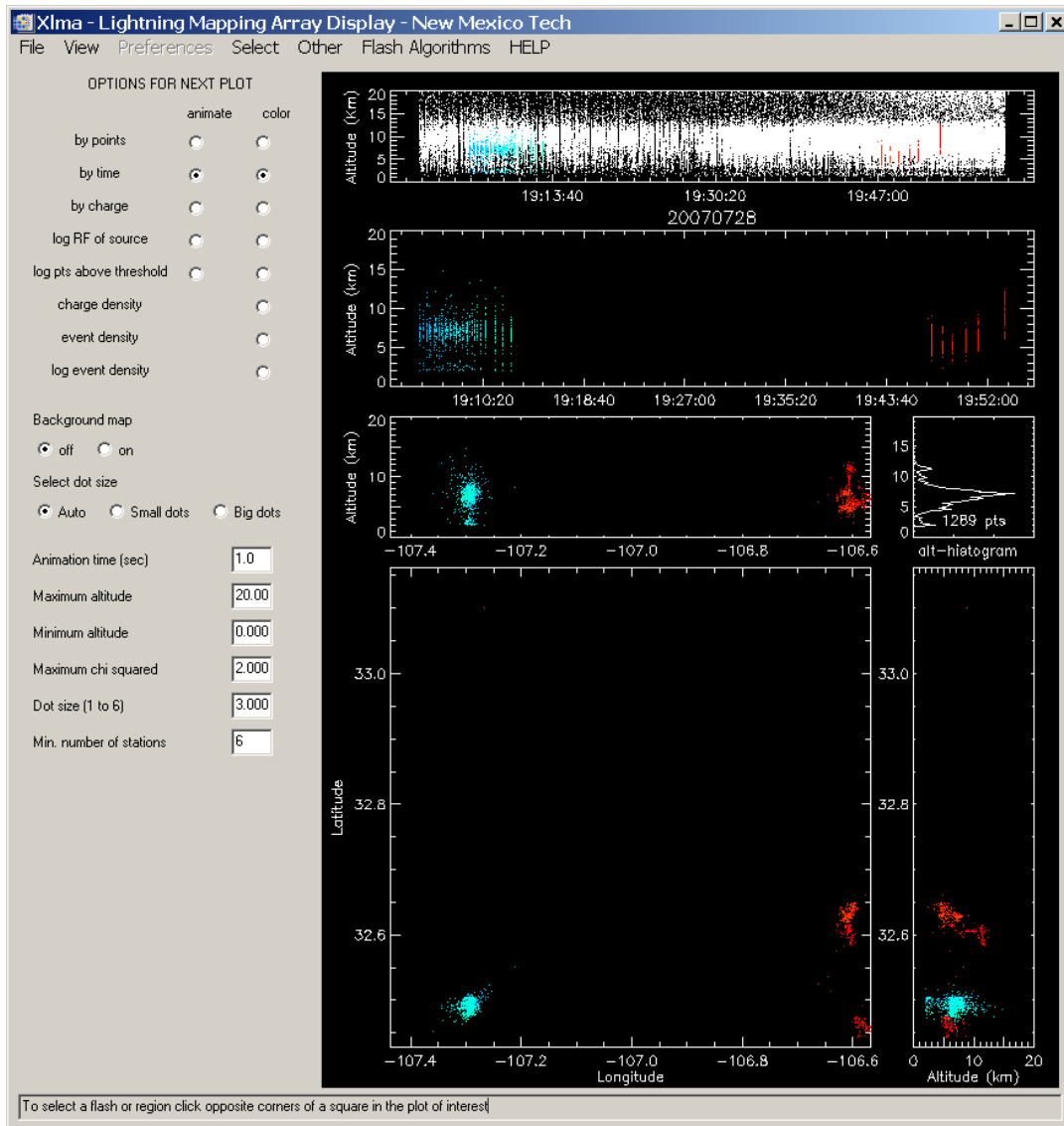


Figure A-22. The nominal area of SA, with three small, air-mass storms during the second hour of interest.

First we zoom in on the two weak storms in the southeast corner of Figure A-22. Figure A-23 shows that these storms together produced only six flashes late during the hour in question. The northern storm here, being well situated relative to the New Mexico LMA network, gives an excellent depiction of a classic, bi-level, IC discharge in Figure A-24. Based on examination of the other five flashes shown here, it seems likely that none of them (with the possible exception of the first) sent a return stroke to ground.

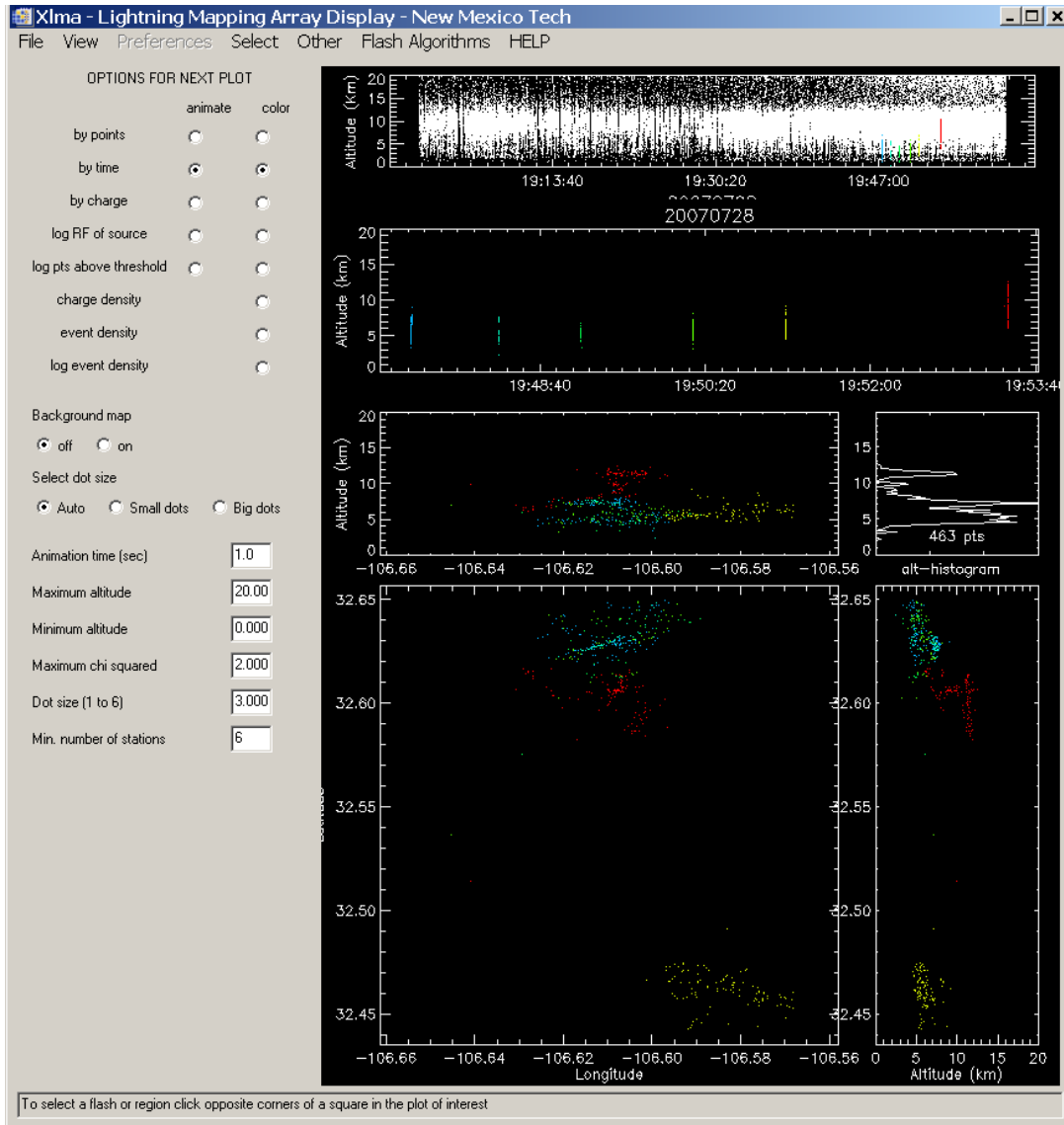


Figure A-23. A magnification of the southeastern storms of Figure A-22. Note that this image extends somewhat east of the eastern boundary of the nominal spaceport area, which is located at longitude -106.57 E.

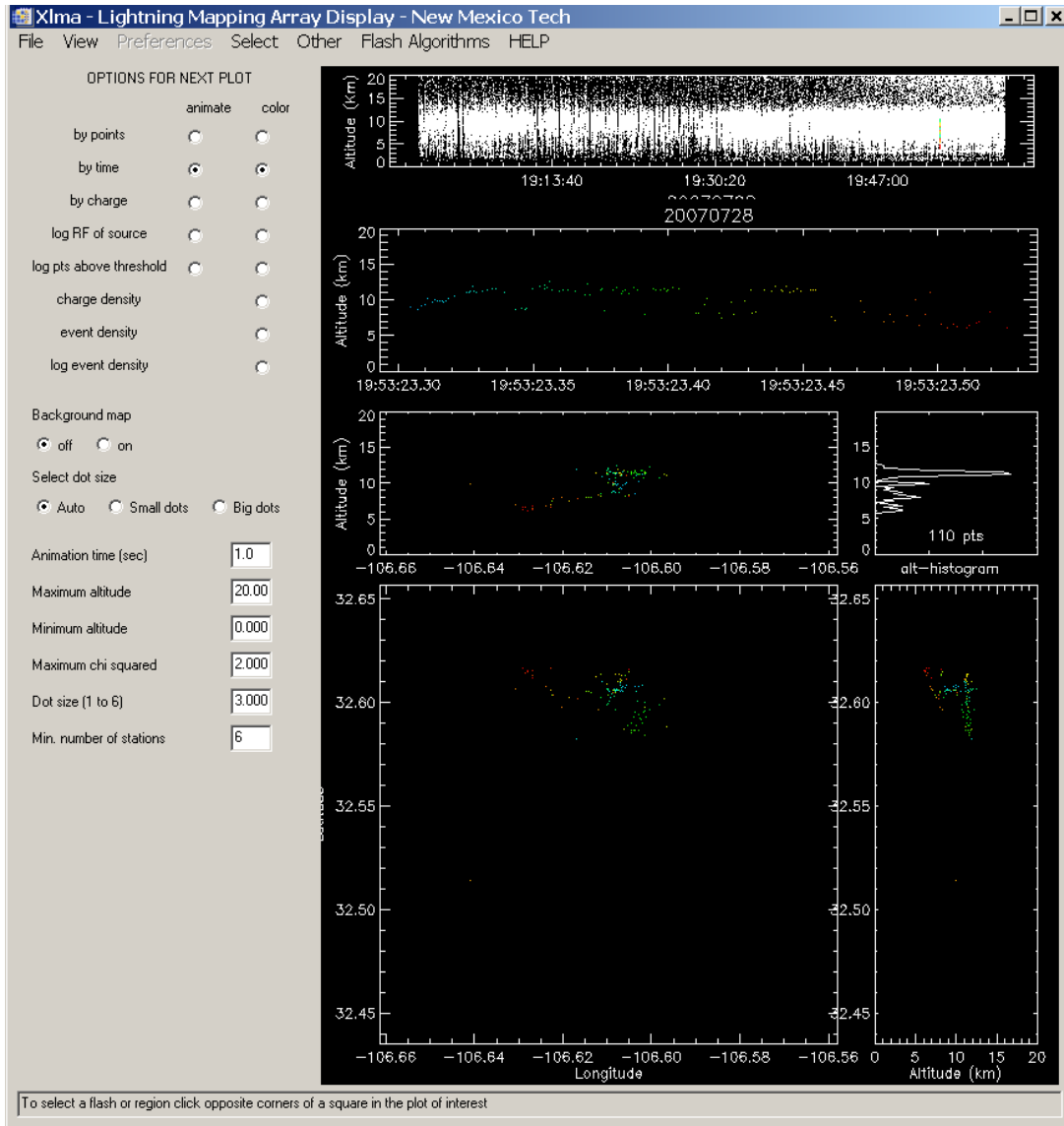


Figure A-24. One stroke from Figure A-23 (with the same scales) constitutes our best example of classic inter-cloud discharge.

Nevertheless, a magnification of the southwestern storm in Figure A-22 (see Figure A-25) shows that it was fairly active, producing some 38 flashes over its 10-minute lifetime. Examination of individual flashes is inconclusive because of the storm's relatively long distance from the LMA, but it is difficult to imagine that all of them were IC flashes. Therefore it seems probable that something was interfering with the ability of the NLDN to locate ground strikes in this storm.

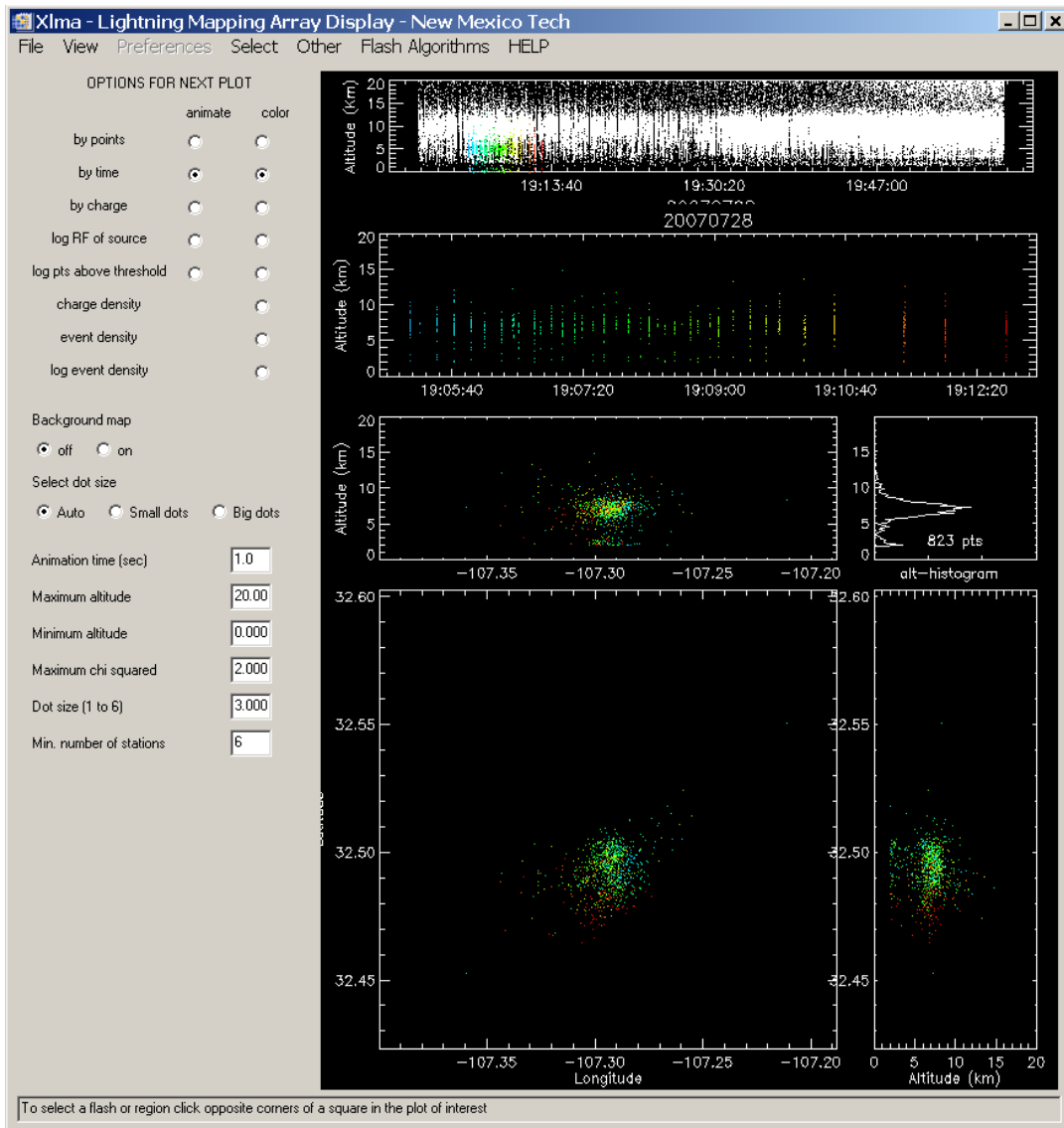


Figure A-25. A magnification of the southwestern storm of Figure A-22. Note that this image extends somewhat south of the southern boundary of the nominal spaceport area, which is located at latitude 32.44 N.

Based on the above examples, the following modifications can be made to the tentative conclusions listed in the section above:

- A few cases of LMA “aircraft tracks” were found to produce lightning events in the absence of any real lightning. Such cases appear to be relatively rare and, in any case, seem likely to represent a potential electrostatic hazard that should probably be avoided by flight operations.
- A few cases were found of the smearing of miss-located sources into the spaceport area from more distant storms to the west in Oklahoma. Again, bogus lightning events due to such smearing appear relatively rare and, given the prevailing meteorology of the region, are likely to be followed shortly by real lightning as the storms move rapidly eastward into the spaceport area.

- There is some indication that the NLDN might be missing some ground strikes in the vicinity of SA. If true, this might be due to terrain shadowing, but our data alone cannot confirm or deny this hypothesis.





## **Appendix B. Reanalysis of the Airborne Field Mill Campaign-I Dataset**

### Reanalysis of the ABFM-I Dataset Final Report

Dr. Douglas Mach

February 25, 2009

#### **Introduction**

This report documents the reanalysis of data from the Airborne Field Mill (ABFM-I) project. The ABFM-I program consisted of 4 deployments to the KSC area with two of the deployments during summer and two during winter conditions found in Florida near KSC. The conditions targeted during the summer deployments included developing cumulus clouds, electric field falloff from mature storms (to assess standoff distances), and electrical decay in thunderstorm debris clouds. The summer goals included determining when developing clouds become a hazard (from triggered or natural lightning) to launch vehicles, how far away from mature clouds are the electric fields hazardous, and when are the thunderstorm debris clouds no longer a hazard to launch vehicles. The main winter target was layered clouds. The winter goals included determining at what overall thickness layered clouds become a hazard to launch vehicles and exploring various measurement approaches to determine if a layered cloud is, or is not, a hazard. The first summer deployment was from July 6 to August 22, 1990 and consisted of 31 data flights. The first winter deployment was between February 14 and March 18, 1991 and had 18 data flights. The second summer deployment was between July 5 and August 26, 1991 and also had 31 data flights. The second winter deployment was between January 16 and March 8, 1992 and had 25 data flights.

At KSC, the ABFM-I program utilized the ground-based field mill (GBFM) system and the Patrick Air Force Base (PAFB) WSR-74C radar. On the aircraft was a set of 5 rotating vane type electric field mills along with Loran-C navigation, altimeters, pressure sensors, air speed indicators, aircraft accelerometer, rough liquid water content, and a sensor that indicated the presence of ice. In this reanalysis, I looked specifically at the e-fields, the ice detector, and the LWC sensor. The electric field mills were an earlier version of the mills described in Bateman et al. [2007]. The radar data, while still “available,” is presently archived in an unreadable legacy format. In addition, during ABFM-I the radar was operated and its data recorded in an uncalibrated mode, rendering the data useless for quantitative analyses. The Loran-C data was inconsistent and that anytime the aircraft penetrated clouds of any substance, it would lose location data. The LWC formula was not well calibrated. It seemed to have a “zero” at about  $0.5 \text{ g m}^{-2}$ . However, at times, when one of the underlying raw components exceeded lower or upper limits, the LWC values would go to zero. Possibly a more detailed examination of the formula and underlying raw components used to calculate the LWC could help make the data more consistent and useful. The ice detector output was simply the voltage difference between an isolated patch of conductor and the aircraft skin.

This re-analysis concentrated on the layered, debris and anvil debris clouds. The work also included a re-calibration of the aircraft field matrix using the new method developed by Mach and Koshak [2007]. Note this report also provides the summary data from each penetration in a spreadsheet (ABFM-I Flight Data.xls) and the plots of each penetration/data run as a series of Portable Network Graphics (PNG) files (included on an accompanying CD).

## Calibration

The calibration procedure documented in Mach and Koshak [2007] was followed for this analysis. The procedure is as follows:

- 1) Find a time period when the aircraft was making roll and pitch maneuvers at a reasonable altitude (in fair weather field conditions).
- 2) Calculate the ideal fields that would be present at the aircraft during the maneuvers based on the Gish [1950] fields and the aircraft roll and pitch angles.
- 3) Use the ideal fields and the field mill outputs to calculate a first iteration calibration matrix.
- 4) Use the calibration matrix and ideal fields to calculate the first iteration true external electric fields.
- 5) Correct the first iteration fields for any known problems.
- 6) Use the corrected first iteration fields and the field mill output to calculate the second iteration calibration matrix.
- 7) Correct the calibration matrix for any known symmetry conditions.
- 8) Use the corrected calibration matrix and the mill outputs to determine a new external field estimate.
- 9) Repeat starting at step 4 with the new version of the external electric fields.
- 10) Repeat as needed.
- 11) After a few iterations, one is left with a relative calibrated aircraft.
- 12) The actual fields vary from the true fields by a constant factor determined by looking for times when the aircraft made low level passes over a calibrated ground-based field mill.
- 13) The ratio of the vertical field measured by the aircraft to the field at the calibrated ground mill determines the final constant factor.

Details of this process are found in Mach and Koshak [2007].

An example of a calibration run raw data is shown in Figure B-1. The aircraft first did a roll maneuver, then a pitch maneuver, and then finally another roll maneuver. The ideal fields in the aircraft coordinate system for that calibration run are shown in Figure B-2. The fields in Figure B-2 are based on the Gish [1950] fair weather profile modified by the actual fields at the ground (based on fly-bys of the KSC ground-based field mills). Figure B-3 shows the measured fields in the aircraft coordinate system. These fields are the raw mill fields from Figure B-1 converted by the calibration matrix determined from the calibration process. A direct comparison of the calculated fields to the ideal fields is shown in Figure B-4. A comparison of the new calibration results to those used in the original analysis is shown in Figure B-5. There are subtle differences between the old  $E_x$  and  $E_z$  while the differences between the old and new  $E_Q$  are quite striking. The changes in the  $E_Q$  are the most important. Removing the contamination from  $E_x$  in the  $E_Q$  data means the fields within clouds will be much better in this current analysis.

## Overall Results

Each penetration of a cloud, fly-by of a cloud, or standoff run was considered a data run. The usual procedure was for the aircraft to fly on a single set heading for each data run, although some data runs were spiral “soundings” of cloud conditions. The two components of the electric field recorded for each data run were the overall magnitude ( $E_{MAX}$ ) and the vertical field ( $E_Z$ ). Figure B-6 shows, on a data run by data run basis, how the vertical and overall field magnitude varied. For most data runs, the vertical field was the dominant component of the field magnitude. Over half of the data runs had the vertical field as 75% or greater of the total electric field magnitude.

The mean altitude of the data run along with the maximum value of LWC and the minimum and maximum value of the ice detector voltage were also recorded. Examples of the other recorded components are shown in Figures B-6 and B-7. Note that plots from all data runs are available and Portable Network Graphics (PNG) files on an accompanying CD. There were a total of 1517 data runs in the re-analysis.

The field distribution for the  $E_{MAX}$  fields for all data runs is shown in Figure B-8. The maximum  $E_{MAX}$  field found for all data runs was  $126 \text{ kV m}^{-1}$ . The mean  $E_{MAX}$  field was  $9.5 \text{ kV m}^{-1}$  and the median field was  $1.9 \text{ kV m}^{-1}$ . The field distribution for the  $E_Z$  fields for all data runs is shown in Figure B-9. The maximum  $E_Z$  field found for all data runs was  $108 \text{ kV m}^{-1}$ . The mean  $E_Z$  field was  $8.0 \text{ kV m}^{-1}$  and the median field was  $1.4 \text{ kV m}^{-1}$ . Some data runs did not penetrate the target cloud mass and so if we restrict the data runs to the 1372 that actually penetrated the target cloud for at least some time, we get Figures B-10 and B-11 for the  $E_{MAX}$  and  $E_Z$  fields, respectively. The maximum  $E_{MAX}$  field found for cloud penetrations was  $126 \text{ kV m}^{-1}$ . The mean  $E_{MAX}$  field was  $10.3 \text{ kV m}^{-1}$  and the median field was  $2.3 \text{ kV m}^{-1}$ . The maximum  $E_Z$  field found for cloud penetrations was  $108 \text{ kV m}^{-1}$ . The mean  $E_Z$  field was  $8.7 \text{ kV m}^{-1}$  and the median field was  $1.6 \text{ kV m}^{-1}$ . Because the analysis was directed to focus on data runs that actually penetrated the target clouds, all subsequent plots will be restricted to those where the cloud was actually penetrated. Table B-1 summarizes the electric field data.

## Rule Specific Results

Subsequent plots will be classified by the Launch Commit Criteria (LCC) rules that were in place at the time of the ABFM-I study. Each rule will have its own section. Here are the rules that were in place at the time of the ABFM-I project:

DO NOT LAUNCH IF:

- A. Any type of lightning is detected within 10 nautical miles of the launch site or planned flight path within 30 minutes prior to launch unless the meteorological condition that produced the lightning has moved more than 10 nautical miles away from the launch site or planned flight path.
- B. The planned flight path will carry the vehicle
  - a. (B1) through cumulus clouds with tops higher than the  $+5^\circ\text{C}$  level; or
  - b. (B2) through or within 5 nautical miles of cumulus clouds with tops higher than  $-10^\circ\text{C}$  level; or
  - c. (B3) through or within 10 nautical miles of cumulus clouds with tops higher than the  $-20^\circ\text{C}$  level; or

- d. (B4) through or within 10 nautical miles of the nearest edge of any cumulonimbus or thunderstorm cloud including its associated anvil.
- C. For ranges equipped with a surface electric field mill network, at any time during the 15 minutes prior to launch time the one minute average absolute electric field intensity at the ground exceed 1 kilovolt per meter within 5 nautical miles of the launch site unless:
- a. There are no clouds within 10 nautical miles of the launch site; and
  - b. Smoke and ground fog are clearly causing abnormal readings.
- D. The planned flight path is through a vertically continuous layer of clouds with an overall depth of 4,500 feet or greater where any part of the clouds is located between the 0 and -20°C temperature levels.
- E. The planned flight path is through any cloud types that extend to altitudes at or above the 0°C level and that are associated with disturbed weather within 5 nautical miles of the flight path.
- F. Do not launch through thunderstorm debris clouds, or within 5 nautical miles of thunderstorm debris clouds not monitored by a field mill network or producing radar returns greater than or equal to 10 dBz.

#### GOOD SENSE RULE

Even when constraints are not violated, if any other hazardous conditions exist, the launch weather officer will report the threat to the launch director. The launch director may hold at any time based on the instability of the weather.

#### Rule A

Rule A violations will be considered as part of rule B4. Both the A and B4 rule clouds were mature thunderstorms usually with lightning.

#### Rule B1

Figure B-12 shows the  $E_{MAX}$  fields distribution for the rule B1 violation penetrations. There were a total of 55 penetrations of clouds that violated the B1 launch rule. The peak  $E_{MAX}$  field found during penetrations of B1 violation clouds was  $11.9 \text{ kV m}^{-1}$ . The mean and median  $E_{MAX}$  fields were  $1.3 \text{ kV m}^{-1}$  and  $0.6 \text{ kV m}^{-1}$ , respectively.

Figure B-13 shows the  $E_Z$  fields distribution for the rule B1 clouds. The peak  $E_Z$  field found during penetrations of B1 violation clouds was  $2.3 \text{ kV m}^{-1}$ . The mean and median  $E_Z$  fields were  $0.5 \text{ kV m}^{-1}$  and  $0.3 \text{ kV m}^{-1}$ , respectively.

The two runs where the fields in the B1 clouds were the highest were clouds that were nearly B2 violations, as indicated by pilot comments. The two very high  $E_{MAX}$  fields may not reflect the true fields in the B1 type clouds.

## Rule B2

Figure B-14 shows the  $E_{MAX}$  fields distribution for the rule B2 violation penetrations. There were a total of 36 penetrations of clouds that violated the B2 launch rule. The peak  $E_{MAX}$  field found during penetrations of B2 violation clouds was  $23.6 \text{ kV m}^{-1}$ . The mean and median  $E_{MAX}$  fields were  $3.9 \text{ kV m}^{-1}$  and  $2.1 \text{ kV m}^{-1}$ , respectively.

Figure B-15 shows the  $E_Z$  fields distribution for the rule B2 clouds. The peak  $E_Z$  field found during penetrations of B2 violation clouds was  $16.1 \text{ kV m}^{-1}$ . The mean and median  $E_Z$  fields for the B2 cloud penetrations were  $2.2 \text{ kV m}^{-1}$  and  $0.9 \text{ kV m}^{-1}$ , respectively.

## Rule B3

Figure B-16 shows the  $E_{MAX}$  fields distribution for the rule B3 violation penetrations. There were a total of 152 penetrations of clouds that violated the B3 launch rule. The peak  $E_{MAX}$  field found during penetrations of B3 violation clouds was  $108. \text{ kV m}^{-1}$ . The mean and median  $E_{MAX}$  fields were  $26.0 \text{ kV m}^{-1}$  and  $24.0 \text{ kV m}^{-1}$ , respectively.

Figure B-17 shows the  $E_Z$  fields distribution for the rule B3 clouds. The peak  $E_Z$  field found during penetrations of B3 violation clouds was  $95.5 \text{ kV m}^{-1}$ . The mean and median  $E_Z$  fields for the B3 cloud penetrations were  $23.1 \text{ kV m}^{-1}$  and  $19.5 \text{ kV m}^{-1}$ , respectively.

## Rule B4/A

Figure B-18 shows the  $E_{MAX}$  field distribution for the rule B4/A violation penetrations. There were a total of 204 penetrations of clouds that violated the B4/A launch rules. The peak  $E_{MAX}$  field found during penetrations of B4/A violation clouds was  $102. \text{ kV m}^{-1}$ . The mean and median  $E_{MAX}$  fields were  $25.5 \text{ kV m}^{-1}$  and  $20.0 \text{ kV m}^{-1}$ , respectively.

Figure B-19 shows the  $E_Z$  fields distribution for the rule B4/A clouds. The peak  $E_Z$  field found during penetrations of B4/A violation clouds was  $88.2 \text{ kV m}^{-1}$ . The mean and median  $E_Z$  fields for the B4/A cloud penetrations were  $22.1 \text{ kV m}^{-1}$  and  $17.5 \text{ kV m}^{-1}$ , respectively.

It would seem counterintuitive that fields inside the more “severe” clouds would actually be lower than the fields in a less severe cloud type. However, due to aircraft flight restrictions (due to lightning in the area or the reflectivity exceeded aircraft safety limits), the aircraft aborted the penetration. This mission operations protocol results in the most severe fields of the B4/A clouds not being detected by the aircraft.

## Rule C

Penetrations associated only with a violation under rule C were not catalogued in this re-analysis because access to the archived GBFM data for this period was not available. Note, nearly all the penetrations had some other rule violation and they were classified by the other rules violated.

## Rule D

There were a total of 571 penetrations where the main rule violated was they layered cloud rule D. Figure B-20 shows the distribution of  $E_{MAX}$  fields for rule D violation penetrations. The maximum fields found were  $48.9 \text{ kV m}^{-1}$ . The mean and median  $E_{MAX}$  fields were  $2.4 \text{ kV m}^{-1}$  and  $1.0 \text{ kV m}^{-1}$ , respectively.

Figure B-21 shows the  $E_Z$  fields distribution for the rule D clouds. The peak  $E_Z$  field found during penetrations of D violation clouds was  $42.9 \text{ kV m}^{-1}$ . The mean and median  $E_Z$  fields for the D cloud penetrations were  $1.9 \text{ kV m}^{-1}$  and  $0.8 \text{ kV m}^{-1}$ , respectively.

## Rule E

Figure B-22 shows the  $E_{MAX}$  fields distribution for the rule E violation penetrations. There were a total of 179 penetrations of clouds that violated the E launch rules. The peak  $E_{MAX}$  field found during penetrations of E violation clouds was  $126. \text{ kV m}^{-1}$ . The mean and median  $E_{MAX}$  fields were  $10.5 \text{ kV m}^{-1}$  and  $4.1 \text{ kV m}^{-1}$ , respectively.

Figure B-23 shows the  $E_Z$  fields distribution for the rule E clouds. The peak  $E_Z$  field found during penetrations of E violation clouds was  $108. \text{ kV m}^{-1}$ . The mean and median  $E_Z$  fields for the E cloud penetrations were  $8.1 \text{ kV m}^{-1}$  and  $2.6 \text{ kV m}^{-1}$ , respectively.

## Rule F

Although debris clouds are often considered two different entities (low level debris and anvil debris), the launch rules considered them a single entity (debris). For this first section, all clouds that were designated as rule F violations were considered as a single category.

Figure B-24 shows the  $E_{MAX}$  fields distribution for the rule F violation penetrations. There were a total of 171 penetrations of clouds that violated the F launch rules. The peak  $E_{MAX}$  field found during penetrations of F violation clouds was  $73.6 \text{ kV m}^{-1}$ . The mean and median  $E_{MAX}$  fields were  $8.7 \text{ kV m}^{-1}$  and  $2.2 \text{ kV m}^{-1}$ , respectively.

Figure B-25 shows the  $E_Z$  fields distribution for the rule F clouds. The peak  $E_Z$  field found during penetrations of F violation clouds was  $68.7 \text{ kV m}^{-1}$ . The mean and median  $E_Z$  fields for the F cloud penetrations were  $7.5 \text{ kV m}^{-1}$  and  $1.7 \text{ kV m}^{-1}$ , respectively.

## Rule F (Anvils)

Using comments from the original ABFM-I operational analyses, some of the general rule F penetrations were identified as anvils. There were a total of 73 identified anvil debris penetrations. There were very likely other anvil debris penetrations, but it was not possible to verify them from the data available.

Figure B-26 shows the  $E_{MAX}$  fields distribution for the rule F anvil debris violation penetrations. The peak  $E_{MAX}$  field found during penetrations of F anvil violation clouds was  $61.1 \text{ kV m}^{-1}$ . The mean and median  $E_{MAX}$  fields were  $6.6 \text{ kV m}^{-1}$  and  $1.7 \text{ kV m}^{-1}$ , respectively.

Figure B-27 shows the  $E_Z$  fields distribution for the rule F anvil clouds. The peak  $E_Z$  field found during penetrations of anvil F violation clouds was  $51.3 \text{ kV m}^{-1}$ . The mean and median  $E_Z$  fields for the anvil F cloud penetrations were  $5.2 \text{ kV m}^{-1}$  and  $1.4 \text{ kV m}^{-1}$ , respectively.

For a smaller subset of anvil debris cloud penetrations, it was possible to determine a “detachment time” so that the age of the anvil debris was determined. Figures B-28 and B-29 show the anvil debris fields as a function of age for  $E_{MAX}$  and  $E_Z$  fields, respectively.

## **Future Work Suggestions**

The main impediment to any future analysis of the ABFM-I data is the age of the data. After 15 years, the radar data is in a format that is currently unreadable (i.e., the software and much of the documentation that was used to decode this unique format no longer exist). Furthermore, even if the radar data were available, it was collected in an uncalibrated manner, greatly limiting quantitative application of this data. The airborne data itself also proved difficult to process due to its format. Simply resurrecting the original code has proved to be a very difficult (and a still somewhat incomplete) process. There are a few areas where further, more detailed analyses may yield results.

## **Anvils**

To increase the amount of anvil debris decay data, a more detailed analysis of the flight summaries and other data will be needed. Finding the times when the various anvils actually detached from their parent cloud could lead to a significant increase in anvil decay cases. Unfortunately, this may require data that is no longer available (i.e., radar or pilots recorded comments).

## **Standoff**

The main obstacle to the standoff distance calculations is the loss of the LORAN-C data any time there were fields of any magnitude. During the original ABFM analysis, a dead reckoning method was used, but it was very susceptible to wind drift and other errors. Converting this code from the old system to a more modern one, and adding factors for wind and other errors could produce a better set of standoff data than what is available in the original analysis. A recent re-examination of the standoff data from both the ABFM-I and ABFM-II was published as Merceret et al. [2008].

## **Liquid Water Content (LWC) Data**

The equation to determine the LWC value from the various available raw measurements proved to be very cryptic and difficult formula to duplicate. A more detailed analysis of the formulas in the code and how those formulas were applied to the raw data might provide a better measurement of the LWC values for any future analysis.

## **Ice Detection (Charge Patch Voltage)**

There are two major problems with the ice detector voltage that restrict the utility of that measurement. The first is the limited voltage range of the data ( $\pm 2.1$  V or so). This limitation cannot be overcome as it is inherent in the data. The second limitation is in the interpretation of the voltage values. It may be possible to understand when and why the voltages change sign and magnitude. From monitoring the charge patch voltage, it seems as if there is more information in the data. There seemed to be a general pattern in the min/max voltage values of the ice detector, but I was not able to relate that pattern to water, mixed phase, or ice clouds from the min/max values during a data run. Determination of the pattern (or patterns) will take a detailed examination of the time series of the ice detector as it often radically changed polarities during a single data run (Figure B-7).

## **Accelerometer Data**

The ABFM-I aircraft recorded the vector acceleration experienced by the aircraft. This data has never been analyzed (not even during the original ABFM-I analysis). It is possible this may detect turbulence or up/down drafts in a quantitative way. The spreadsheet data contains any recorded pilot

comments about turbulence, but the accelerometer output may provide more quantitative data on down/up drafts and/or turbulence. The data was recorded at a rate that might be useful, but the underlying resolution of the data is unknown.



## References for Appendix B

Bateman, M. G., M. F. Stewart, R. J. Blakeslee, S. J. Podgorny, H. J. Christian, D. M. Mach, J. C. Bailey, and D. Daskar. "A Low-noise, Microprocessor-controlled, Internally Digitizing Rotating-vane Electric Field Mill for Airborne Platforms." *J. Atmos. Ocean. Tech.* 24 (2007): pp. 1245–1255, DOI: 10.1175/JTECH2039.1.

Gish, O. H., and G. R. Wait. "Thunderstorms and the Earth's General Electrification." *J. Geophys. Res.* 55 (1950): 473–484.

Mach, D. M., and W. J. Koshak. "General Matrix Inversion Technique for the Calibration of Electric Field Sensor Arrays on Aircraft Platforms." *J. Atmos. Ocean. Tech.* 24 (2007): pp. 1576–1587, DOI: 10.1175/JTECH2080.1.

Merceret, F. J., J. G. Ward, D. M. Mach, M. G. Bateman, and J. E. Dye. "On the Magnitude of the Electric Field near Thunderstorm-Associated Clouds." *J. Appl. Met. Climate* 47 (2008): pp. 240–248, DOI: 10.1175/2007JAMC1713.1.

Table B-1. Summary of Airborne Field Mill Electric Field Data

Rule	Type	E <sub>MAX</sub>			E <sub>z</sub>			Total
		Mean	Median	Max	Mean	Median	Max	
B1	all	1.3	0.6	11.9	0.5	0.3	2.3	58
	penetrations	1.3	0.6	11.9	0.5	0.3	2.3	55
B2	all	2.9	1.3	23.6	1.7	0.6	16.1	49
	penetrations	3.9	2.1	23.6	2.2	0.9	16.1	36
B3	all	24.4	20.4	108.4	21.7	18.4	95.5	162
	penetrations	26.0	24.0	108.4	23.1	19.5	95.5	152
B4/A	all	21.8	15.5	102.1	18.8	11.2	88.2	243
	penetrations	25.5	20.0	102.1	22.1	17.5	88.2	204
D	all	2.3	0.9	48.9	1.9	0.7	42.9	595
	penetrations	2.4	1.0	48.9	1.9	0.8	42.9	571
E	all	9.5	3.5	126.1	7.4	2.2	107.5	201
	penetrations	10.5	4.1	126.1	8.1	2.6	107.5	179
F	all	7.7	1.6	73.6	6.7	1.5	68.7	197
	penetrations	8.7	2.2	73.6	7.5	1.7	68.7	171
Anvil F	all	5.6	1.3	61.1	4.5	1.0	51.3	86
	penetrations	6.6	1.7	61.1	5.2	1.4	51.3	73
All	all	9.5	1.9	126.1	8.0	1.4	107.5	1516
	penetrations	10.3	2.3	126.1	8.7	1.6	107.5	1372

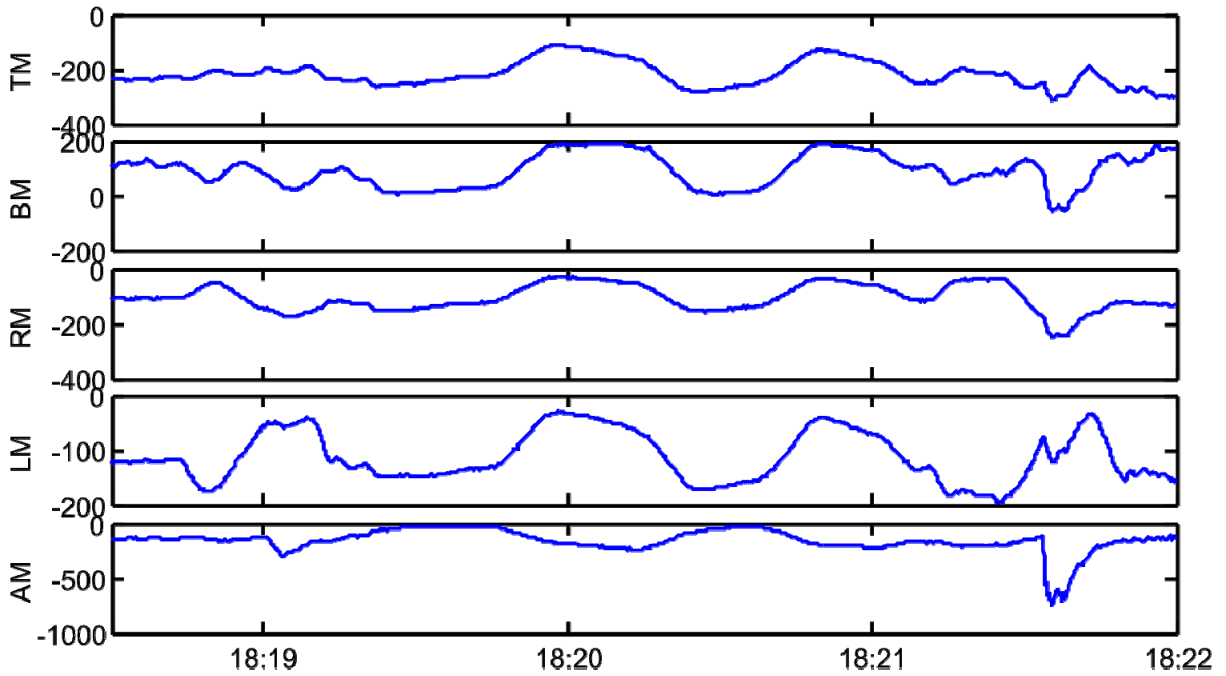


Figure B-1. Raw ABFM-1 mill outputs during a calibration run. The mills are the Top Mill (TM), the Bottom Mill (BM), the Right Mill (RM), the Left Mill (LM), and the Aft Mill (AM). The first four mills were located forward of the wing at the same aircraft location while the AM mill was located in the tail of the aircraft.

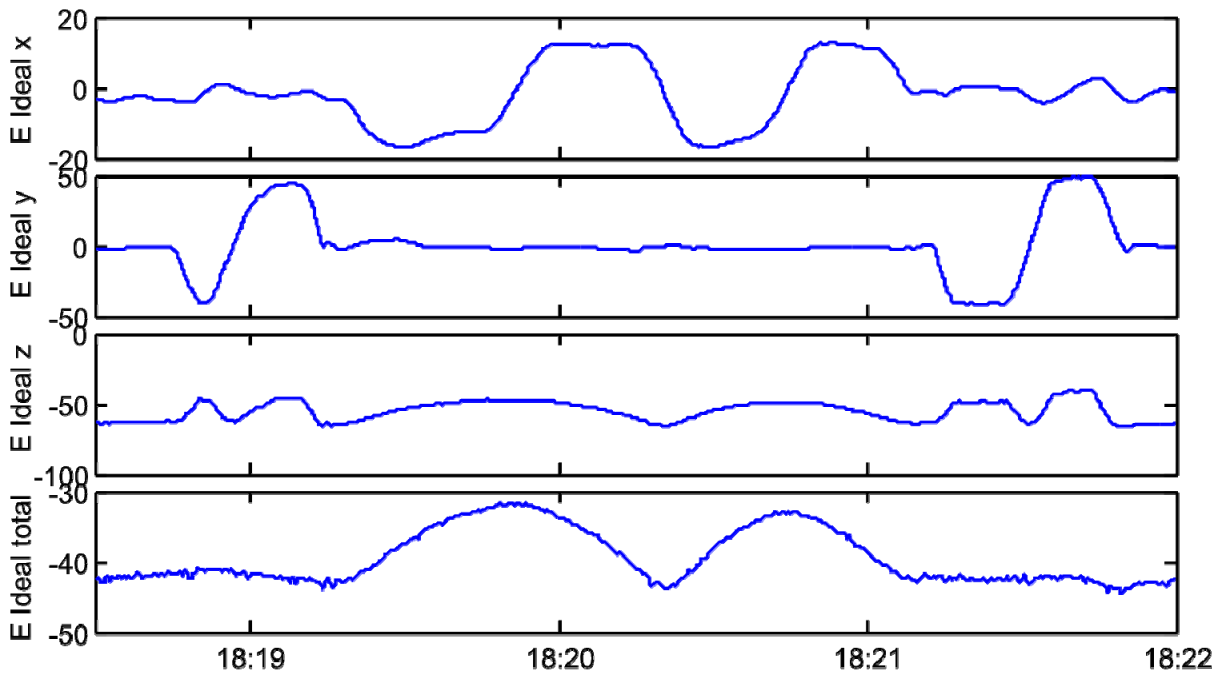


Figure B-2. Ideal mill outputs for the calibration maneuvers. The ideal fields include the effects of altitude, roll & pitch maneuvers, and the surface electric field during a ground based mill fly-by. The last plot (bottom) is the fair weather field at the aircraft altitude. Note the change in the field as the aircraft altitude changes.

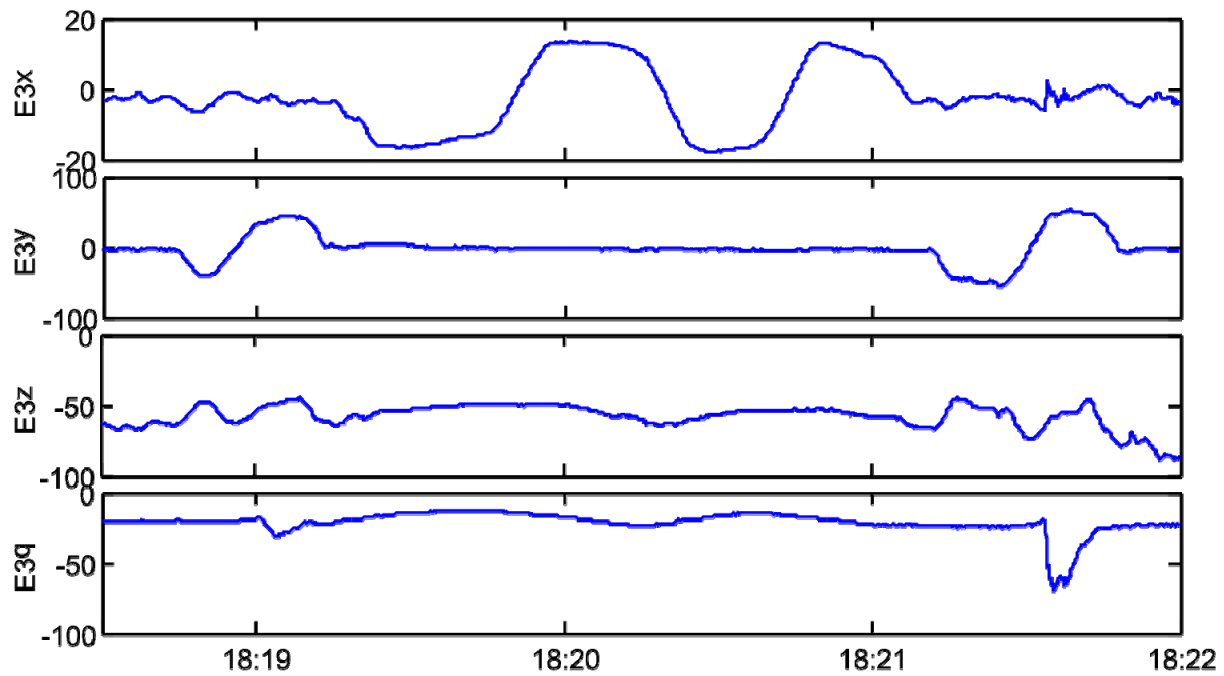


Figure B-3. Final fields after using the calibration method of Mach and Koshak [2007].

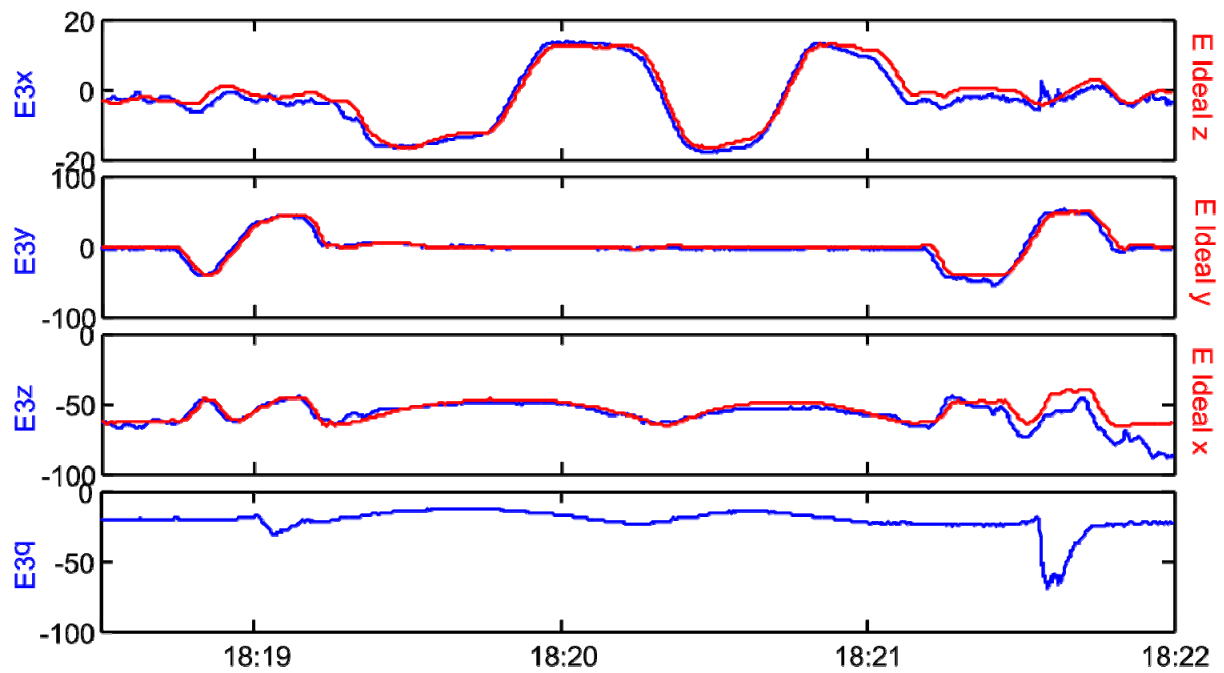


Figure B-4. Comparison of 'ideal' fields (red) with the calibration matrix based fields (blue). There is no "ideal" aircraft charge component.

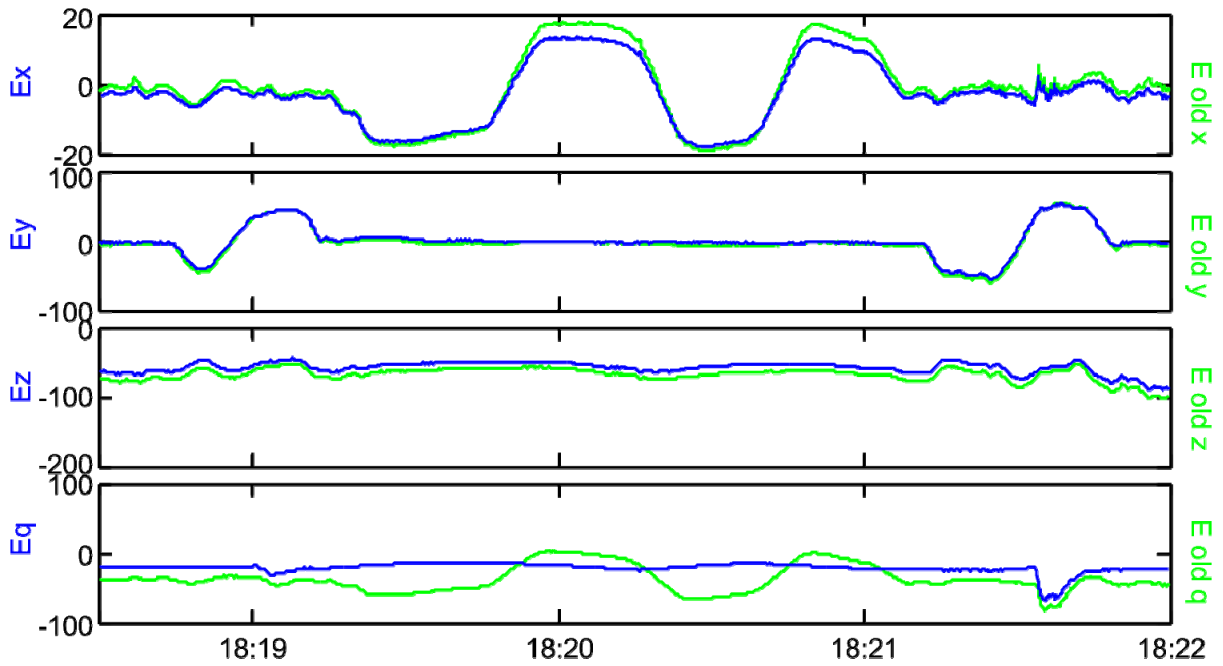


Figure B-5. Comparison of old ABFM calibrated fields (green) with the new ABFM calibrated fields (blue). There are minor differences in the X, Y, & Z components, but a major difference in the Q component. The Q component improvements will increase the accuracy of the fields during cloud penetrations when the charge on the aircraft is large compared to the external field.

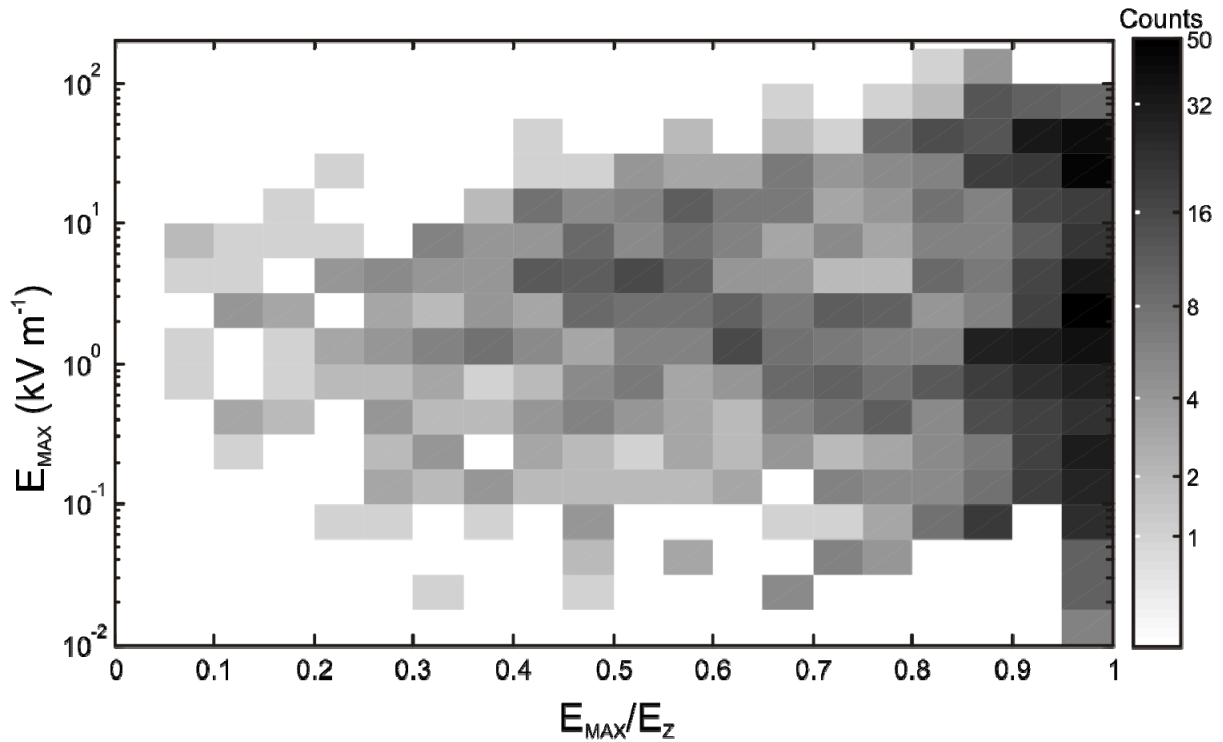


Figure B-6. Distribution of the ratio of  $E_{MAX}/E_Z$  as a function of  $E_{MAX}$ . Most  $E_Z$  fields were nearly the same as the  $E_{MAX}$  fields.

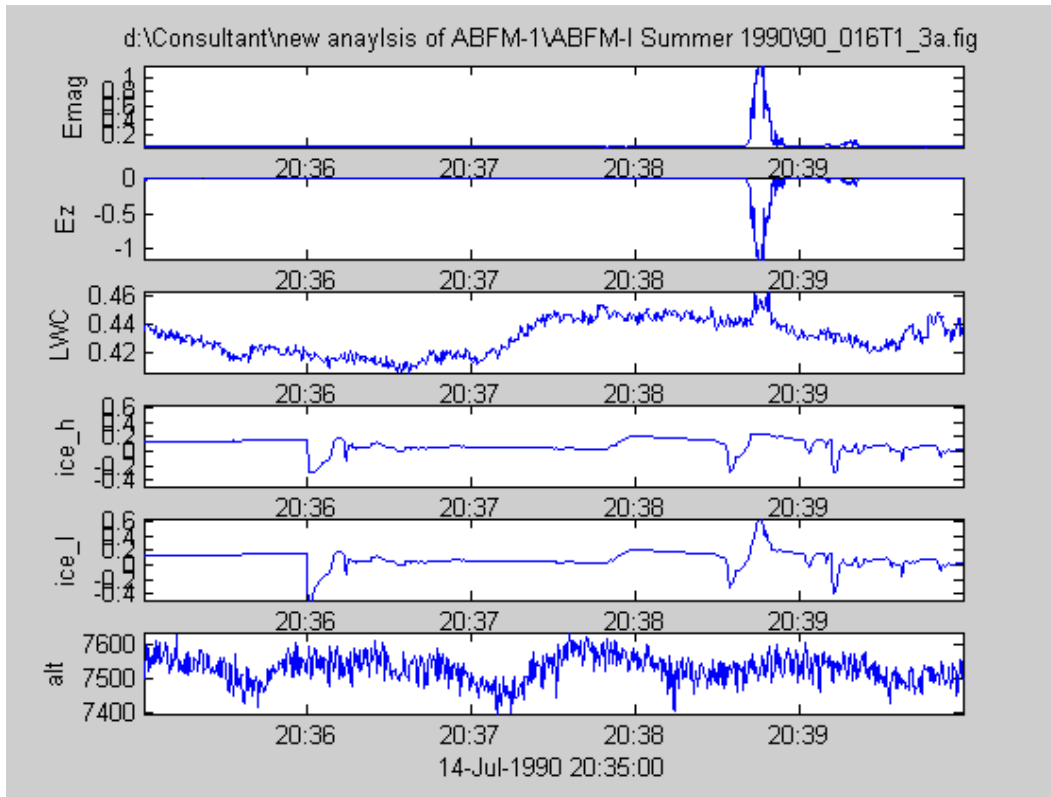


Figure B-7. Example of other data (ice, LWC, and altitude). Note the ice detector voltage changing polarity during the single penetration. The polarity change is not obvious in the ice\_h plot because of saturation of the channel.

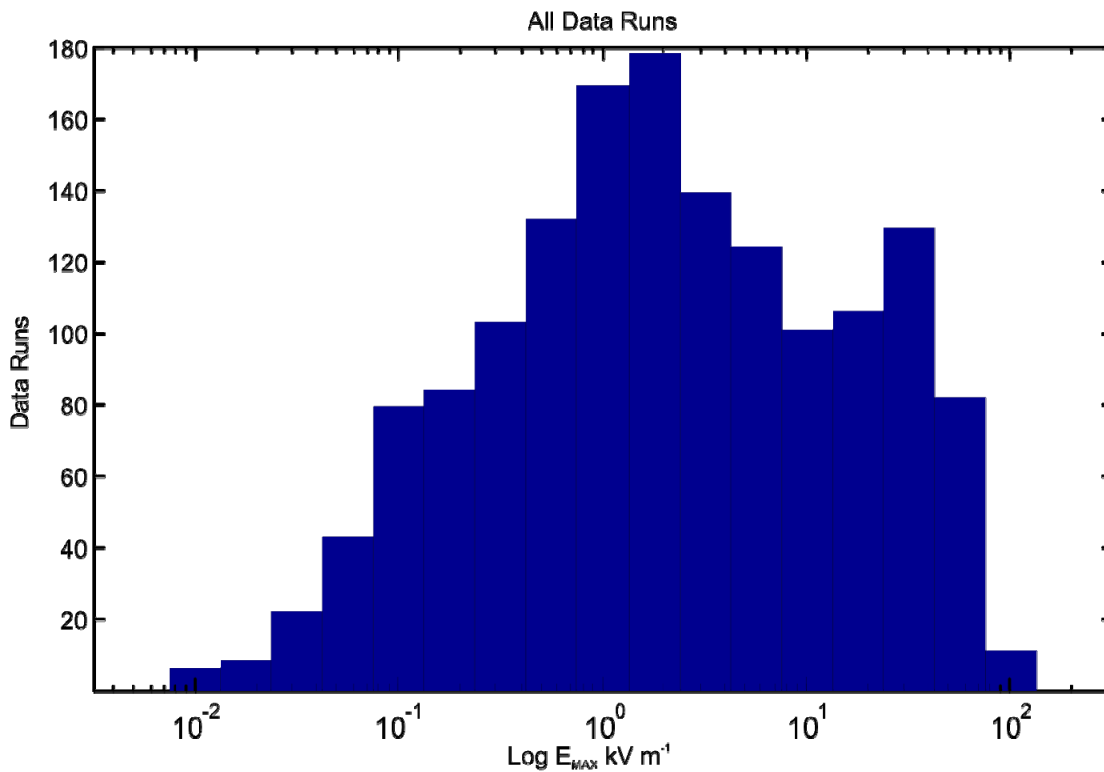


Figure B-8.  $E_{MAX}$  field distribution for all ABFM-1 data runs. The horizontal scale is logarithmic. All data runs include those that did and did not penetrate a cloud.

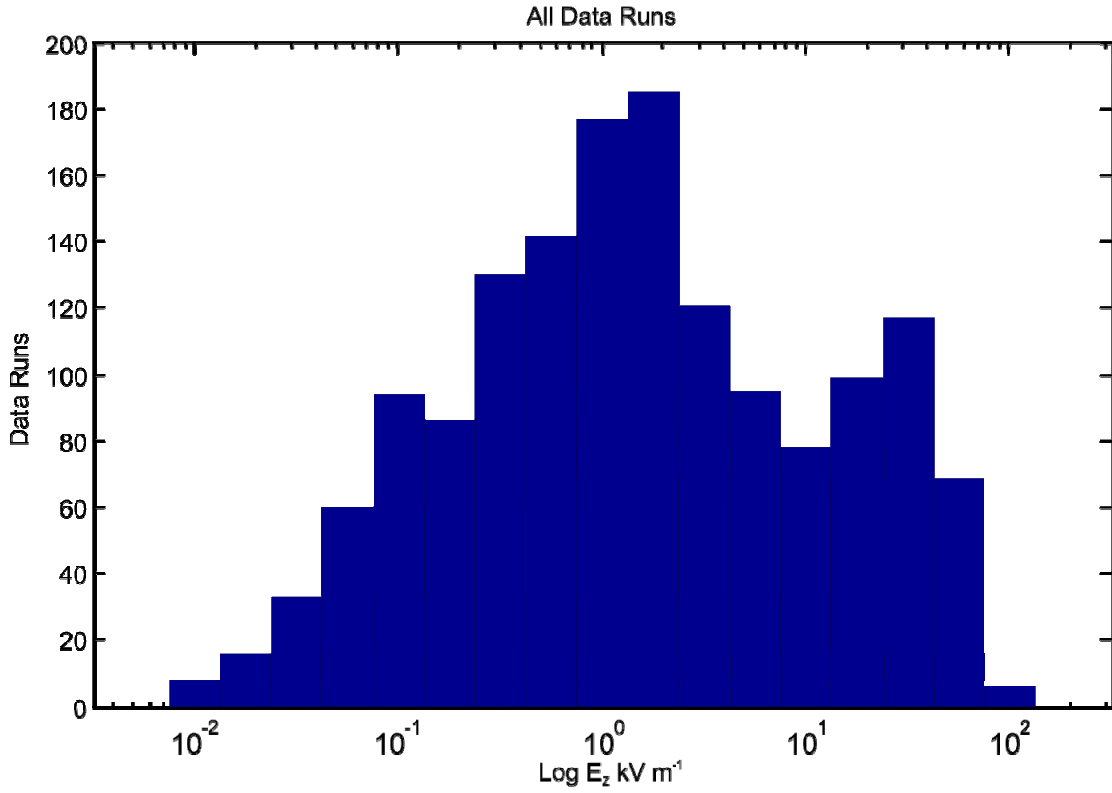


Figure B-9.  $E_z$  field distribution for all ABFM-1 data runs. The horizontal scale is logarithmic. All data runs include those that did and did not penetrate a cloud.

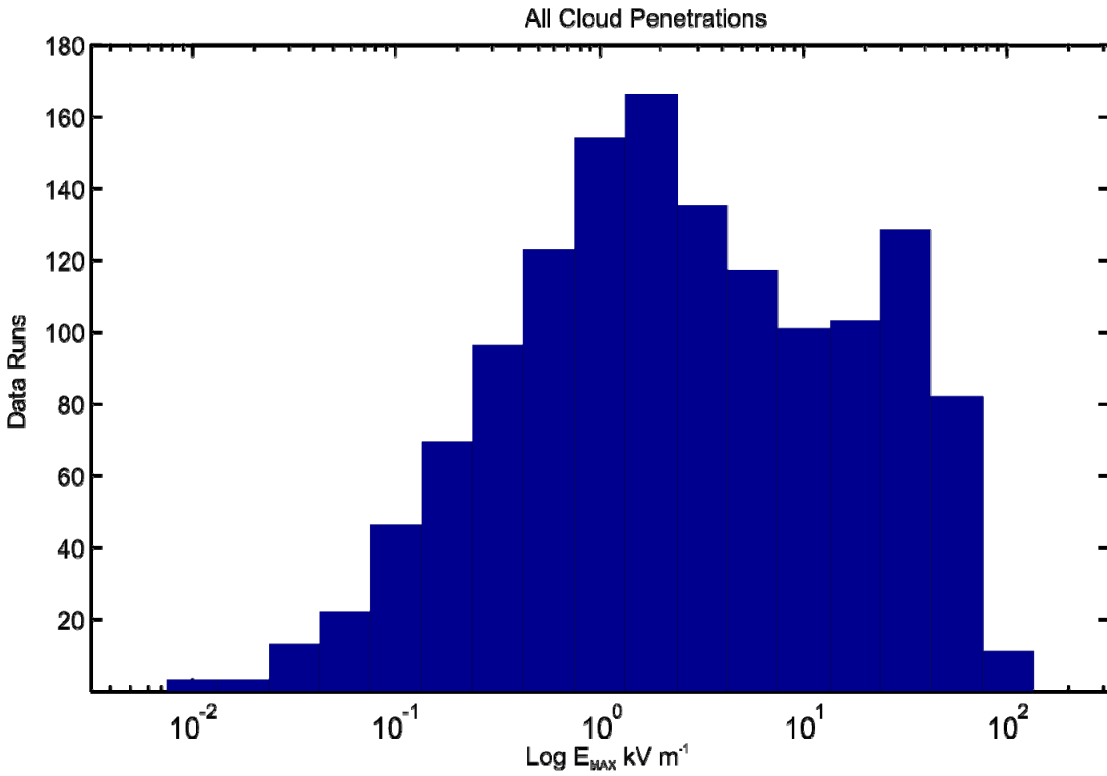


Figure B-10.  $E_{MAX}$  field distribution for all ABFM-1 penetrations. The horizontal scale is logarithmic. Penetrations include only those data runs that penetrated a cloud.

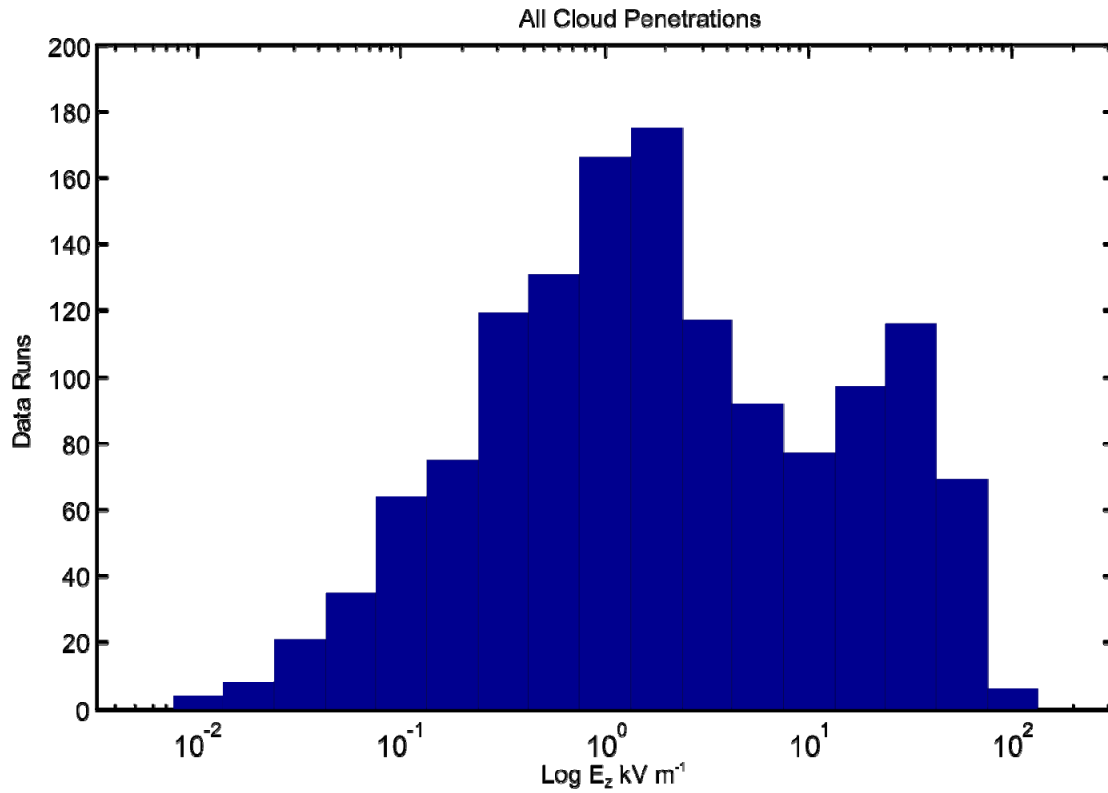


Figure B-11.  $E_z$  field distribution for all ABFM-1 penetrations. The horizontal scale is logarithmic. Penetrations include only those data runs that penetrated a cloud.

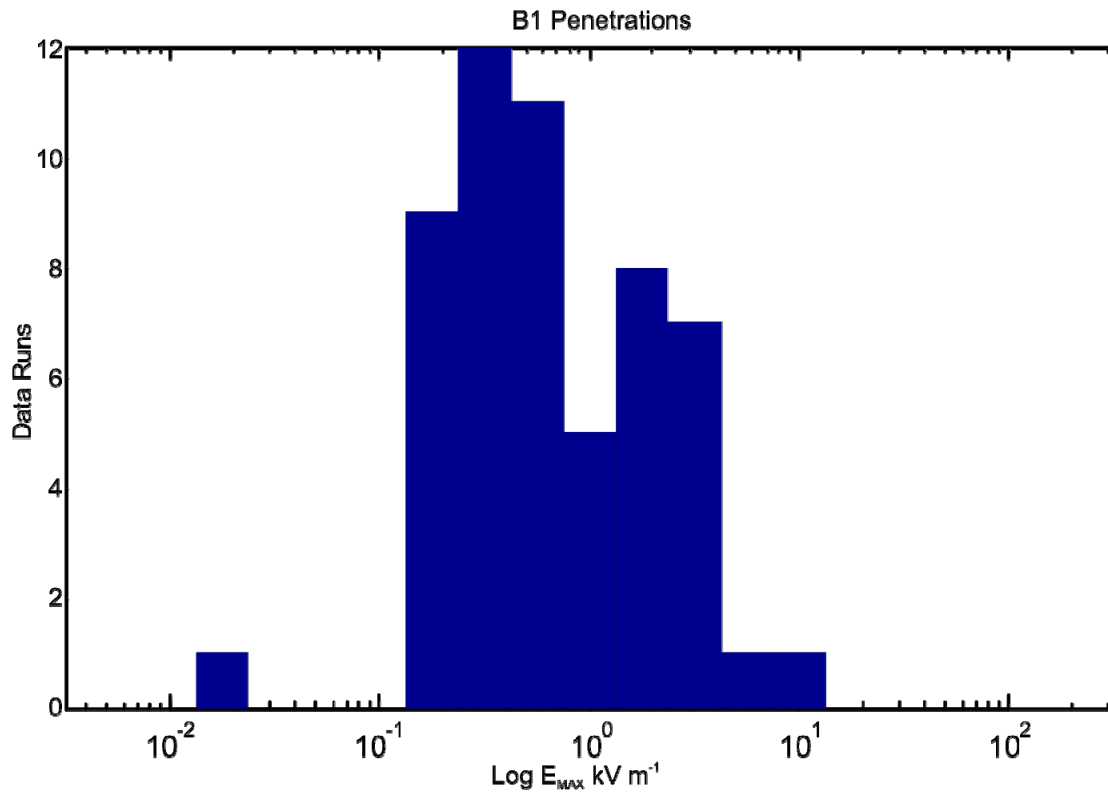


Figure B-12. Distribution of  $E_{MAX}$  fields for B1 rule violation cloud penetration. The horizontal scale is logarithmic.



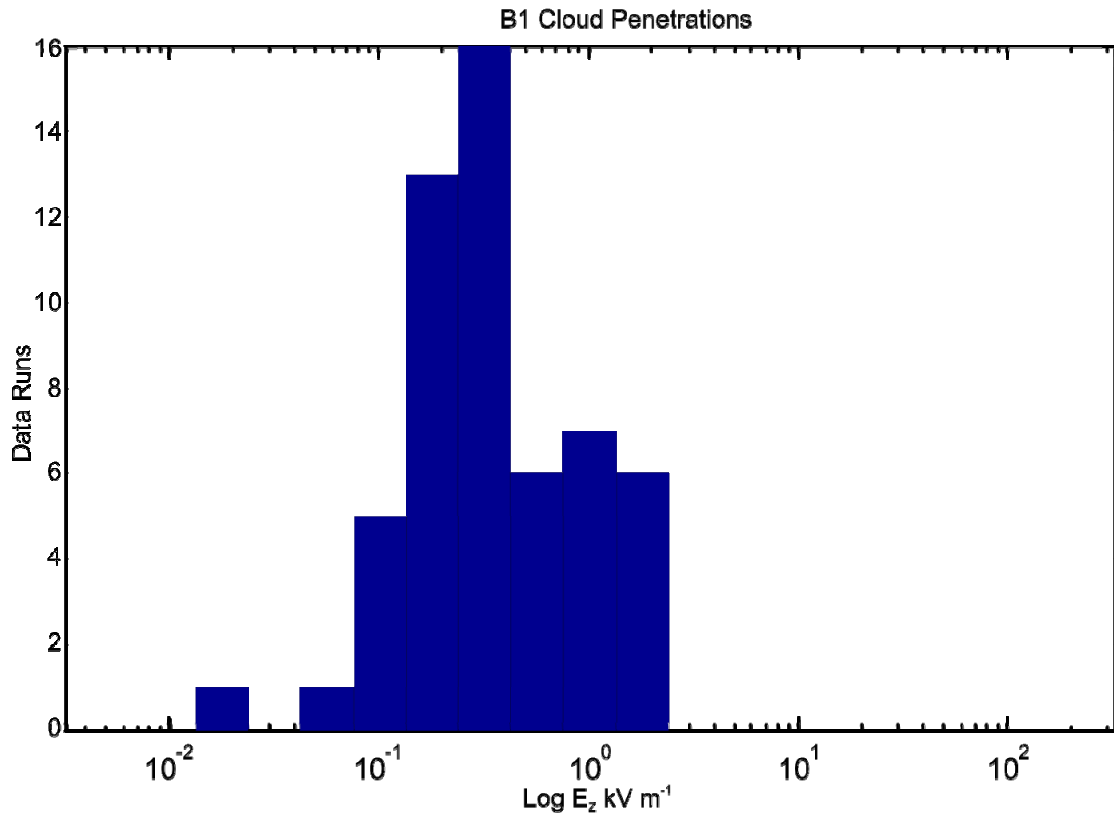


Figure B-13. Distribution of  $E_z$  fields for B1 rule violation cloud penetration. The horizontal scale is logarithmic.

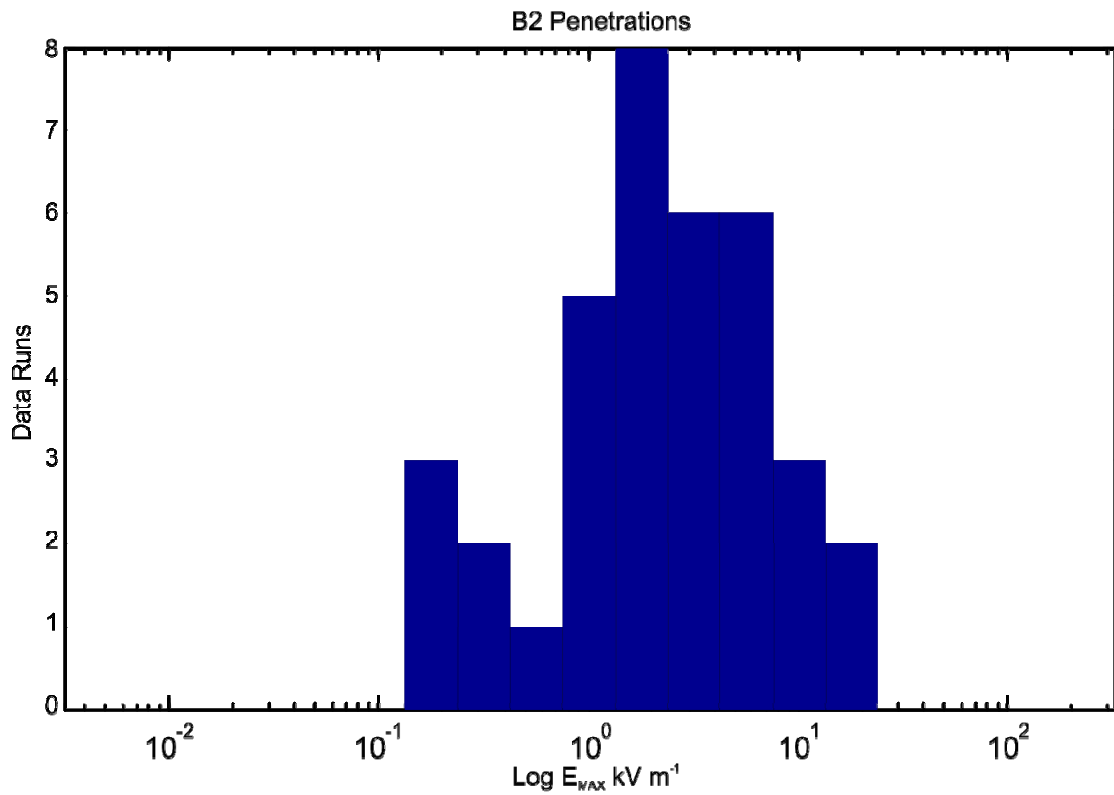


Figure B-14. Distribution of  $E_{MAX}$  fields for B2 rule violation cloud penetration. The horizontal scale is logarithmic.

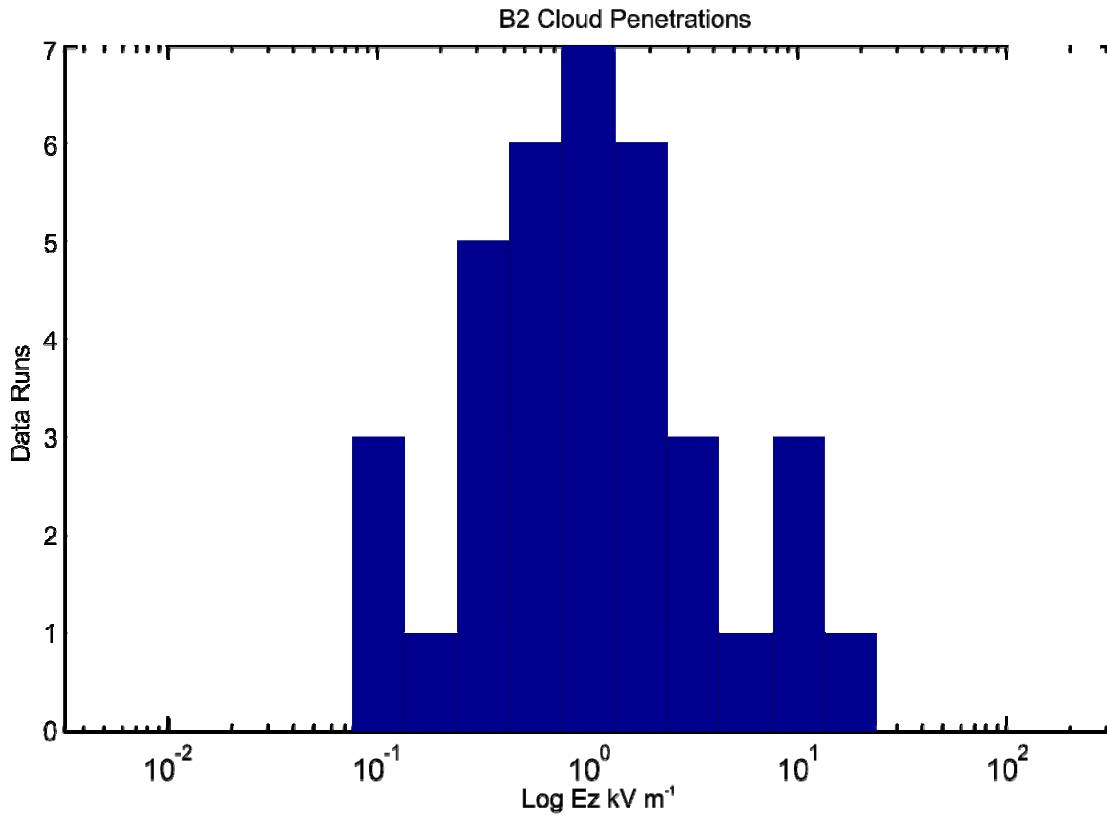


Figure B-15. Distribution of  $E_z$  fields for B2 rule violation cloud penetration. The horizontal scale is logarithmic.

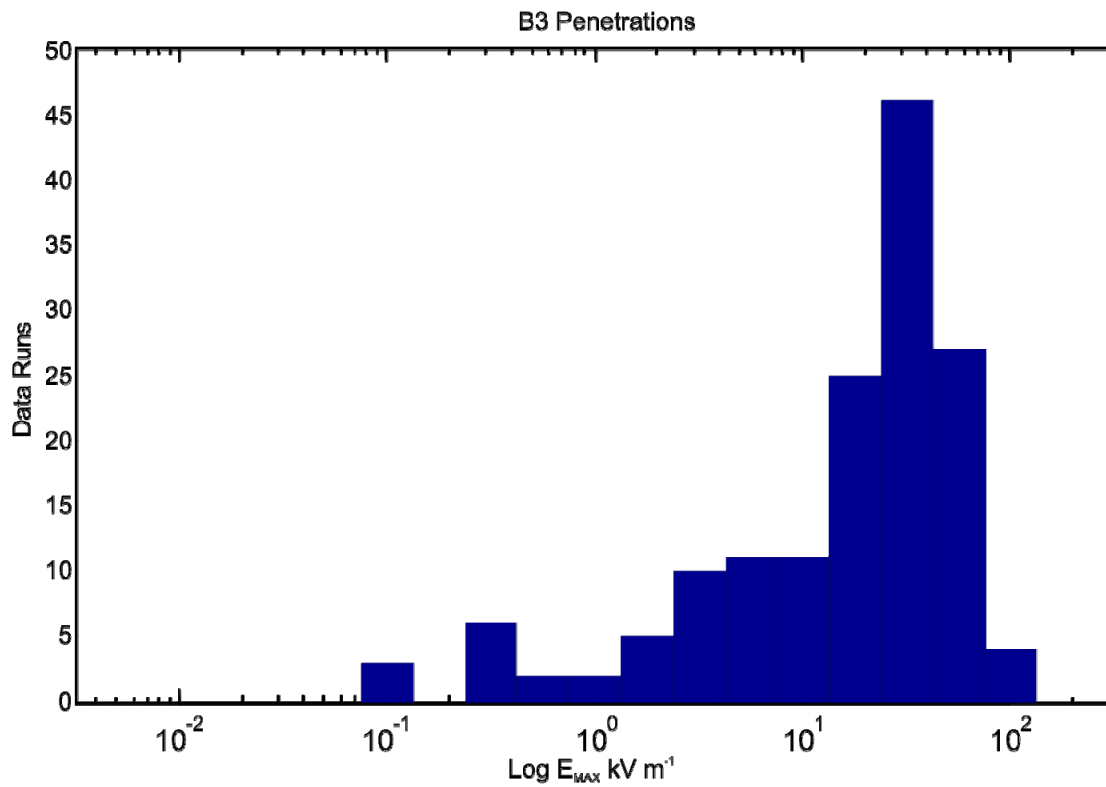


Figure B-16. Distribution of  $E_{MAX}$  fields for B3 rule violation cloud penetration. The horizontal scale is logarithmic.

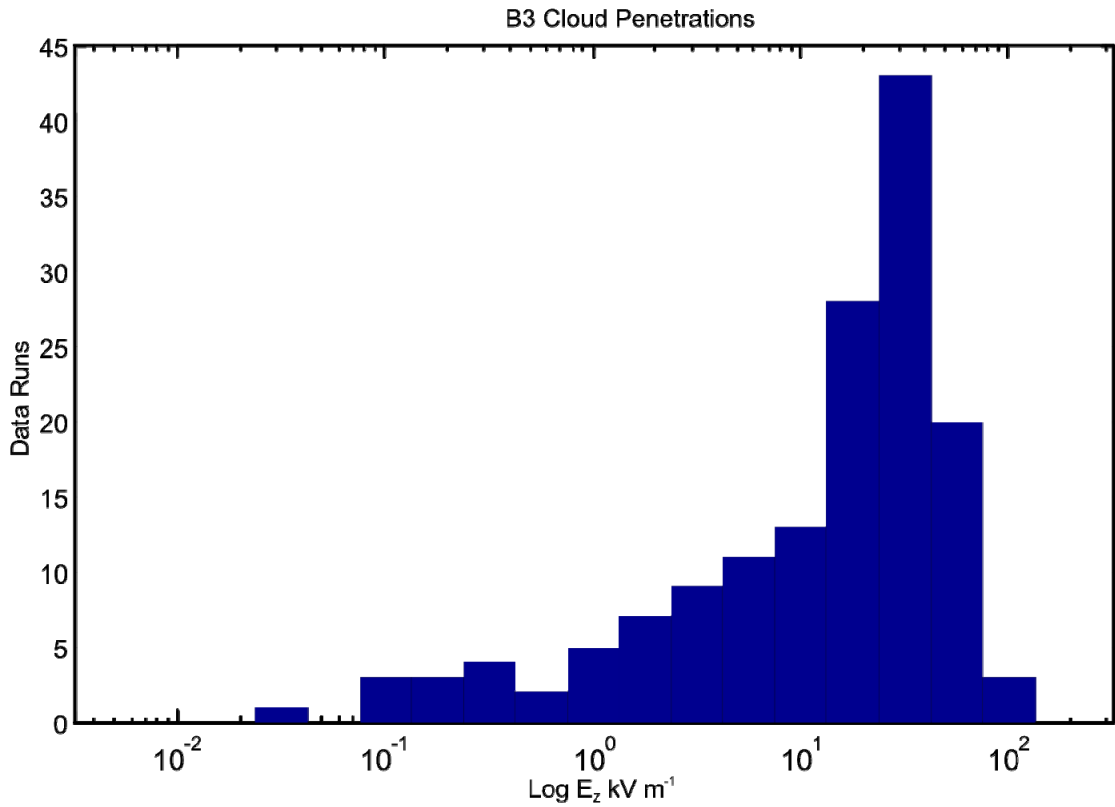


Figure B-17. Distribution of  $E_z$  fields for B3 rule violation cloud penetration. The horizontal scale is logarithmic.

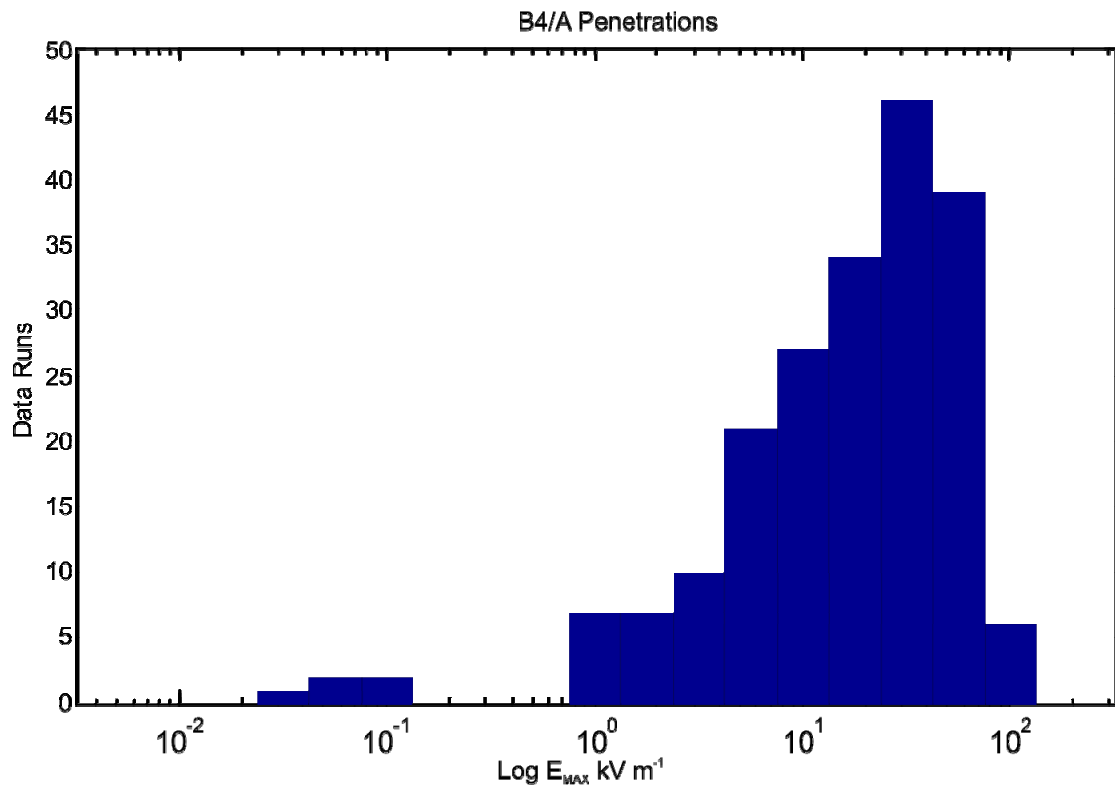


Figure B-18. Distribution of  $E_{MAX}$  fields for B4/A rule violation cloud penetration. The horizontal scale is logarithmic.

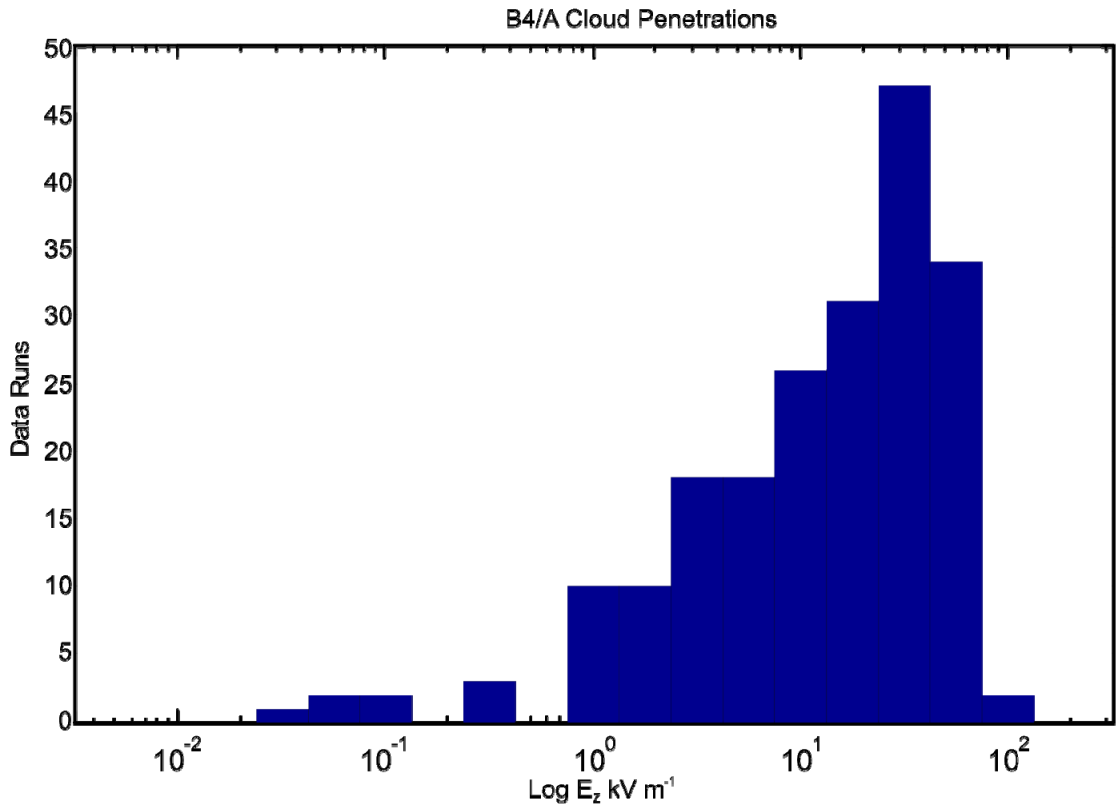


Figure B-19. Distribution of  $E_z$  fields for B4/A rule violation cloud penetration. The horizontal scale is logarithmic.

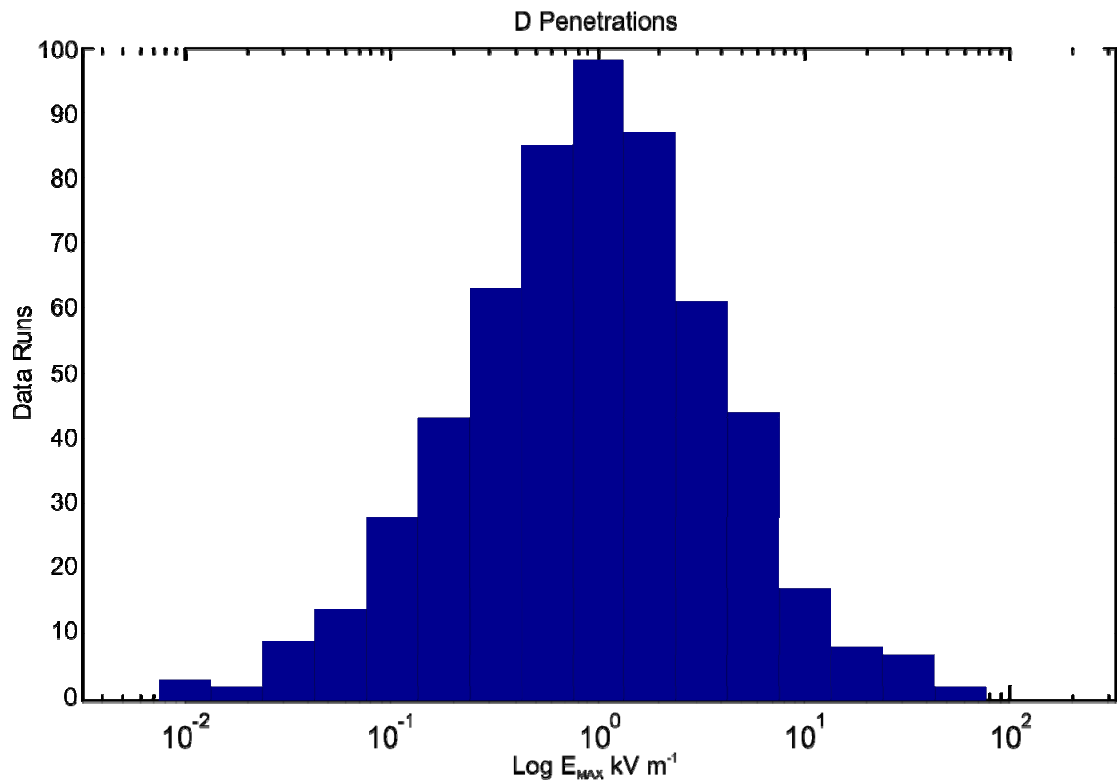


Figure B-20. Distribution of  $E_{MAX}$  fields for D rule violation cloud penetration. The horizontal scale is logarithmic.

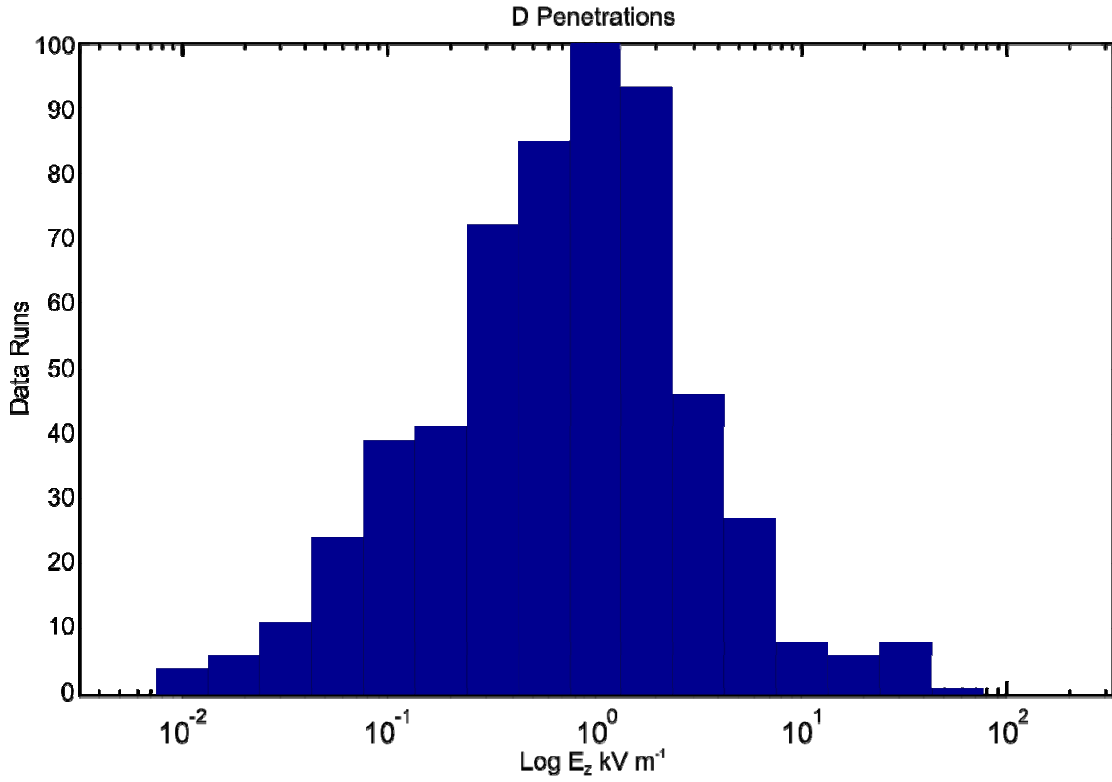


Figure B-21. Distribution of  $E_z$  fields for D rule violation cloud penetration. The horizontal scale is logarithmic.

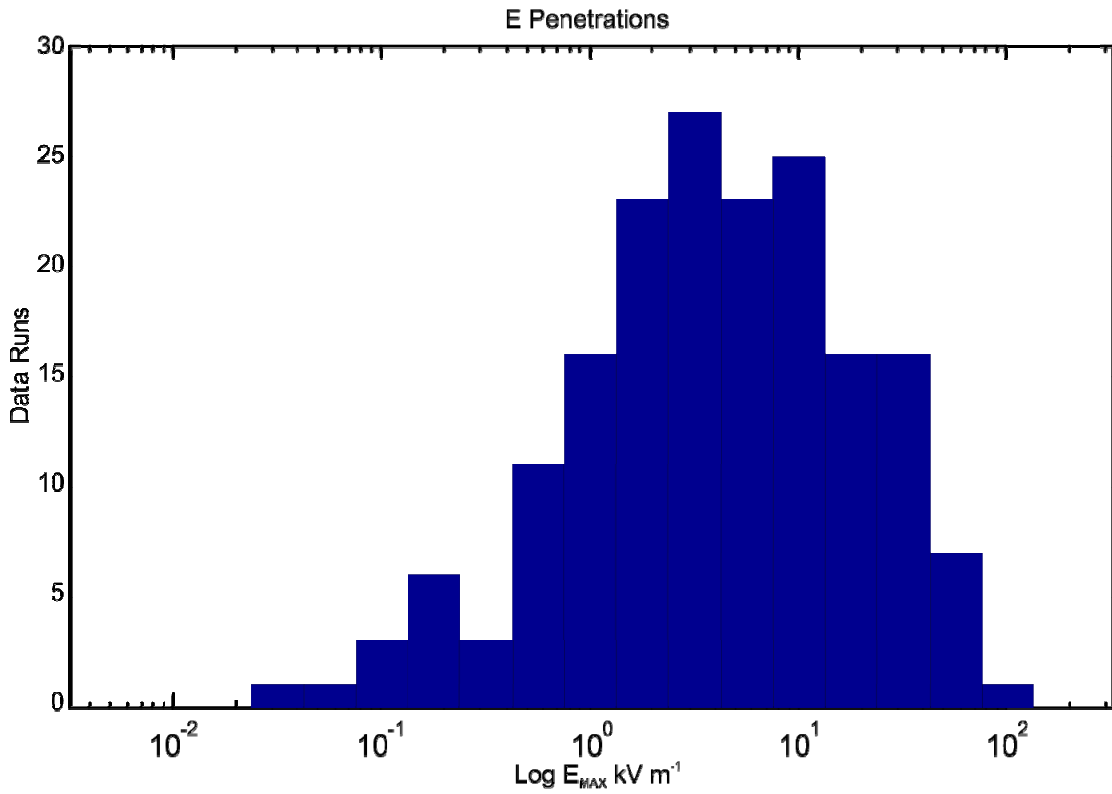


Figure B-22. Distribution of  $E_{MAX}$  fields for E rule violation cloud penetration. The horizontal scale is logarithmic.

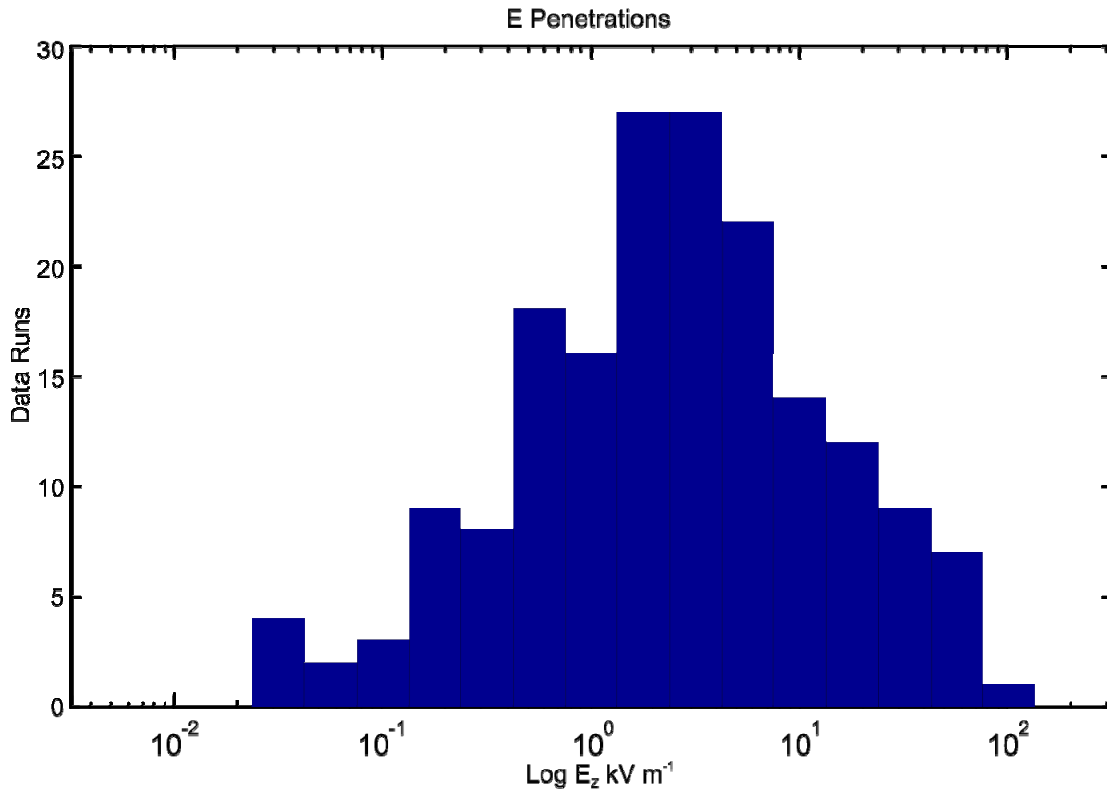


Figure B-23. Distribution of  $E_z$  fields for E rule violation cloud penetration. The horizontal scale is logarithmic.

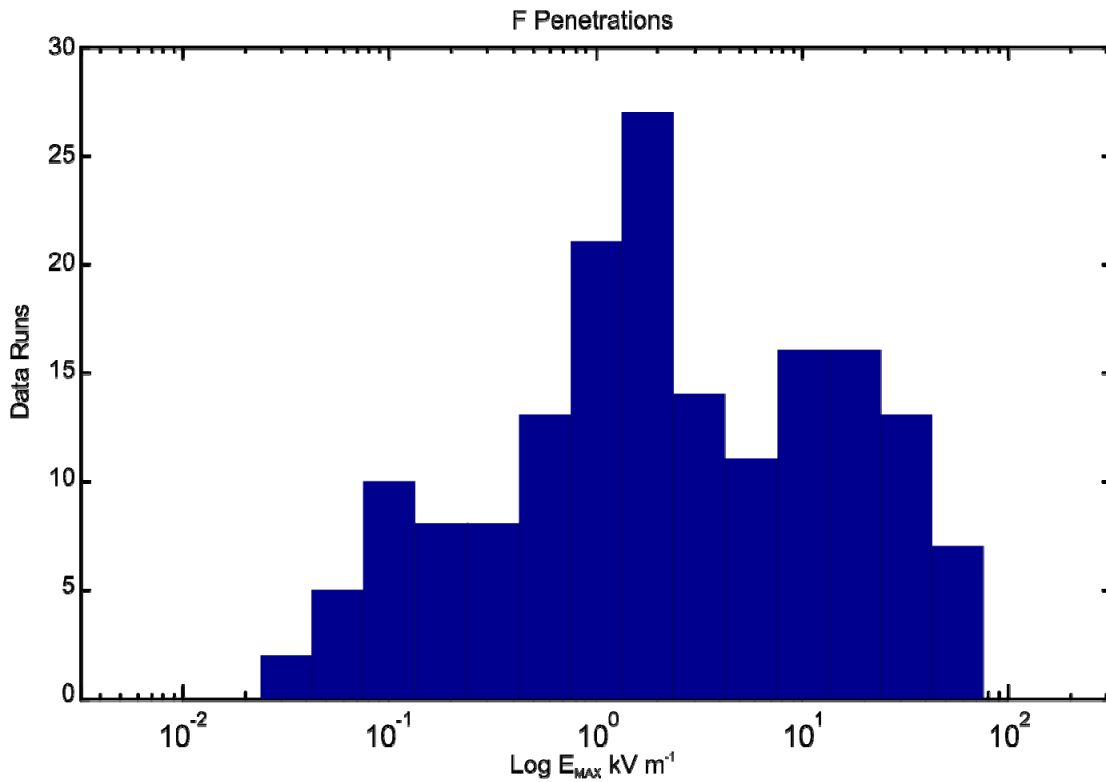


Figure B-24. Distribution of  $E_{MAX}$  fields for F rule violation cloud penetration. The horizontal scale is logarithmic.

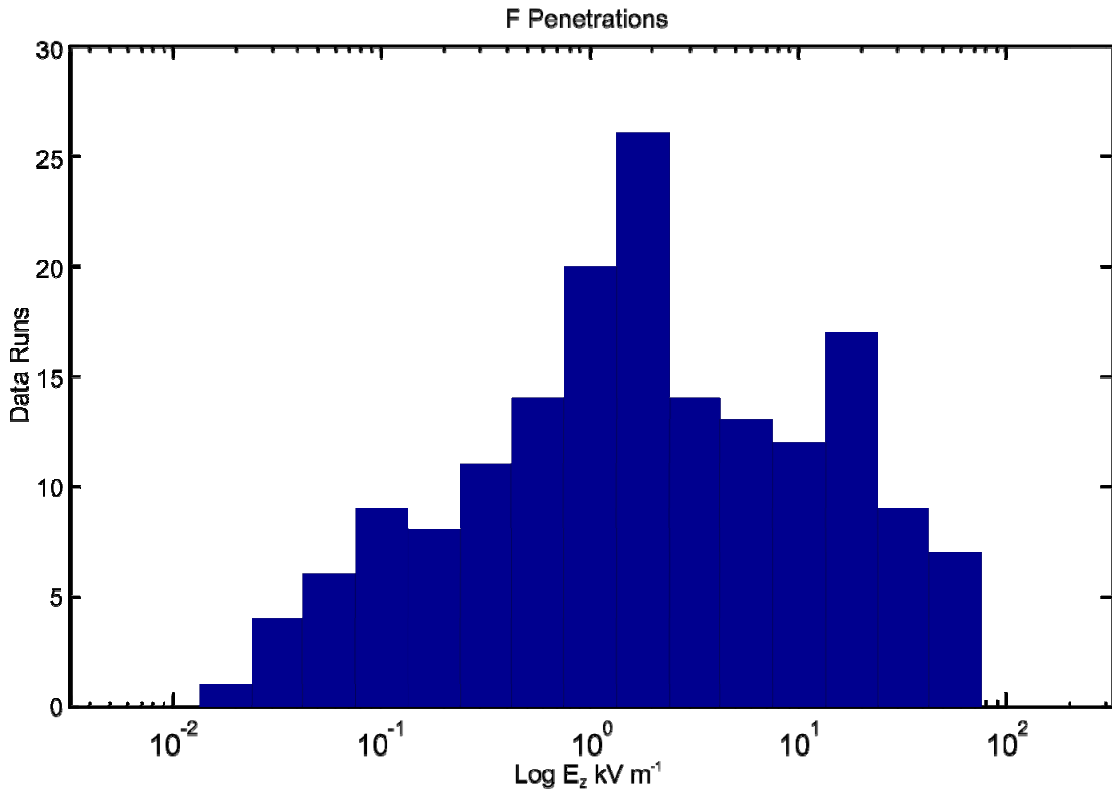


Figure B-25. Distribution of  $E_z$  fields for F rule violation cloud penetration. The horizontal scale is logarithmic.

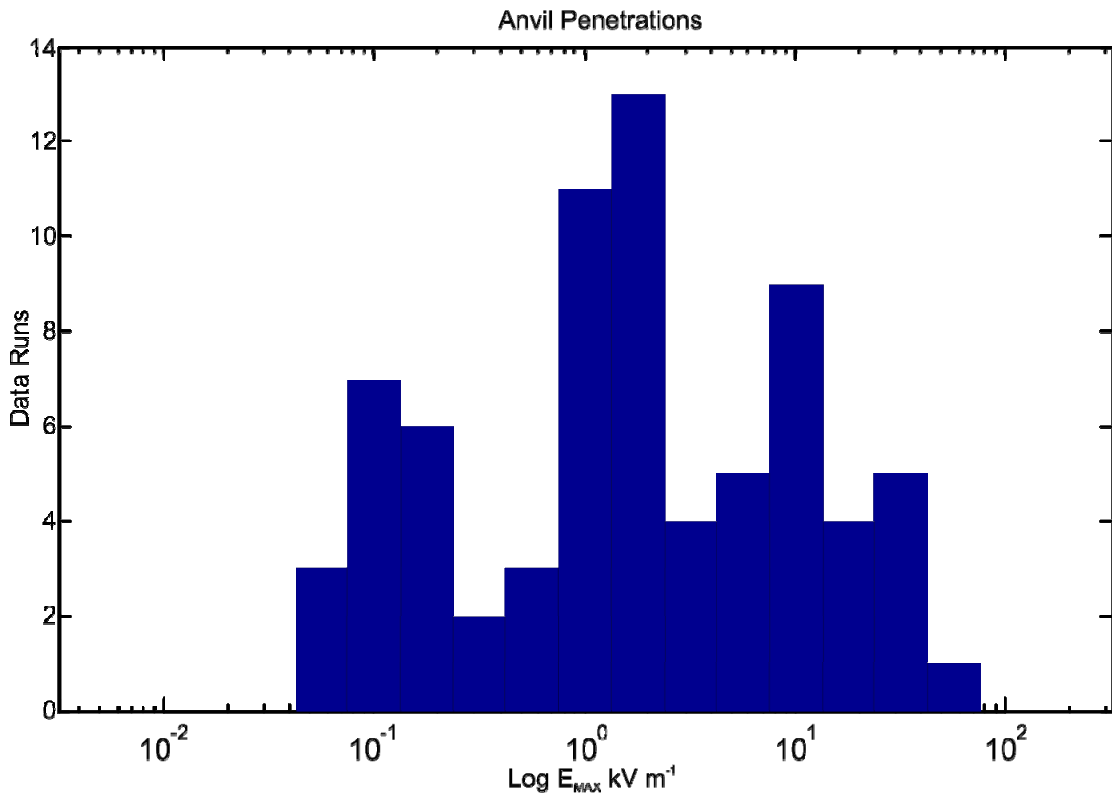


Figure B-26. Distribution of  $E_{MAX}$  fields for detached anvil cloud penetration. The horizontal scale is logarithmic.

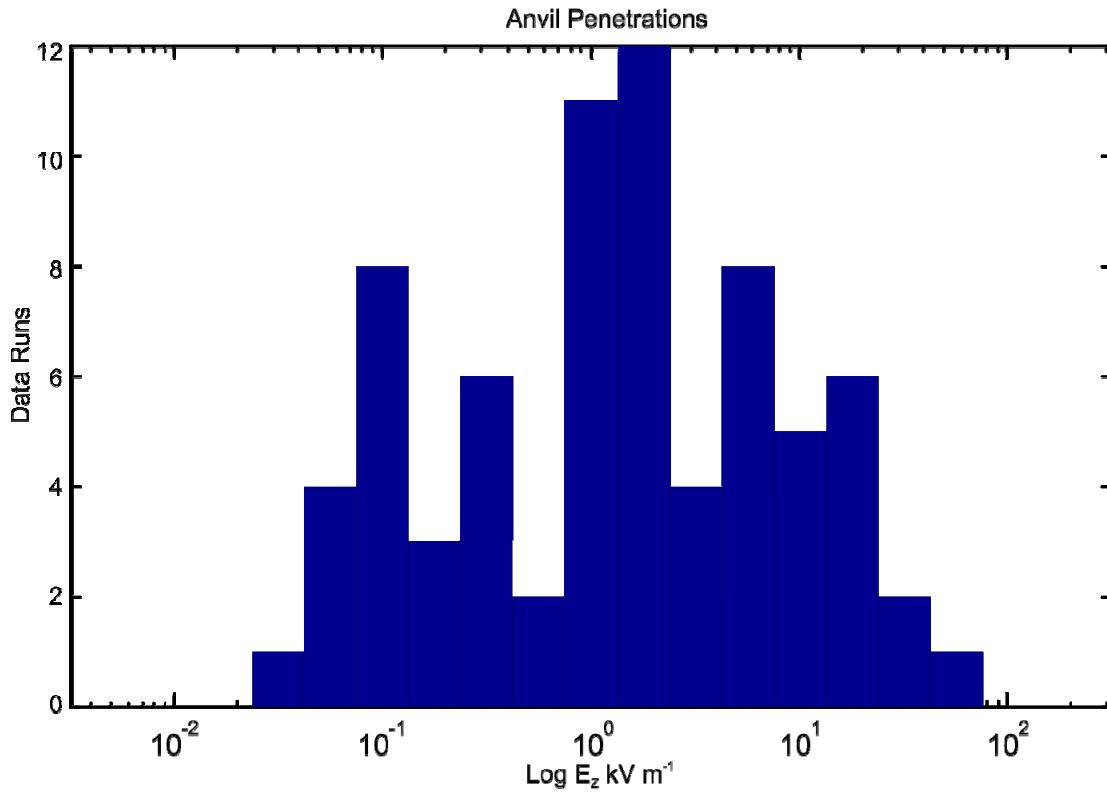


Figure B-27. Distribution of  $E_z$  fields for detached anvil cloud penetration. The horizontal scale is logarithmic.

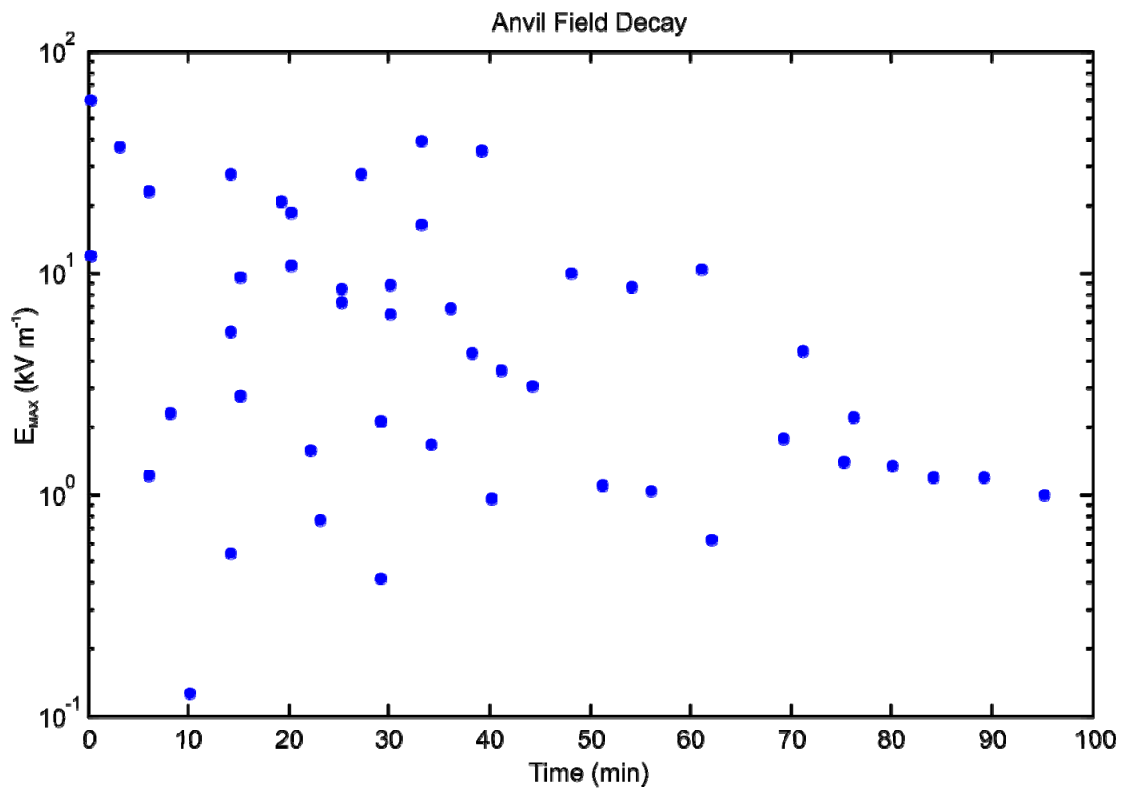


Figure B-28. Detached anvil field fall-off with time for  $E_{\text{MAX}}$  fields. The vertical scale is logarithmic.



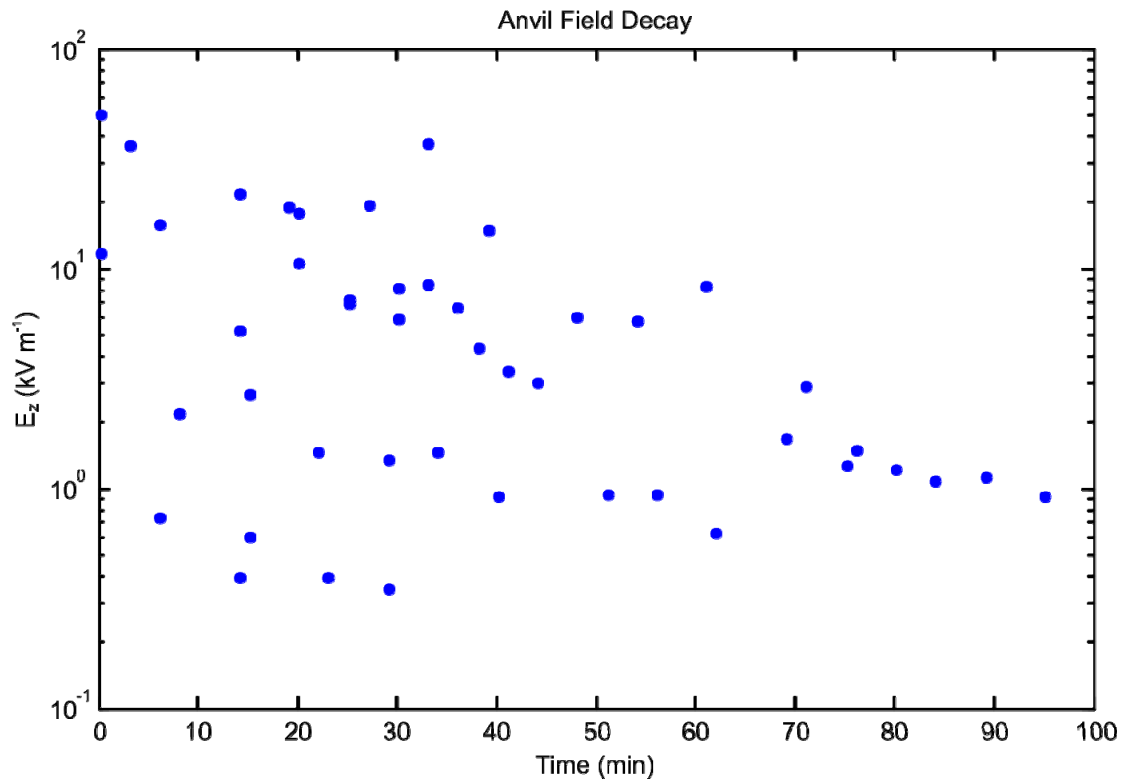


Figure B-29. Detached anvil field fall-off with time for  $E_z$  fields. The vertical scale is logarithmic.



## Appendix C. Proposed Natural and Triggered Lightning Flight Commit Criteria with Radar-Based Changes

The existing LFCC are given in 14 CFR Part 417 APPG (finalized August 25, 2006). This appendix gives a later proposed revision of the rules that were approved by the Lightning Advisory Panel in October 2008. This revised set is currently undergoing review by the FAA. The main revisions to the rules were changes to improve the ease of application and to incorporate changes to the debris and anvil rules based on a statistical analysis of radar and ABFM data from the ABFM II campaign.

### A. G417.1 General

Each of the Lightning Flight Commit Criteria (LFCC) requires clear and convincing evidence to trained weather personnel that its constraints are not violated. A launch operator must not initiate flight unless the constraints of all LFCC are satisfied. Whenever there is ambiguity about which of several LFCC applies to a particular situation, all potentially applicable LFCC must be applied. Under some conditions trained weather personnel can make a clear and convincing determination that the LFCC are not violated based on visual observations alone. However, if the weather personnel have access to additional information such as measurements from weather radar, lightning sensors, electric “field mills,” and/or aircraft, this information can be used to increase both safety and launch availability. If the additional information is within the criteria outlined in the LFCC, it would allow a launch to take place where a visual observation alone would not.

(a) This appendix provides flight commit criteria to protect against natural lightning and lightning triggered by the flight of a launch vehicle. A launch operator must apply these criteria under § 417.113 (c) for any launch vehicle that utilizes a flight safety system.

(b) The launch operator must employ:

(1) Any weather monitoring and measuring equipment needed to satisfy the lightning flight commit criteria.

(2) Any procedures needed to satisfy the lightning flight commit criteria.

(c) If a launch operator proposes any alternative lightning flight commit criteria, the launch operator must clearly and convincingly demonstrate that the alternative provides an equivalent level of safety.

### B. G417.3 Definitions, Explanations and Examples

For the purpose of this appendix, distance from an electric “field mill” is measured differently than distance from any other object or measurement point: Distance between a “radar reflectivity” or “VAHIRR” measurement point and any object or the “flight path” is the *shortest separation* (horizontal, vertical, or slant range) between that point and the *nearest part* of the object or “flight path.” Similarly, distance between the “flight path” and any object is the *shortest separation* between any point on the “flight path” the *nearest part* of that object. For example, “every point less than or equal to 1 nautical mile from the ‘flight path’” [see F. G417.11(c)(2) Attached “Anvil Clouds”] means that the “VAHIRR” threshold must be satisfied at every point throughout the entire volume defined by a 1 nautical mile radius from every point on the “flight path.” (See also the additional explanation beneath the definition of “cloud.”) In contrast, distance between a “field mill” or an “electric field measurement” and any object or the “flight path” is always measured *horizontally* between that mill or measurement point and the nearest part of the *vertical projection* of the object or “flight path” onto the surface of Earth. For example, “from the center of the ‘cloud top’ to at least

one working ‘field mill’” [see E. G417.9(d)(2) Cumulus “Clouds”] means that the *horizontal* distance between the “field mill” and a point on the surface directly beneath the center of the “cloud top” must be less than 2 nautical miles.

The following bold-face terms are defined here and appear in quotes wherever they are used in accordance with these definitions elsewhere in this appendix:

Anvil cloud means a stratiform or fibrous “cloud” produced by the upper outflow or blow-off from “thunderstorms” or convective “clouds” having tops at altitudes where the temperature is colder than or equal to -10 degrees Celsius.

Associated means that two or more “clouds” are causally related to the same “disturbed weather” system or are physically connected. “Clouds” occurring at the same time are not necessarily “associated.” A cumulus “cloud” formed locally and a cirrus layer that is physically separated from that cumulus “cloud” and that is generated by a distant source are not “associated,” even if they occur over or near the launch point at the same time.

Average cloud thickness is the altitude difference (in kilometers, km hereafter) between the average top and the average base of all clouds in the “specified volume.” The cloud base to be averaged is the higher of (1) the 0 degree Celsius level and (2) the lowest extent (in altitude) of all “radar reflectivity” measurements of 0 dBZ or greater. Similarly, the cloud top to be averaged is the highest extent (in altitude) of all “radar reflectivity” measurements of 0 dBZ or greater. Given the grid-point representation of a typical radar processor, allowance must be made for the vertical separation of grid points in computing “average cloud thickness”: The cloud base at any horizontal position shall be taken as the altitude of the corresponding base grid point minus half of the grid-point vertical separation. Similarly, the cloud top at that horizontal position shall be taken as the altitude of the corresponding top grid point plus half of this vertical separation. Thus, a cloud represented by only a single grid point having a “radar reflectivity” equal to or greater than 0 dBZ in the “specified volume” would have an “average cloud thickness” equal to the vertical grid-point separation in its vicinity.

Bright band means an enhancement of “radar reflectivity” caused by frozen hydrometeors falling and beginning to melt at any altitude where the temperature is 0 degrees Celsius or warmer.

Cloud means a visible mass of suspended water droplets or ice crystals. The “cloud” is considered to be the entire volume enclosed by the visible, “nontransparent cloud” boundary as seen by an observer, or, in the absence of a visual observation, by the 0 dBZ “radar reflectivity” boundary. A visual evaluation of transparency is preferred whenever possible.

Distance from the “cloud” to a point in question refers to the separation between the point and the nearest part of that “cloud.” Specifically, the wording, “less than or equal to 10 nautical miles from any cumulus ‘cloud’” means that the “flight path” must not penetrate either the *interior* of the “cloud” itself or the volume between 0 and 10 nautical miles, inclusive, *outside* the “cloud” boundary [for example, see E. G417.9(a), Cumulus “Clouds”]. On the other hand, “between 0 and 3 nautical miles, inclusive, from” refers *only* to the volume at a distance that is greater than or equal to 0, but less than or equal to 3, nautical miles *outside* the “cloud” boundary, specifically omitting the interior of the “cloud” itself [for example, see H. G417.15(a), “Debris Clouds”].

Cloud layer means a vertically continuous array of “clouds,” not necessarily of the same type, whose bases are approximately at the same level.

Cloud top means the visible top of the cloud, or, in the absence of a visual observation, the 0 dBZ radar top. A visual evaluation of “cloud top” is preferred whenever possible.

Cone of silence means the volume in an inverted circular cone centered on the radar that is generated by all elevation angles greater than the maximum elevation angle used in the radar scan strategy. For the purpose of “VAHRR” calculation this volume is capped by the observed maximum “cloud top” height, the observed tropopause height, or an altitude of 20 km (66 kft), whichever is lowest.

Cumulonimbus cloud means any convective “cloud” with any part at an altitude where the temperature is colder than  $-20$  degrees Celsius.

Debris cloud means any “cloud,” except an “anvil cloud,” that has become detached from a parent “cumulonimbus cloud” or “thunderstorm,” or that results from the decay of a parent “cumulonimbus cloud” or “thunderstorm.”

Disturbed weather means a weather system where dynamical processes destabilize the air on a scale larger than individual “clouds” or cells. Examples of “disturbed weather” include fronts, troughs, and squall lines.

Electric field measurement means the 1-minute arithmetic average of the vertical electric field ( $E_z$ ) at the surface of Earth, measured by a ground-based “field mill.” The polarity of the electric field is the same as that of the potential gradient; that is, the polarity of the field at Earth's surface is the same as the dominant charge overhead. Do not use interpolated electric field contours for purposes of this appendix. An “electric field measurement” less than or equal to 5 nautical miles from the “flight path” [e.g., C. G417.5(a) Surface Electric Fields] is not applicable if the altitude of the flight path everywhere above the 5 nautical mile circle around the “field mill” in question is greater than 20 km (66 kft).

Field mill is a specific class of electric-field sensor that uses a moving, grounded conductor to induce a time-varying electric charge on one or more sensing elements in proportion to the ambient electrostatic field.

Flight path means the planned nominal flight trajectory, including its vertical and horizontal uncertainties specified by the three-sigma guidance and performance deviations.

Moderate precipitation means a “precipitation” rate of 0.1 inches/hr or a “radar reflectivity” factor of 30 dBZ.

Nontransparent. “Cloud” cover is “nontransparent” if one or more of the following conditions is present:

(a) Objects above, including higher “clouds,” blue sky, and stars, are blurred, indistinct, or obscured as viewed from below; or objects below, including terrain, buildings, and lights on the ground, are blurred, indistinct, or obscured as viewed from above; when looking through the “cloud” cover at visible wavelengths (the sun and moon may not be used to evaluate transparency);

(b) Such objects are seen distinctly only through breaks in the “cloud” cover; or

(c) The “cloud” cover has a “radar reflectivity” factor of 0 dBZ or greater.

Precipitation means detectable rain, snow, hail, graupel, or sleet at the ground; virga; or a “radar reflectivity” factor greater than 18 dBZ at any altitude above the ground.

Radar reflectivity means the radar return from hydrometeors, in dBZ, measured by a meteorological radar operating at a wavelength greater than or equal to 5 cm. A “radar reflectivity” measurement is valid only in the absence of significant attenuation by intervening “precipitation” or by water or ice on the radome.

Specified volume. The volume bounded in the horizontal by vertical planes with perpendicular sides located 5.5 km (3 nautical miles) north, east, south, and west of the point at which “VAHIRR” is being computed. The volume is bounded on the bottom at the altitude where the temperature is 0 degrees Celsius, and on the top by a fixed altitude of 20 km (66 kft).

Thick cloud layer means one or more “cloud layers” whose combined vertical extent from the base of the bottom layer to the “cloud top” of the uppermost layer exceeds a thickness of 4,500 feet. “Cloud layers” are combined with neighboring layers for determining total thickness only when they are physically connected by vertically continuous “clouds,” as, for example, when towering “clouds” in one layer contact or merge with “clouds” in a layer (or layers) above.

Thunderstorm means any convective “cloud” that produces lightning.

Transparent. Any “cloud” that is not “nontransparent” is “transparent.”

Treated means that a launch vehicle satisfies both of the following conditions:

(a) All surfaces of the launch vehicle susceptible to ice particle impact are such that the surface resistivity is less than  $10^9$  “Ohms per square,” and

(b) All conductors on surfaces (including dielectric surfaces that have been coated with conductive materials) are bonded to the launch vehicle by a resistance that is less than  $10^5$  ohms.

Triboelectrification means the transfer of electrical charge between ice particles and the launch vehicle when the ice particles collide with the vehicle during flight.

Volume-Averaged, Height-Integrated Radar Reflectivity (VAHIRR) is the product of the “volume-averaged radar reflectivity” and the “average cloud thickness” in a “specified volume” surrounding any point at which “VAHIRR” is being computed (units of dBZ-km). The “specified volume” must not contain any portion of the “cone of silence” above the radar, nor any portion of any sectors that may have been blocked out for payload-safety reasons.

VAHIRR application criteria: The individual grid-point reflectivity measurements used to determine either the “volume-averaged radar reflectivity” or the “average cloud thickness” must be meteorological “radar reflectivity” measurements. For “VAHIRR”-evaluation points along the “flight path” itself (*not* those at a prescribed distance away from the “flight path”), the “volume-averaged, height-integrated radar reflectivity” is not applicable at any point that is less than or equal to 10 nautical miles from any “radar reflectivity” of 35 dBZ or greater at altitudes of 4 km (13 kft) or greater above mean sea level, nor is it applicable at any point that is less than or equal to 10 nautical miles from any type of lightning that has occurred in the previous 5 minutes.

Volume-averaged radar reflectivity is the arithmetic average (in dBZ) of the “radar reflectivity” in the “specified volume.” Normally, a radar processor will report reflectivity values interpolated onto a regular, three-dimensional array of grid points. Any such grid point in the “specified volume” is included in the average if and only if it has a “radar reflectivity” equal to or greater than 0 dBZ. If fewer than 10% of the grid points in the “specified volume” have “radar reflectivity” measurements equal to or greater than 0 dBZ, then the “volume-averaged radar

reflectivity” is either the maximum “radar reflectivity” (in dBZ) in the “specified volume,” or 0 dBZ, whichever is greater.

### **C. G417.5 Surface Electric Fields**

(a) A launch operator must not initiate flight for 15 minutes after the absolute value of any “electric field measurement” less than or equal to 5 nautical miles from the “flight path” has been greater than or equal to 1500 volts/meter.

(b) A launch operator must not initiate flight for 15 minutes after the absolute value of any “electric field measurement” less than or equal to 5 nautical miles from the “flight path” has been greater than or equal to 1000 volts/meter unless either Section 1 or Section 2 is satisfied:

(1) All clouds less than or equal to 10 nautical miles from the “flight path” are “transparent;”  
or

(2) All “clouds” less than or equal to 10 nautical miles from the “flight path” have “cloud tops” at altitudes where the temperature is warmer than +5 degrees Celsius and have not been part of convective “clouds” with “cloud tops” at altitudes where the temperature is colder than or equal to -10 degrees Celsius during the last 3 hours.

### **D. G417.7 Lightning**

(a) A launch operator must not initiate flight for 30 minutes after any type of lightning occurs in a “thunderstorm” if the “flight path” will carry the launch vehicle less than or equal to 10 nautical miles from that “thunderstorm.” An attached “anvil cloud” is not considered part of its parent “thunderstorm,” but is covered instead by Section F, Attached “Anvil Clouds.”

(b) A launch operator must not initiate flight for 30 minutes after any type of lightning occurs less than or equal to 10 nautical miles from the “flight path” unless all three of the following conditions are satisfied:

(1) The “cloud” that produced the lightning is greater than 10 nautical miles from the “flight path;”

(2) There is at least one working “field mill” less than 5 nautical miles from each such lightning discharge; and

(3) The absolute values of all “electric field measurements” less than or equal to 5 nautical miles from the “flight path,” and at each “field mill” specified in paragraph (b)(2) of this section, have been less than 1000 volts/meter for 15 minutes or longer.

### **E. G417.9 Cumulus “Clouds”**

For the purposes of this section, “cumulus ‘clouds’” do not include cirrocumulus, altocumulus, or stratocumulus “clouds.” An attached “anvil cloud” is never considered part of its parent cumulus “cloud,” but is covered instead by Section F, Attached “Anvil Clouds.” Section G, Detached “Anvil Clouds,” applies to any detached “anvil cloud.” Section H, “Debris Clouds,” applies to “debris clouds.”

(a) A launch operator must not initiate flight if the “flight path” will carry the launch vehicle less than or equal to 10 nautical miles from any cumulus “cloud” that has a “cloud top” at an altitude where the temperature is colder than or equal to -20 degrees Celsius.

(b) A launch operator must not initiate flight if the “flight path” will carry the launch vehicle less than or equal to 5 nautical miles from any cumulus “cloud” that has a “cloud top” at an altitude where the temperature is colder than or equal to -10 degrees Celsius.

(c) A launch operator must not initiate flight if the “flight path” will carry the launch vehicle through any cumulus “cloud” with its “cloud top” at an altitude where the temperature is colder than or equal to -5 degrees Celsius.

(d) A launch operator must not initiate flight if the “flight path” will carry the launch vehicle through any cumulus “cloud” that has a “cloud top” at an altitude where the temperature lies in the range from warmer than -5 degrees Celsius to colder than or equal to +5 degrees Celsius unless all three of the following conditions are satisfied:

(1) The “cloud” is not producing “precipitation;”

(2) The distance from the center of the “cloud top” to at least one working “field mill” is less than 2 nautical miles; and

(3) All “electric field measurements” less than or equal to 5 nautical miles from the “flight path,” and at each “field mill” specified in paragraph (d)(2) of this section, have been greater than -100 volts/meter, but less than +500 volts/meter, for 15 minutes or longer.

#### **F. G417.11 Attached “Anvil Clouds”**

For the purposes of this section, if there has never been lightning in or from the parent “cloud” or “anvil cloud,” sub-sections (a) and (b) shall be considered satisfied, but sub-section (c) shall still apply.

(a) A launch operator must not initiate flight if the “flight path” will carry the launch vehicle less than or equal to 10, but greater than 5, nautical miles from any attached “anvil cloud” for the first 30 minutes after the last lightning discharge in or from the parent “cloud” or “anvil cloud” unless the portion of the attached “anvil cloud” less than or equal to 10 nautical miles from the “flight path” is located entirely at altitudes where the temperature is colder than 0 degrees Celsius.

(b) A launch operator must not initiate flight if the “flight path” will carry the launch vehicle less than or equal to 5, but greater than 3, nautical miles from any attached “anvil cloud” for the first three hours after the last lightning discharge in or from the parent “cloud” or “anvil cloud” unless the portion of the attached “anvil cloud” less than or equal to 5 nautical miles from the “flight path” is located entirely at altitudes where the temperature is colder than 0 degrees Celsius.

(c) A launch operator must not initiate flight if the “flight path” will carry the launch vehicle less than or equal to 3 nautical miles from any attached “anvil cloud” unless all three of the following conditions are satisfied:

(1) The portion of the attached “anvil cloud” less than or equal to 5 nautical miles from the “flight path” is located entirely at altitudes where the temperature is colder than 0 degrees Celsius;

(2) The “volume-averaged, height-integrated radar reflectivity” is less than +10 dBZ-km (+33 dBZ-kft) at every point less than or equal to 1 nautical mile from the “flight path;” and

(3) All of the “VAHIRR application criteria” are satisfied.



## **G. G417.13 Detached “Anvil Clouds”**

For the purposes of this section, detached “anvil clouds” are never considered “debris clouds.”

For the purposes of this section, if there has never been lightning in or from the parent “cloud” or “anvil cloud,” sub-sections (a), (b), (c), and (d)(1)(i) shall be considered satisfied, but sub-sections (d)(1)(ii), and (d)(2), shall still apply.

(a) A launch operator must not initiate flight if the “flight path” will carry the launch vehicle less than or equal to 10, but greater than 3, nautical miles from a detached “anvil cloud” for the first 30 minutes after the last lightning discharge in or from the parent “cloud” or “anvil cloud” before detachment or after the last lightning discharge in or from the detached “anvil cloud” after detachment unless the portion of the detached “anvil cloud” less than or equal to 10 nautical miles from the “flight path” is located entirely at altitudes where the temperature is colder than 0 degrees Celsius.

(b) A launch operator must not initiate flight if the “flight path” will carry the launch vehicle between 0 (zero) and 3 nautical miles, inclusive, from a detached “anvil cloud” for the first 30 minutes after the time of the last lightning discharge in or from the parent “cloud” or “anvil cloud” before detachment or after the last lightning discharge in or from the detached “anvil cloud” after detachment unless all three of the following conditions are met:

(1) The portion of the detached “anvil cloud” less than or equal to 5 nautical miles from the “flight path” is located entirely at altitudes where the temperature is colder than 0 degrees Celsius;

(2) The “volume-averaged, height-integrated radar reflectivity” is less than +10 dBZ-km (+33 dBZ-kft) at every point less than or equal to 1 nautical mile from the “flight path;” and

(3) All of the “VAHIRR application criteria” are satisfied.

(c) A launch operator must not initiate flight if the “flight path” will carry the launch vehicle between 0 (zero) and 3 nautical miles, inclusive, from a detached “anvil cloud” less than or equal to 3 hours, but greater than 30 minutes, after the time of the last lightning discharge in or from the parent “cloud” or “anvil cloud” before detachment or after the last lightning discharge in or from the detached “anvil cloud” after detachment unless Section (1) or Section (2) is satisfied:

(1) This section is satisfied if all three of the following conditions are met:

(i) There is at least one working “field mill” less than 5 nautical miles from the detached “anvil cloud;”

(ii) The absolute values of all “electric field measurements” less than or equal to 5 nautical miles from the “flight path,” and at each “field mill” specified in paragraph (c)(1)(i) of this section, have been less than 1000 V/m for 15 minutes; and

(iii) The maximum radar reflectivity from any part of the detached “anvil cloud” less than or equal to 5 nautical miles from the “flight path” has been less than +10 dBZ for 15 minutes.

(2) This section is satisfied if all three of the following conditions are met:

(i) The portion of the detached “anvil cloud” less than or equal to 5 nautical miles from the “flight path” is located entirely at altitudes where the temperature is colder than 0 degrees Celsius;

(ii) The “volume-averaged, height-integrated radar reflectivity” is less than +10 dBZ-km (+33 dBZ-kft) at every point less than or equal to 1 nautical mile from the “flight path;” and

(iii) All of the “VAHIRR application criteria” are satisfied.

(d) A launch operator must not initiate flight if the “flight path” will carry the launch vehicle through a detached “anvil cloud” unless Section (1) or Section (2) is satisfied

(1) This section is satisfied if both of the following conditions are met.

(i) At least 4 hours have passed since the last lightning discharge in or from the detached “anvil cloud;” and

(ii) At least 3 hours have passed since the time that the “anvil cloud” is observed to be detached from the parent “cloud.”

(2) This section is satisfied if all three of the following conditions are met.

(i) The portion of the detached “anvil cloud” less than or equal to 5 nautical miles from the “flight path” is located entirely at altitudes where the temperature is colder than 0 degrees Celsius;

(ii) The “volume-averaged, height-integrated radar reflectivity” is less than +10 dBZ-km (+33 dBZ-kft) everywhere along the “flight path;” and

(iii) All of the “VAHIRR application criteria” are satisfied.

#### **H. G417.15 “Debris Clouds”**

The 3-hour time period defined in this Section must begin again at the time of any lightning discharge in or from the “debris cloud.”

(a) A launch operator must not initiate flight if the “flight path” will carry the launch vehicle between 0 and 3 nautical miles, inclusive, from a “debris cloud” for 3 hours after the “debris cloud” is observed to be detached from the parent “cloud;” or after the “debris cloud” is observed to have formed by the collapse of the parent “cloud top” to an altitude where the temperature is warmer than –10 degrees Celsius unless Section (1) or Section (2) is satisfied:

(1) This section is satisfied if all three of the following conditions are met:

(i) There is at least one working “field mill” less than 5 nautical miles from the “debris cloud;”

(ii) The absolute values of all “electric field measurements” less than or equal to 5 nautical miles from the “flight path” and at each “field mill” employed by paragraph (a)(1)(i) of this section has been less than 1000 volts/meter for 15 minutes or longer; and

(iii) The maximum radar reflectivity from any part of the “debris cloud” less than or equal to 5 nautical miles from the “flight path” has been less than +10 dBZ for 15 minutes or longer.

(2) This section is satisfied if all three of the following conditions are met:

(i) The portion of the “debris cloud” less than or equal to 5 nautical miles from the “flight path” is located entirely at altitudes where the temperature is colder than 0 degrees Celsius;

(ii) The “volume-averaged, height-integrated radar reflectivity” is less than +10 dBZ-km (+33 dBZ-kft) at every point less than or equal to 1 nautical mile from the “flight path;” and

(iii) All of the “VAHIRR application criteria” are satisfied.

(b) A launch operator must not initiate flight if the “flight path” will carry the launch vehicle through any “debris cloud” during the 3-hour period defined in paragraph (a) of this section, unless all three of the following conditions are met:

(1) The portion of the “debris cloud” less than or equal to 5 nautical miles from the “flight path” is located entirely at altitudes where the temperature is colder than 0 degrees Celsius;

(2) The “volume-averaged, height-integrated radar reflectivity” is less than +10 dBZ-km (+33 dBZ-kft) everywhere along the “flight path;” and

(3) All of the “VAHIRR application criteria” are satisfied.

#### **I. G417.17 “Disturbed Weather”**

(a) A launch operator must not initiate flight if the “flight path” will carry the launch vehicle through a “cloud” “associated” with “disturbed weather” that has “clouds” with “cloud tops” at altitudes where the temperature is colder than or equal to 0 degrees Celsius and that contains, less than or equal to 5-nautical miles from the “flight path,” either:

(1) “Moderate precipitation” or greater; or

(2) Evidence of melting “precipitation” such as a radar “bright band.”

#### **J. G417.19 “Thick Cloud Layers”**

For the purposes of this section neither attached nor detached “anvil clouds” are considered “thick cloud layers.”

(a) A launch operator must not initiate flight if the “flight path” will carry the launch vehicle through a “cloud layer” that is either:

(1) Greater than or equal to 4,500 feet thick and any part of the “cloud layer” along the “flight path” is located at an altitude where the temperature is between 0 degrees Celsius and –20 degrees Celsius, inclusive; or

(2) Connected to a “thick cloud layer” that, less than or equal to 5 nautical miles from the “flight path,” is greater than or equal to 4,500 feet thick and has any part located at an altitude where the temperature is between 0 degrees Celsius and –20 degrees Celsius, inclusive.

(b) A launch operator need not apply the lightning commit criteria in paragraphs (a)(1) and (a)(2) of this section if the “thick cloud layer” is a cirriform “cloud layer” that has never been “associated” with convective “clouds,” is located entirely at altitudes where the temperature is colder than or equal to –15 degrees Celsius, and shows no evidence of containing liquid water.

#### **K. G417.21 Smoke Plumes**

(a) A launch operator must not initiate flight if the “flight path” will carry the launch vehicle through any cumulus “cloud” that has developed from a smoke plume while the “cloud” is attached to

the smoke plume, or for the first 60 minutes after the cumulus “cloud” is observed to be detached from the smoke plume.

(b) Section E, Cumulus “Clouds,” applies to cumulus “clouds” that have formed above a fire but have been detached from the smoke plume for more than 60 minutes.

#### **L. G417.23 “Triboelectrification”**

A launch operator must not initiate flight if the “flight path” will carry the launch vehicle through any part of a cloud, *specifically including all “transparent” parts*, at any altitude where both Section (a) and Section (b) are satisfied:

- (a) The temperature is colder than or equal to –10 degrees Celsius; and
- (b) The launch vehicle’s velocity is less than or equal to 3000 feet/second;

unless Section (1) or Section (2) is satisfied:

- (1) The launch vehicle is “treated” for surface electrification; or
- (2) A launch operator has previously demonstrated by test or analysis that electrostatic discharges on the surface of the launch vehicle caused by “triboelectrification” will not be hazardous to the launch vehicle or the spacecraft.

## Appendix D. Criteria for Converting Cloud and Lightning Data to Lightning Launch Constraint Rule Violations

This appendix describes the scheme for converting Cloud Depiction and Forecast System Version 2 (CDFS2) cloud data, European Center for Medium Range Weather Forecasting (ECMWF) temperatures, and National Lightning Detection Network (NLDN) lightning data to infer LFCC violations according to the rules used in connection with the ABFM I campaign (see Appendix B).

**Cloud data** (CDFS II Cloud types):

cldtypes = ['cirrus', 'cirrostr', 'altocumu', 'altostra', 'stratocu', 'stratus', 'cumulus', 'cb', 'nimbostr']

cldlabel = ['Cirrus', 'Cirrostratus', 'Altostratus', 'Altostratus', 'Stratocumulus', 'Stratus', 'Cumulus', 'Cumulonimbus', 'Nimbostratus']

Let  $L = \{A, B1, B2, B3, B4, D, E, FD, FA, DLCCV\}$  contain a set of flags taking on values of 0, 1, or 2, indicating whether launch is green, red, or undetermined with respect to a given rule. The goal is to assign a value to each element of  $L$  for every hour. Rule C is the field mill rule and is not applicable and not included in the analysis.

### Rule A

*Any type of lightning is detected within 10 nautical miles of the launch site or planned flight path within 30 minutes prior to launch unless the meteorological condition that produced the lightning has moved more than 10 nautical miles away from the launch site or planned flight path.*

A=0

IF Lightning = FALSE GO TO Rule B

Launch = RED (A=1)

The area considered for Rule A must cover a 10 nm circle centered on the launch site.

### Rule B

*The planned flight path will carry the vehicle*

*(B1) through cumulus clouds with tops higher than the +5°C level; or*

*(B2) through or within 5 nautical miles of cumulus clouds with tops higher than -10°C level; or*

*(B3) through or within 10 nautical miles of cumulus clouds with tops higher than the -20°C level; or*

*(B4) through or within 10 nautical miles of the nearest edge of a cumulonimbus or thunderstorm cloud, including its associated anvil.*

{B} = {0}

IF NOT (Cu = TRUE OR Cb = TRUE) GO TO Rule D

If  $T(Z_{top}) \geq 5^{\circ}\text{C}$ , GO TO Rule D.

B1: IF ( $Cu = \text{TRUE}$  AND  $T(Z_{top}) < +5^{\circ}\text{C}$  AND  $CF > 0.2$ ) Launch = RED (B1=1)

B2: IF ( $Cu = \text{TRUE}$  AND  $T(Z_{top}) < -10\text{C}$ ), Launch = RED (B2=1)

B3: IF ( $Cu = \text{TRUE}$  AND  $T(Z_{top}) < -20\text{C}$ ), Launch=RED (B3=1)

B4: IF

$Cb = \text{TRUE}$  OR

Attached Anvil = TRUE

Launch = RED (B4=1)

Attached Anvil = TRUE IFF [ $\text{Cirrostratus} = \text{TRUE}$  AND  $\text{Lightning} = \text{TRUE}$ ]

$CF > 0.2$  is the cloud fraction associated with “through.”

For B2 the area considered must cover a 5 nm circle centered on the launch site.

For B3 and B4 the area considered must cover a 10 nm circle centered on the launch site.

## Rule D

*The planned flight path is through a vertically continuous layer of clouds with an overall depth of 4,500 feet or greater, where any part of the clouds is located between the 0 and  $-20^{\circ}\text{C}$  temperature levels.*

D = 0

IF

Cloud = LAYERED AND

$(Z_{top} - Z_{base}) \geq 4500 \text{ ft}$  AND

NOT [ $T(Z_{bot}) < -20\text{C}$  OR  $T(Z_{top}) > 0\text{C}$ ] AND

$CF > 0.8$

THEN Launch = RED (D=1)

LAYERED here denotes layered clouds (not cumulus, or cumulonimbus) and excludes cirrus (Ci).

## Rule E

*The planned flight path is through any cloud types that extend to altitudes at or above the 0°C level and that are associated with disturbed weather within 5 nautical miles of the flight path. E = 0*

E = 0

If (Nimbostratus (Ns) = TRUE AND CF > 0.6), Launch = RED (E=1)

CF > 0.6 is the fractional coverage associated with disturbed weather.

## Rule F

*Do not launch through thunderstorm debris clouds, or within 5 nautical miles of thunderstorm debris clouds not monitored by a field mill network or producing radar returns greater than or equal to 10 dBz. [Note that here we separate low/mid-level debris from high-level debris (which we call Detached Anvil) to conform to Doug Mach's ABFM I analysis.]*

FD=0

IF [Clouds = OR (Altostratus, Altostratus, Stratocumulus, Stratus, Nimbostratus) AND (Lightning at T-1 Hour = TRUE)] AND CF > 0.2 THEN FD = 1

FA=0

IF [Clouds = Cirrostratus AND (Lightning at T-1 Hour = TRUE)] AND CF > 0.6 THEN FA = 1

GO TO T+1 hour

CF > 0.2 is the cloud fraction associated with “through.”

CF > 0.6 is the cloud fraction associated with an anvil cloud.

The area considered must cover a 5 NM circle centered on the launch site.

[Among the cloud types identified in the database, the ones that might be identified as high- or lower-level debris clouds are cirrostratus, altostratus, stratocumulus, stratus, and nimbostratus.]

Since the AFBM data associates only one rule violation with a given measurement it was necessary to order the rule violations to reflect the logic used to assign a rule violation to a measurement when more than one violation occurred simultaneously. This ordering was based on discussions with Dr. Douglas Mach (NASA Marshall Space Flight Center) and Launa Maier (NASA/KSC). The ordering is given below. Lower numbers (except zero) have higher priority:

- 1 - Detached Anvil (FA)
- 2 - Lightning/Cumulonimbus/Attached Anvil (A/B4)
- 3 - Towering Cumulus (B3)
- 4 - Large Cumulus (B2)
- 5 - Modest Cumulus (B1)
- 6 - Debris clouds (FD)
- 7 - Disturbed weather (E)
- 8 - Thick cloud (D)
- 0 - No Rules Violated



## Appendix E. Table of U.S. NEXRAD Locations

Table E-1. Complete Listing of NEXRAD Sites for the U.S., Including Alaska and Hawaii  
(<http://www.roc.noa.gov>)

NCDCID	ICAO	Name	St	County	Lat	Lon
30001794	KABR	Aberdeen	SD	Brown	45.45583	-98.4131
30001795	KABX	Albuquerque	NM	Bernalillo	35.14972	-106.823
30001796	KAKQ	Norfolk Rich	VA	Sussex	36.98389	-77.0075
30001797	KAMA	Amarillo	TX	Potter	35.23333	-101.709
30001798	KAMX	Miami	FL	Dade	25.61056	-80.4131
30001799	KAPX	Gaylord	MI	Antrim	44.90722	-84.7197
30001800	KARX	La Crosse	WI	La Crosse	43.82278	-91.1911
30001801	KATX	Seattle	WA	Island	48.19472	-122.494
30001802	KBBX	Beale Afb	CA	Butte	39.49611	-121.632
30001807	KBGM	Binghamton	NY	Broome	42.19972	-75.985
30001808	KBHX	Eureka	CA	Humboldt	40.49833	-124.292
30001809	KBIS	Bismarck	ND	Burleigh	46.77083	-100.76
30001810	KBIX	Keesler Afb	MS	Harrison	30.52389	-88.9847
30001811	KBLX	Billings	MT	Yellowstone	45.85389	-108.606
30001812	KBMX	Birmingham	AL	Shelby	33.17194	-86.7697
30001813	KBOX	Boston	MA	Bristol	41.95583	-71.1375
30001814	KBRO	Brownsville	TX	Cameron	25.91556	-97.4186
30001815	KBUF	Buffalo	NY	Erie	42.94861	-78.7369
30001816	KBYX	Key West	FL	Monroe	24.59694	-81.7033
30001781	KCAE	Columbia	SC	Lexington	33.94861	-81.1186
30001782	KCBW	Houlton	ME	Aroostook	46.03917	-67.8069
30001817	KCBX	Boise	ID	Ada	43.49083	-116.234
30001783	KCCX	State College	PA	Centre	40.92306	-78.0039
30001818	KCLE	Cleveland	OH	Cuyahoga	41.41306	-81.86
30001819	KCLX	Charleston	SC	Beaufort	32.65556	-81.0422
30001821	KCRP	Corpus Christi	TX	Nueces	27.78389	-97.5108
30001822	KCXX	Burlington	VT	Chittenden	44.51111	-73.1664
30001823	KCYS	Cheyenne	WY	Laramie	41.15194	-104.806
30001824	KDAX	Sacramento	CA	Yolo	38.50111	-121.677
30001825	KDDC	Dodge City	KS	Ford	37.76083	-99.9683
30001826	KDFX	Laughlin Afb	TX	Kinney	29.2725	-100.28
30001827	KDGX	Jackson Brandon	MS	Rankin	32.28	-89.9844
30001828	KDIX	Philadelphia	NJ	Burlington	39.94694	-74.4111
30001829	KDLH	Duluth	MN	St Louis	46.83694	-92.2097
30001830	KDMX	Des Moines	IA	Polk	41.73111	-93.7228
30001831	KDOX	Dover Afb	DE	Sussex	38.82556	-75.44
30001832	KDTX	Detroit	MI	Oakland	42.69972	-83.4717

NCDCID	ICAO	Name	St	County	Lat	Lon
30001833	KDVN	Davenport	IA	Scott	41.61167	-90.5808
30001834	KDYX	Dyess Afb	TX	Shackelford	32.53833	-99.2542
30001835	KEAX	Kansas City	MO	Cass	38.81028	-94.2642
30001836	KEMX	Tucson	AZ	Pima	31.89361	-110.63
30001837	KENX	Albany	NY	Albany	42.58639	-74.0644
30001838	KEOX	Ft Rucker	AL	Dale	31.46028	-85.4594
30001839	KEPZ	El Paso	NM	Dona Ana	31.87306	-106.698
30001841	KESX	Las Vegas	NV	Clark	35.70111	-114.891
30001842	KEVX	Eglin Afb	FL	Walton	30.56417	-85.9214
30001843	KEWX	Austin San Antonio	TX	Comal	29.70361	-98.0281
30001943	KEYX	Edwards	CA	Santa Barbara	35.09778	-117.56
30001844	KFCX	Roanoke	VA	Floyd	37.02417	-80.2742
30001845	KFDR	Altus Afb	OK	Tillman	34.36222	-98.9761
30001846	KFDX	Cannon Afb	NM	Curry	34.63528	-103.629
30001847	KFFC	Atlanta	GA	Fayette	33.36333	-84.5658
30001944	KFSD	Sioux Falls	SD	Minnehaha	43.58778	-96.7289
30001848	KFSX	Flagstaff	AZ	Coconino	34.57444	-111.197
30001849	KFTG	Denver Front Range Ap	CO	Arapahoe	39.78667	-104.545
30001850	KFWS	Dallas	TX	Tarrant	32.57278	-97.3028
30001851	KGWV	Glasgow	MT	Valley	48.20639	-106.624
30001852	KGJX	Grand Junction	CO	Mesa	39.06222	-108.213
30001853	KGLD	Goodland	KS	Sherman	39.36694	-101.7
30001854	KGRB	Green Bay	WI	Brown	44.49833	-88.1111
30001855	KGRK	Ft Hood	TX	Bell	30.72167	-97.3828
30001856	KGRR	Grand Rapids	MI	Kent	42.89389	-85.5447
30001857	KGSP	Greer	SC	Spartanburg	34.88306	-82.2203
30001858	KGWX	Columbus Afb	MS	Monroe	33.89667	-88.3289
30001859	KGYX	Portland	ME	Cumberland	43.89139	-70.2569
30001945	KHDX	Holloman Afb	NM	Dona Ana	33.07639	-106.122
30001860	KHGX	Houston	TX	Galveston	29.47194	-95.0789
30001861	KHNX	San Joaquin Valley	CA	Kings	36.31417	-119.631
30001862	KHPX	Ft Campbell	KY	Todd	36.73667	-87.285
30001863	KHTX	Huntsville	AL	Jackson	34.93056	-86.0836
30001864	KICT	Wichita	KS	Sedgwick	37.65444	-97.4425
30001865	KICX	Cedar City	UT	Iron	37.59083	-112.862
30001866	KILN	Cincinnati	OH	Clinton	39.42028	-83.8217
30001867	KILX	Lincoln	IL	Logan	40.15056	-89.3367
30001868	KIND	Indianapolis	IN	Marion	39.7075	-86.2803
30001869	KINX	Tulsa	OK	Rogers	36.175	-95.5644
30001870	KIWA	Phoenix	AZ	Maricopa	33.28917	-111.669
30001871	KIWX	Ft Wayne	IN	Kosciusko	41.40861	-85.7

NCDCID	ICAO	Name	St	County	Lat	Lon
30001872	KJAX	Jacksonville	FL	Duval	30.48444	-81.7019
30001873	KJGX	Robins Afb	GA	Twiggs	32.675	-83.3511
30001874	KJKL	Jackson	KY	Breathitt	37.59083	-83.3131
30001875	KLBB	Lubbock	TX	Lubbock	33.65417	-101.814
30001876	KLCH	Lake Charles	LA	Calcasieu	30.125	-93.2158
30001877	KLIX	New Orleans	LA	St Tammany	30.33667	-89.8253
30001878	KLNX	North Platte	NE	Logan	41.95778	-100.576
30001879	KLOT	Chicago	IL	Will	41.60444	-88.0847
30001880	KLRX	Elko	NV	Lander	40.73972	-116.803
30001881	KLSX	St Louis	MO	St Charles	38.69889	-90.6828
30001882	KLTX	Wilmington	NC	Brunswick	33.98917	-78.4292
30001883	KLVX	Louisville	KY	Hardin	37.97528	-85.9439
30001884	KLWX	Sterling	VA	Loudoun	38.97528	-77.4781
30001885	KLZK	Little Rock	AR	Pulaski	34.83639	-92.2619
30001886	KMAF	Midland Odessa	TX	Midland	31.94333	-102.189
30001887	KMAX	Medford	OR	Jackson	42.08111	-122.716
30001888	KMBX	Minot Afb	ND	Mchenry	48.3925	-100.864
30001889	KMHX	Morehead City	NC	Carteret	34.77583	-76.8764
30001890	KMKX	Milwaukee	WI	Waukesha	42.96778	-88.5506
30001891	KMLB	Melbourne	FL	Brevard	28.11306	-80.6544
30001892	KMOB	Mobile	AL	Mobile	30.67944	-88.2397
30001893	KMPX	Minneapolis	MN	Carver	44.84889	-93.5653
30001894	KMQT	Marquette	MI	Marquette	46.53111	-87.5483
30001895	KMRX	Knoxville	TN	Hamblen	36.16833	-83.4019
30001896	KMSX	Missoula	MT	Missoula	47.04111	-113.986
30001897	KMTX	Salt Lake City	UT	Salt Lake	41.26278	-112.447
30001898	KMUX	San Francisco	CA	Santa Clara	37.15528	-121.898
30001899	KMVX	Grand Forks	ND	Traill	47.52806	-97.325
30001900	KMXX	Maxwell Afb	AL	Tallapoosa	32.53667	-85.7897
30001901	KNKX	San Diego	CA	San Diego	32.91889	-117.042
30001902	KNQA	Memphis	TN	Shelby	35.34472	-89.8733
30001903	KOAX	Omaha	NE	Douglas	41.32028	-96.3664
30001904	KOHX	Nashville	TN	Wilson	36.24722	-86.5625
30001905	KOKX	New York City	NY	Suffolk	40.86556	-72.8644
30001906	KOTX	Spokane	WA	Spokane	47.68056	-117.626
30001907	KPAH	Paducah	KY	Mccracken	37.06833	-88.7719
30001908	KPBZ	Pittsburgh	PA	Allegheny	40.53167	-80.2183
30001909	KPDT	Pendleton	OR	Umatilla	45.69056	-118.853
30001910	KPOE	Ft Polk	LA	Vernon	31.15528	-92.9758
30001911	KPUX	Pueblo	CO	Pueblo	38.45944	-104.181
30001912	KRAX	Raleigh Durham	NC	Wake	35.66528	-78.49

NCDCID	ICAO	Name	St	County	Lat	Lon
30001913	KRGX	Reno	NV	Washoe	39.75417	-119.461
30001914	KRIW	Riverton	WY	Fremont	43.06611	-108.477
30001915	KRLX	Charleston	WV	Kanawha	38.31194	-81.7239
30001916	KRMX	Portland	OR	Washington	45.715	-122.964
30001917	KSFX	Pocatello	ID	Bingham	43.10583	-112.685
30001918	KSGF	Springfield	MO	Greene	37.23528	-93.4003
30001920	KSHV	Shreveport	LA	Caddo	32.45056	-93.8411
30001921	KSJT	San Angelo	TX	Tom Green	31.37111	-100.492
30001922	KSOX	Santa Ana Mountains	CA	Orange	33.81778	-117.635
30001948	KSRX	Ft Smith	AR	Sebastian	35.29056	-94.3617
30001923	KTBW	Tampa	FL	Hillsborough	27.70528	-82.4019
30001925	KTFX	Great Falls	MT	Cascade	47.45972	-111.384
30001924	KTLH	Tallahassee	FL	Leon	30.3975	-84.3289
30001926	KTLX	Oklahoma City	OK	Oklahoma	35.33306	-97.2775
30001927	KTWX	Topeka	KS	Wabaunsee	38.99694	-96.2325
30001946	KTYX	Ft Drum	NY	Lewis	43.75583	-75.68
30001928	KUDX	Rapid City	SD	Pennington	44.125	-102.829
30001929	KUEX	Hastings	NE	Webster	40.32083	-98.4417
30001947	KVAX	Moody Afb	GA	Lanier	30.89	-83.0019
30001930	KVBX	Vandenberg Afb	CA	Santa Barbara	34.83806	-120.396
30001931	KVNX	Vance Afb	OK	Alfalfa	36.74083	-98.1275
30001932	KVTX	Los Angeles	CA	Ventura	34.41167	-119.179
30001609	KVWX	Evansville	IN	Gibson	38.26	-87.7247
30001934	KVWX	Yuma	AZ	Pima	32.49528	-114.656
30001939	PABC	Bethel Faa	AK	Bethel	60.79278	-161.874
30001940	PACG	Sitka	AK	Sitka	56.85278	-135.529
30001941	PAEC	Nome	AK	Nome	64.51139	-165.295
30001942	PAHG	Anchorage	AK	Kenai Peninsula	60.72639	-151.349
30001958	PAIH	Middleton Island	AK	Valdez-Cordova	59.46194	-146.301
30001959	PAKC	King Salmon	AK	Bristol Bay	58.67944	-156.629
30001960	PAPD	Fairbanks	AK	Fairbanks North Star	65.03556	-147.499
30001962	PHKI	South Kauai	HI	Kauai	21.89417	-159.552
30001963	PHKM	Kamuela	HI	Hawaii	20.12556	-155.778
30001964	PHMO	Molokai	HI	Hawaii	21.13278	-157.18
30001965	PHWA	South Shore	HI	Hawaii	19.095	-155.569

## Appendix F. The Variation of Lightning Occurrence Versus the Current Icing Potential Index

Table F-1. Lightning Occurrence in CIP Bins for 4 Months over a 4-Year Data Set (2004–2007) for the Various Spaceports (MJSP, OS, SA, and WTLS)

<b>Lightning Occurrences &lt; 100 km</b>					
<b>Site\Bin</b>	<b>0.0–0.2</b>	<b>0.2–0.4</b>	<b>0.4–0.6</b>	<b>0.6–0.8</b>	<b>0.8–1.0</b>
<b>January</b>					
MJSP	3	0	6	6	3
OS	4	2	5	16	16
SA	3	2	5	1	0
WTLS	10	6	1	0	4
<b>Totals</b>	<b>20</b>	<b>10</b>	<b>17</b>	<b>23</b>	<b>23</b>
<b>April</b>					
MJSP	27	5	6	18	8
OS	98	28	8	12	50
SA	83	33	16	12	52
WTLS	98	24	10	11	45
<b>Totals</b>	<b>306</b>	<b>90</b>	<b>40</b>	<b>53</b>	<b>155</b>
<b>July</b>					
MJSP	112	4	8	0	11
OS	231	22	12	23	34
SA	512	74	71	74	109
WTLS	410	64	38	36	70
<b>Totals</b>	<b>1265</b>	<b>164</b>	<b>129</b>	<b>133</b>	<b>224</b>
<b>October</b>					
MJSP	25	7	8	14	32
OS	95	25	13	15	51
SA	126	30	14	19	47
WTLS	125	20	15	22	43
<b>Totals</b>	<b>371</b>	<b>82</b>	<b>50</b>	<b>70</b>	<b>173</b>

Table F-2. The Number of CIP Determinations in CIP Bins for 4 Months over a 4-Year Data Set (2004–2007) for the Various Spaceports (MJSP, OS, SA, and WTLS)

<b>Total CIP Determinations per Bin</b>					
<b>Site\Bin</b>	<b>0.0–0.2</b>	<b>0.2–0.4</b>	<b>0.4–0.6</b>	<b>0.6–0.8</b>	<b>0.8–1.0</b>
<b>January</b>					
MJSP	861	115	48	66	54
OS	1835	230	130	163	183
SA	1900	234	129	112	167
WTLS	1433	208	118	94	134
<b>Totals</b>	<b>6029</b>	<b>787</b>	<b>425</b>	<b>435</b>	<b>538</b>
<b>April</b>					
MJSP	1900	115	66	87	72
OS	1789	194	68	79	112
SA	1913	159	65	33	72
WTLS	1839	187	68	57	90
<b>Totals</b>	<b>7441</b>	<b>655</b>	<b>267</b>	<b>256</b>	<b>346</b>
<b>July</b>					
MJSP	2223	35	33	15	30
OS	2112	60	52	48	64
SA	1733	160	132	146	165
WTLS	1840	159	99	95	142
<b>Totals</b>	<b>7908</b>	<b>414</b>	<b>316</b>	<b>304</b>	<b>401</b>
<b>October</b>					
MJSP	2248	84	38	39	66
OS	2068	109	88	81	128
SA	2125	125	67	69	88
WTLS	2161	99	71	61	82
<b>Totals</b>	<b>8602</b>	<b>417</b>	<b>264</b>	<b>250</b>	<b>364</b>

Table F-3. The Lightning Occurrence Frequency in CIP Bins for 4 Months over a 4-Year Data Set (2004–2007) for the Various Spaceports (MJSP, OS, SA, and WTLS). Values are Determined from Tables F-1 and F-2.

<b>Occurrence Frequencies</b>					
<b>Site\Bin</b>	<b>0.0–0.2</b>	<b>0.2–0.4</b>	<b>0.4–0.6</b>	<b>0.6–0.8</b>	<b>0.8–1.0</b>
<b>January</b>					
MJSP	0.00	0.00	0.13	0.09	0.06
OS	0.00	0.01	0.04	0.10	0.09
SA	0.00	0.01	0.04	0.01	0.00
WTLS	0.01	0.03	0.01	0.00	0.03
<b>Totals</b>	<b>0.00</b>	<b>0.01</b>	<b>0.04</b>	<b>0.05</b>	<b>0.04</b>
<b>April</b>					
MJSP	0.01	0.04	0.09	0.21	0.11
OS	0.05	0.14	0.12	0.15	0.45
SA	0.04	0.21	0.25	0.36	0.72
WTLS	0.05	0.13	0.15	0.19	0.50
<b>Totals</b>	<b>0.04</b>	<b>0.14</b>	<b>0.15</b>	<b>0.21</b>	<b>0.45</b>
<b>July</b>					
MJSP	0.05	0.11	0.24	0.00	0.37
OS	0.11	0.37	0.23	0.48	0.53
SA	0.30	0.46	0.54	0.51	0.66
WTLS	0.22	0.40	0.38	0.38	0.49
<b>Totals</b>	<b>0.16</b>	<b>0.40</b>	<b>0.41</b>	<b>0.44</b>	<b>0.56</b>
<b>October</b>					
MJSP	0.01	0.08	0.21	0.36	0.48
OS	0.05	0.23	0.15	0.19	0.40
SA	0.06	0.24	0.21	0.28	0.53
WTLS	0.06	0.20	0.21	0.36	0.52
<b>Totals</b>	<b>0.04</b>	<b>0.20</b>	<b>0.19</b>	<b>0.28</b>	<b>0.48</b>





## Appendix G. The Monthly and Seasonal Variation of Rule Violations

This appendix gives the rule violation statistics by site and by month, averaged over all hours and by hour averaged over all months. The rules are summarized in Table G-1. These rules are based on the rules that were used to identify rule violations in the ABFM I campaign. They are discussed in more detail in Appendix D.

Table G-1. Weather Categories Used to Prioritize rule Violations During the ABFM I Campaign

Priority Category	Description
1	Detached Anvil
2	Lightning or Cumulonimbus or Attached Anvil
3	Large Cumulus
4	Moderate Cumulus
5	Small Cumulus
6	Debris Cloud
7	Disturbed Weather
8	Layered Cloud

### G.1 Rule Violations by Hour

Figures G-1 through G-6 show the rule violations by hour, averaged over all representative months (January, April, July, and October).

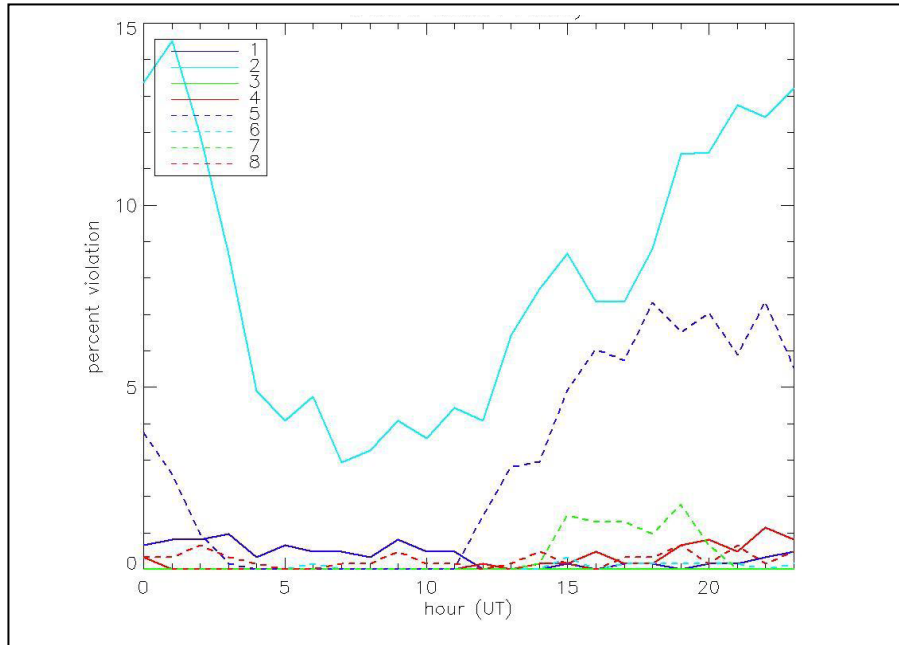


Figure G-1. Variation of the frequency of rule violations by Priority Category (see Table G-1) by hour at CCAFS. The statistics are averaged over the months of January, April, July, and October and averaged over the year.

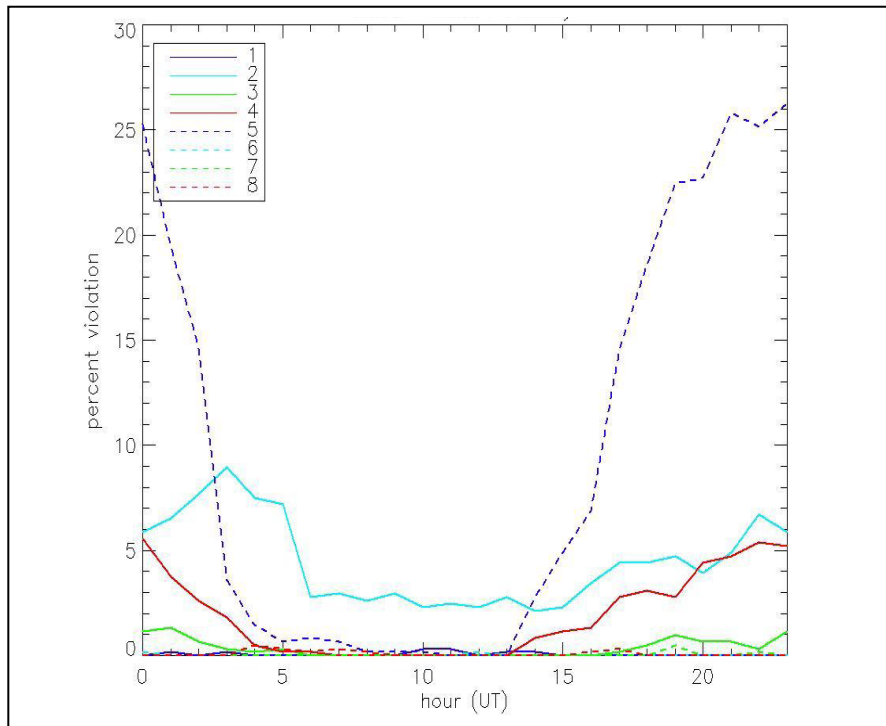


Figure G-2. Same as Figure G-1 except for MJSP.

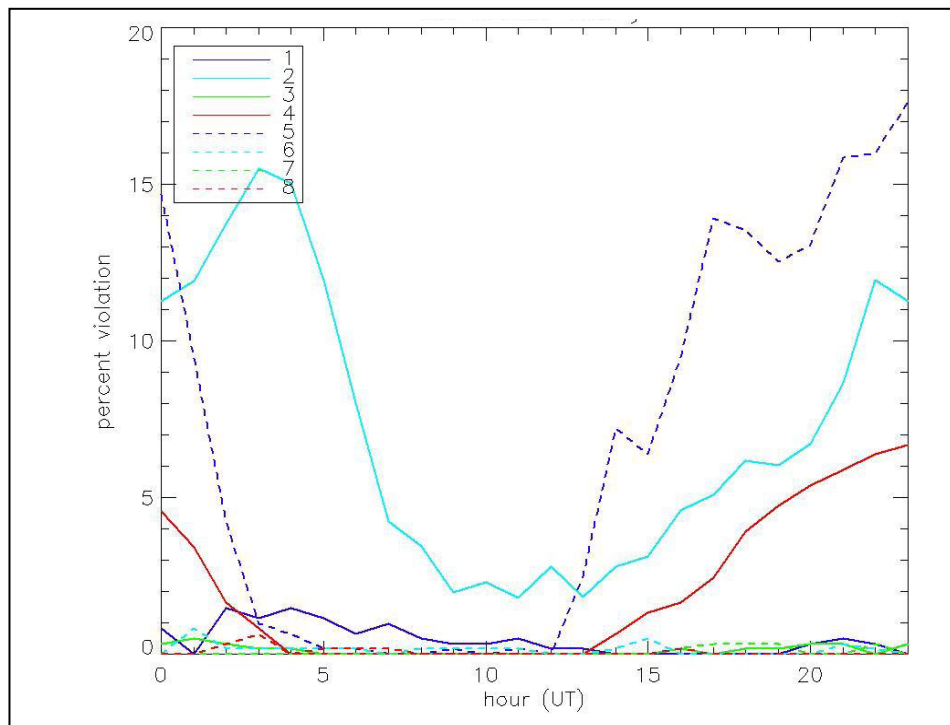


Figure G-3. Same as Figure G-1 except for SA.

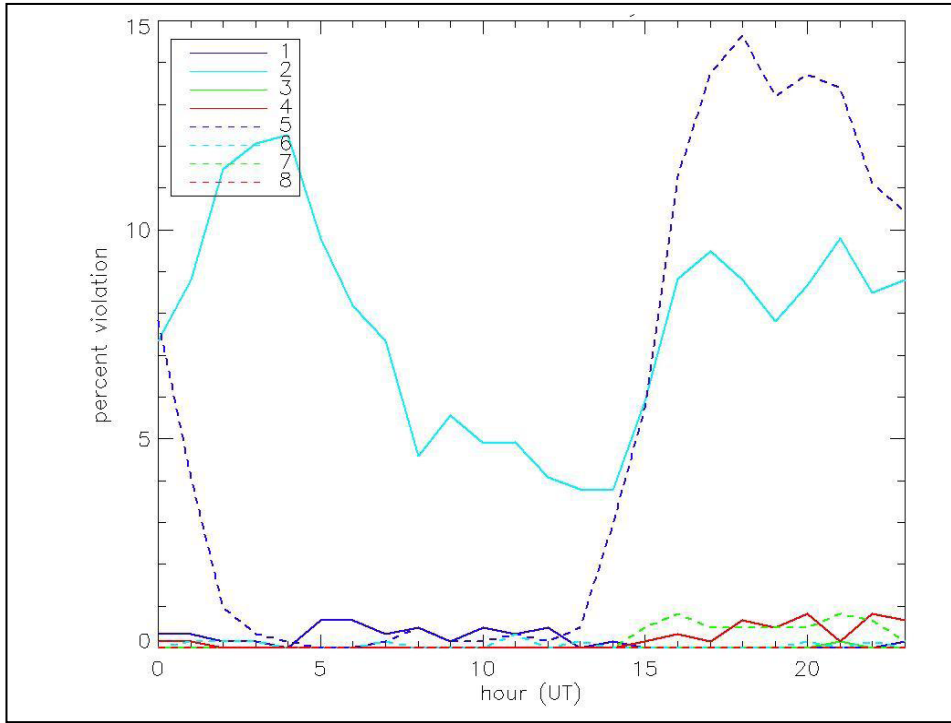


Figure G-4. Same as Figure G-1 except for OS.

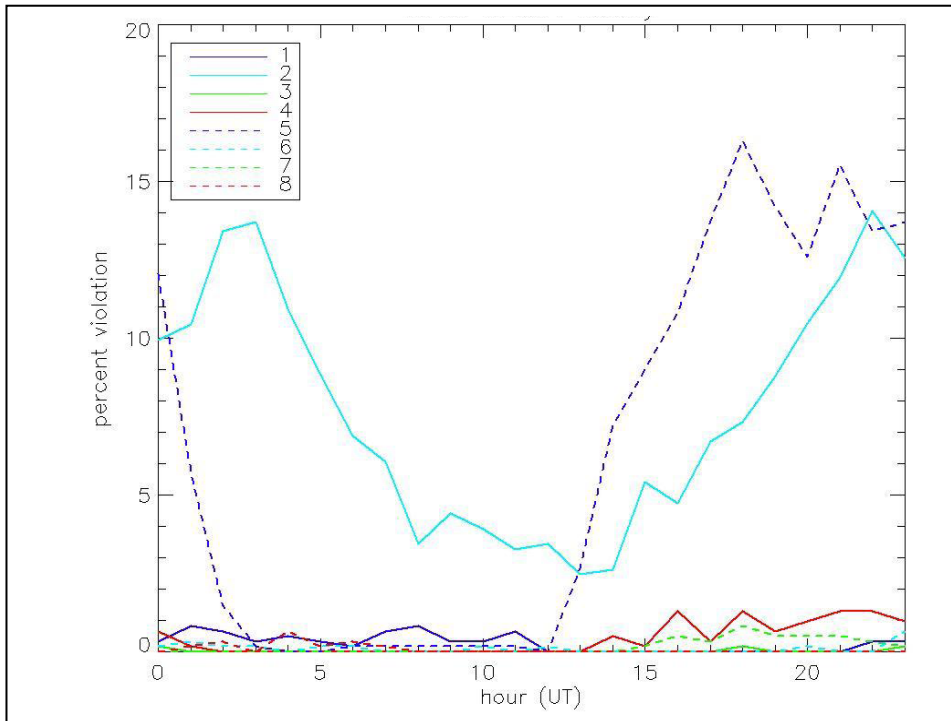


Figure G-5. Same as Figure G-1 except for WTLS.

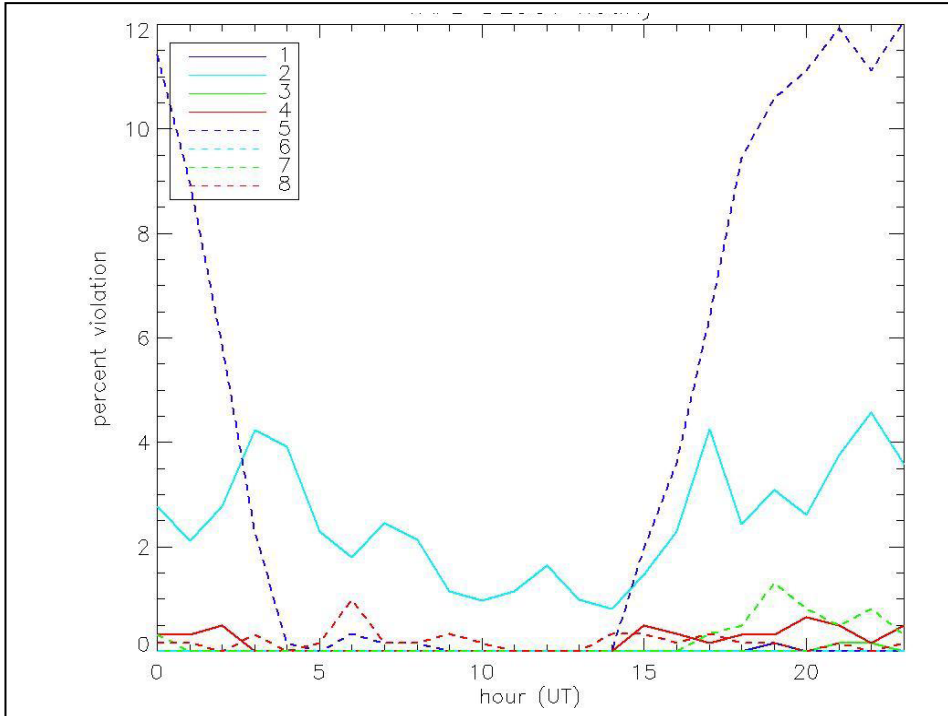


Figure G-6. Same as Figure G-1 except for VAFB.

## G.2 Rule Violations by Month

Figures G-7 through G-12 show the rule violations by month, averaged over all hours.

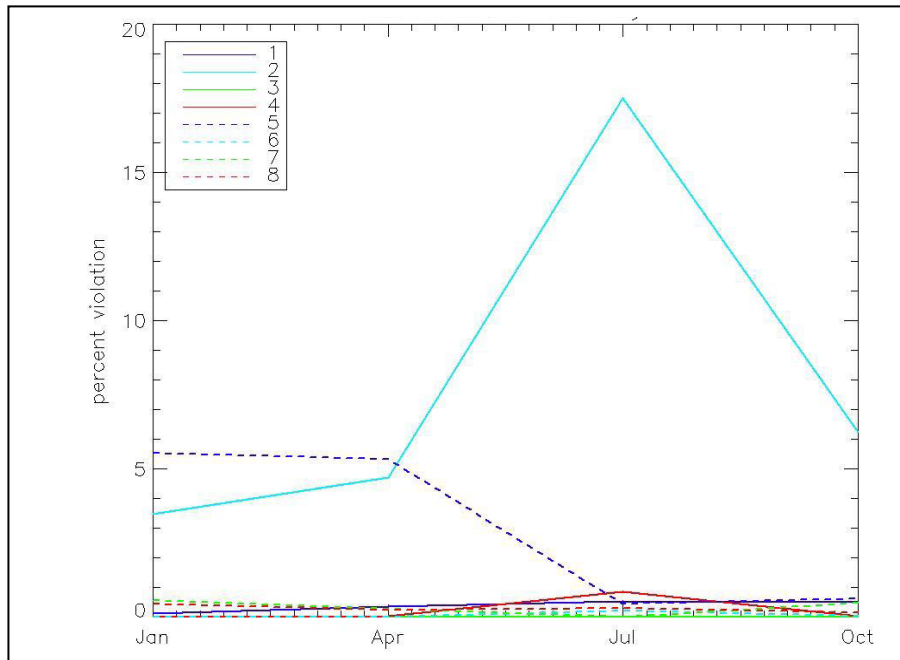


Figure G-7. This figure shows the variation of the frequency of rule violations by Priority Category (see Table G-1) by month at CCAFS. The statistics are averaged over all hours.

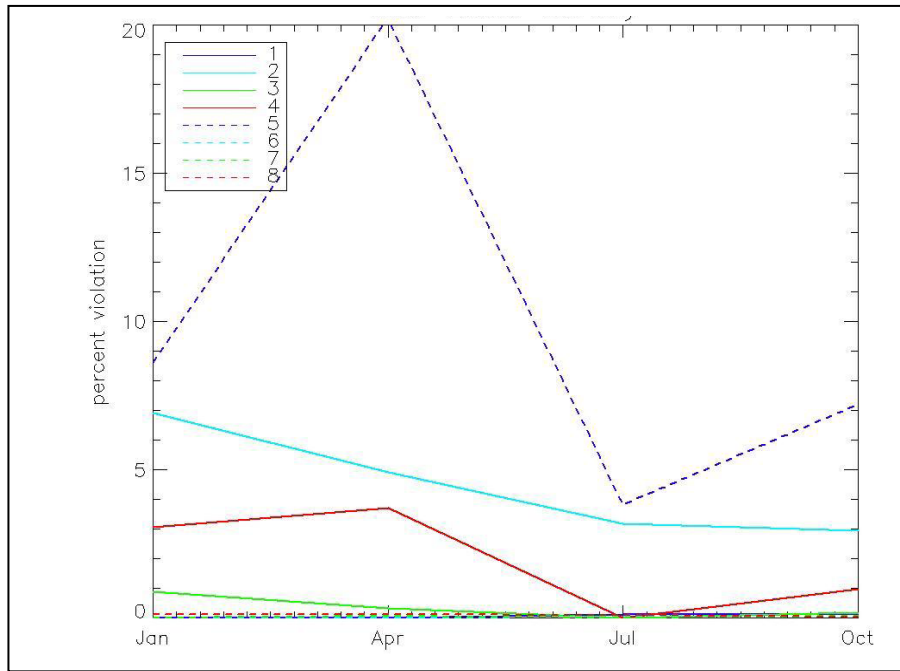


Figure G-8. Same as G-7 except for MJSP.

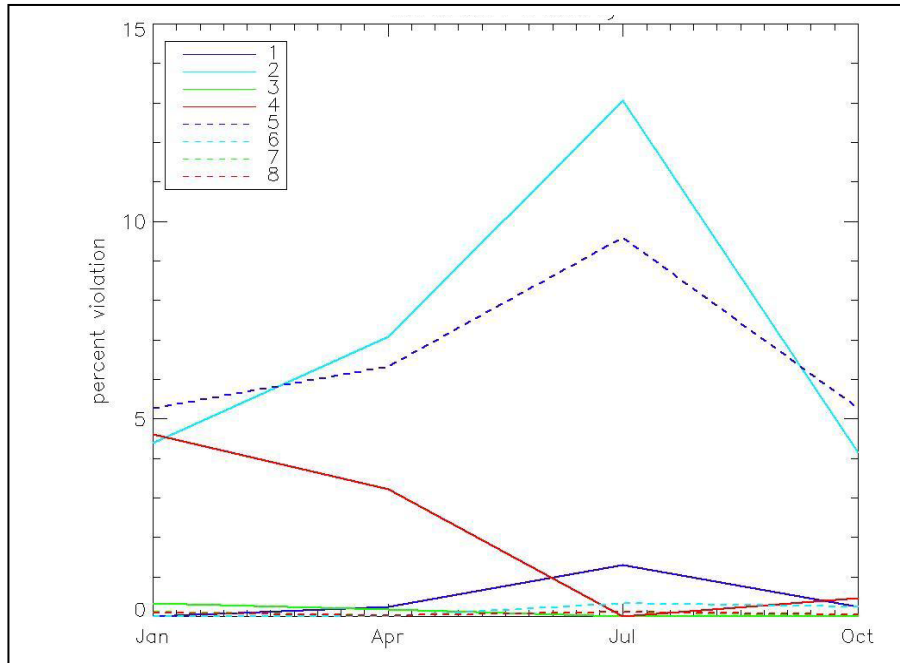


Figure G-9. Same as G-7 except for SA.

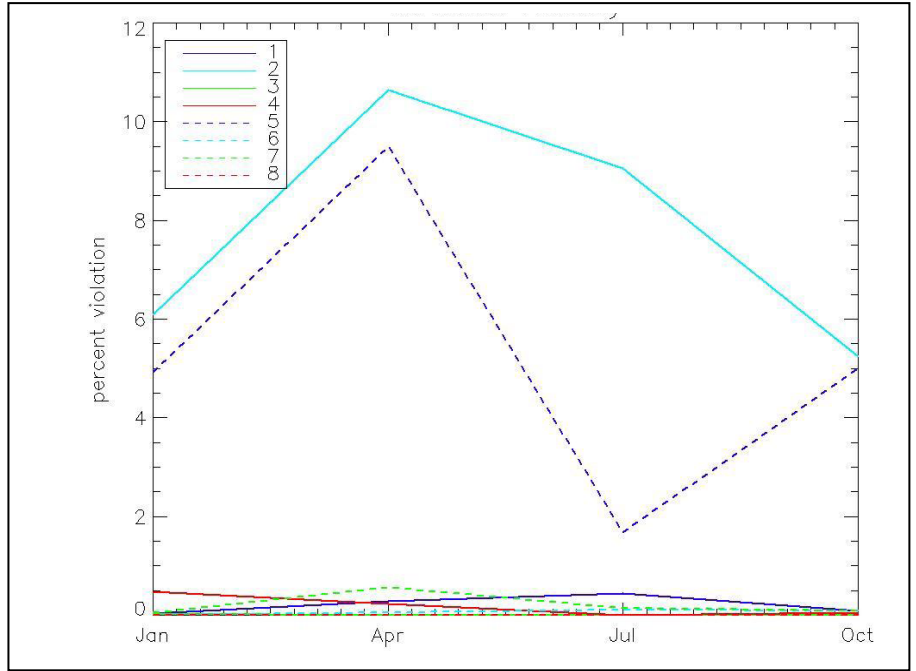


Figure G-10. Same as G-7 except for OS.

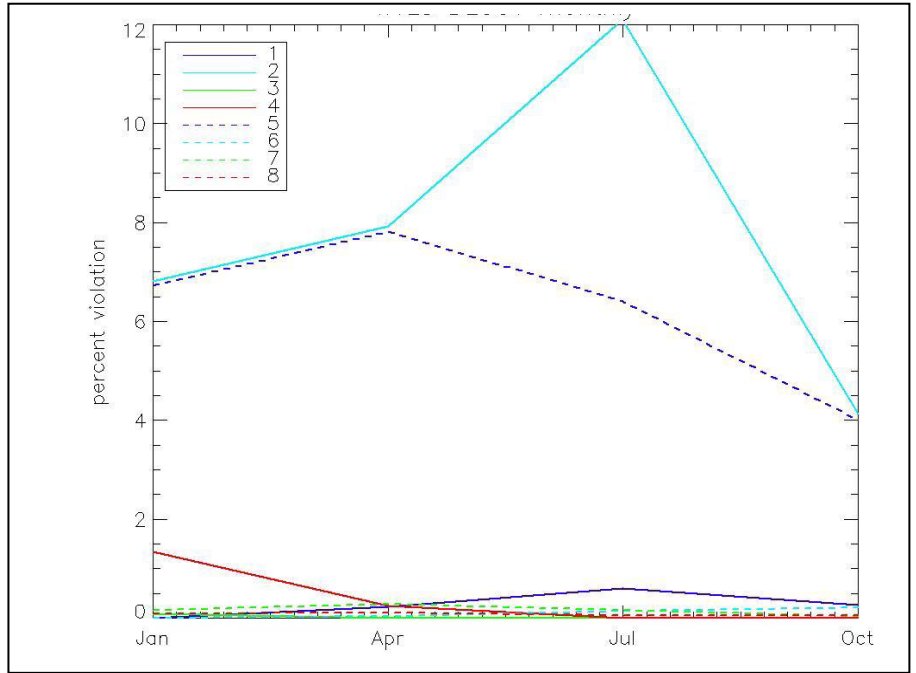


Figure G-11. Same as G-7 except for WTLS.

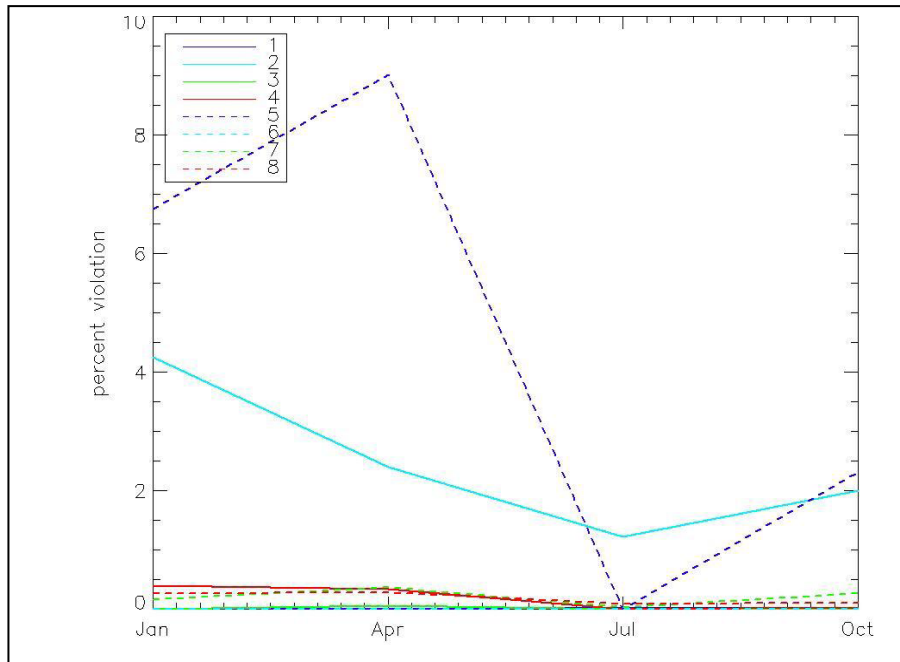


Figure G-12. Same as G-7 except for VAFB.